UNIVERSITY OF CAMBRIDGE

Hydrodynamic coupling and synchronization of colloidal oscillators

Nicolas Bruot

Corpus Christi College

Thesis submitted for the Degree of
Doctor of Philosophy

Version history:

1.0	(14/08/2013)	Examiners' version
1.1	(23/10/2013)	Minor corrections
1.2	(21/11/2013)	Online version

Hydrodynamic coupling and synchronization of colloidal oscillators

Nicolas Bruot

Summary

The synchronization of cilia in biological tissues was first observed decades ago, attracting the attention of researchers across various disciplines. Firstly, cilia interact with a surrounding fluid, described by the laws of hydrodynamics at low Reynolds number. This regime of the Navier-Stokes equation was largely unknown at the beginning of the 20th century, and the way objects like cilia interact with the fluid started to be studied in pioneering work by Taylor, Gray and Hancock in the 1950s. Secondly, the hydrodynamics at play in microscopic active systems like cilia leads to a coupling interaction between the objects of the system, and represents a class of synchronizing systems. Synchronization in general has been a very active and broad topic from the end of the 20th century. However, many questions regarding the synchronization of cilia were only addressed in the last decade, and remain open to date. This research is motivated by the idea that knowing how cilia act as active elements to generate a fluid flow, and how the cooperative behaviour of cilia arrays emerges, could help screening and understanding rare genetic diseases involving the loss of synchronization or motility of cilia. Understanding the hydrodynamics and swimming at micrometric scales is also a prerequisite for building some microrheology devices and, maybe in the future, nanobots.

This thesis focuses on experimental models of oscillators, made of colloidal particles driven by optical tweezers. Several oscillators are coupled through the hydrodynamic interaction only, and help understanding the properties of synchronization of cilia and flagella.

Chapter 1 provides background on the hydrodynamic interaction at low Reynolds number, explaining in particular how to describe the forces exerted

from the fluid on a spherical particle, coming from the motion of other surrounding particles. Such hydrodynamic interactions lead to coupling forces between different objects, and is possibly the key to the synchronization of cilia. Chapter 2 is an introduction to cilia and flagella, and reviews the existing models of oscillators designed to describe the cyclic motion of these biological micro-motors and study how different oscillators couple.

Most of the models described above are first studied analytically and/or in numerical simulations. This thesis presents the experimental implementation of two models of oscillators, and the extension of the theory that was associated with them. In Chapter 3, I describe the optical tweezers setup used to apply controlled forces to the particles to implement the oscillators.

Chapters 4, 5 and 6 present results on "rowers" that are one-dimensional (with a well defined beat direction), intrinsically nonlinear, two-state oscillators. This simple model lead to many findings: determination of a threshold of Brownian motion for the loss of synchronization, control of the locked state of two "rowers", and a normal modes analyzis method to obtain information on the dynamical solution of any given configuration of rowers. Chapter 7 describes an extension of this model of oscillator that adds freedom in the direction of beating. Arrays of these oscillators can synchronize, but also align, making the hydrodynamic interaction a good candidate to explain the alignment of cilia during their growth.

In Chapters 8 and 9, the synchronization of another model oscillator is discussed, the "rotors". These are beads driven along circular trajectories. In Chapter 8, a two-rotors experiment validates two existing theoretical mechanisms leading to synchronization: the shape of the driving force profile, and the flexibility of the orbit compared to the prescribed trajectory. The cooperative behaviour of configurations of more than two rotors, like chains propagating a phase pattern (metachronal wave) are described in Chapter 9.

Declaration

This thesis:

- is my own work and contains nothing which is the outcome of work done in collaboration with others, except where specified in the text;
- is not substantially the same as any that I have submitted for a degree or diploma or other qualification at any other university; and
- does not exceed the prescribed limit of 60,000 words.

Nicolas Bruot
14 August 2013

Acknowledgements

I would like to thank the people that helped me accomplishing this work, in particular my supervisor, Pietro Cicuta, who provided excellent advice on the directions this thesis should take, resulting in a very productive work. It always followed from meetings with him, a lot of ideas on how to solve a problem, or what new aspects should be considered. Another special thank also comes to Jurij Kotar, who has built the two optical tweezers setups that I used in my experiments. His knowledge on electronics and programming was critical to the success of the experiments, as they require an equipment pushed to its limits. I am also very grateful to Aidan Brown, Young-Zoon Yoon, Simon Wongsuwarn, Lucia Parolini and Will Fletcher, as well as the rest of the Biological and Soft Systems group, that helped me in the lab, to Romain Lhermerout, Maya Juenet and Antonin Gallet, who are master students that contributed to the work, and Marco Cosentino Lagomarsino, Marco Polin, Hermes Gadêlha, Douglas Brumley, Luke Debono, Nariya Uchida, Ramin Golestanian and Roberto Di Leonardo for useful discussions.

Contents

II Methods 55

III Synchronization of two-state rowers 71

5 Effect of the driving force profile on the state of synchronization of two rowers 85

6 Understanding the dynamics in systems of many rowers 99

Publications list

Some chapters of this thesis are partly reproduced from the the following research articles:

- **Noise and synchronization of a single active colloid**
  N. Bruot, L. Damet, J. Kotar, P. Cicuta and M. Cosentino Lagomarsino
  Phys. Rev. Lett., vol. 107, p. 094101, 2011
- **Collective synchronization states in arrays of driven colloidal oscillators**
  R. Lhermerout, N. Bruot, G. M. Cicuta, J. Kotar and P. Cicuta
  New J. Phys., vol. 14, p. 105023, 2012
- **Driving potential and noise level determine the synchronization state of hydrodynamically coupled oscillators**
  N. Bruot, J. Kotar, F. de Lillo, M. Cosentino Lagomarsino and P. Cicuta
  Phys. Rev. Lett., vol. 109, p. 164103, 2012
- **Emergence of polar order and cooperativity in hydrodynamically coupled model cilia**
  N. Bruot and P. Cicuta
  J. R. Soc. Interface, vol. 10, 2013
- **Optimal hydrodynamic synchronization of colloidal rotors**
  J. Kotar, L. Debono, N. Bruot, S. Box, D. Phillips, S. Simpson, S. Hanna and P. Cicuta
  Submitted, 2013

Part I

Introduction

Chapter 1

Hydrodynamic interaction at micrometric scales

1.1 Introduction

Hydrodynamics describes a wide range of natural phenomena at various scales. Convective motions in the Earth's mantle [1, 2], air flows in meteorology or in the study of the drag of a plane, the swimming of fish or smaller millimetric aqueous organisms, or even smaller, bacteria, are all described by the same Navier-Stokes equation of hydrodynamics. However, depending on the system, different terms can dominate in this equation, leading to different behaviours. In particular, the dimensionless Reynolds number, which compares the viscous forces and the inertial forces, separates different regimes of behaviour of the fluid. In the previous examples, the Earth's mantle and the bacteria are systems dominated by viscous forces [3], while fish and planes rely on inertial forces. In intermediate systems like small aqueous organisms, both resistive forces and acceleration are important, which makes the hydrodynamics of such systems very complex [4].

This chapter describes hydrodynamics from the perspective of colloidal sciences, at a micrometric length scale. It presents the equation of fluid dynamics and its simplification at low Reynolds number. Under some assumptions, the interaction between solid objects in a fluid can be described by a mobility tensor relating the forces acting on the objects to their velocities. Different tensors can be used, depending on the geometric parameters describing the objects and their positions, and depending on the presence of a solid wall that adds a no-slip boundary condition of the fluid in the vicinity of the wall.

1.2 Navier-Stokes equation

The evolution of the velocity field $\mathbf{u}(\mathbf{r}, t)$ of an incompressible fluid is described by the Navier-Stokes equation [5]

$$\rho\left[\frac{\partial \mathbf{u}}{\partial t} + \left(\mathbf{u} \cdot \vec{\nabla}\right)\mathbf{u}\right] = -\vec{\nabla} p + \eta \nabla^2 \mathbf{u} + \mathbf{f} \ , \tag{1.1}$$

where $p(\mathbf{r}, t)$ is the pressure field, η the viscosity of the fluid, ρ its density and $\mathbf{f}(\mathbf{r}, t)$ includes all external volumetric forces, such as gravity. This nonlinear equation can describe the fluid dynamics of very different systems, from weather predictions to the flow generated by a swimming bacteria. It cannot be solved analytically in the general case. Solving it in particular cases usually also involves the use of the equation of conservation of mass in the system [5]

$$\frac{\partial \rho}{\partial t} + \vec{\nabla} \cdot (\rho \mathbf{u}) = 0 \tag{1.2}$$

that simplifies into

$$\vec{\nabla} \cdot \mathbf{u} = 0 \tag{1.3}$$

for an incompressible fluid.

1.3 Low Reynolds number flows

Hydrodynamics at the scale of cells or bacteria exhibit large differences with the fluid dynamics of conventional macroscopic systems. The main difference resides in the Reynolds number which is the ratio between the inertial forces and the viscous forces of a system of a typical size L, with typical flow velocity u:

$$Re = \frac{F_{\text{inertial}}}{F_{\text{viscous}}} = \frac{\rho u L}{\eta} \ . \tag{1.4}$$

Considering a biological system of *E. coli* bacteria in water, $L \sim 1$ μm, $u \sim 10$ μm·s^{-1}, $\rho \sim 10^3$ kg·m^{-3} and $\eta \sim 10^{-3}$ Pa·s. The corresponding Reynolds number is 10^{-5}. (For comparison, $Re \sim 10^4$ for a human swimmer.) In this low Reynolds number regime, the flow is laminar and dominated by viscous forces that lead to simplifications in the Navier-Stokes equation (1.1):

$$\rho \frac{\partial \mathbf{u}}{\partial t} = -\vec{\nabla} p + \eta \nabla^2 \mathbf{u} + \mathbf{f} \ . \tag{1.5}$$

The inertial term $\rho\left(\mathbf{u} \cdot \vec{\nabla}\right)\mathbf{u}$ has been neglected compared to the viscous forces $\eta \nabla^2 \mathbf{u}$. In micrometric systems, "usual" volumetric forces, such as gravitation, can be neglected in the external volumetric force field $\mathbf{f}$, so that $\mathbf{f} = 0$.

1.4 Stokes equation

Eq. (1.5) can be solved for a semi-infinite fluid at $z > 0$ lying on top of an infinite plane in the directions (x, y) that is subject to sinusoidal oscillations of amplitude U_0 along x at an angular frequency ω. At the surface of the plane at $z = 0$, a no-slip boundary condition is assumed. This condition is valid for most surfaces and fluids, when looking at colloidal length scales (1 μm minimum), as the slip length is typically of the order of 10 nm [6, 7]. The velocity of the fluid at $z = 0$ is therefore equal to the velocity of the plane:

$$u_x(0, t) = U_0 \exp\left(\mathrm{i}\,\omega t\right) \ . \tag{1.6}$$

The resulting velocity field of the flow, obtained by solving the Navier-Stokes equation, describes a fluid that oscillates by following the motion of the plane in its vicinity and does not move far from the plane:

$$u_x(z, t) = U_0 \exp\left[-(1 + \mathrm{i})\frac{z}{\delta}\right] \exp\left(\mathrm{i}\,\omega t\right) \ , \tag{1.7}$$

with $\delta = \sqrt{\dfrac{2\eta}{\omega\rho}}$ that characterizes the attenuation length of the oscillations. At the bacteria scale, in water, $\eta \sim 10^{-3}$ Pa·s, $\rho \sim 10^{3}$ kg·m^{-3} and $\omega \sim$ 50 rad·s^{-1}, so $\delta \sim 200$ μm. This length is much larger than the size of the bacteria and — at least in this thesis — the range at which the hydrodynamic interaction is studied. It can therefore be considered that the action of a moving particle induces all changes to the fluid instantly, which leads to the Stokes equation [5, 8]:

$$0 = -\vec{\nabla} p + \eta \nabla^2 \mathbf{u} + \mathbf{f} \ . \tag{1.8}$$

As no more time derivatives appear in the equation of motion of the fluid, a "swimmer" with a *cyclic* motion needs to use at least two configurational degrees of freedom to be able to modify the drag coefficient and generate an average net flow. This is known as the scallop theorem, well explained by Purcell in 1977 [3]:

> (...) I change my body into a certain shape and then I go back to the original shape by going through the sequence in reverse. (...) Time, in fact, makes no difference — only configuration. (...) So if the animal tries to swim by a reciprocal motion, it *can't go anywhere.*

This problem occurs at low Reynolds number, because, if an organism stops to move, all the fluid around it will stop moving as well. Micro-swimmers are therefore very different from macroscopic swimmers. As Sir Geoffrey Taylor mentioned in 1951 [9], the latter take advantage of the inertial forces to propel themselves in one direction. By swimming, they create circulations of the fluid that are not stopped when the propulsive motion is stopped. These inertial flows create an efficient propulsive force by dynamical reaction. A scallop is a good example of a "swimmer", with only one degree of freedom (the opening angle of the shell) that uses these inertial forces. By closing its shell quickly, the scallop will move forward over a large distance, while by opening it slowly, the inertial forces will be reduced and it will create a reverse motion of the scallop much smaller than the preceding forward move. This results in a net forward motion over a cycle. In a low Reynolds number environment, the scallop would just move back and forth, without net direction of motion. Small swimmers like flagellated microorganisms cannot use this property to move:

if they stop their configuration change, the surrounding fluid stops moving instantaneously and no propulsive force is maintained by inertia. Therefore, to move in a given direction in average, they need a more complex cycle of body deformation [10, 11], with at least two degrees of freedom, often referred as *non-reciprocal cycle.*

An analogy helps to understand how dramatic the situation is for micrometric swimmers: By estimations of the Reynolds number, microorganisms swim in an environment that is equivalent to an ant trying to propel in very viscous fluid, typically such as peanut butter, at a velocity of a few millimetres per second. This image gives both an idea of how swimming looks like in a flow dominated by viscosity, and of the big forces the organism has to deploy to move one part of its body in the fluid (keeping in mind the small size of the swimmer).

Taking the numbers for *E. coli* in Section 1.3, two quantities related to inertial effects can be estimated: The characteristic time for the bacteria to stop after being given an impulse u is about $Re \times L/u \sim 1$ μs (assuming the mass of the bacteria is ρL^3), and the distance it would travel thanks to the impulse is only 10 pm, thus justifying that inertial effects can be neglected for microswimmers.

1.5 Stokes drag on a sphere

Similarly to the oscillating plane that was generating an oscillating flow, a single driven particle excerts a force on the fluid. More precisely, if the particle is maintained at a constant velocity $\mathbf{v}$ in the fluid (with no angular momentum), it will feel a resistive force $-\mathbf{F}$ opposite to the force $\mathbf{F}$ acting on the fluid [8]:

$$\mathbf{F} = \boldsymbol{\gamma}\mathbf{v} \ , \tag{1.9}$$

where $\boldsymbol{\gamma}$ is the resistance matrix (of size 3×3 in 3d). Note that a torque might also result from the applied translational momentum.

This is a general result, in which inertial terms are neglected as a consequence of the low Reynolds number. The matrix $\boldsymbol{\gamma}$ depends on the shape of the object and can be calculated in simple geometries. For a spherical particle of radius a, the problem can be solved analytically, and $\boldsymbol{\gamma}$ is diagonal such that $\mathbf{F}$ is simply proportional to $\mathbf{v}$:

$$\mathbf{F} = \gamma \mathbf{v} \ , \tag{1.10}$$

with $\gamma = 6\pi\eta a$ (Stokes drag) [12].

The fluid flow $\mathbf{u}(\mathbf{r})$ generated by the particle at $\mathbf{r}_0$ can be calculated in the far field by assuming that the particle exerts a single-point force on the fluid:

$$\mathbf{f}(\mathbf{r}) = \mathbf{F}\delta(\mathbf{r} - \mathbf{r}_0) \ . \tag{1.11}$$

Here, δ is the Dirac delta function. Note that $\mathbf{f}$ is a volumetric force, but its integral over the whole space is $\mathbf{F}$.

Since Eqs. (1.3) and (1.8) are linear, and since the dynamics is supposed slow enough to assume an instant propagation of the fluid flow because of the application of the force $\mathbf{f}$ (see Section 1.4), the fluid flow far from the sphere can be written

$$\mathbf{u}(\mathbf{r}) = \mathbf{T}(\mathbf{r} - \mathbf{r}_0)\mathbf{F} \ . \tag{1.12}$$

Here, $\mathbf{u}(\mathbf{r})$ represents the solution of the equations of the flow generated by a point-like delta force. Such a solution is called a *Stokeslet* [13]. $\mathbf{T}$ is a 3×3 matrix (in 3d), the Oseen matrix, and can be calculated by solving Eqs. (1.3) and (1.8). To the leading term in a/r, the solution is [5, 14]:

$$\mathbf{T}(\mathbf{r}) = \frac{1}{8\pi\eta r}(\mathbf{I} + \hat{\mathbf{e}}_r \otimes \hat{\mathbf{e}}_r) \ , \tag{1.13}$$

where $\hat{\mathbf{e}}_r$ is the unit vector in the direction of $\mathbf{r}$, $\mathbf{I}$ is the unit matrix and $\otimes$ represents the dyadic tensorial product.

1.6 Oseen tensor

The aim of this section is to derive the hydrodynamic interaction that couples the velocities of several particles depending on the driving forces acting on them. Eqs. (1.12) and (1.13) give the fluid flow generated by a single particle

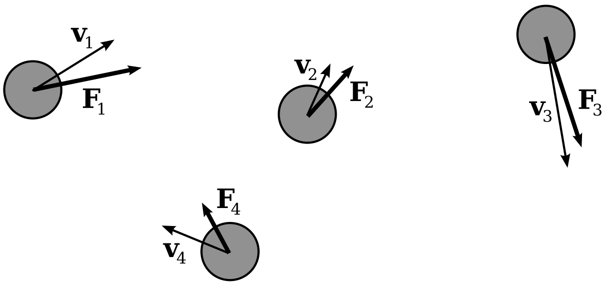

Figure 1.1: N particles are driven by forces $\mathbf{F}_i$. This driving results in the velocities $\mathbf{v}_i$, constant if the forces are constant, as inertia is neglected. The individual velocities are not exactly in the same direction as the forces, because of hydrodynamic coupling through the fluid that surrounds the particles.

driven with a force $\mathbf{F}$. Because of the no-slip boundary condition on any particle, if another particle, not driven, is placed at a position $\mathbf{r}$, the velocity of that particle, induced by the presence of the first driven particle, is the velocity of the fluid $\mathbf{u}(\mathbf{r})$, as given by Eq. (1.12).

By superposition it is easy to generalize the previous result to a system of N spherical particles, like in Fig. 1.1. This is a powerful method, as non-spherical objects, like filaments can be described as an ensemble of spheres, each acting as a Stokeslet [15]. Each particle i, at a position $\mathbf{r}_i$, is driven by a force $\mathbf{F}_i$. It also has a velocity $\mathbf{v}_i$ that results from the driving force acting on that particle, but also from all the coupling forces from the other particles that propagate through the fluid flow. In the general case, the superposition of Stokeslets created by several moving particles can be written:

$$\mathbf{v}_i = \sum_{j=1}^{n} \boldsymbol{\mu}_{i,j} \mathbf{F}_j \ . \tag{1.14}$$

$\boldsymbol{\mu}$ is called the mobility matrix and is a $N \times N$ array which elements $\boldsymbol{\mu}_{i,j}$ are second-rank tensors (3×3 matrices in 3d). The whole mobility matrix is therefore described by $(3N)^2$ scalars. When superposing Stokeslets described by Eqs. (1.12) and (1.13),

$$\boldsymbol{\mu} = \mathbf{H} \ , \tag{1.15}$$

with **H** the Oseen tensor, equal to [5, 14]:

$$\mathbf{H}_{i,j} = \begin{cases} \dfrac{1}{8\pi\eta r_{i,j}}(\mathbf{I} + \hat{\mathbf{e}}_{i,j} \otimes \hat{\mathbf{e}}_{i,j}) & \text{if} \quad i \neq j \\ \dfrac{\mathbf{I}}{6\pi\eta a} & \text{if} \quad i = j \end{cases} . \tag{1.16}$$

$r_{i,j} = |\mathbf{r}_i - \mathbf{r}_j|$ is the distance between particles i and j, **I** denotes the unit tensor, and $\hat{\mathbf{e}}_{i,j}$ is a unit vector in the direction defined by the two particles i and j. In the above expression, the diagonal terms $i = j$ are given by the Stokes formula for the drag for a spherical particle, and the non diagonal terms are given by Eq. (1.12). This result holds for particles far away ($r_{i,j} \gg a$), as it neglects the size of the particles.

The Oseen tensor estimates the hydrodynamic coupling very well in most of the experiments described later in this thesis. It can be used both in numerical simulations and theoretical calculations, to input hydrodynamic coupling in the equations of motion of a system of several colloidal particles. An important comment about this formula is that the coupling between different beads decays slowly, as $1/r$. The hydrodynamic coupling is therefore often referred as a long-range interaction [5, 16, 17] which suggests that it can lead to strong synchronization [18] in large arrays of oscillators like cilia.

1.7 Rotne-Prager tensor

The calculation of the Oseen tensor assumed that the flows generated by each bead could be superposed separately. This is a calculation of the hydrodynamic interaction to the leading order in $a/r_{i,j}$. A more accurate higher order calculation takes into account the fact that the flow $\mathbf{u}_1(\mathbf{r})$ created by a moving particle $i = 1$ will be perturbed by the presence of another particle $i = 2$ (moving or not), that is building a “reflected” flow $\mathbf{u}_2(\mathbf{r})$ [5, 8]. When considering only a single reflection, the total flow is $\mathbf{u} = \mathbf{u}_1 + \mathbf{u}_2$. Looking at the effect of the presence of particle 2 on the velocity of the particle 1 requires another step of reflection, leading to the flow field $\mathbf{u} = \mathbf{u}_1 + \mathbf{u}_2 + \mathbf{u}_3$. This flow can then be used to deduce the velocity $\mathbf{v}_1$ of the first particle. The first corrective term added by this “reflections” method to the previous Oseen tensor is in $(a/r_{i,j})^3$ [19]. To include this term, it is however required to take into account two other corrections. The first one is to write Eqs. (1.12) and (1.13) up to the third order:

$$\mathbf{T}(\mathbf{r}) = \frac{1}{6\pi\eta r}\left[\frac{3a}{4r}(\mathbf{I} + \hat{\mathbf{e}}_r \otimes \hat{\mathbf{e}}_r) + \frac{1}{4}\left(\frac{a}{r}\right)^3 (\mathbf{I} - 3\,\hat{\mathbf{e}}_r \otimes \hat{\mathbf{e}}_r)\right] . \tag{1.17}$$

The second correction takes into account that a spherical particle at position $\mathbf{r}$ in a non-uniform flow field $\mathbf{u}(\mathbf{r})$ undergoes translation motion slightly different from the only flow velocity $\mathbf{u}(\mathbf{r})$:

$$\mathbf{v} = \frac{1}{6\pi\eta a}\mathbf{F} + \left(1 + \frac{a^2}{6}\nabla^2\right)\mathbf{u}(\mathbf{r}) \ , \tag{1.18}$$

assuming that the particle also feels a driving force $\mathbf{F}$. This is called the *Faxén theorem for translation* [5].

All together, the corrections above lead to the following mobility matrix, called the Rotne-Prager tensor [5]:

$$\boldsymbol{\mu}_{i,j} = \begin{cases} \dfrac{1}{6\pi\eta a}\left[\dfrac{3a}{4r_{i,j}}(\mathbf{I} + \hat{\mathbf{e}}_{i,j} \otimes \hat{\mathbf{e}}_{i,j}) + \dfrac{1}{2}\left(\dfrac{a}{r_{i,j}}\right)^3 (\mathbf{I} - 3\hat{\mathbf{e}}_{i,j} \otimes \hat{\mathbf{e}}_{i,j})\right] & \text{if} \quad i \neq j \\ \dfrac{\mathbf{I}}{6\pi\eta a} & \text{if} \quad i = j \end{cases} , \tag{1.19}$$

to the third order in $a/r_{i,j}$. Note that it was considered that only translational forces were applied to the particles. If external torques are also acting on the particles, the Rotne-Prager tensor is described by four matrices that can be calculated [5]: $\boldsymbol{\mu}^{\mathrm{tt}}$, $\boldsymbol{\mu}^{\mathrm{rr}}$, $\boldsymbol{\mu}^{\mathrm{tr}}$ and $\boldsymbol{\mu}^{\mathrm{rt}}$ where “t” denotes translation and “r” rotation. For example $\boldsymbol{\mu}^{\mathrm{tr}}$ describes the effect of torques on particles on their translational velocities. With these notations, the Rotne-Prager tensor is written

$$\begin{pmatrix} \mathbf{v}_i \\ \boldsymbol{\omega}_i \end{pmatrix} = \sum_{j=1}^{N} \begin{pmatrix} \boldsymbol{\mu}^{\mathrm{tt}}_{i,j} & \boldsymbol{\mu}^{\mathrm{tr}}_{i,j} \\ \boldsymbol{\mu}^{\mathrm{rt}}_{i,j} & \boldsymbol{\mu}^{\mathrm{rr}}_{i,j} \end{pmatrix} \begin{pmatrix} \mathbf{F}_j \\ \mathbf{G}_j \end{pmatrix} , \tag{1.20}$$

with $\mathbf{G}_i$ the external driving torque acting on particle i, and $\boldsymbol{\omega}_i$ its angular velocity.

The reflection method can be iterated several times to obtain higher order corrections.

1.8 Blake tensor

The tensors derived in Sections 1.6 and 1.7 are valid for an infinite fluid (unbounded). However, many biological systems involve the hydrodynamic coupling between objects that are moving close to a wall, with a no-slip boundary condition. The Blake tensor aims to address this question. This section provides expressions for the mobility matrix for a system of N particles, in the case of a wall located in the (x, y) plane at $z = 0$, as depicted on Fig. 1.2.

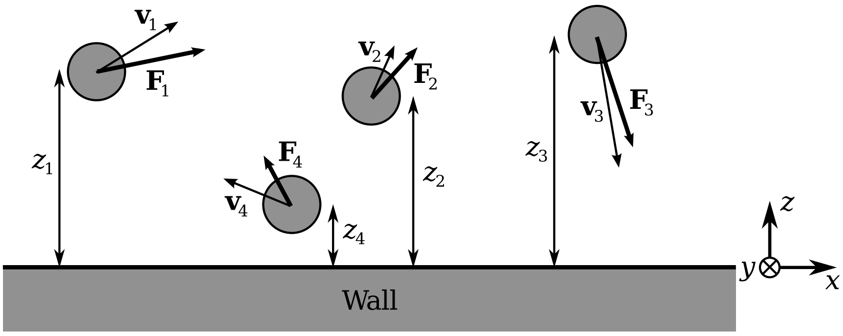

Figure 1.2: N particles, driven by forces $\mathbf{F}_i$ move at velocities $\mathbf{v}_i$. The wall, with a no-slip boundary condition, sets a new constraint on the fluid flow, that changes the hydrodynamic coupling between the particles, compared to the case of an infinite fluid.

1.8.1 Drag on a sphere near a surface

The presence of a wall with no-slip boundary conditions changes the drag coefficient on a sphere. Correcting terms to the Stokes drag can be added as a series expansion in a/z_i with a the sphere radius and z_i the distance between the particle and the surface [20]. An expansion to the sixth order has already been used to study the flow generated by arrays of artificial cilia [21]. The corresponding diagonal terms of $\boldsymbol{\mu}$ are:

$$\boldsymbol{\mu}_{i,i}^{x,x} = \boldsymbol{\mu}_{i,i}^{y,y} = \frac{1}{6\pi\eta a}\left[1 - \frac{9a}{16z_i} + \frac{1}{8}\left(\frac{a}{z_i}\right)^3 - \frac{1}{16}\left(\frac{a}{z_i}\right)^5\right] \tag{1.21a}$$

$$\boldsymbol{\mu}_{i,i}^{z,z} = \frac{1}{6\pi\eta a}\left[1 - \frac{9a}{8z_i} + \frac{1}{2}\left(\frac{a}{z_i}\right)^3 - \frac{1}{8}\left(\frac{a}{z_i}\right)^5\right] \tag{1.21b}$$

$$\boldsymbol{\mu}_{i,i}^{\alpha,\beta} = 0 \text{ for } \alpha \neq \beta \ . \tag{1.21c}$$

1.8.2 Non-diagonal terms neglecting the size of the particles

To find the non diagonal terms $\boldsymbol{\mu}_{i,j}$ $(i \neq j)$ of the mobility matrix, Blake proposed in [22] to describe the fluid flow created by a Stokeslet near a surface by an image method (as in electrostatics). In this method, the no-slip boundary condition at the wall is satisfied by describing the effect of the wall as equivalent to an infinite fluid, but with a second Stokeslet at the mirror position of the first Stokeslet and with an opposite force. For N particles, this leads to the following expressions for the Blake mobility matrix [22, 23]:

$$\boldsymbol{\mu}_{i,j}^{\mathrm{B}} = \frac{1}{8\pi\eta}\left[\mathbf{G}^{\mathrm{S}}(\mathbf{r}_i - \mathbf{r}_j) - \mathbf{G}^{\mathrm{S}}(\mathbf{r}_i - \bar{\mathbf{r}}_j) + 2z_j^2\mathbf{G}^{\mathrm{D}}(\mathbf{r}_i - \bar{\mathbf{r}}_j) - 2z_j\mathbf{G}^{\mathrm{SD}}(\mathbf{r}_i - \bar{\mathbf{r}}_j)\right] \ . \tag{1.22}$$

Here, the wall is at $z = 0$, $\mathbf{r}_i = (x_i, y_i, z_i)$ and $\bar{\mathbf{r}}_i = (x_i, y_i, -z_i)$. The elements of the Green functions are given by [22, 23]

$$\mathbf{G}^{\mathrm{S}}_{\alpha,\beta}(\mathbf{r}) = \frac{\delta_{\alpha,\beta}}{r} + \frac{r_\alpha r_\beta}{r^3} \tag{1.23a}$$

$$\mathbf{G}^{\mathrm{D}}_{\alpha,\beta}(\mathbf{r}) = (1 - 2\delta_{\beta,z})\frac{\partial}{\partial r_\beta}\left(\frac{r_\alpha}{r^3}\right) \tag{1.23b}$$

$$\mathbf{G}^{\mathrm{SD}}_{\alpha,\beta}(\mathbf{r}) = (1 - 2\delta_{\beta,z})\frac{\partial}{\partial r_\beta}\mathbf{G}^{\mathrm{S}}_{\alpha,z}(\mathbf{r}) \ , \tag{1.23c}$$

with $\alpha, \beta \in \{`x', `y', `z'\}$ and $\mathbf{r} = (r_x, r_y, r_z)$.

The power of the scaling of the hydrodynamic interaction in the presence of the wall is not obvious in the formulas above. To simplify the problem, one can consider two particles separated by a distance r, both at a height h from the surface. The coordinates of the particles can be written $(0, 0, h)$ and $(r, 0, h)$. The x, x component of the Blake mobility matrix for the coupling between the two particles is

$$(\boldsymbol{\mu}^{\mathrm{B}}_{1,2})_{x,x} = \frac{1}{8\pi\eta}\left(\frac{2}{r} - \frac{1}{\rho} - \frac{r^2 + 2h^2}{\rho^3} + \frac{6h^2r^2}{\rho^5}\right) , \tag{1.24}$$

with $\rho = \sqrt{r^2 + 4h^2}$. Close to the surface, when $h \ll r$, the coupling term simplifies to

$$(\boldsymbol{\mu}^{\mathrm{B}}_{1,2})_{x,x} \approx \frac{3h^2}{2\pi\eta r^3} . \tag{1.25}$$

This coupling term decays in $1/r^3$. It has to be compared to the $1/r$ decay in a bulk fluid (Oseen tensor). The hydrodynamic interaction between particles is a rather short range interaction at the vicinity of a surface. When $h \to 0$, the coupling term also tends towards 0. This is expected, since the wall constrains the fluid to have a zero velocity at the surface, which leads to a vanishing coupling between the particles, as the motion of a single particle cannot create a fluid flow as big as in a bulk fluid.

Towards the other limit, $h \gg r$, Eq. (1.24) leads to the mobility term

$$(\boldsymbol{\mu}^{\mathrm{B}}_{1,2})_{x,x} \approx \frac{1}{4\pi\eta r} , \tag{1.26}$$

which is the same as the x, x cross-mobility $(\mathbf{H}_{1,2})_{x,x}$ of the Oseen tensor.

The Blake tensor above provides an accurate description of the hydrodynamic interaction when the size of the particles is negligible compared to the spacing between them and the distance from the wall.

1.8.3 Non-diagonal terms corrected for the size of the particles

In the most general case, when the size of the particles a is not negligible compared to $r_{i,j}$ or z_i, the Blake tensor can be corrected for the beads radii.

In a derivation similar to the Rotne-Prager tensor, the Faxén theorem gives [21, 24, 25]

$$\boldsymbol{\mu}_{i,j} = \left(1 + \frac{a^2}{6}\nabla^2_{\mathbf{r}_i}\right)\left(1 + \frac{a^2}{6}\nabla^2_{\mathbf{r}_j}\right)\boldsymbol{\mu}^{\mathrm{B}}_{i,j} \ , \tag{1.27}$$

for $i \neq j$. The expanded version of this formula is very heavy and is not printed here. Section D.8 shows formulas for the x, x and y, y components of the hydrodynamic coupling $\boldsymbol{\mu}_{1,2}$ with the Blake tensor corrected for the beads radii in a simple system of two beads, both at a height h from the surface, and spaced by a distance r. The corresponding coupling terms $\boldsymbol{\mu}^{\alpha,\beta}_{1,1}/\boldsymbol{\mu}^{\alpha,\beta}_{1,2}$ are plotted as solid lines in Fig. 1.3 depending on h. Far from the wall, the coupling term converges almost to the coupling given by the Oseen tensor (dashed lines). The slight discrepancy at large h, almost not visible on the graph, comes from the approximation in the Oseen tensor that particles act like point-like Stokeslets.

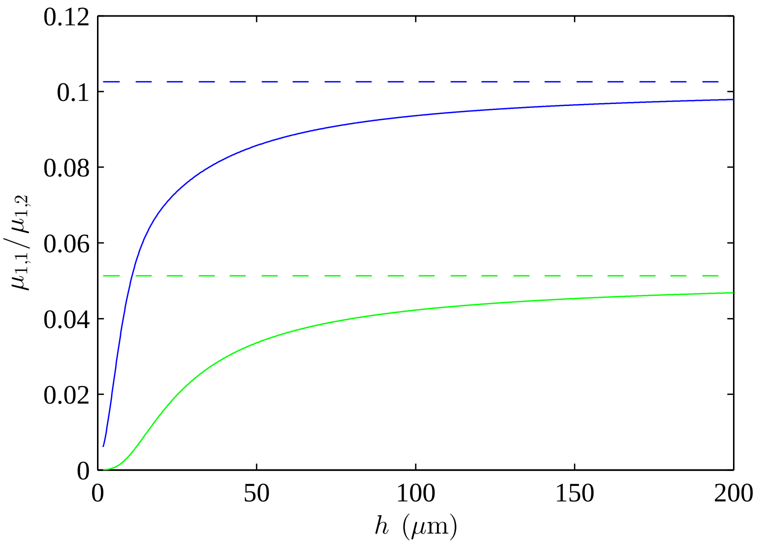

Figure 1.3: Hydrodynamic coupling $1/\boldsymbol{\mu}^{\alpha,\beta}_{1,2}$ between two particles at a height h from a planar surface. The coupling is renormalized by the drag $1/\boldsymbol{\mu}^{\alpha,\beta}_{1,1}$. The solid lines represent the $\alpha, \beta = x, x$ (blue) and y, y (green) components of the Blake mobility matrix corrected for the beads sizes [Eq. (1.27)], while the dashed lines represent the Oseen tensor, that does not take into account the wall. Parameters are $a = 1.74$ μm and $r = 25.4$ μm.

1.9 Brownian motion

As a consequence of the small scales involved, small biological systems are subject to Brownian motion. Thermal fluctuations on a spherical particle act as a force $\mathbf{f}(t)$ that originates from the molecules of the fluid that hit the particle. $\mathbf{f}(t)$ is in practice well approximated by white noise, that is written [26]

$$\begin{cases} \langle \mathbf{f}(t) \rangle = 0 \\ \langle \mathbf{f}(t) \cdot \mathbf{f}(t') \rangle = 2\nu\, \gamma k_B T\, \delta(t-t') \ , \end{cases} \tag{1.28}$$

with $\gamma = 6\pi\eta a$, and $\nu \in \{1, 2, 3\}$ the dimension of the system. Frequency-coloured noise (non white noise) has been observed as a consequence of the interaction of particles with the fluid, introducing a characteristic time scale $\tau = a^2\rho/\eta$ [27, 28]. For typical colloids of size $a \sim 1$ μm in water ($\eta = 1$ mPa·s and $\rho = 10^3$ kg·m^{-3}), $\tau \sim 1$ μs. This is well below all the relevant characteristic time scales in micrometric oscillators in biological fluids like cilia and flagella. White thermal noise is therefore always assumed in this thesis.

In a system of several particles, this thermal fluctuating force has to be included in the forces $\mathbf{F}_j$ of the mobility matrix in (1.14). It leads to coupled terms of noise in the velocities $\mathbf{v}_i$ [29, 30]. Thermal noise also induces rotation of the particles and this rotation couples to the translation [31].

Chapter 2

Cilia, flagella and model oscillators

2.1 Introduction

This chapter reviews what cilia (and flagella) are, and the current models used to understand their synchronization and collective behaviour. The first section focuses on biological aspects and observations in cilia: how motile cilia work and oscillate to perform their task of flow generation, and in particular, what kind of synchronization can be seen. The second section presents simplified models of oscillators, that have been introduced to understand the key features of the collective behaviour from a few to big arrays of cilia. Most of these models started to be studied before the beginning of this thesis by my group and others. This was however done mainly in numerical simulations and/or theory. It provided the motivations to realize these systems experimentally during the course of this Ph.D., and to extend the models to discover new features related to them.

Understanding how cilia work is useful in biology, to get a knowledge of the full metabolic path from energy input to actual mechanical work performed by the filaments, in medicine, to understand how malfunctioning cilia are involved in pathologies [32], thus helping developing diagnostics of such diseases [33, 34], and in microrheology to create flows in microfluidic devices or even micro-robots [35].

2.2 Cilia and flagella

2.2.1 Swimmers at the micrometric scale

Cell locomotion and swimming of microorganisms play an important role in the achievement of various biological tasks. Spermatozoa propel themselves and travel a long distance up to the ovum [36]. Green algae such as *Chlamydomonas reinhardtii* or the marine *Dunaliella salina* swim to generate feeding currents to help fetching nutrients, which would not be concentrated enough is the organism was only relying diffusion [37, 38]. Moving towards a region, depending on concentration gradients is called *chemotaxis*. Bacteria, such as *Escherichia coli* also adapt their swimming according to gradients of nutrients, such as glucose [39–41].

Other cells do not swim, but generate a fluid flow by staying anchored on a surface [42]. These surface flows are essential in various physiological processes including clearance of mucus in the airways [43], circulation of cerebrospinal fluid in the brain [44], transport of ovules in the fallopian tube [45], breaking of the left/right symmetry in the embryonic development [46–48]...

All these organisms are intensively studied, since many can now be accessed experimentally, especially since improvements in the use of genetically modified animals with fluorescently tagged proteins, imaging techniques (phase contrast microscopy, SEM...) [49] and manipulation techniques of small objects (optical tweezers [50–52]).

2.2.2 Cilia and flagella

Interestingly, all the microorganisms or organs mentioned above use motile cilia or flagella, that have embedded molecular motors and can generate a fluid flow. Cilia and flagella are long filaments extruding from the surface of the cell (Fig. 2.1) that beat in a cyclic pattern. They are highly conserved organelles, present in a wide range of eukaryotic and prokaryotic organisms [53, 54], which suggest that they are very efficient in performing swimming at the micrometric scale [55, 56].

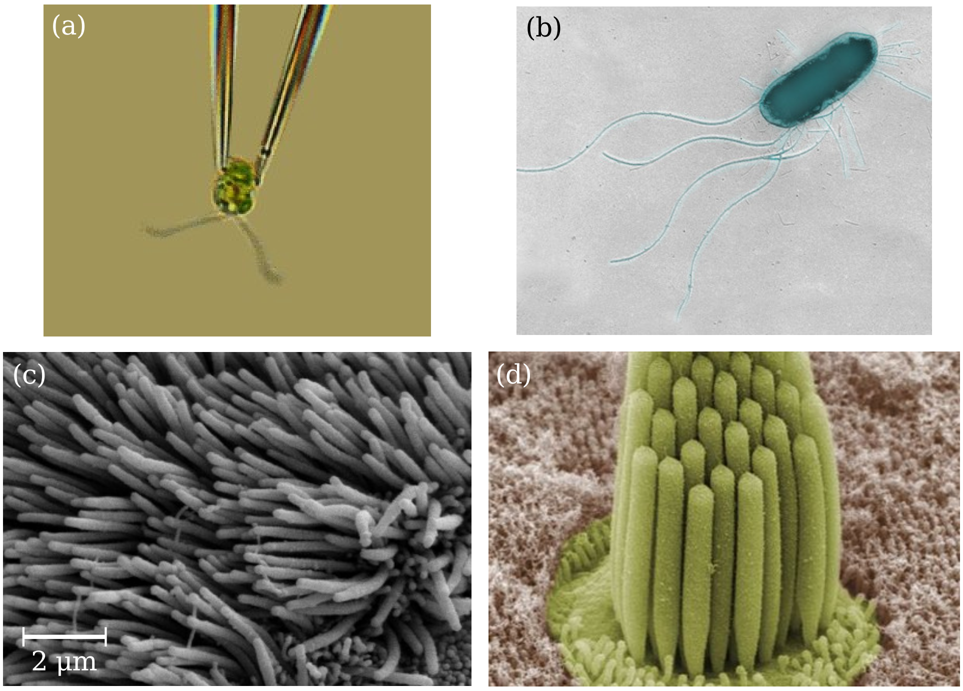

Figure 2.1: Cilia and flagella in the living world. (a) Eukaryotic *Chlamydomonas* alga with two flagella. The alga is being held on a micropipette. (b) Prokaryotic *E. coli* bacteria with four long helical flagella. (c) Dense array of cilia in bronchiolar epithelium. (d) Bundle of tightly packed sensorial stereocilia. Sources: (a) [57], courtesy of M. Polin, (b) [58], (c) [59] and (d) [60].

2.2.2.1 In eukaryotic cells

Most eukaryotic cells are ciliated. However, many of them have non motile cilia, also referred as *primary cilia*, in which case the cilia act as chemical or mechanical sensors [61]. For example, primary cilia in the kidney can detect urine flows (mechanical sensing), and chemical sensors in bones involve primary cilia [62]. Primary cilia are also known to play a signalling role in the development of vertebrate cells [63].

Other cells have motile cilia, with the purpose of swimming or to generate a flow. Mammalian sperm cells have a single 70 μm long flagellum attached to the body, while the *Chlamydomonas* alga has two flagella, about 12 μm in length [64]. In the dense arrays of cilia in the airways (2400 cilia$\cdot$cm^{-2}, [65]), the filaments are much shorter: 7 μm in average for human airways [66].

While the length of cilia or flagella can vary significantly depending on the system, the internal structure of both cilia and flagella in eukaryotic cells is very conserved, leading to a fairly constant diameter of about 200 nm. In most of the cases, when looking at a cross-section of a cilium, the internal structure (axoneme) consists in 9 microtubules doublets arranged on a circle in primary cilia, and 9 microtubules doublets in circle that surrounds two central single tubules in motile cilia (Fig. 2.2) [54]. The two structures are often called “9 + 0” and “9 + 2” respectively.

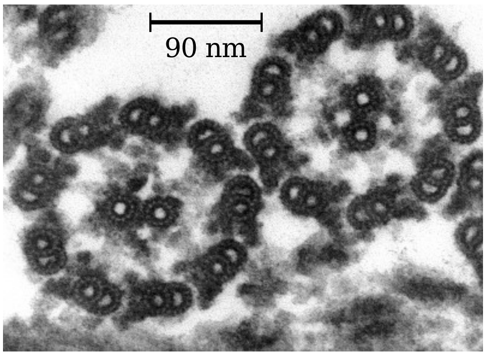

Figure 2.2: SEM image of the “9 + 2” structure of *Chlamydomonas* flagella [67]. The picture shows a cross-section of two flagella. Each of them is composed of 9 microtubules doublets encircling two single microtubules in the centre. In primary cilia, the two central microtubules would be missing.

The microtubules doublets are responsible for the movement of motile cilia. In a cilium or flagellum, each doublet is a pair of dynein arms that slide against each other [36]. This causes the whole cilium to bend. The energy required for the sliding is provided by ATP. The details of the motion of the filament are still being debated [68, 69], but it is well known that the outcome of all the activity from the molecular up to the single cilium level is an oscillating filament. A typical cycle is shown in Fig. 2.3. In this cycle, the cilium starts with a straight shape that changes its orientation, thus pushing the fluid. It returns to its initial position curled up, in order to minimize the interaction with the fluid. The two parts of the cycle are called *power* and *recovery strokes* [70]. In the power stroke, the cilium has a shape corresponding to a high drag coefficient, while in the recovery stroke, the drag coefficient is smaller. This asymmetry of the beating cycle makes the cycle non reciprocal, as required to provide a net force on the fluid over a period in a low Reynolds number environment (see Section 1.3). Cilia typically beat at a frequency of 5 to 100 Hz [53]. In another possible beating cycle, found for example in uniflagellar spermatozoa, a wave-like planar or helical pattern propagates along the filament [36, 71], pushing the cell forward. This is somehow similar to the S-shape slithering motion of snakes, although the problem is more complex since the fluid is not immobile [9]. The details of the mechanisms at work within a cilium have been modelled quantitatively [72, 73] and models to reproduce the cycle of oscillation have been proposed [74, 75].

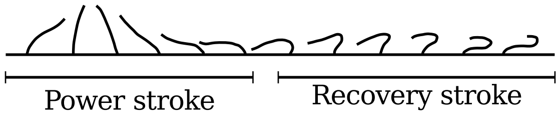

Figure 2.3: Evolution in time of the shape of a cilium. The cycle is made of two parts: the power stroke, during which the cilium pushes the fluid, and the recovery stroke, during which the cilium comes back to its initial position.

In some cases, the origin of motility is still unclear. For example, stereocilia, found in hair cells in the inner ear, as tight bundles of tens of cilia [Fig. 2.1(d)], act as mechanical sensors that can detect and amplify oscillations. They are therefore active elements, and they show indeed spontaneous oscillations [76, 77], but the origin of their activity is unknown.

2.2.2.2 In prokaryotic cells

Bacterial flagella have a different structure and beating cycle than eukaryotic flagella. For example, in the bacteria *E. coli* and *Salmonella typhimurium*, the cell body, a cylinder of about 2 μm in length and 0.5 μm radius, is covered by about 6 to 10 flagella, that extend up to 10 μm in length. Each flagellum is made of a helical protein (flagellin) [78] and has a diameter of about 20 nm, much smaller that eukaryotic flagella [79]. In this case, the cilia are not active on all their length: the filaments are fairly stiff and rotate only at their base, where the active element is located (Mot complex). This results in a helical pattern, that generates a flow [80] and can propel the bacteria at a speed up to about 30 μm·s^{-1} [81].

2.2.3 Synchronization and collective behaviour

The understanding of the motion of cilia at the single cilium level, and the interaction of the filament with the fluid provide very useful information on the swimming of microorganisms. One hopes to conclude on what is the force during a cilium cycle, what effect a time dependent perturbation would have on the cilium dynamics, and what effect is expected from changes in physical parameters such as the length of the cilium or the viscosity (or even viscoelasticity) of the surrounding fluid. Single cilium experiments are being carried out on various biological organisms, in particular the alga *Chlamydomonas* [64, 82] and sperm [83], which are both easily accessible with current technology.

But it has been seen experimentally that cilia often display a cooperative behaviour, such as synchronization. Hence, an understanding of the systems at a multi-cilia level is necessary. This section presents some cooperative behaviours on a few examples of cilia and flagella.

Synchronization is a common phenomenon in biology. Pacemaker cells in the heart [84, 85] are synchronized through neuronal signals. Crickets sing in unison [86], fireflies colonies synchronize their light emission by observing the light emitted by the other members, while cultures of yeast cells can show glycotic oscillations [87]. Synchronization always requires a coupling between the oscillators of the system. In the case of cilia and flagella, hydrodynamic coupling is obviously present (see Chapter 1), and hydrodynamics has already been able to explain some of the collective properties that will be described below. However, it cannot be ruled out that other communication pathways could also help to synchronize. Inspired by known biological systems, other common candidates for communication channels between cilia, are neuronal or biochemical signals, in which each oscillator of the assembly would probably be synchronized to the same control signal [88], and quite importantly other forms of mechanical coupling not mediated by the fluid.

Below are a few examples of organisms that illustrate various types of cooperative behaviour.

2.2.3.1 Coordination of sperm cells

In the case of single-flagellated swimmers, like spermatozoa, hydrodynamic cooperativity can arise between neighbouring swimmers. When two sperm cells are brought close together, the flagella oscillate in synchrony [9, 89]. Furthermore, it was observed experimentally that, once synchronized, two sperm cells tend to attract and stay together, by forming a tight cluster (Fig. 2.4) [89]. Typically, it takes a few cycles for the two flagella to lock their phase. This come from the stress that the viscous fluid applies on the moving flagella [9, 89]. The attraction is weaker, as it takes more than a few cycles to reach a state like in Fig. 2.4.

At a larger scale, sperm cells can synchronize and create vortices [90] that involve each around 10 spermatozoa. Sperm cells also tend to swim close to surfaces [91, 92], which might help them to travel longer distances than if the motion was in 3d.

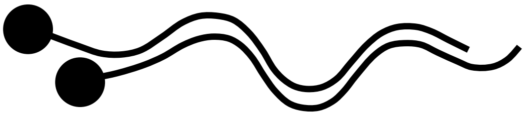

Figure 2.4: The flagella of two sperm cells brought close together beat in synchrony and show an attraction of the filaments, leading to an aggregation of the two cells.

2.2.3.2 Synchronization of the two flagella in *Chlamydomonas reinhardtii*

The alga *Chlamydomonas reinhardtii* has been the object of numerous experiments and studies. It can be easily handled experimentally, and many mutants are available to tune several parameters (like making it uniflagellar) [54]. With only two flagella, it also makes it an ideal system to develop simple physical models in order to understand swimming patterns.

In the wild type of *Chlamydomonas*, the two flagella spend most of their time at doing a "breaststroke" motion (Fig. 2.5): the filaments are therefore strongly locked. However, the swimming of the alga also includes short periods of phase drifts during which the flagella oscillate asynchronously [57, 93]. Over long times, *Chlamydomonas* displays periods of long straight (or little curved) trajectories alternating with short asynchronous periods [94] that have for consequence the change of direction of the alga. This resulting motion is called *run-and-tumble*, and is more often found in prokaryotes than eukaryotes. A recent study [57] found consistency between this behaviour of the two flagella and a generic model of two coupled noisy phase oscillators with a coupling strength consistent with hydrodynamic interactions. However, the mechanochemical aspects of ciliary synchronization are still not well known, but there is growing evidence that mechanical coupling between the flagella through the central cell body also plays a role in the emergence of synchronization in the *Chlamydomonas* flagella [82, 95–97].

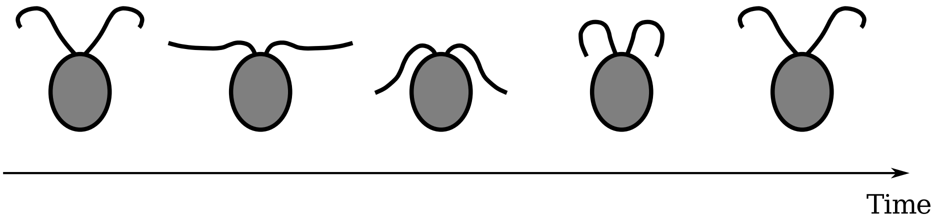

Figure 2.5: When synchronized, the flagella of *Chlamydomonas* beat in a "breaststroke" fashion, pulling the cell forward (upwards direction on this sketch).

2.2.3.3 Metachronal waves in *Paramecium* and *Volvox*

Paramecium and *Volvox carteri* are respectively unicellular and multicellular organisms, a few hundreds of micrometers in size, and their outer surface is covered with thousands of cilia [54, 98]. In the colonial alga *Volvox*, each of the ciliated cells composing the carpet of filaments is biflagellated. These two organisms show an interesting collective motion, in which the flagella do not all beat with the same phase. Instead, two neighbouring flagella will keep a constant (usually small) phase difference [88]. When oscillating, this leads to the formation of a propagating pattern called a metachronal wave that can be seen at the surface of various cells or tissues [99–104]. This synchronized state is similar to a Mexican wave in a stadium (Fig. 2.6), in which each member of the crowd is almost in phase with its neighbours, leading to a phase pattern propagating with a well defined velocity at a larger length scale. In-phase synchronization and metachronal waves are believed to optimize the flow generated by an assembly of cilia [55, 105].

1

Figure 2.6: A Mexican wave in a stadium is a cooperative behaviour between individuals similar to metachronal waves in cilia [106].

2.2.3.4 Alignment of cilia in a carpet

Apart from synchronization, cilia also raise other interesting questions related to cooperative behaviour. In particular, in the case of carpets of many cilia, the collective motion in a metachronal wave, with cilia all beating in the same direction, poses the question of how the direction is chosen, and how the alignment of all the cilia beats (in a plane perpendicular to the surface of the cells) emerges.

Cilia grow outwards from a structure called the basal body, which is anchored to a cell's cytoskeleton [107]. The basal body is itself generated from centrioles, which are subcellular structures responsible for microtubular organization.

Once fully grown, a cilium transverses the cell's plasma membrane extending typically several microns out of the cell body.

In mammalian cilia (in the brain ventricles, fallopian tubes, airways, etc.), the cilia belong to multi-ciliated cells, and there are typically of order 200 cilia per cell; each cilium is separated by approximately 200 nm. The same is true and has been explored in the outer surface of various "model" biological organisms, such as the *Paramecium* [108] and the algae colony *Volvox* [109] as well as developing embryos of mice [110, 111] and *Xenopus* frogs [112]. These ciliated cells, together with mucus-producing cells (goblet cells, in mammals), and ion-regulating cells, form a general tissue type known as muco-ciliary epithelium.

In fully developed epithelial tissue, the direction of beating is well defined relative to the organ, for example it is parallel to the trachea in mammalian airways. This is essential for the generation of fluid flow, mucus clearance away from the lungs in this case, which relies on coordinated beating of cilia to produce transport-efficient metachronal waves [113], similarly to *Paramecium* and *Volvox* in Section 2.2.3.3. An open question in developmental biology is to find the rules and the cues that enable this fairly complex, and well organized tissue, to be made. The first symmetry to be broken in the development of vertebrates is the anterior/posterior. For example the planar cell polarity (PCP) pathway sets the initial direction in a developmental stage of the epithelium in *Xenopus* embryos, a tissue which includes multiciliate cells [114]. From this point on, there are gradients of a variety of biochemical elements along this axis. Cells can be polarized, both in the intracellular protein localization, and in their shape. This process happens before cilia-genesis, and the standard view in biology is that the gradients in biochemical markers control most, if not all, of the subsequent organ development. However, once cilia are generated, they contribute to long-range flows, which can transport chemical factors directionally, or act as a mechanical cue for organization [115–118].

In the specific case of developing orientational cilia order in the airway tissue, there is a hypothesis that flow-induced self organization might be important. A fraction of the cells in the tissue that will develop into the airway epithelium express a few hundred centrioles, which become basal bodies and grow cilia. At this stage, the cells themselves are already polarized (biochemically and in shape) but the basal bodies when they first appear are not oriented. There have been very recent studies suggesting that the network of microtubules connecting the basal bodies could couple to the cell shape or to the emerging tissue architecture, and possibly orient the cilia [119]. On the other hand, the newly made cilia are exposed to a directional flow from the mucus being produced by other cells. These cilia will also be exposed to the flow that they themselves generate, i.e. they interact with each other through hydrodynamic interaction forces [102]. The question of how are cilia aligned has also been addressed looking at mouse brain ventricles [120], where it was shown that cilia first dock apically with random orientations, and then reorient in a common direction through a coupling between hydrodynamic forces and the PCP protein Vangl2.

The evidence of the role of flows in determining the orientation of cilia is therefore present in the experiments in the *Xenopus* larval skin [115, 121] and in mouse brain ventricles [120]. However, there are only very few physical models to explain this behaviour [122].

2.3 Model oscillators to describe the collective behaviour of cilia and flagella

Understanding the role of the hydrodynamic interaction in the synchronization of cilia and flagella can be done by means of *in vitro* experimental observations, or by working on simplified physical models that describe the beating pattern of cilia. Since it is increasingly accepted that the hydrodynamic interaction plays a key role in the synchronization of these systems systems [43, 102, 122, 123], the models should include that coupling. Other interactions, such as mechanical, concentration gradients, or steric repulsion might also be relevant [124].

Such models are often simple enough to carry out numerical simulations or analytical calculations. Reducing the multiple degrees of freedom of the complex systems into a few control parameters which can be tuned helps to understand theoretically the biological systems. It also makes it easier to account for the hydrodynamic interaction. For example, sperm flagella have been first modelled by a waving sheet [9, 125] or by a 2d or 3d filament [126–128], in order to determine the fluid flow they create. Experimental realizations of actuated filaments that can mimic the motion of a cilium also exist, at the micrometric [21, 129, 130] and macroscopic [131] scales.

With the recent possibility of performing computer simulations, it has become very useful to coarse-grain the filaments in various systems. In a quite accurate description, the filament can be replaced by a chain of spherical beads or rods [21, 89, 91, 129, 132, 133] [Fig. 2.7(b)], for which the drag coefficients are known. This can also be realized experimentally with magnetic particles self-assembling in chains [21, 134–136]. These models are useful to study the flow generated close to the filament and to obtain its shape during a beating cycle.

To look at the synchronization between different cilia, an even more coarse-grained model can be used. Since in the far field, the filament can be seen as a point, it can be assumed that the fluid flow generated by the cilium is the same as the one created by a moving sphere. Hence, a cilium can be just modelled as a sphere [Fig. 2.7(c)]. Many recent models use this level of coarse-graining [88, 95, 137–164]. This greatly simplifies the calculation of drag forces, both those acting on the individual object, and the force induced by one object on another. With the single sphere, the shape of the cycle that the oscillating bead is undergoing has to be inputted manually in the model. Also, when designing a single-sphere oscillator to look at the synchronization properties, one requirement is that each oscillator must have a free phase. Having a free phase means that the oscillator is not driven with an imposed phase or fixed frequency. The phase should be able to drift because of external forces like hydrodynamic coupling and thermal noise.

In this section is a short presentation of the two single sphere models of a cilium that were used in this thesis and that are suitable to study synchronization. For a review describing also other models, see [18]. The section here contains the key references required to understand the context in which I worked. Many research groups are actively studying these systems, in particular in theory and simulations; their results are summarized here.

The simplicity of the models allows to understand the processes that lead to synchronization. It also helps finding the relevant parameters that control the states of synchronization and to compare with the states obtained in biological systems: phase locked, metachronal wave, not synchronized... Experimentally, the single-sphere model can be realized by using colloidal particles driven by optical tweezers.

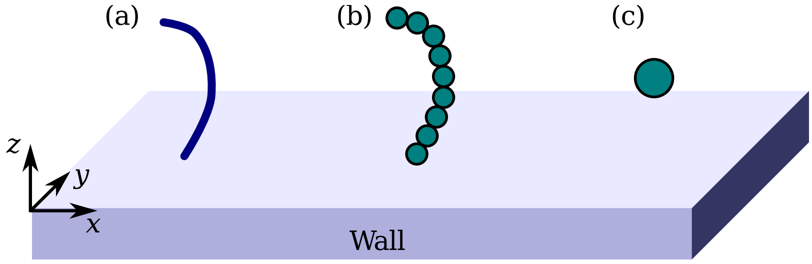

Figure 2.7: In a coarse-grained approach, a single cilium (a) can be modelled by a chain of spherical colloidal particles (b), or even by a single bead (c). Typically, the bead position in (c) would be at the centre of mass of the filament it is modelling. This retains the same far field hydrodynamic flows.

2.3.1 Oscillators moving along orbits: rotors

2.3.1.1 Basic model

When a cilium beats, its centre of mass moves along a given orbit that can be a 2d or 3d path. A way to model a cilium is to prescribe an orbit for the particle. With ϕ the phase of the oscillator, the orbit is described by its shape $\mathbf{r}(\phi)$ and the driving force acting on the particle $F(\phi)$, that represents the force provided by the cilium, in the direction tangent to the path at ϕ, as shown on Fig. 2.8.

In order to generate a net flow, the trajectory can be tilted and close to a surface, so that the drag coefficient changes during the cycle because of the

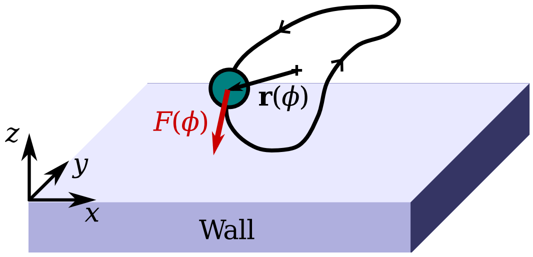

Figure 2.8: Colloidal rotor. A cilium is modelled by a spherical particle driven along a path $\mathbf{r}(\phi)$ with a tangential force $F(\phi)$.

variable height from the wall (see Section 1.8.1 in Chapter 1). This idea of the possible importance of wall effects in the flows generated by cilia and flagella was already emphasized by Blake [165].

An important comment on this model is that the centre of an oscillator is held at a fixed position, compared to the fluid at rest far from the oscillator. This assumption is verified in biological systems such as in the bronchiolar epithelium, where the cilia are all thethered to a surface at rest. In the case of swimmers like *Chlamydomonas*, the anchoring surface moves and rotates constantly because of the motion of the flagella. The global motion of the body comprises an average displacement and rotation after a cycle, but also variations within a cycle. Since in these real systems the average effect is a consequence of the flow generated by the swimmer, including a correction to the model for that behaviour would require first to use rotors that generate a flow, and second to modify the model in a way such that the rotors might not keep a constant position and orientation. The fluctuations within a cycle are however still present even in oscillators that do not generate a net motion. Since this thesis focuses on synchronization and not swimming, only oscillators that do not generate any net flow are considered, and the aspect mentioned above is neglected. When comparing the states of synchronization found in this thesis to the states of real systems, one should keep in mind that the swimming of the system can change synchronization properties.

2.3.1.2 Golestanian model for synchronization

In [137], Vilfan and Jülicher showed with numerical simulations that two beads driven on elliptical, and tilted trajectories near a wall can synchronize, with the state controlled by the relative position of the orbits. In this case, synchronization comes from the hydrodynamic coupling between the two oscillators that allows the particle to move faster or slower on its trajectory than if it was just pulled by its driving force. This way of synchronization was later addressed by Uchida and Golestanian that derived generic conditions for synchronization [142, 143]. They applied their conditions to the particular cases of circular $\mathbf{r}(\phi) = r_0\hat{\mathbf{e}}_\mathbf{r}(\phi)$, elliptical, and linear $\mathbf{r}(\phi) = r(\phi)\hat{\mathbf{e}}_\mathbf{x}$ trajectories, with and without a wall. In the case of the circular trajectories (Fig. 2.9), they proved by stability analyzis that, in an infinite fluid, a constant driving force $F(\phi) = F_0$ would not generate synchronization, while a force profile of the form

$$F(\phi) = F_0[1 - A_2 \sin(2\phi)] \ , \tag{2.1}$$

with $A_2 \in [0, 1]$ provides optimal (strongest) synchronization.

More recently, this model was used by Golestanian and Bennett to study the synchronization of *Chlamydomonas* in simulations: Two colloidal rotors were maintained close to a third sphere that is modelling the cell body. In the presence of noise, this model showed a run-and-tumble behaviour [144], similar to the actual alga. The synchronized states and their stability have also been studied without noise, depending on the choice of the driving force profile [145].

2.3.1.3 Lenz model for synchronization

Another way to build a synchronized state in orbiting particles modelling cilia is to add flexibility in their trajectories. That means that instead of following exactly the trajectory set by the path $\mathbf{r}(\phi)$, the particles can deviate from their orbits, for example because of the coupling with other particles. To stay close to the predefined path, a restoring force is added and tends to pull the particle back to the track. The restoring force can, to the lowest order, be described by spring constant. This idea of synchronization through flexibility of the system also exists in the problems of phase-locking and bundling of the helical flagella in *E. coli* [17, 166] and was also observed experimentally in a system of two paddles [167]. Flexibility might have a leading role in the synchronization of flagella [168]. In the case of the spherical particles driven along circular orbits with a constant force, Niedermayer, Eckhardt and Lenz determined the state of synchronization and strength [88]. For two beads (Fig. 2.10), they found that the decay rate of the phase, that converges to the synchronized state (in phase), is proportional to the inverse of the spring constant k_r that tends to maintain the beads on the circles. In long chains of oscillators, they also saw in simulations metachronal waves in both cases of periodic and free boundary conditions at the ends of the chain.

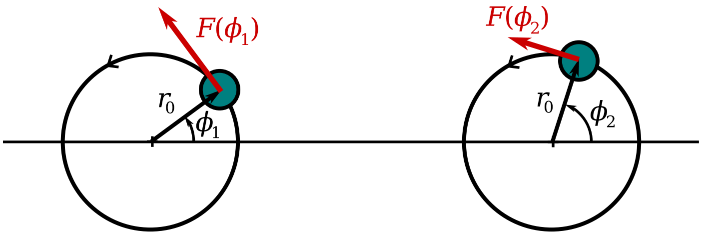

Figure 2.9: Golestanian model. Each of the two oscillators shown here is a bead driven along a circular trajectory. Depending on the choice of the driving force profile $F(\phi)$, the oscillators can synchronize more or less. The system does not synchronize is $F(\phi) = F_0 = \text{cnst}$.

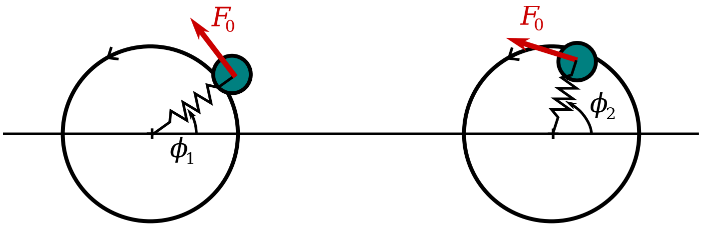

Figure 2.10: Lenz model. The driving force is constant, but the beads can deviate from the circular trajectory, because of flexibility introduced in the orbit. The stiffness of the spring that acts in the radial direction, k_r, is a parameter of the oscillators.

2.3.2 Two-state oscillators: rowers

2.3.2.1 The model

In the previous rotor model, in order to drive the particle along the orbit, the position (more precisely, the phase) of the particle needs to be known so that the direction and amplitude of the force can be set to the wanted value. This model requires to update the force continuously. Another model, called *rower*, performs such an update of the driving potential only two times every cycle. In this case, the particle is driven back and forth in 1d by two potential $U_{\mathrm{L}}(x)$ and $U_{\mathrm{R}}(x)$, respectively pulling the bead to the left and to the right. Fig. 2.11 shows an example with harmonic potentials, that can be implemented with optical tweezers with traps centred to the left and right of the oscillator. A rule needs to be applied to switch the potential from $U_{\mathrm{L}}(x)$ and $U_{\mathrm{R}}(x)$ and vice versa, in such way that the oscillator has a free phase. In the rowers model introduced by Cosentino Lagomarsino in [153], the traps are switched when the bead comes closer than a given distance ς from the centre of the active trap (black dashed lines in Fig. 2.11). This rule is called a *geometric switch* and leads to oscillations with a constant amplitude, A, that depends on both the distance between the centres of the traps λ and ς: $A = \lambda - 2\varsigma$. Because the instants at which the potentials are switching depend on the position of the particle, it is an oscillator with a free phase.

Compared to the rotors model, the driving force is discontinuous, because of the switching rule. It is fair to say that it is still an open question which of these models represents better the internal degrees of freedom of a cilium, and work is under way to elucidate commonalities and differences in the collective dynamics. Driving forces extracted from tracks of a biological cilium during a cycle are quite smooth, suggesting that rotors could well describe cilia. But the asymmetric beating cycle (power and recovery stroke) suggests that an internal two-state feedback system could be driving real cilia.

It is harder to implement rowers than rotors in a way such that they generate a net fluid flow, as the bead is going back and forth on the same path. Swimmers or micropumps in which the traps are switched with a known frequency (hence no free phase oscillators), were however realized experimentally by Cicuta *et al.* [148, 149] with two or three beads (some of them being in static traps), based on model swimmers proposed in [139, 169–171].

Like for rotors, the centre of the rowers are maintained at constant positions. Care should be taken when comparing the synchronized states obtained with such rowers with states of biological swimmers.

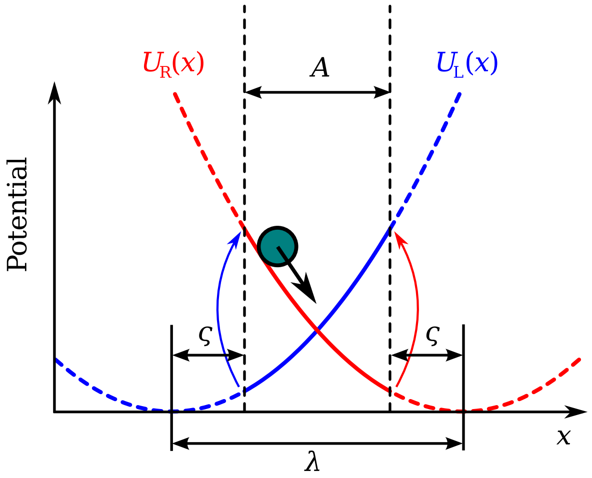

Figure 2.11: Rower model. Two driving potentials $U_L(x)$ and $U_R(x)$ (harmonic in this sketch) are switched on and off alternatively to drive the particle back and forth along the x direction. If the bead is on the right side and the potential U_L is on, the bead will move to the left. When it reaches a distance ς from the centre of the U_L potential, the potential U_L is switched off and U_R is switched on. The bead then moves to the right, and a symmetric switching rule is applied: The traps switch back to U_L when the bead is at a distance ς from the centre of U_R.

2.3.2.2 Synchronization of rowers

Rowers started to be studied in simulations and experimentally before the beginning of my Ph.D. It displays very interesting coupled dynamics. For two oscillators coupled through the fluid, (for which the interaction can be described by the Oseen tensor), synchronization occurs in antiphase for harmonic driving forces and if the beads are close enough [147]. For beads far away, synchronization is lost because of thermal noise that adds random fluctuations in the phase difference between the two oscillators. As well as imposing a threshold on the coupling strength for synchronization, thermal noise was shown to induce distinct cross-particle phase correlations.

The shape of the driving potential also affects the state of synchronization. Wollin and Stark showed this in the geometry of a linear chain of oscillators studied numerically in the absence of noise [146]. For two driven particles, the curvature of the potential determines the stable synchronized state: in-phase or in antiphase [146, 154].

Metachronal waves have also been reported numerically and analytically in chains of rowers [146, 153].

Part II

Methods

Chapter 3

Materials and methods

3.1 Introduction

The rowers and rotors are implemented both experimentally and in simulations. The first section provides the experimental details on the preparation of the samples and on the two tweezers setups that were used. The tweezers were build and are maintained by Jurij Kotar. They are relatively unique, as they allow to control the traps depending on the position of the particles. This is required to create active oscillators, as they need controlled forces on the particles. The second section describes the numerical methods used in the simulations.

3.2 Optical tweezers setups

3.2.1 Sample preparation

Samples are diluted solutions of spherical, silica (density = 2.0 g/cm^3, refractive index ≈ 1.45), non functionalized (SiOH free ends), monodisperse colloidal beads from Bangs Laboratories (cat. no SS05N, [172]). For the results presented in this report, unless specified otherwise, the diameter of the particles is 3.47 μm. Particles of this size and density sediment in the solutions prepared below. The initial aqueous colloidal solution (≈ 10 % of colloids in mass) is diluted to 10^{-3} to 10^{-5} (in volume) in a water/glycerol solution (deionized water, and Fisher, Analyzis Grade glycerol). The fraction of glycerol in the solution is chosen depending on the wanted viscosity, according to a look-up table [173]. Viscosities can be varied between 1 (pure water) to 8 mPa·s. Above 8 mPa·s, the refractive index of the solution becomes too close to the index of the particles, reducing dramatically the trapping force and the contrast of the image.

Sealed microscope slides are created to be usable in the tweezers setup. The thickness of the solution on the slide is approximately 150 μm and most of the experiments were performed at a height (of the focal plane from the surface) of 75 μm, in order to limit any interaction with the glass surfaces.

3.2.2 First setup

Two optical tweezers setups were used in this work. In the first, a custom-built inverted microscope focalizes an IR laser beam (from an Ytterbium fiber laser, IPG Photonics, PYL-1-1064-LP, wavelength = 1.064 μm) in the same focal plane as the imaging plane. The laser beam goes first through a set of lenses, mirrors and acousto-optic deflectors (AOD, AA.DTS.XY-250@1064, from AA Opto-Electronic) see Fig. 3.1, before being focalized by a water-immersion objective (Zeiss Achroplan IR, 63x, NA = 0.90). All the optical elements before the objective are enclosed and do not need frequent realignments. The AODs allow to move the (x, y) position of the beam in the focal plane with a subnanometric precision at a refreshing rate of 20 kHz. The sample is placed on a 3d translation stage that allows to move it with micrometric precision. The maximum possible laser power just after the objective is about 0.3 W.

The image of the focal plane is projected on a Marlin F131B CMOS camera from Allied Vision Technologies that receives the light going through the dichroic mirror (see Fig. 3.1).

A C program on a computer running a Linux (Fedora) distribution controls, through a USB connection, a custom-build electronics that controls the state of the AODs. The computer itself also controls the motorized stage and the laser.

With only one laser beam (TEM00), this setup allows to create, by scanning, several harmonic optical traps at different positions (x, y) and with different intensities. When the scanning period is fast compared to the characteristic time scales in an experiment where colloids are trapped and driven, it can be considered that the sample is illuminated with several beams of constant intensity, thus enabling, the possibility to trap several beads. The power of the laser is shared between all the harmonic traps, limiting the number of beads that can be trapped in 3d to about 10, with the colloids samples described in Section 3.2.1.

The traps can be created and controlled (position, intensity, on-off state) with the mouse on the video image of the sample, or with XML scripts when the number of traps becomes important and when they need to be at well defined positions. The XML scripts and the program interface, make the setup very versatile. With little training, new users can start simple tweezing experiments without having to learn how all the setup works.

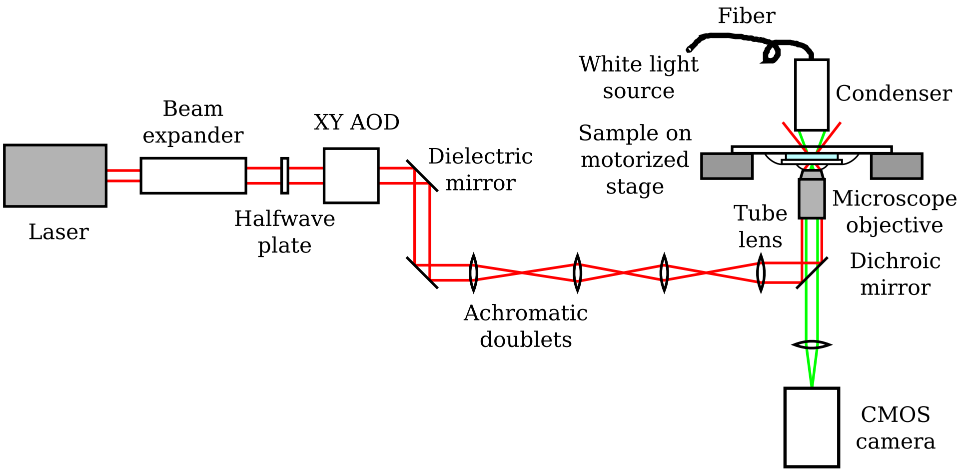

Figure 3.1: First optical tweezers setup. An infrared laser beam is expanded, deflected by AODs, and passes through a water immersion objective and the sample to trap the colloids. The sample is observed by illuminating it with white light. After passing the sample, and the objective, the imaging light is separated from the laser beam by a dichroic mirror, and imaged on a CMOS camera.

Rowers (experiments in Part III) were realized on this setup.

3.2.3 Second setup

The second setup is an upgrade of the first optical tweezers, that became available towards the midpoint of my Ph.D. The main difference is that it is mounted on a commercial microscope (Nikon inverted Eclipse Ti-E microscope). It uses a water-immersion objective (Nikon Plan Apo VC 60x, NA = 1.20), and the laser is a diode-pumped solid-state laser (CrystaLaser IRCL-2W-1064 with wavelength of 1.064 μm). The commercial microscope brings a lot of advantages, particulary relevant to the observation of biological systems: The image quality is better, it is easy to add elements on the optical path, enabling with ease fluorescence and phase contrast microscopy, and the transmitted light can be easily directed to various cameras (AVT Marlin F131B CMOS camera for the experiments in this thesis). The downside is that some elements are quite loosely attached to the skeleton of the microscope. In particular, the frame of reference of the camera can move relatively to the frame of the trap positions (AODs' frame) during a few hours long experiment. It was also observed that the two frames cannot be superposed by simple translation, because of optical aberrations. Experiments that are sensitive to the relative position of the two frames (like rotors) require a calibration of the frames. This is done by measuring the position of a bead in the camera frame for different x and y positions of a trap (typically on a 20×20 grid covering the 63 μm-sized square area of available trap positions). The position-dependent discrepancy between the measured bead position and the trap centre in used to generate a calibration table to match the two frames.

This setup also has a better control of the intensity of the traps, hence the trap stiffnesses. First, the parameter controlling the intensity of a trap, called *gain*, was, in the first setup, linear with the power on the piezo-electric elements of the AODs. But this power is not proportional to the intensity of the first diffraction mode at the output of the AODs. On the second tweezers, a calibration curve can be measured by scanning the gain and measuring the intensity after the AODs. It is then used to linearize the gain parameter such that it becomes proportional to the measured intensities. Second, when changing the position of the trap (by changing the driving frequency of the AODs), the intensity can also vary. Similarly to the gain linearization, measuring the intensity in a grid of x and y positions of the trap allows to make the intensity become independent on the position (*field flattening*).

The setup is also improved for better real-time feedback (see Section 3.2.6). A high speed USB interface is used, and the program controlling the setup runs with a higher priority on the operating system than in the previous setup.

Rotors (experiments in Part IV) were implemented on this setup, taking advantage of the improvements mentioned above.

3.2.4 Customized potential landscapes

A single Gaussian beam (waist $\sim 1\ \mu$m) leads to a harmonic trapping potential, at least close to the centre of the beam. Other potentials were realized to drive rowers and rotors. The aim is to build a customized potential shape in one dimension, with a strong confinement in the other directions. Since the force from the tweezers on the particle is proportional to the gradient of laser intensity, custom laser gradients need to be built. In this thesis, AODs are used to create potentials landscapes, but other methods like holographic optical tweezers could also be used [174–177].

The tweezers allow to put a large number of traps at different positions. One single harmonic trap (referred as *simple trap*) is used as a “pixel” characterized by its intensity. By arranging several traps along a line it is possible to create various intensity profiles (see Fig. 3.2). As the force felt by a colloidal particle in this field is proportional to the gradient of intensity, this method creates an arbitrary potential landscape. The ensemble of simple traps constituting the landscape is called a *complex trap.*

The implementation of complex trap landscapes requires to satisfy some constraints. On one hand, the distance between two harmonic traps (two “pixels”) has to be small compared to the waist, so the landscape appears smooth for the particle [Fig. 3.2(b)]. On the other hand, the number of traps should not be too large, as it increases the time to scan all the positions with

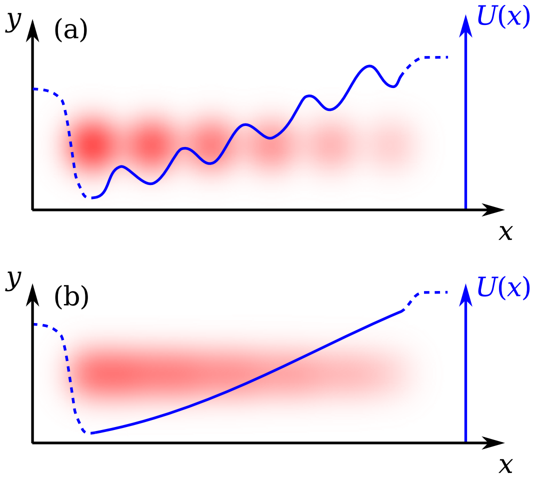

Figure 3.2: Schematic of complex potential landscapes. By placing several traps with different intensities along the x axis, various potentials can be created. The sketch represents the focal plane with the red shadings being the laser intensity. The corresponding potentials are plotted qualitatively in blue. (a) shows six simple traps with an intensity that decreases when x increases. Each dot is a harmonic potential (Gaussian beam) and appears as local minimum on the potential curve. When the density of the simple traps is doubled [12 traps, in (b)], such that the spacing between the traps is less than the waist, the traps overlap and create a gradient of intensity, thus building a potential corresponding to a smooth potential that would drive the bead towards small x. The region of interest of the custom landscape is the solid part of the curve, the shape of which can be tuned by changing the intensities of each simple trap.

the laser beam. More precisely, the scanning period of all the traps has to be much lower than all the characteristic times of the system studied. In fact, to limit further the effect of scanning, the traps are scanned in a random sequence within a potential landscape.

Complex trap landscapes are used in two contexts in this thesis: in the rowers, to change the curvature of the driving potentials, and in rotors to explore a range of low radial spring constants (high flexibility).

3.2.5 Image analyzis

The pictures from the camera are analyzed to obtain the position of the particles. Since the colloids are very uniform in size, diluted, and stay close to the focal plane when trapped, their shape on the picture is the same from one colloid to the other. The position of a colloid is measured by maximizing the 2d cross-correlation function

$$f(i_1, j_1) = \sum_{i,j} I(i,j)\, I_0(i - i_1, j - j_1) \;, \tag{3.1}$$

where (i,j) are pixel coordinates, $I(i,j)$ is the intensity of the image to analyze, and $I_0(i,j)$ is a bead profile. A bead profile is a typical intensity pattern of a colloid centred on $(0,0)$. Two kinds of bead profiles with rotational symmetry were used:

- A profile made of two or three dark/bright rings. The profile is determined on a base image of a colloid by estimating manually the rings radii and intensities.
- An angle-average $I_0(r)$ radial profile converted into the $I_0(i,j)$ cartesian function. It is computed by a Matlab script that only requires to input a base image of the colloid, and the position of the centre of the colloid.

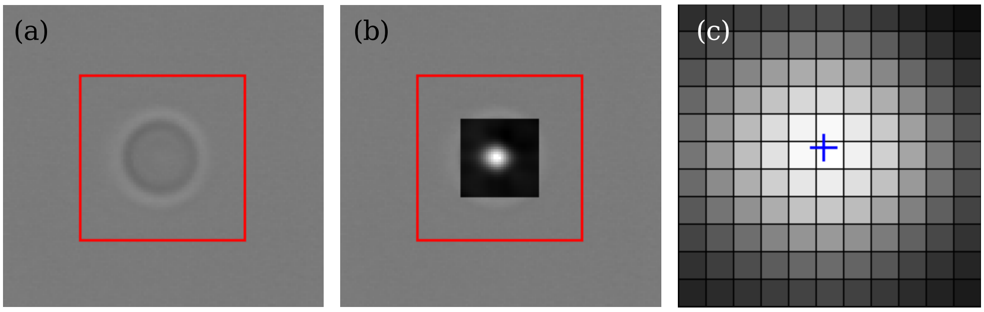

Figure 3.3: Determination of the position of a particle (3.47 μm diameter silica particle in an η = 6 mPa·s water/glycerol solution). (a) Camera image of a colloid. A region (red rectangle) is defined around the particle to localize. The region is centred to the position of the particle found in the previous frame, or set manually for the first frame. (b) A correlation filter is applied inside the region. The bead profile used in the filter is defined as a 35 px × 35 px intensity matrix so that the function f in Eq. (3.1) can be estimated in an area inside the red rectangle cropped by 17 pixels on each side. In that region, the greyscale shows the value of f, with white colour representing high values of f. (c) Zoom on the maximum of f in (b). The centre of the particle (blue cross) is determined with subpixel resolution by fitting a 2d parabola around the pixel with maximal f.

$f(i_1, j_1)$ is maximized by fitting a 2d parabola close to the maximum (typically using the data points within a radius of 1.5 pixels of the maximum of f), thus obtaining a maximum at (i_0, j_0) with subpixel resolution, see Fig. 3.3 (i_0 and j_0 are scalars, in pixel units: 1 px = 0.093 μm in the first setup, 1 px = 0.11 μm in the second setup). The precision of the particle position can be down to about 10 nm. However, optical aberrations and fluctuations of the particles along z reduce the precision by introducing systematic errors. f is only maximized in a small region in which the particle is believed to be. When analyzing a movie frame, this region is simply centred to the measured particle position in the previous frame. The analyze of the first image requires to select manually a region around each of the particles.

The two setups are able to record movies that contain a sequence of camera images and trap states. Such movies can be analyzed after the experiment. The second setup was also able to directly record the position of the beads (when analyzed in real time) and the traps, without having to record a movie. In any case, the data of an experiment consists in files containing the positions of the particles depending on time, recorded at the rate of the camera, and the state of the traps.

3.2.6 Real-time image analyzis and traps update

A feedback loop can analyze in real time the position of the beads and send commands to the electronics that controls the traps' positions (Fig. 3.4). The image analyzis is done on the computer at the rate of the camera (typically between 100 and 400 frames per second). This allows a lot of flexibility in the rules, written in C language, that can be used to update the position of the traps. In particular, rotors and rowers, as described in Chapter 2 (Sections 2.3.1 and 2.3.2) can be implemented.

Specific details of each of the implementations are provided in Parts III and IV, in the relevant chapters.

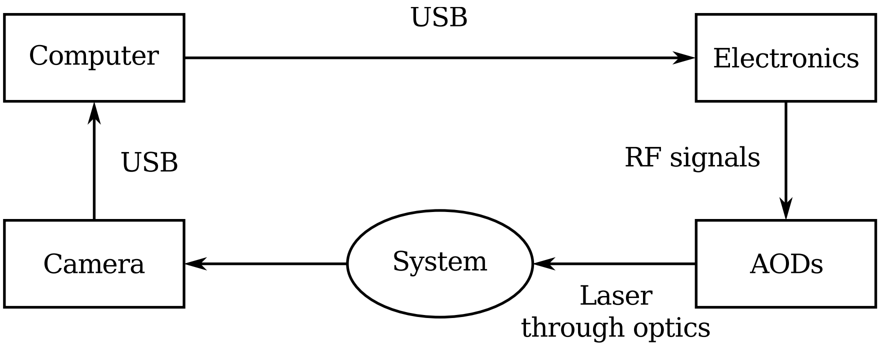

Figure 3.4: Feedback loop in the tweezers. The camera first takes a picture of the system (trapped colloids). It is sent to the computer to analyze the position of the particles and apply a feedback rule to decide where to put the traps. The command to change the states of the traps is sent through USB to the AODs controller. It generates the RF signals that drive the AODs to apply the desired traps on the system. The whole cycle takes about 6.5 ms. The major delay comes from the transmission through the USB cables and the computer processing time. This loop is also characterized by a second time: the frame rate of the camera, which defines the refreshing rate of the traps.

3.2.7 Example: V-shaped potential

Here is an illustration of a combined use of potential landscapes and a feedback loop. The aim is to create a potential of the form $U(x) = k|x|$ to study the fluctuations of a colloid trapped in the minimum at $x = 0$. A naive idea would be to create a trap landscape with $2N$ simple traps equally spaced of the form

$$g(i) = k'(N - |i|) \ , \tag{3.2}$$

with $i \in \{-N, ..., N-1\}$ the trap index, g the gain and k' a constant. Although the function g has an inverted “V” shape with a sharp maximum (discontinuous derivative at $x = 0$), the corresponding intensity gradient would also be an inverted “V”, but smooth near the maximum, because of the averaging effect due to the size of the waist. The potential would therefore also be smooth.

To overcome this problem, and have a sharp potential in the range of thermal fluctuations of the particle, a solution is to use two linear gain profiles:

$$g_{\mathrm{L}}(i) = k'_{\mathrm{L}}(N + i) \tag{3.3}$$

and

$$g_{\mathrm{R}}(i) = k'_{\mathrm{R}}(N - i) \ . \tag{3.4}$$

These profiles lead to a constant force $F_{\mathrm{L}} < 0$ for g_{L} and $F_{\mathrm{R}} > 0$ for g_{R} [which respective potentials are $U_{\mathrm{L}}(x)$ and $U_{\mathrm{R}}(x)$]. An exact "V" potential can be obtained by applying the potential U_{L} if the bead is at a position corresponding to $x > 0$, and the landscape U_{R} if $x < 0$ (see Fig. 3.5). This switching rule, is implemented as a feedback loop in the setup, and the corresponding experimental potential is shown in Fig. 3.6. The potential is calculated by measuring the probability density function $\mathcal{P}(x)$ of the particle. The potential is deduced from Boltzmann statistics through the relation

$$\mathcal{P}(x) \propto \exp\left(\frac{-U(x)}{k_B T}\right) , \tag{3.5}$$

with k_B the Boltzmann constant and T the ambient temperature. In Fig. 3.6, the minimum shows two portions of lines, except in a small region near the minimum of about 0.1 μm width, where it is smooth. This region is still much smaller than the waist. It differs from the perfect sharp "V" shape, because of the feedback time (363 frames per second) and the delay in updating the traps: When the bead passes the centre, the switch of the potentials is retarded, leading to the wrong linear potential (U_{L} or U_{R}) being applied for a short time.

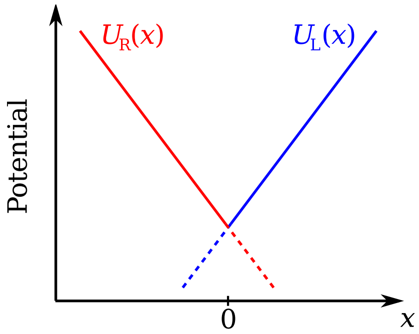

Figure 3.5: Implementation of a V-shaped potential. Two linear potentials U_{L} and U_{L} are used. Both are defined to the left and right of $x = 0$ (solid and dashed lines), but U_{L} is activated when $x > 0$ only and U_{R} is activated when $x < 0$ only. The resulting potential is the red and blue solid line.

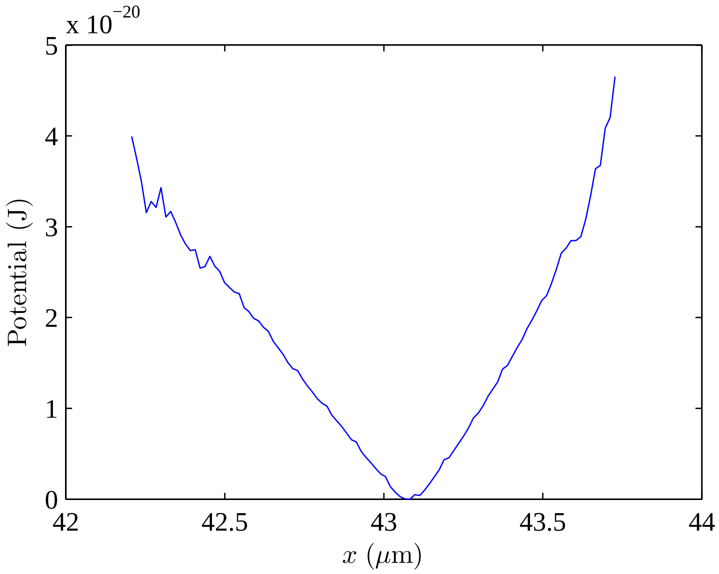

Figure 3.6: V-shaped potential obtained by using two sloppy potentials U_L and U_R, as shown in Fig. 3.5. The duration of the experiment is 1 hour.

3.3 Numerical simulations

3.3.1 Ermak McCammon algorithm

The simulations in this thesis were carried out with a Brownian dynamics algorithm developed by Ermak and McCammon. It provides a numerically fast way to integrate the equations of motion of N interacting particles, with hydrodynamically coupled Brownian fluctuations.

For a system of N particles, with velocities v_n and positions r_n (in two dimensions, $n \in \{1, \ldots, 2N\}$, as each bead has an x and y component), the coupled equations of motion are [178]:

$$\sum_{m=1}^{2N} \mu_{n,m} v_m = F_n + \sum_{m=1}^{2N} D_{n,m}^{1/2} f_m \; . \tag{3.6}$$

Here, inertia is neglected, so that the equation of motion is just a balance of the driving force F_n, the hydrodynamic coupling force (left-hand side, introducing a mobility matrix μ) and a hydrodynamically coupled noise term. The latter is written as a product of a white noise variable characterized by

$$\begin{cases} \langle f_n(t) \rangle & = & 0 \\ \langle f_n(t) f_m(t') \rangle & = & \delta_{n,m}\delta(t'-t) \end{cases} \tag{3.7}$$

and a coupling matrix $D^{1/2}$ that satisfies

$$\left(D^{1/2}\right)^2 = D = k_B T \mu \ . \tag{3.8}$$

D is called the diffusion matrix.

In the Ermak McCammon algorithm, Eq. (3.6) is integrated to obtain $r_n(t+\Delta t)$ depending on $r_n(t)$, with Δt a small time step [178]:

$$r_n(t+\Delta t) = r_n(t) + \sum_{m=1}^{2N} \frac{\partial D_{n,m}(t)}{\partial r_m}\Delta t + \sum_{m=1}^{2N} \frac{D_{n,m}(t) F_m(t)}{k_B T}\Delta t + R_n(\Delta t) \ , \tag{3.9}$$

with $R_n(\Delta t)$ a multi-variate Gaussian distribution satisfying

$$\begin{cases} \langle R_n(\Delta t) \rangle & = & 0 \\ \langle R_n(\Delta t) R_m(\Delta t) \rangle & = & 2D_{n,m}\Delta t \end{cases} . \tag{3.10}$$

When the mobility matrix is the Oseen or the Rotne-Prager tensor,

$$\sum_{m=1}^{2N} \frac{\partial D_{n,m}(t)}{\partial r_m}\Delta t = 0 \ , \tag{3.11}$$

so that Eq. (3.9) simplifies to

$$r_n(t+\Delta t) = r_n(t) + \sum_{m=1}^{2N} \frac{D_{n,m}(t) F_m(t)}{k_B T}\Delta t + R_n(\Delta t) \ . \tag{3.12}$$

3.3.2 Program

The C++ simulation program was initially written by a master student in 2010, Loïc Damet [179]. It is solving Eq. (3.12) by using a Cholesky decomposition of the diffusion matrix to calculate efficiently the noise $R_n(\Delta t)$

(GNU scientific library GSL). It was initially able to simulate N rowers in a chain or a ring configuration with the Oseen and Rotne-Prager tensors. Updated versions have been used to simulate the other systems in this thesis, by changing the driving forces and switching rules of the traps.

The program output is made of text data files containing the positions of the particles and the optical traps depending on time. These files can be analyzed the same way as experimental data files.

Part III

Synchronization of two-state rowers

Chapter 4

Effect of the noise on the synchronization of a single colloid

4.1 Introduction

In this chapter, a two-state rower is realized experimentally, with intrinsic dynamics defined by linear potentials that undergo configuration-coupled transitions. It is also externally driven by a piece-wise constant periodic force of varying amplitude and frequency. This elementary example of "active matter" has the minimal elements that allow to study synchronization in presence of thermal fluctuations and of a possible mismatch in natural frequency between driving force and oscillator. Experiments reveal the presence of synchronized states (and Arnol'd tongues), when the clock period is close to the natural period of the phase oscillator which is explained using analytical and numerical calculations. The system maintains synchronization over different clock periods by adjusting the phase between the bead and the clock. The relevance of this model to synchronization in real-world systems, ciliary and general micro-motor systems, is discussed, including the role of thermal noise.

Synchronization problems in biological active systems are two-fold. It involves how the internal degrees of freedom are coupled to the external perturbations arising from the other active elements, and the effects of thermal fluctuations. Thermal noise is relevant given the length scales and typical coupling forces involved in cilia and flagella [57, 93]. Despite a few existing computational studies [57, 147, 180], the role of noise in these systems remains largely to be addressed. In order to do so, the rower model is used as an active oscillator to focus on the role of the geometric switch mechanics in synchronization. The setting is further simplified to address the response of a single two-state oscillator with linear potential to an external periodic force. This allows a deeper quantitative understanding of the synchronization properties and the role of noise in the experiment. The results have relevance for the wider field of synchronizing systems, where few controlled experiments exist.

4.2 Model of externally perturbed rower

In the experiment, a complex trap landscape is used to create a potential energy landscape which is linear in one direction. This allows to apply a constant force F to an overdamped particle. In the absence of noise a bead of radius a would be driven at a constant velocity $v = F/\gamma$, with $\gamma = 6\pi\eta a$ and η the viscosity. The oscillation cycle of the perturbed rower is built from piece-wise constant slopes [Fig. 4.1(a)]. The main driving force F_d is applied to the particle (blue arrows). At the geometric boundary, represented by a blue dashed line in Fig. 4.1(a), this force is switched to its opposite, so that the particle is pushed the opposite way. The internal drive state is represented by a discrete variable $\sigma_d = \pm 1$. Such an oscillator is a rower driven by piece-wise constant forces.

On top of this driven motion, in which the switch of potential is determined at the first-passage condition of the particle, an external perturbing "clock" signal is superposed, the period of which is set externally [green arrows in Fig. 4.1(a)]. The clock is realized itself as a time-variable tilt in the linear potential constructed by time-shared traps. It applies on the bead a weak force F_c that is also constant, and either strengthens or weakens the basic

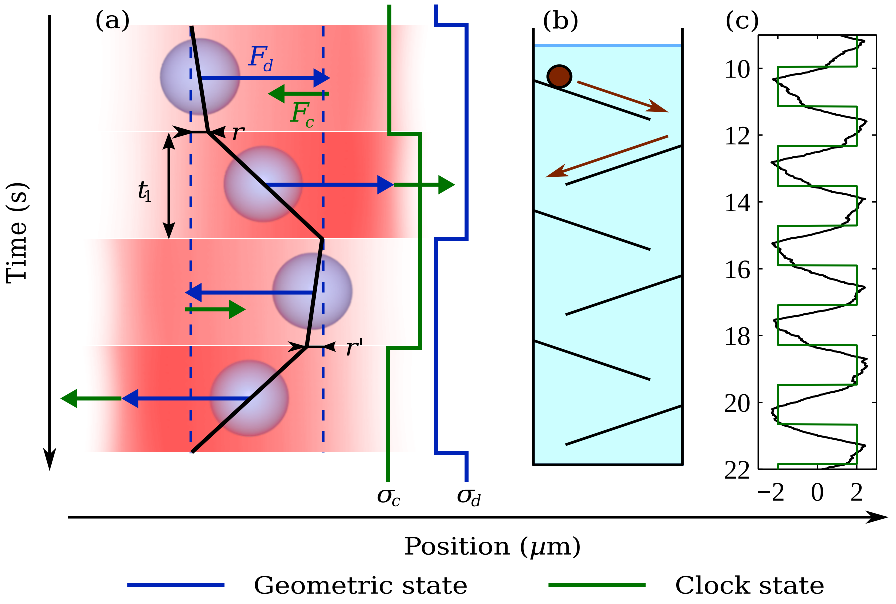

Figure 4.1: A colloidal bead is driven with a combination of a fixed-period piece-wise-constant force (the "clock") and a linear potential with configuration-coupled switching. (a) Scheme of the experiment. The blue arrows represent the force arising from the internal potential and the green arrows the clock. Both are realized with time-shared optical tweezers (red shades). Blue dashed lines are the switching positions, used to determine the state of the internal driving force. (b) Mechanical analogy with an overdamped ferromagnetic bead falling in an infinite set of slides and subject to a piece-wise constant oscillating magnetic field gradient. (c) Oscillations from one experimental track (black). Experimental parameters are $A = 4.66$ μm, $v = 3.91$ μm/s, $\epsilon = 0.5$ and $T_c = T_d = 2.38$ s.

drive, depending on the clock state, which can be parameterized by a discrete variable $\sigma_c = \pm 1$. Therefore, at any time, the particle feels a force $\sigma_d F_d + \sigma_c F_c$, with the switches of σ_d and σ_c determined according to the geometric condition and the clock ticks. Experimentally, the total force is controlled by a computer that analyzes the position of the bead to get σ_d and uses its internal clock to get σ_c, and apply one of the four potential landscapes corresponding to the four possible total driving forces $\pm F_c \pm F_d$. Experiments were performed at room temperature (296 K) in water-glycerol solutions of viscosity 2.2 mPa·s, with spherical silica beads of radius $a = 1.74$ μm. Each linear potential landscape is made of 62 simple traps.

4.3 State of the system

4.3.1 Fixed point without thermal noise

The geometric switch condition, which sets the amplitude of oscillations to A, is analogous to a bead driven by gravity and falling through a system of tilted linear slides, in a high-viscosity environment [Fig. 4.1(b)]. In this analogy, the external clock provides a modulating force in the right or left directions, or changes the tilt of the slides at fixed time intervals. Thus the equation of motion is

$$\dot{x} = v[\sigma_d(t) + \epsilon\sigma_c(t)] + \zeta(t) \tag{4.1}$$

where $\epsilon v = F_c/\gamma$ and ζ is thermal (Gaussian, white) noise.

Let us consider first a clock of period $T_c = 2A/v$, thus equal to the natural period of the oscillator T_d. The experimental trajectories of the colloidal particle position show synchronization with the clock state as a function of time [Fig. 4.1(c)]. The synchronized state is such that the configurational switches occur at mid-points between two clock switches. The existence of this synchronized state can be easily understood considering the system in absence of noise. Supposing we start from the position r immediately after a clock switch [Fig. 4.1(a)], and the clock is coherent with the internal state ($\sigma_c = \sigma_d = 1$). The time to the first geometric switch will be

$$t_1 = \frac{A - r}{v(1+\epsilon)} \ . \tag{4.2}$$

Subsequently, $\sigma_d = -1$, and the clock will contrast the internal state for a time $t_2 = T_c/2 - t_1$, during which the rower will reach the position

$$r' = \kappa(A\epsilon + r) \tag{4.3}$$

with

$$\kappa = \frac{1-\epsilon}{1+\epsilon} \ . \tag{4.4}$$

The remaining half of the cycle will follow an identical dynamics by symmetry,

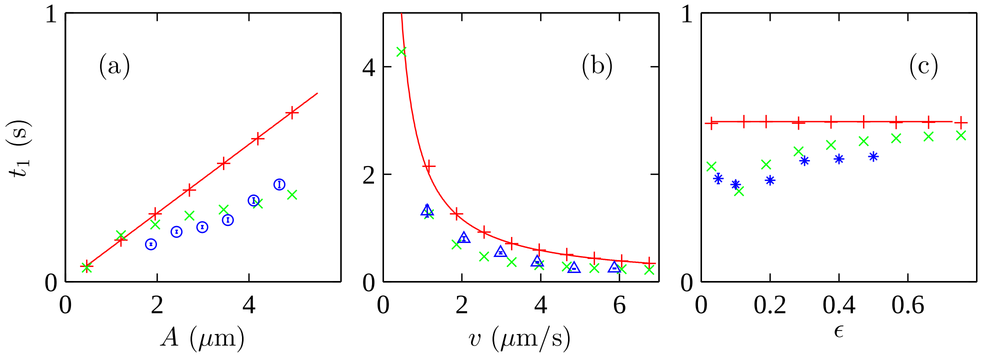

Figure 4.2: Comparison of experiments, simulations and theory for the mean delay t_1 between a geometric switch and a clock switch for $T_c = T_d$. Experiments (blue $\circ$, $\triangle$ and * markers) and simulations including an adjustment for the bead size and delays in traps switches (green $\times$) agree and simulations without any correction (red $+$) fit perfectly the theoretical formula for the fixed point (solid red line). The dependence of t_1 with three parameters has been explored: (a) the amplitude A, (b) the mean velocity v and (c) the strength of the perturbation ϵ. The theoretical dependence always corresponds to a constant phase equal to 1/4. While one parameter is varying, the others are fixed to the following values: $a = 4.66$ μm, $v = 3.91$ μm/s and $\epsilon = 0.1$.

leading to the following fixed point:

$$r_{\mathrm{fp}} = \frac{(1-\epsilon)A}{2} \ . \tag{4.5}$$

This fixed point indicates the position where the particle will be found after a clock switch in the synchronized state. It can be substituted to r in Eq. (4.2), to obtain t_1, and the three other time differences t_i between consecutive clock switches and geometric switches. These are all equal to $T_c/4$. In other words, the system always puts itself at a phase difference

$$\phi_1^{\mathrm{fp}} = \frac{t_1^{\mathrm{fp}}}{T_c} = \frac{1}{4} \tag{4.6}$$

between oscillator and clock.

The experimental results agree well with these predictions (see Fig. 4.2). The small (5 to 10 %) deviations can be understood as byproducts firstly of the finite image-analyzis time and secondly of the uncertainty in the bead radius used in the experiment. First, the rate at which images are analyzed is not negligible (100 frames per second). Then, a further delay is added and represents the time between an image capture and the successive implementation of the trap position switch. Inputting these two effects as an equivalent frame rate of 40 fps in the simulations fits with the experiments. Second, since calibration of the optical landscape is a lengthy process of refining the intensity of the 62 traps, the experiments were of necessity performed on different beads, and there is a small variation in bead size between the experiment and the calibration, which is estimated by measuring its velocity. The correction is then included in the simulations as a modified Stokes drag. Both corrections have been included in the simulations, giving excellent agreement with data of Fig. 4.2.

4.3.2 Thermal fluctuations around the fixed point

In the presence of thermal noise, each geometric switch time t_i needs to be treated as a random variable, corresponding to the first-passage time between the previous clock switch and the geometric switch. This is a complex situation where uncertainties in subsequent switching times propagate between different sub-portions of a cycle. However a simple argument is sufficient to capture the salient features of the fluctuations. Supposing that, for an half-cycle of index i,

$$t_1(i) = t_1^{\mathrm{fp}} + q(i) \ , \tag{4.7}$$

i.e. it is a sum of a deterministic value and some fluctuations, one obtains the effective equation

$$\begin{aligned} \delta q &= q(i+1) - q(i) & (4.8) \\ &= -2q(i)\, \frac{\epsilon}{1+\epsilon} + \chi(i) \ , & (4.9) \end{aligned}$$

where $\chi(i)$ is a random variable accounting for the effects of noise. χ can be estimated by summing two kinds of contributions. The first comes from the diffusion from the geometric switch point to the clock switch point, giving a variance

$$V_1 \approx 2D\, \frac{T_c/2 - \langle t_1 \rangle}{v^2(1+\epsilon)^2} \ , \tag{4.10}$$

with $D = k_B T/\gamma$ the diffusion coefficient. The second contribution comes from the trajectory between clock switch and the subsequent geometric switch. It can be estimated as the difference between the first-passage time of a particle under drift $v(1+\epsilon)$ (with initial condition corresponding to the mean position at the clock switch at distance x from the geometric switch) and the mean of the same first-passage time. This first-passage time is known to follow an inverse Gaussian distribution [181] which can be approximated by a Gaussian with variance

$$V_2 = \frac{2Dx}{v^3(1+\epsilon)^3} \approx \frac{2D\,\langle t_1 \rangle}{v^2(1+\epsilon)^2} \ . \tag{4.11}$$

In the particular case where the diffusion time $x^2/2D$ is much larger than the deterministic time x/v, the skewness of this distribution is small, and it can be well approximated with a Gaussian. In this case, the evolution of δq can be approximated as a simple continuous Langevin equation. Since over a half-cycle, the variance of χ is

$$\mathrm{var}(\chi) = V_1 + V_2 \ , \tag{4.12}$$

the fluctuations for the switching time are estimated by

$$\left\langle q^2 \right\rangle = \frac{DT_c}{4\epsilon v^2(1+\epsilon)} \ . \tag{4.13}$$

A better estimate of the continuum limit for δq (presented in Appendix A) leads to the refined solution

$$\left\langle q^2 \right\rangle = \frac{DT_c}{4\epsilon v^2} \ , \tag{4.14}$$

or, equivalently,

$$\mathrm{std}(\phi_1) = \mathrm{std}\left(\frac{t_1}{T_c}\right) = \sqrt{\frac{\xi}{16\epsilon}} \ , \tag{4.15}$$

where std denotes the standard deviation and $\xi = 2D/(Av)$ is a non-dimensional measure of noise strength. This expression for the fluctuations around the synchronized state describes very well both experiments and simulations (Fig. 4.3).

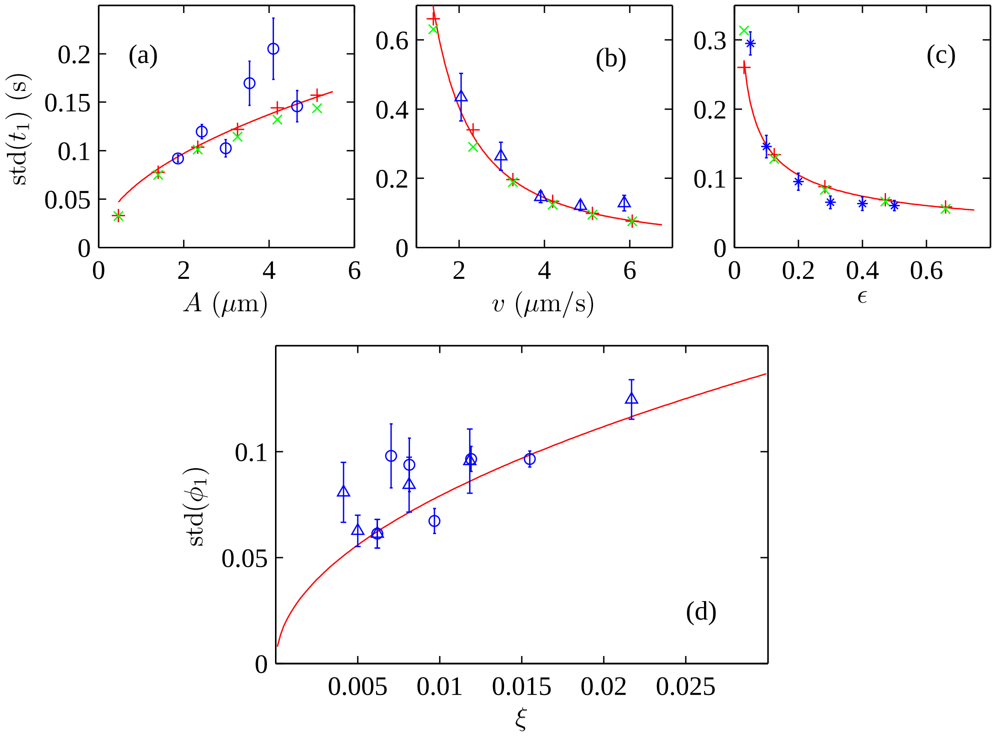

Figure 4.3: Increasing noise ξ leads to higher fluctuations of the delay (phase) between a geometric switch and a clock switch. (a,b,c) Theoretical predictions at 296 K (line) fit with both experiments (blue $\circ$, $\triangle$ and $*$) and simulations with (green $\times$) or without (red $+$) experimental corrections. Parameters are the same as in Fig. 4.1. (d) As shown in the formula for the fluctuations ϕ_1, Eq. (4.15), represented by the solid red line, the amplitude A and the mean velocity v can be merged in the strength parameter $\xi = 2D/(Av)$ which is the ratio of the noise amplitude gained in one half-cycle and A. Error bars are the standard deviation of four different data sets.

4.3.3 Effect of a detuned clock

Here, the consequences of a clock period that does not match the natural oscillation time of the oscillator is analyzed. The period of the clock can be longer or shorter by a time δ:

$$T_c = \frac{2A}{v} + \delta \; . \tag{4.16}$$

Repeating the calculation sketched above, it can be seen that the fixed point position r_{fp} is shifted by the quantity $(1-\epsilon^2)v\delta/(4\epsilon)$. In terms of switching times, this behaviour is translated in the synchronized "phase difference"

$$\phi_1 = \frac{t_1^{\mathrm{fp}}}{T_c} = \frac{1}{4}\left(1 - \frac{1-\tau}{\epsilon}\right) \, , \tag{4.17}$$

where $\tau = T_d/T_c$ measures the mismatch between oscillator and drive. This formula assumes that the sequence of geometric and clock switches is as shown in Fig. 4.1. It is therefore only valid for $\tau \in [1-\epsilon, 1+\epsilon]$. In other words, when changing the clock period, the system adapts its phase in the interval $[0, 1/2]$ in order to remain synchronized. Note that t_2 will shift in the opposite direction in order to maintain the sum $t_1 + t_2 = T_c/2$ constant. When noise and detuning are present at the same time, the argument presented above can be repeated step by step with no further complications, leading to the expression

$$\mathrm{std}(\phi_1) = \sqrt{\frac{\xi\tau}{16\epsilon}} \; . \tag{4.18}$$

4.3.4 Phase diagram

Fig. 4.4(a) presents experimental data showing phase slips emerging with detuning, and Fig. 4.4(b) explores numerically the dependence on τ of the phase difference accumulated in each cycle. The plateaus in Fig. 4.4(b) correspond to synchronized states [87], where the accumulated phase difference locks. The plateau at zero, around $\tau \approx 1$, is the basic synchronized state and other synchronized states exist at particular integer ratios (identical to the Arnol'd tongues of nonlinear oscillators [87]). The synchronization plateaus

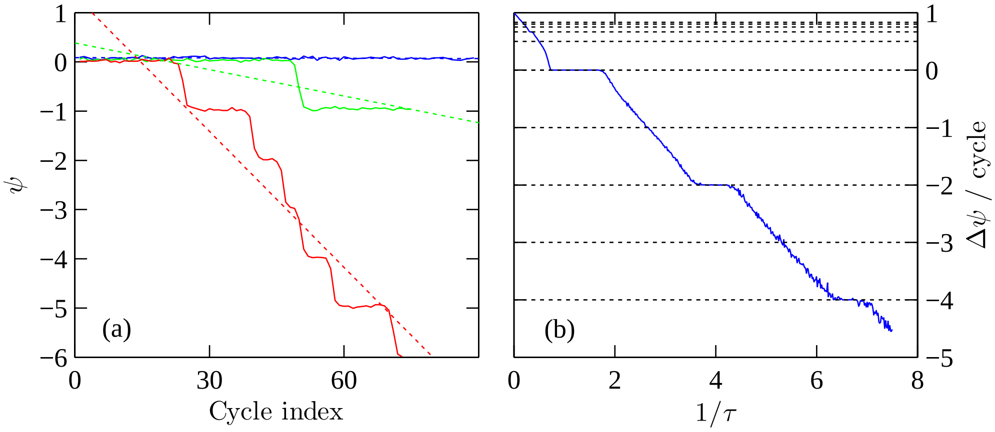

Figure 4.4: Synchronization in presence of mismatch in the natural frequencies of oscillator and clock. (a) shows how the experimental accumulated phase in time ψ depends on the detuning between the clock and the natural bead period (solid lines). $1/\tau = 1.43$ (blue), 1.68 (green) and 1.75 (red). For high detuning, phase slips occur, leading to phase difference accumulation. Dashed lines are linear fits, the gradient of which are the phase difference accumulated in each cycle. Extensive simulations in (b) show plateaus in the phase accumulation, at integer frequency ratios between oscillator and clock (integer ratios are highlighted by dashed lines). $T = 296$ K, $A = 4.66$ μm, $v = 3.91$ μm/s and $\epsilon = 0.5$.

are affected by both noise level and detuning strength [Fig. 4.5(a,b)]. The positions defining the plateaus can be collected as a phase diagram as a function of τ and the noise strength ξ, for a given modulation strength ϵ [Fig. 4.5(c)].

The values that delimit the synchronization region for the locked state with equal frequency can be estimated analytically using the expressions derived above for the fixed point of ϕ_1 and its variability. As a criterion for stability, to be considered as synchronized, the system should have a fixed point ϕ_1 placed at least two standard deviations (of ϕ_1) away from the boundaries of 0 and 1/2 set by the positions of the geometric switch. In this condition, the probability of phase-slips is small, as there will be a slip every 43 cycles on average. This gives the thresholds observed in Fig. 4.5(c), in very good agreement with experiment and simulations.

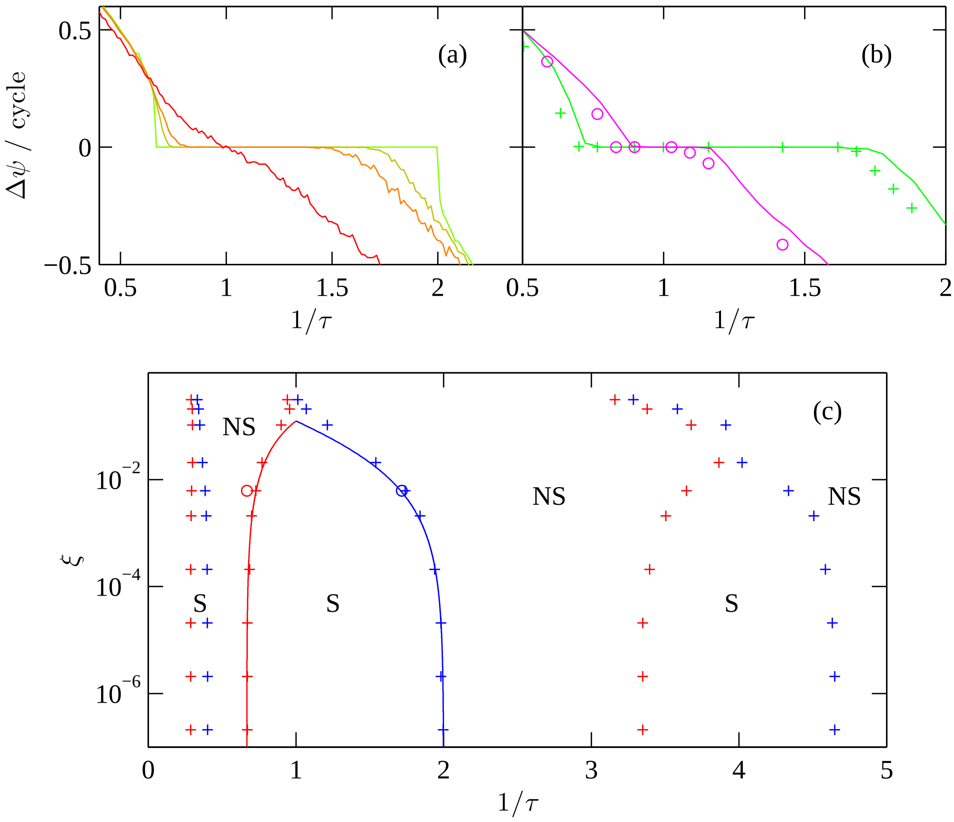

Figure 4.5: The synchronization plateau width is affected by both noise level (a) (simulations with $\xi = 2.09 \times 10^{-7}, 6.20 \times 10^{-3}, 2.09 \times 10^{-2}, 0.209$ from green to red, and $\epsilon = 0.5$) and coupling strength ϵ (b) [simulations as lines, and experiments ($\circ$) at 296 K for perturbations $\epsilon = 0.2$ (magenta) and 0.5 (green)]. $A = 4.66$ μm and $v = 3.91$ μm/s. Note in (a) that for $T = 296$ K (i.e. $\xi = 6.20 \times 10^{-3}$), the synchronization is lost for $1/\tau \approx 1.7$, in agreement with Fig. 4.4(a). (c) Phase diagram representing the lower (red) and upper (blue) plateau boundaries depending on the noise $\xi = 2D/(Av)$. Three plateaus are found in the $1/\tau \in [0.1, 5]$ range. Simulations (+), experiments ($\circ$) and theory (lines). The regions identify synchronized (S) and non-synchronized states (NS).

4.4 Application to cilia and flagella

The two-state geometric-switch oscillator analyzed here exhibits many features typical of a noisy nonlinear oscillator [87], similarly to rotor models for cilia [88, 142]. This is by itself remarkable, as the definition of its dynamics (with a discontinuous velocity) puts it *a priori* in a peculiar class of systems. As shown above, its synchronization dynamics and the role of thermal noise as measured in experiments can be understood by simple quantitative arguments.

Considerations can be made on the noise threshold where synchronization is lost. At a given detuning level τ, this is set by the external perturbation ϵ and the variable $\xi = 2D/(Av) \sim k_B T/W_{\text{stroke}}$, where $W_{\text{stroke}} = \gamma v A$ is the work performed by the rower on the fluid during one stroke. For synchronization to be observed, the ratio ξ/ϵ should not exceed a critical value of order 1. The ratio can be seen as an inverse Péclet number, for which the force in the advective term has to be the coupling force (hence proportional to ϵ). This sets a minimum scale for the size of the oscillator and its rowing amplitude. Plugging in realistic numbers [93], it was estimated that the condition is always satisfied for flagella and cilia ($\xi \approx 10^{-4}$ to 10^{-5}, $\epsilon \approx 10^{-1}$). On the other hand, this might not always be the case for smaller systems. As an example, ξ could be of the order of 10^{-2} for stereocilia [182], which might put them near the critical limit. Indeed, it is observed that different bundles of stereocilia do not synchronize. While realistic situations are likely to involve more complex external drive and collective behaviour, the simple system studied here highlights conditions and limits that are likely to apply to a range of systems including future artificial swimmers or synchronized micromotors.

Chapter 5

Effect of the driving force profile on the state of synchronization of two rowers

5.1 Introduction

Motile cilia generate transport of fluid by periodic beating, through remarkably organized behaviour in space and time. It is not known how these spatiotemporal patterns emerge and what sets their properties. Individual cilia are non-equilibrium systems with many degrees of freedom. However, in a coarse-grained model (see Section 2.3), their description can be represented by simpler effective force laws that drive oscillations, and paralleled with nonlinear phase oscillators studied in physics. Here, a two-rowers experiment proves the role of the average force profile in establishing the type and strength of synchronization. It is found that highly curved driving potentials are required for synchronization in the presence of noise. The applicability of this approach to biological data is also illustrated by successfully mapping the behaviour of cilia in the alga *Chlamydomonas* onto the coarse-grained model.

The system studied here is sketched in Fig. 5.1. Two rowers are placed on the x axis, and oscillate along that direction. Previous work on two oscillators

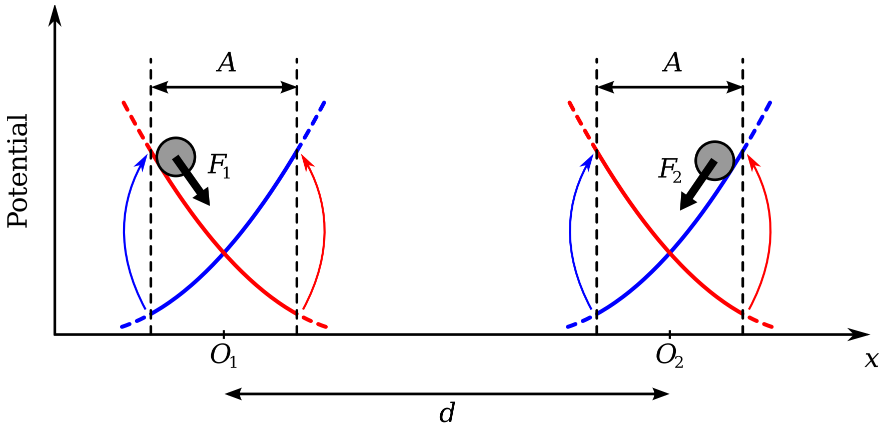

Figure 5.1: Two rowers driven by forces F_1 and F_2 and spaced by a distance d are coupled through the fluid. This chapter focuses on the state of synchronization and its strength depending on the shape of the driving potentials.

showed that the hydrodynamic coupling between the oscillators leads to synchronization in antiphase when the particles are driven by *harmonic* potentials [147]. Wollin and Stark [146] also recently showed numerically that in a system of active oscillators, driven with the geometric switch rule, the potential shape determines the in-phase or antiphase character of motion between nearest neighbours. Other work in my group [155] also suggest that the state of synchronization depends on the shape of the driving forces.

With experiments, it is shown in this chapter how the driving potential, which in a coarse grained fashion represents the internal force engine with which the active unit of a flagellum pushes the fluid during each beating cycle, determines the dynamical steady state in competition with thermal noise. The experimental findings are related to fully stochastic Brownian dynamics simulations, and the system is also studied analytically (simplifying the role of thermal noise by neglecting the coupling of thermal fluctuations).

5.2 Coupled equations of motion

The motion of two externally driven spherical particles at low Reynolds number is described by the force balance

$$0 = \mathbf{F}_i - \sum_j \mathbf{H}_{i,j}^{-1} \dot{\mathbf{r}}_j + \mathbf{f}_i(t) \ , \tag{5.1}$$

where $i \in \{1, 2\}$ indexes the bead. $\mathbf{F}_i$ represents the driving force acting on bead i and $\dot{\mathbf{r}}_i$ its velocity. The drag is modelled by the Oseen tensor $\mathbf{H}$ (see Section 1.6) and $\mathbf{f}_i$ is a stochastic term describing the Brownian force on bead i. For the time scales considered here, the noise is adequately described by $\langle f_i(t) \rangle = 0$ and $\langle f_i(t) f_j(t') \rangle = 2k_B T \, \mathbf{H}_{i,j}^{-1} \, \delta(t - t')$ (see Section 1.9). Only the case of driving forces $\mathbf{F}_i$ parallel to the direction of alignment of the particles x is considered here, which leads to coupling forces along x too. Projected along this direction, the system of equations becomes

$$\left\{ \begin{array}{lcl} 0 & = & F_1(x_1, t) - \gamma \left(\dot{x}_1 - \epsilon \dot{x}_2 \right) + f_1(t) \\ 0 & = & F_2(x_2, t) - \gamma \left(\dot{x}_2 - \epsilon \dot{x}_1 \right) + f_2(t) \end{array} \right. , \tag{5.2}$$

where $\epsilon = 3a/(2d)$ is the coefficient describing coupling between the particles, a is the bead radius, d the mean distance between the two beads and $\gamma = 6\pi\eta a$ is the drag coefficient given a viscosity η. The non-diagonal terms of the Oseen tensor originate from the flow field created by one bead and acting as a drag on the other bead. In the equation above, it is supposed that the amplitude of the oscillations A is much smaller than d, so that the distance between the particles is constant to d.

5.3 Implementation of the rowers

The switch rule maintains the colloids out of equilibrium [Fig. 5.2(a)]. The basic oscillation cycle of each bead is built by alternatively activating two traps, the rule being described in Fig. 2.11. The two rowers are characterized by the same potential, but centred on different positions (Fig. 5.1). The

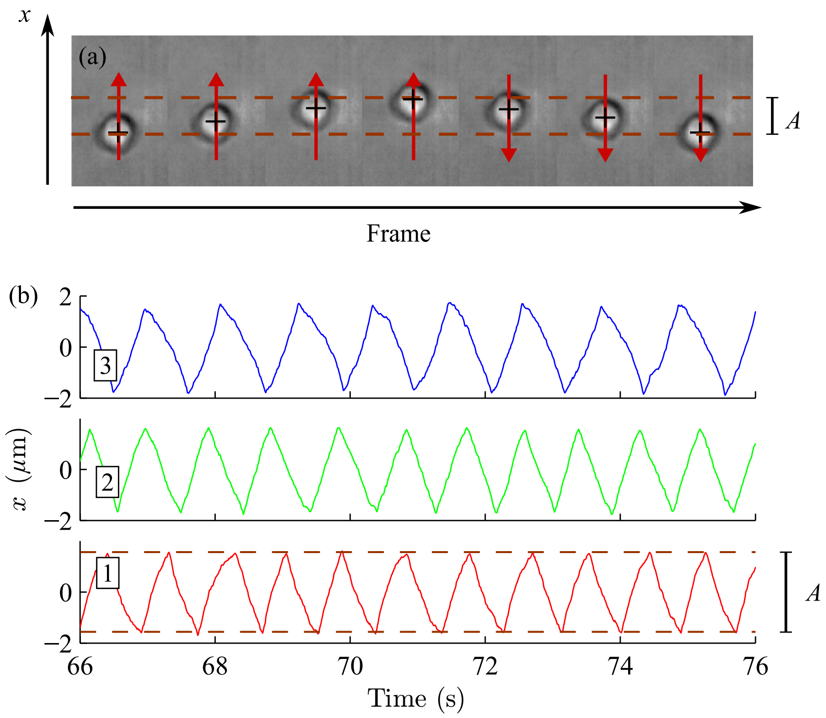

Figure 5.2: (a) Selected frames showing a single bead driven by optical traps through the geometric switch rule. The direction of the gradient of laser intensity is shown in red arrows. It is reversed when the particle reaches a position defined by the dashed line. (b) Tracks of a single driven particle. The three different graphs correspond to different driving potentials with positive (red), null (green) and negative (blue) curvature. The shape of the potential affects the curvature of the tracks.

simulations consider potentials of the form $k_\alpha x^\alpha$, where the parameter α characterizes the curvature. The force $F_i(x_i, t)$ can therefore be written

$$F_i[x_i, \sigma_i(t)] = -\sigma_i \alpha k_\alpha \left| x + \sigma_i \frac{\lambda}{2} \right|^{\alpha-1} . \tag{5.3}$$

Here, $\sigma_i = \pm 1$ is the state of the switch acting on bead i and defines in which direction F_i is dragging the bead, and x_i is measured from the mean position (point O_i in Fig. 5.1). λ is the distance between the centres of the two traps driving one of the beads. The geometric switch imposes a constant amplitude of oscillations $A = \lambda - 2\varsigma$, with ς an input paramater in the simulations.

The experimental setup produces potential landscapes of varying curvatures by using time-shared optical traps, with a designed gradient of laser intensity as explained in Section 3.2.4. Each landscape is made of 62 traps, so that

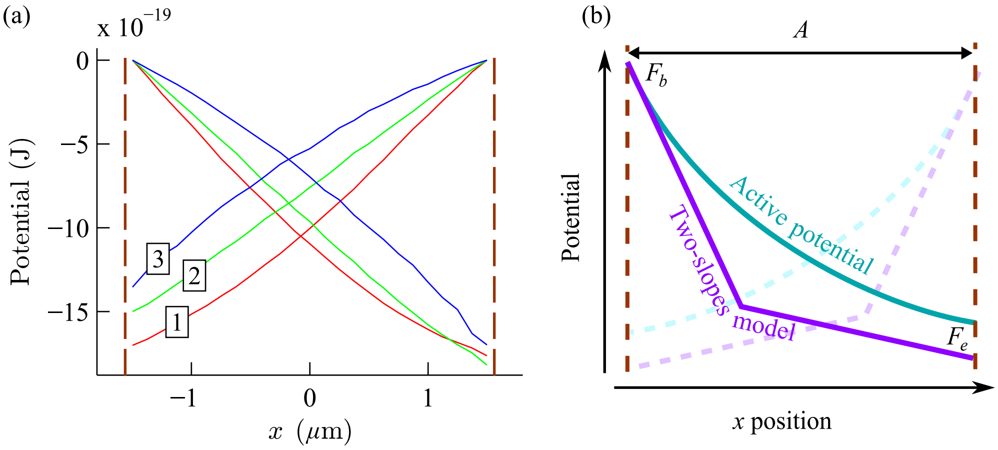

Figure 5.3: (a) Mean driving potentials for a bead driven in potentials of positive (red), null (green) and negative (blue) curvature, measured from the tracks in Fig. 5.2 (2 min long movies). (b) A potential (cyan) is modelled in the theory as "two-slopes" (purple). The curvature parameter c is measured from the mean potential in (a) by fitting the slopes at $-A/2$ and $A/2$, giving F_b and F_e for both decreasing and increasing potentials. Experimental parameters in (a): $A = 3.1$ μm, $d = 10$ μm, $T = 296$ K, $F_0 \sim 0.53$ pN and $c = 0.38$ (red), -0.11 (green) and -0.40 (blue).

at a given instant, 124 simple traps are active for the whole system of two rowers. Experimental potentials can be approximated by the power laws in simulations. More simply, their shape is captured by a parameter

$$c = \frac{F_b - F_e}{F_b + F_e} \tag{5.4}$$

which depends only on the forces F_b and F_e at the beginning and the end switch positions respectively, see Fig. 5.3(b). As it will be show in this chapter, all the effects due to potential shape can be related to this curvature parameter c and to the mean force $F_0 = (F_b + F_e)/2$, as also suggested in [146].

Experimental potentials are created with different curvatures, as shown in Figures 5.2(b) and 5.3(a). The potentials are measured from the position $x(t)$ of a single bead oscillating, by constructing a histogram of the position of the bead in time, relative to the switches of the traps. This procedure averages out the thermal noise, showing clearly the difference of curvature in the three experiments in Fig. 5.3(a). Experiments are conducted with 3.47 μm diameter silica beads from Bangs Laboratories, diluted in a water-glycerol solution with a viscosity of 2.2 mPa·s. Trapped beads are maintained at least 70 μm far from any surface of the microscope slides in order to avoid effects of wall interaction.

5.4 In-phase to antiphase transition

Two rowers are now put close to each other and interact through the fluid. Figures 5.4 and 5.5(a,b) show a clear antiphase behaviour observed in the steady state for potentials with positive curvature, and in-phase behaviour with negative curvature. The system with linear drive is not synchronized.

In Fig. 5.5, a synchronization order parameter $Q(k)$ is calculated for each half-cycle k of oscillation of the bead 1 [147],

$$Q(k) = \frac{-1}{s_{k+1} - s_k} \int_{s_k}^{s_{k+1}} \mathrm{d}t \, \sigma_1(t)\sigma_2(t) \ , \tag{5.5}$$

with s_k the time at the k^{th} switch of bead 1 and $\sigma_i(t) = \pm 1$ the variable defining the state of the potential for bead i (indicates if the driving force is pushing the bead towards increasing or decreasing positions). Q is normalized so that $-1 < Q < 1$, with $Q = -1$ describing in-phase motion and $Q = 1$ antiphase. As defined in Eq. (5.5), it is calculated for each half-cycle. Fig. 5.5(a) shows its average over an experiment $\langle Q \rangle_k$, while Fig. 5.5(b) shows its distribution.

These optically driven oscillators are the first experimental realization of a

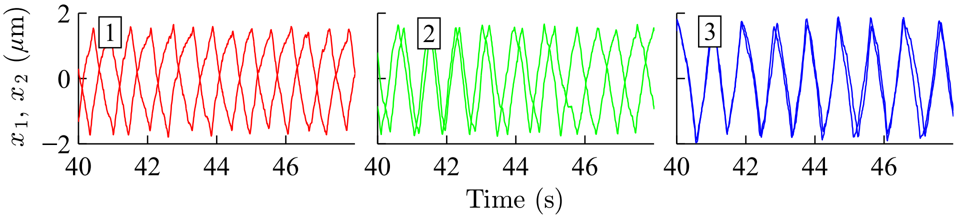

Figure 5.4: Experimental tracks of two beads coupled hydrodynamically, for the three driving potentials characterized in Fig. 5.3(a). Positive curvature leads to antiphase (AP) synchronization while negative curvature leads to in-phase (P) synchronization. In the limit case of linear potentials (zero curvature; central section of the plot), the beads do not synchronize.

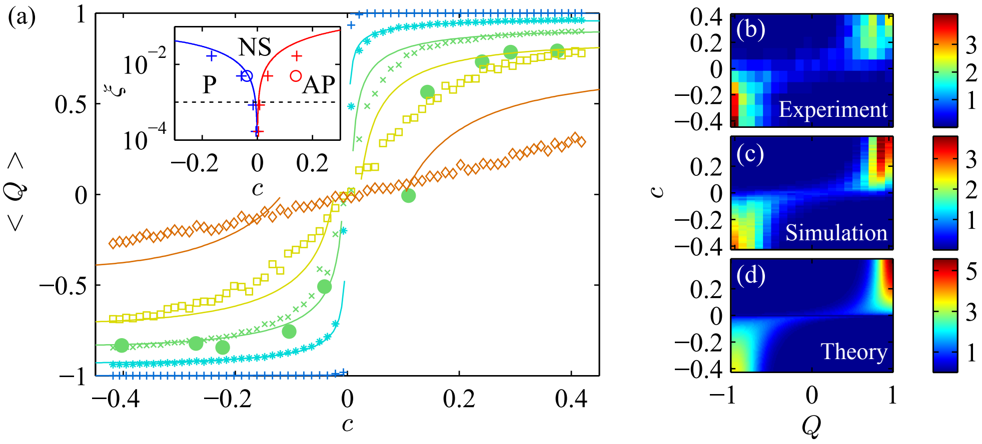

Figure 5.5: (a) The phase/antiphase transition in the oscillation dynamics of the two particles is observed in experiments (∘), simulations (+) and adequately captured by theory (lines). Conditions are $A = 3.1\ \mu$m and $F_0 \sim 0.53$ pN, and noise strength $\xi = 2k_BT/(AF_0)$ is varied by changing the temperature [from blue to orange: $\xi \approx 1.68 \times 10^{-7}$, 8.38×10^{-4}, 4.96×10^{-3} (room temperature), 1.68×10^{-2} and 8.38×10^{-2}]. $\langle Q \rangle$ characterizes the state of oscillations (1 in AP and −1 in P). Experiments should be compared with the simulations in green. At any temperature, the state of synchronization is either in phase or in antiphase, depending on the sign the curvature c, with a sharper transition at lower temperature. The transition is smoother when noise is added. Theory fits very well with experiments and simulations up to room temperature. Inset: Phase diagram showing synchronized states in phase (P), in antiphase (AP) or not synchronized (NS). Theory (lines), simulations (+) and experiments (∘) show, for each value of the noise strength ξ, the value of c for which $|\langle Q \rangle| = 1/2$. The dotted line shows the noise strength estimated for *Chlamydomonas*. The probability distributions of Q at $T = 296$ K in experiments (b), simulations (c) and from the theoretical argument (d) show that in presence of noise, the peaks are still centred around ±1 but with a large spreading. The theoretical curves are chopped when crossing 0 as the analytical formula fails to describe the state when synchronization is very weak or lost (see Appendix B). In the experiments, the two-rowers movies are 5 min long, while simulations are equivalent to 2000 s. In the simulations, $\varsigma = 1\ \mu$m.

hydrodynamically synchronized system transitioning between in-phase (P) and antiphase (AP). The transition is obtained by varying the curvature of the potentials. Numerical simulations of power law potentials are carried out, with different exponents α while choosing stiffnesses k_α such that the period of a cycle stays constant [Fig. 5.5(a,c)]. These show in general synchronized dynamics, with a transition at the linear drive condition, i.e. at $\alpha = 1$ (which corresponds to $c = 0$).

In the limit of no-noise (which is not accessible experimentally), the known result that the pure P and AP are the only possible stable states is recovered, and the system converges to either one depending on the sign of c. Only for $\alpha = \pm 2$ this result can be obtained analytically, as previously shown for $\alpha = 2$ [147]. However, the main question lies in the role of noise in the crossover between positive and negative curvature, and therefore requires a more general approach.

5.5 Theory for the synchronization of two rowers

5.5.1 Without thermal noise

The general deterministic (no noise) behaviour can be estimated analytically using an approximating two-slopes potential [Fig. 5.3(b)] which is adequate to approximate both the simulated results, which use power law potentials, and experimental results, for which the shape is not a specific analytical function. The calculation is only outlined here. For the full calculation, see Appendix B.

The two-slopes model might seem like a crude simplification, but it produces remarkably robust estimates, and it is necessary to obtain simple expressions for the particles' first-passage times in the presence of noise (see Fig. B.2). Note that the two-slopes model introduces an additional parameter defining the position of the slope break [visible in Fig. 5.3(b)], but the synchronization state does not depend on this parameter. This is justified in the appendix.

The case for $c < 0$, for which in-phase synchronization is expected, is explicitly illustrated here. As a proxy for the phase, the time difference t_1 between the nearest switch of the second bead that occurs closest in time to a switch of the first bead is considered (it is defined for every half-cycle k of one of the beads). The aim is to provide an expression of $t_1^{(k+1)}$ depending on $t_1^{(k)}$. Note that $t_1 = 0$ can correspond to either a P or AP oscillation depending on the sign of $\sigma_1(t)\sigma_2(t)$ at the simultaneous switch time, but an initial condition close to the in-phase state is assumed here for sake of argument. Since in this approximation the driving potentials are only defined with constant forces, and the hydrodynamic coupling term in Eq. (5.2) is linear, the half-cycle k can be split into four parts within which the velocities of the beads will be constant at $\pm\frac{1}{\gamma}(F_u \pm \epsilon F_v)$ with $u, v \in \{`b', `e'\}$. Therefore, $t_1^{(k)}$, $t_1^{(k+1)}$, the start times of each part and the positions at these times are all related by a linear system of equations that is solved in Appendix B and leads to a simple iterative map for t_1:

$$t_1^{(k+1)} = \kappa_P t_1^{(k)} \ , \tag{5.6}$$

with

$$\kappa_P = 1 + 2\epsilon \frac{F_b^2 - F_e^2}{F_e F_b} \ , \tag{5.7}$$

to first order in the coupling coefficient ϵ. For $c < 0$, $F_e > F_b$ and $\kappa_P < 1$, leading to the known result that in-phase synchronization is stable. Identical equations hold for the antiphase state with a κ_{AP} having reversed sign for ϵ, and hence give stability for $c > 0$. This simple model shows that the state of synchronization depends on the sign of c. Note that for $c = 0$, $\kappa_P = \kappa_{AP} = 1$ and the system does not synchronize. This particular case is expected, since the driving force over a cycle should be non-reversible in time to allow synchronization, at least in the absence of thermal fluctuations [18].

5.5.2 With thermal noise

Most importantly, having approximated the driving potentials, it is possible to estimate analytically the role of noise in synchronization. Thermal noise adds fluctuations to t_1 at each half-cycle, represented as a random variable

$\zeta(i)$ added to Eq. (5.6):

$$t_1^{(k+1)} = \kappa t_1^{(k)} + \zeta(k) \ . \tag{5.8}$$

Here κ simply represents either κ_P or κ_{AP} depending on the sign of c, allowing to solve both P and AP cases at the same time. For one bead, the time difference between two consecutive switches is a first-passage time. Its distribution is estimated by considering each of the two linear portions of the potential separately, and neglecting the change of velocity of the beads due to the coupling term, as well as the correlations in the noise. By combining the supposed independent fluctuations for each bead (generalizing the procedure carried out in Chapter 4), $\zeta(i)$ is approximated as a zero-mean Gaussian random variable of variance

$$\mathrm{var}\left[\zeta(k)\right] = \frac{4AD\gamma^3}{F_0^3}\frac{1+c^2}{(1-c^2)^2} \ , \tag{5.9}$$

with $D = k_BT/\gamma$ the diffusion coefficient of a particle. By iterating Eq. (5.8), the autocorrelation function of t_1 is deduced:

$$g_{t_1}(k) = \kappa^k g(0) \ , \tag{5.10}$$

with $g_{t_1}(0) = \mathrm{var}(\zeta)/(1-\kappa^2)$ the variance of t_1. g_{t_1} is compared to simulations in Fig. 5.6. As t_1 is linked to the phase between the two beads, $\langle Q\rangle_k$ can be written in terms of $g_{t_1}(0)$ and the analytical function $\langle Q\rangle_k$ is displayed in Fig. 5.5(a). Further details concerning this calculation are provided in Appendix B.

From the degree of order in the dynamics (for which a threshold of $|\langle Q\rangle_k| > 1/2$ is taken to consider the system as synchronized), it is possible to draw a phase diagram for the synchronized states, as a function of the two important parameters: curvature and noise amplitude. As shown in the inset of Fig. 5.5(a), the analytical estimate agrees very well with the Brownian dynamics simulations, up to considerable levels of noise. Fig. 5.6 shows that the simulated autocorrelation functions decays in a few cycles for highly curved potentials (large $|c|$), and slower near the transition, where κ tends towards 1.

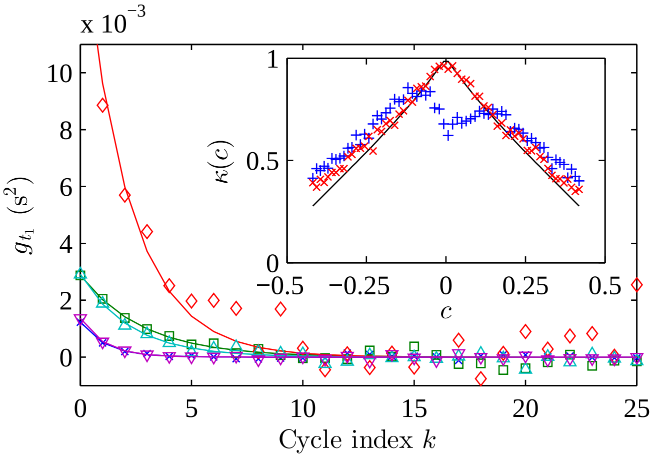

Figure 5.6: Autocorrelation of the phase t_1 between the two beads in simulations (+) for different values of c: -0.42 (blue), -0.20 (green), -0.0071 (red), 0.20 (cyan) and 0.42 (purple) fitted to exponential decays (solid lines). Inset: simulated decay coefficients κ for $\xi = 4.96 \times 10^{-3}$ (blue markers) and $\xi = 8.38 \times 10^{-4}$ (red markers) are in good agreement with the theoretical values (black line). The strength of synchronization is the strongest for the highest curvatures (high $|c|$). Theory and simulations differ for $c \approx 0$ because the assumption that oscillations are nearly in phase or in antiphase becomes wrong; when the noise strength increases this happens for larger values of c. Parameters are the same as in Fig. 5.5. Experiments are not shown as the statistical noise is too large in the 5 min long experimental data sets.

5.6 Application to the *Chlamydomonas* alga

The predictive power of the bilinear model demonstrates that the relevant feature of the internal engine affecting the synchronized state is the difference between the forces at the instances of switch. This is relevant to synchronization in biological cilia and flagella. This section illustrates it by taking as an example the biflagellated alga *C. reinhardtii* where the synchronization state of the two beating filaments can be tuned, leading to different swimming modes: directed runs, and random tumbling [93].

In order to map the synchronization of the two flagella of *Chlamydomonas* with the coarse-grained model made of two beads, one need (a) to reconstruct the driving potentials of each flagellum and (b) to project the oscillations along one particular direction. This is done by using data of flagellum configurations during beating in a uniflagellated *Chlamydomonas* [64] by modelling a flagellum at instant t by a bead located at the centre of mass of the filament that is subject to a driving force that is the opposite of the total force from the fluid acting on the flagellum. The model is one-dimensional (i.e. the coupling forces from the Oseen tensor are in the same direction as the driving forces) in two particular cases: when the driving forces are along x or along y, with x the direction of the line defined by the average position of the two beads (Fig. 5.7). The case of oscillations along x is explicitly detailed here. The other case is described by the same model in which x is replaced by y and the coupling term ϵ is replaced by $3a/(4d)$.

Projecting forces from *Chlamydomonas* parallel and perpendicular to the direction of motion, effective one-dimensional switching potentials can be obtained. More details on the matching of the parameters from the data on *Chlamydomonas* to the model are discussed in Appendix C. From this matching procedure several conclusions were found. First, the mapping recovers the correct synchronized state both when projected along x and y: flagella oscillate in phase along x and in antiphase along y. Second, as illustrated by the dotted line in Fig. 5.5(a), the biological system appears quite far from the noise threshold. Third, the model predicts that the component of the hydrodynamic interaction which dominates the synchronization is y, i.e.

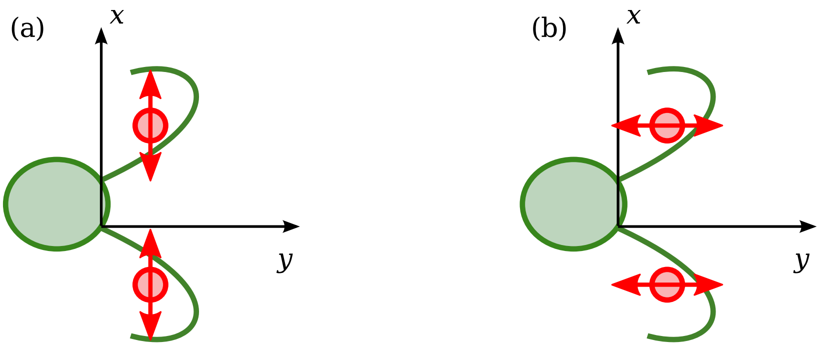

Figure 5.7: The biflagellated *Chlamydomonas* organism can be modelled as a unidimensional system of two rowers along the x or y axes. Because of the "breaststroke" of the flagella, when projected along x [red rowers represented in (a)], the system is expected to be in antiphase, while it is expected to be in phase for rowers projected along y [as in (b)].

transverse to the swimming direction of the microorganisms. This last point would be relevant in conditions where the presence of multiple organisms contributes to additional periodic forces.

5.7 Conclusions on the role of curvature of the driving forces

The two possible states for the synchronization of two rowers — phase and antiphase — have been observed experimentally. The transition between the two states was observed by Wollin and Stark [146] without thermal noise, for which the system has no threshold. This work shows the importance of balancing the curvature of the driving potential to the level of noise: a stronger curvature makes the steady state more robust, pointing to a requirement of time asymmetry in the driving potential for strong synchronization. It might as well be related to another model of oscillator studied recently by Leoni and Liverpool, in which the driving force F_i is made dependent on the particle position by setting its time derivative as being a third order polynomial of the particle position x [150]. In-phase and antiphase synchronization is obtained in this system and depends on the sign of the coefficient for x^3, that would be equivalent to the sign of the curvature of the driving potentials for the rowers.

The phase diagram of the dynamical state versus curvature and noise enables biological systems to be mapped onto the model. This is useful in two ways: For systems (like *Chlamydomonas*) for which the cilia's force cycle has been measured, it is possible to predict the state of synchronization from the coarse-graining of internal degrees of freedom. On the contrary, from the observation of cilia correlations at steady state, it is possible to set boundaries on the cilia geometric parameters (distance, filament length) and on the average properties of the active force cycle, which results from the activity of molecular motors and the filament structure.

Chapter 6

Understanding the dynamics in systems of many rowers

6.1 Introduction

The phenomenon of metachronal waves in cilia carpets has been well known for decades; these waves are widespread in biology, and have fundamental physiological importance. While it is accepted that in many cases cilia are mainly coupled together by the hydrodynamic velocity field, a clear understanding of what aspects determine the collective wave properties is lacking. It is a difficult problem, because both the behaviour of the individual cilia, and their coupling together, are nonlinear. In this chapter, rowers are used to investigate experimentally the coupling through hydrodynamics in systems of many oscillators, showing that collective dynamics emerges. This work generalizes to a wider class of systems the recent finding that the non-equilibrium steady state can be understood based on the equilibrium properties of the system, i.e. the positions and orientations of the active oscillators. In this model system it is possible to design configurations of oscillators with the desired collective dynamics. The other face of this problem is to relate the collective patterns found in biology to the architecture and behaviour of the individual active elements.

Most of this work was done with Romain Lhermerout, a master student under my supervision in 2011.

The main result of this chapter is to prove that even in apparently complex arrangements of oscillators (disordered and lacking rotational or translational symmetries), it is possible to predict the collective dynamics from just the knowledge of the positions and orientations of the oscillators. In a biological tissue with a carpet of cilia, plenty of oscillators at various positions will be oscillating, quite possibly exerting forces in different principal directions, and their phases will be free to couple. The result obtained here with harmonic potential driving is therefore a key step, albeit in a simple model system, in establishing the important link between microscopic and macroscopic behaviour in systems of hydrodynamically coupled oscillators.

6.2 Background

The problem of understanding the collective dynamical pattern of systems with large number of particles was already approached in different contexts: particles confined in static traps, and rowers. The state of understanding of these two coupled systems prior to the start of my Ph.D. is summarized in this section.

6.2.1 Decoupling of the equations of motion for interacting particles in static potentials

Systems of several particles, each of them trapped in a harmonic static potential, were studied by different groups, namely Meiners and Quake [29] for two particles, Polin, Grier and Quake [183] in a linear chain of particles, and Di Leonardo *et al.* [184] and our group [30] for particles equally spaced along a circle. The fluctuations in position of the particles that originate from Brownian motion show a complex dynamics because of the hydrodynamic coupling. However, since the Oseen tensor leads to linear equations of motion when the distances between the particles are constant (which is a fairly good approximation for particles that are confined and far apart), the dynamics simplifies, when the set of $(x_i)_{i\in\{1,\dots,2N\}}$ coordinates (in 2d) of the particles is observed in a space of new coordinates in which the Oseen tensor is a diagonalized. In this space, each of the positions along each coordinate $\tilde{x}_i$ shows fluctuations that are characterized by a time autocorrelation that decays exponentially [29, 30, 183]:

$$\langle \tilde{x}_i(0)\tilde{x}_i(t)\rangle \propto \mathrm{e}^{-t/\tau_i} \ , \tag{6.1}$$

with a characteristic decay time τ_i related to the eigenvalues of the diagonalized Oseen tensor. This result is obtained by using (a) that individual uncoupled beads have exponentially decaying autocorrelations in position, (b) the linearity of the coupled equations of motions, and (c) that the Oseen tensor can always be diagonalized. In the new coordinates, the different modes are also uncoupled:

$$\langle \tilde{x}_i(0)\tilde{x}_j(t)\rangle = 0 \quad \text{for} \quad i \neq j \ . \tag{6.2}$$

Hence, in the diagonalized space, the system is fully understood in terms of the dynamics of "normal modes".

6.2.2 Dynamic solutions of interacting rowers

In an attempt to use the results above on configurations of active oscillators, rowers experiments were performed in my group before I started my Ph.D. [155]. For simple configurations of rowers arranged along a circle, equally spaced, and oscillating tangentially to the circle, the decomposition on normal modes was used to determine analytical solutions of the dynamics of the system. The calculation was tractable, because of the high level of symmetry of these configurations.

The basic idea developed in [154] and [155] is that the dynamic solution of the system is simply described by a combination of normal modes in all the time intervals during which none of the oscillators undergoes a geometric switch. After solving the problem in a first time interval, the equations can be solved in the next interval (after the first trap switch), taking into account the continuity of the particles' positions. The evolution in time of an initial condition can therefore be written explicitly, solving step by step the equations. Periodic solutions can be found by setting as a constraint that the system should come back to its initial condition. The calculation can only be carried out in simple highly symmetric configurations, like a small number of rowers on a circle. The point made in [154], was that while there is no simple recipe to predict the stable synchronized state (out of a great variety of solutions that can be found), its main properties are determined by the normal mode with the longest relaxation time (for harmonic drive).

This chapter describes the continuation of this work in which more complex configurations (defined by the positions and directions of the rowers) are studied. It presents a method to extract information on the dynamics of *any* configuration of rowers coupled through the Oseen tensor, by using an "effective Oseen tensor" that reduces the dimensionality of the system. For example, the dynamics of a system of nine rowers realized experimentally (Fig. 6.1) could be understood in terms of normal modes of oscillation. Unlike in [154], solutions are not explicitly calculated, but rather characterized by the mode with longest relaxation time.

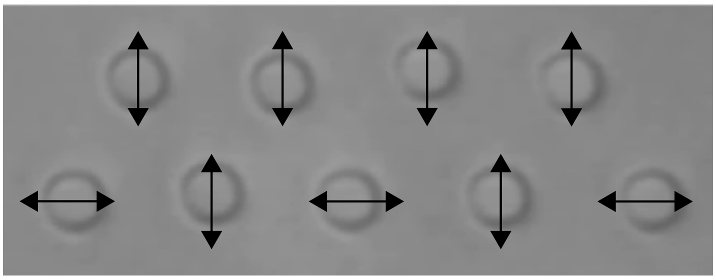

Figure 6.1: Optical microscopy image obtained in the optical tweezers setup showing nine rowers. The average distance between nearest neighbours is $d = 8$ μm. Arrows indicate the orientation of the driven oscillations, for each bead. This configuration of nine beads is the largest of the ones investigated experimentally in this work, and is presented in Section 6.5.4.

6.3 Coupled rowers driven by harmonic potentials

This work is limited to rowers driven by harmonic traps [$U(x) = kx^2/2$ for a single oscillator], as shown in Fig. 2.11. The results obtained in this chapter do not apply to the potentials with other curvatures discussed in Chapter 5 (in particular potentials with a curvature $c < 0$).

6.3.1 Driven dynamics of a single oscillator

For a single oscillator, the equation of motion is a balance of the configuration-dependent driving force $\mathbf{F}(\mathbf{x}, \text{config})$, the drag and the thermal forces:

$$\mathbf{F}(\mathbf{x}, \text{config}) = \gamma\dot{\mathbf{x}} + \mathbf{f}(t) \ , \tag{6.3}$$

where $\gamma = 6\pi\eta a$, η is the viscosity of the solvent, and $\mathbf{f}(t)$ is white noise with mean square amplitude set by the fluctuation dissipation theorem. If the potentials are harmonic, and the motion is along the x-axis, then $F_x(x, \text{config}) = \pm k(x \pm \lambda/2)$, with the signs depending on the configuration history, see Fig. 2.11. Up to a geometric switch boundary, Eq. (6.3) describes on average an exponentially decaying trajectory with relaxation time γ/k.

6.3.2 Dynamics of many oscillators

Here we consider N oscillators at positions $\mathbf{r}_n = x_n\hat{\mathbf{e}}_x + y_n\hat{\mathbf{e}}_y$. The Oseen tensor describes the relation between the set of all velocities $\{\mathbf{v}_i\}$ and forces $\{\mathbf{F}_j\}$ (see Section 1.6):

$$\mathbf{v}_n = \sum_{m=1}^{N} \mathbf{H}(\mathbf{r}_{n,m})\mathbf{F}_m \ , \tag{6.4}$$

with

$$\mathbf{H}_{n,m}(\mathbf{r}_{n,m}) = \begin{cases} \dfrac{1}{8\pi\eta r_{n,m}} (\mathbf{I} + \hat{\mathbf{e}}_{n,m} \otimes \hat{\mathbf{e}}_{n,m}) & \text{if} \quad n \neq m \\ \dfrac{\mathbf{I}}{6\pi\eta a} & \text{if} \quad n = m \end{cases} , \tag{6.5}$$

where $\hat{\mathbf{e}}_{n,m} = \mathbf{x}_{n,m}/r_{n,m}$.

The steady state dynamics of the geometric switch model can be obtained in principle by solving the dynamic system of equations

$$\mathbf{F}_i(\mathbf{r}_i, \text{config}) - \sum_{j=1}^{N} \mathbf{H}_{i,j}^{-1} \frac{\mathrm{d}\mathbf{r}_j(t)}{\mathrm{d}t} + \mathbf{f}_i(t) = 0 \ , \quad \text{for} \quad i \in \{1, \dots, N\} \ , \tag{6.6}$$

where the second term describing the Oseen coupling forces scales with distance $r_{i,j}$ as $1/r_{i,j}$, and the force $\mathbf{F}_i$ acting on the i^{th} particle is harmonic. The equation is valid in between any two switches, with $\mathbf{F}_j(\mathbf{r}_j, \text{config})$ driving the j^{th} particle towards some fixed minimum; $\mathbf{F}_j(\mathbf{r}_j, \text{config})$ then changes form once a j^{th} particle reaches a geometric switch position.

The stochastic force $\mathbf{f}_i(t)$ in Eq. (6.6) represents the thermal noise on the i^{th} particle. It is characterized by the expressions given in Section 1.9, and is present experimentally (see Chapters 4 and 5, and [147, 155]). It complicates considerably the behaviour of the nonlinear system. It can be included in the Brownian dynamics simulations, but it is neglected to make analytical progress in this chapter.

The fact that Eq. (6.6) changes structure at every switch, makes its solution complex even in the absence of thermal noise. In the presence of noise it then becomes an intractable many-particle first-passage time problem. In a recent paper [154] it was shown how to build analytical solutions in the absence of noise, for some special configurations with high symmetry, starting from a knowledge of the hydrodynamic modes. Here below, the class of systems on which hydrodynamic modes of the actively driven system can be calculated and related to the steady state solution is generalized.

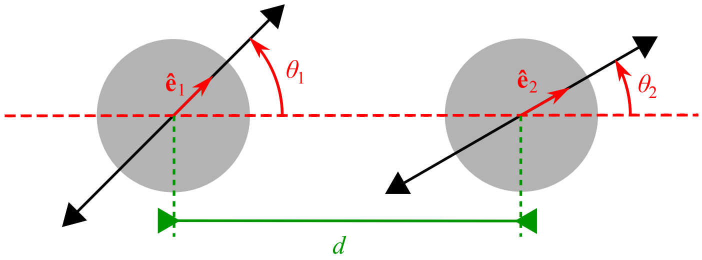

Figure 6.2: Diagram illustrating the configuration of two beads with directions of oscillation θ_1 and θ_2.

(a)

(b)

Figure 6.3: In the simplest case of two beads oscillating on axis [i.e. $(\theta_1, \theta_2) = (0, 0)$], the two normal modes of oscillations $\tilde{v}_1$ and $\tilde{v}_2$ are simply antiphase motion (a) and in-phase motion (b). The geometry of the modes is illustrated by the vector pairs $\tilde{v}_1$ and $\tilde{v}_2$; the eigenvectors are labelled from $1, \ldots, N$ (in this case $N = 2$) in order of decreasing relaxation time scale, and this convention is followed throughout this chapter. The percentage indicates the fractional amplitude observed experimentally from the decomposition of the steady state solution onto the normal modes, as defined in Eq. (6.16).

6.3.3 An effective Oseen tensor accounts for the constraints

The oscillators are driven at fixed angles θ_n, i.e. directions $\hat{\mathbf{e}}_n = (\cos\theta_n, \sin\theta_n)$ (see Fig. 6.2 for a simple two-rowers configuration). In other words the driving forces, and to a good approximation also the displacements in Eq. (6.6), are oriented at a fixed angle θ_i; so we can impose this as a condition that the active driving of each bead along its fixed direction is also constraining each bead to move only along that fixed direction. As in [154, 155], since for each bead most of its displacement takes place along the direction of its drive, this is a fair approximation of the main component of the motion. Based on this, we now show how the general coupling Eqs. (6.6) can be recast in a more transparent way for the system with driven motion. This will enable to show that the main properties of the steady state solutions can be predicted quite simply from the equilibrium coupling tensor, and hence depend on N and on the spatial distribution and arrangement of angular drives.

The direction of the forces is known:

$$\begin{aligned}\mathbf{F}_m &= F_m \hat{\mathbf{e}}_m \\ &= F_m \left(\hat{\mathbf{e}}_x \cos\theta_m + \hat{\mathbf{e}}_y \sin\theta_m\right) \ .\end{aligned} \tag{6.7}$$

With the movement assumed confined in the θ_m direction, we approximate the velocities as

$$v_n \approx \mathbf{v}_n \cdot \hat{\mathbf{e}}_n \quad \text{for} \quad n \in \{1, \ldots, N\} \ . \tag{6.8}$$

Substituting Eqs. (6.5) and (6.7) into Eq. (6.8) leads to:

$$\begin{aligned} v_n \approx \frac{F_n}{6\pi\eta a} + \sum_{m\neq n} \frac{F_m}{8\pi\eta r_{n,m}^3} \Big[& \left(r_{n,m}^2 + x_{n,m}^2\right)\cos\theta_m \cos\theta_n \\ & + \left(r_{n,m}^2 + y_{n,m}^2\right)\sin\theta_m \sin\theta_n \\ & + x_{n,m} y_{n,m} \left(\cos\theta_m \sin\theta_n + \sin\theta_m \cos\theta_n\right) \Big] \ . \end{aligned} \tag{6.9}$$

Eq. (6.9) is a linear relation between the scalar velocities v_n and the scalar driving forces F_m. By analogy with the general Oseen coupling tensor of Eq. (6.4), we can define an effective Oseen tensor that satisfies

$$v_n = \sum_{m=1}^{N} H_{n,m}^{\text{eff}} F_m \ , \tag{6.10}$$

with

$$H_{n,m}^{\text{eff}} = \begin{cases} \dfrac{1}{6\pi\eta a} & \text{if } \ n = m \\ \dfrac{1}{8\pi\eta r_{n,m}^3} \Big[\left(r_{n,m}^2 + x_{n,m}^2\right)\cos\theta_m \cos\theta_n & \\ \quad + \left(r_{n,m}^2 + y_{n,m}^2\right)\sin\theta_m \sin\theta_n & \\ \quad + x_{n,m} y_{n,m} \left(\cos\theta_m \sin\theta_n + \sin\theta_m \cos\theta_n\right) \Big] & \text{if } \ n \neq m \end{cases} \ . \tag{6.11}$$

Confining the motion to one dimension for each bead, we have reduced the system from $2N$ [set of Eqs. (6.4)] to N [set of Eqs. (6.10)] coupled equations.

When working with systems where the amplitude of driving is much smaller than the distance between particles, i.e. $A \ll r_{n,m}$, it is a good approximation to consider the average distance $\langle \mathbf{r}_{n,m} \rangle$ in the Oseen tensor, rather than the time dependent quantity. This time-independent tensor is then what we consider in the following.

From here onwards, to maintain light notation, we will call by $\mathbf{r}_n$ the displacement of bead n from its time average position.

6.3.4 There is a dominant mode in the steady state dynamics

We now show how the effective Oseen tensor allows to describe the main properties of the synchronized state of any system of several oscillators (extending the case of driven colloids on circles [154, 155]).

H^{eff} can be diagonalized (since it is a real and symmetric matrix) to obtain the different normal modes of the coupled system. This follows a similar logic to previous work in my group [147, 154, 155]. Projecting the velocities onto the eigenvectors gives the set of uncoupled equations:

$$\tilde{v}_k = \lambda_k \tilde{F}_k \tag{6.12}$$

The relaxation time of the mode k is $\tau_k = 1/(k\lambda_k)$. The N-bead system has N normal modes and in general N time constants (although certain modes may be degenerate and have the same τ).

The collective dynamics of the driven system is dominated by the mode (or one of the degenerate modes) with the longest relaxation time. The reason why this holds is currently only understood qualitatively, as discussed in [154, 155], and the purpose of this work is to show experimentally that this observation is very general: several experimental configurations are considered in Section 6.5.

6.4 Experimental details

The rowers were implemented on the tweezers setup described in Section 3.2.2.

The silica beads (Bangs Laboratories) have a radius $a = 1.74$ μm. The solvent is a solution of 31 % glycerol and 69 % water by weight, corresponding to a nominal viscosity of $\eta = 3$ mPa·s at 20 °C [173]. Experiments are performed in a room with controlled temperature at $T = 21\,^\circ$C. The trapping plane is positioned several particle diameters above the flat bottom of the sample, in a sample volume that is around 150 μm thick.

The geometric switch is implemented experimentally with images acquired at 100 Hz. Colloidal particles are always being driven, never reaching the minimum of the active trap.

The optical trap potential is harmonic to a very good approximation, used here with a stiffness k of 0.2 pN/μm when trapping two beads (stiffness was maintained fairly constant when changing the number of beads trapped, and is calibrated from the distribution of displacements in static traps, typically with a 10 % precision). The relaxation time $\tau_0 = \gamma/k$ is of the order of 0.44 s. The experiments have been performed with $\lambda = 1$ μm, $\varsigma = 0.31$ μm (see Fig. 2.11 for the notations) and a distance between nearest neighbours $d = 8$ μm. The deterministic period of an isolated oscillator is $T_0 = 2\tau_0 \log[(\lambda - \varsigma)/\varsigma]$ [147], which under the experimental conditions is about 0.7 s. With the image acquisition operating at the frame rate of 100 frames per second (depending on the system size, hence captured region of interest) there are multiple frames captured within the relevant time scales τ_0 and T_0. Video is acquired for over 5 minutes, i.e. over 30000 frames. There is typically a transient lasting around a few periods before the systems reach the steady state discussed below.

6.5 Experimental examples of configurations of oscillators

6.5.1 Two coupled oscillators

The most simple case we consider here is that of two oscillators with variable angles θ_1 and θ_2, see Fig. 6.2. Within this class, three particular cases can be solved with the only approximation that the distance between the particles can be supposed constant: horizontal-parallel, vertical-parallel and horizontal-vertical, giving coupling terms $3a/(2d)$, $3a/(4d)$ and 0 respectively.

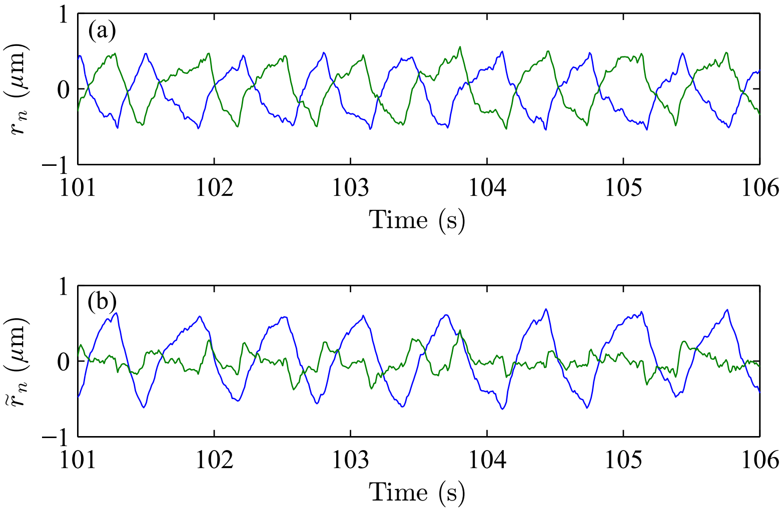

Figure 6.4: Two particles on axis, $(\theta_1, \theta_2) = (0, 0)$, synchronize in antiphase. The displacements are shown in (a), while the amplitude of the oscillations projected onto the two normal modes in shown in (b).

In general for this $N = 2$ case, the effective Oseen tensor H^{eff} is

$$H^{\text{eff}} = \frac{1}{\gamma} \begin{pmatrix} 1 & C \\ C & 1 \end{pmatrix}, \tag{6.13}$$

with C the hydrodynamic coupling term between the two beads that depends on the directions of oscillation θ_1 and θ_2:

$$C(\theta_1, \theta_2) = \frac{3a}{4d} \left(2 \cos\theta_1 \cos\theta_2 + \sin\theta_1 \sin\theta_2\right). \tag{6.14}$$

The diagonalization of H^{eff} gives the eigenvalues $\lambda_1 = (1-C)/\gamma$ and $\lambda_2 = (1+C)/\gamma$, and the eigenvectors:

$$\begin{cases} \tilde{v}_1 = \dfrac{1}{\sqrt{2}}(v_1 - v_2) \\ \tilde{v}_2 = \dfrac{1}{\sqrt{2}}(v_1 + v_2) \end{cases} . \tag{6.15}$$

The first mode (smaller λ, hence higher relaxation time) represents a motion of the beads in opposite directions, i.e. antiphase oscillations, while the second mode is oscillations in phase. To visualize a mode n, we represent its decomposition on $(v_i)_{i\in\{1,\dots,N\}}$ as follows: for each oscillator i, a vector is drawn, centred on the average position $\mathbf{r}_i$, with a direction $\hat{\mathbf{e}}_i$ (angle θ_i) and a length (positive or negative) proportional to the coefficient of the component v_i in the eigenvector describing the mode. As an example, the two modes for the $(\theta_1, \theta_2) = (0, 0)$ configuration are shown in Fig. 6.3. The trajectories of two beads in this horizontal parallel configuration are shown in Fig. 6.4(a).

In configurations (θ_1, θ_2) for which the coupling C is non zero, the mode with the longest relaxation time is $\tilde{v}_1$. Therefore, we expect the system to synchronize in antiphase. This is evident in the trajectories of Fig. 6.4(a) and is confirmed by the projection of these experimental trajectories onto the eigenvectors, as shown in Fig. 6.4(b).

To estimate more quantitatively from experimental data the fraction of oscillations in each mode, we proceed in two steps. (a) We calculate the projections of the oscillations onto the modes; and (b) we define the relative amplitude of a mode n from

$$f_n = \frac{\mathrm{std}(\tilde{r}_n)}{\sum_{i=1}^{N} \mathrm{std}(\tilde{r}_i)} , \tag{6.16}$$

where $\mathrm{std}(\tilde{r}_n)$ denotes the standard deviation of the $\tilde{r}_n(t)$ mode. For example in the case of $(\theta_1, \theta_2) = (0, 0)$ of Fig. 6.4, we found a high fraction $f_1 = 87$ % in the "antiphase" (AP) mode. This is as expected, and consistent with [147], where the small existing fraction f_2 in the "in-phase" (P) mode was shown to be due to the thermal fluctuations. In the particular configuration $(\theta_1, \theta_2) = (0, \pi/2)$, the fraction of the antiphase mode and in phase mode are almost

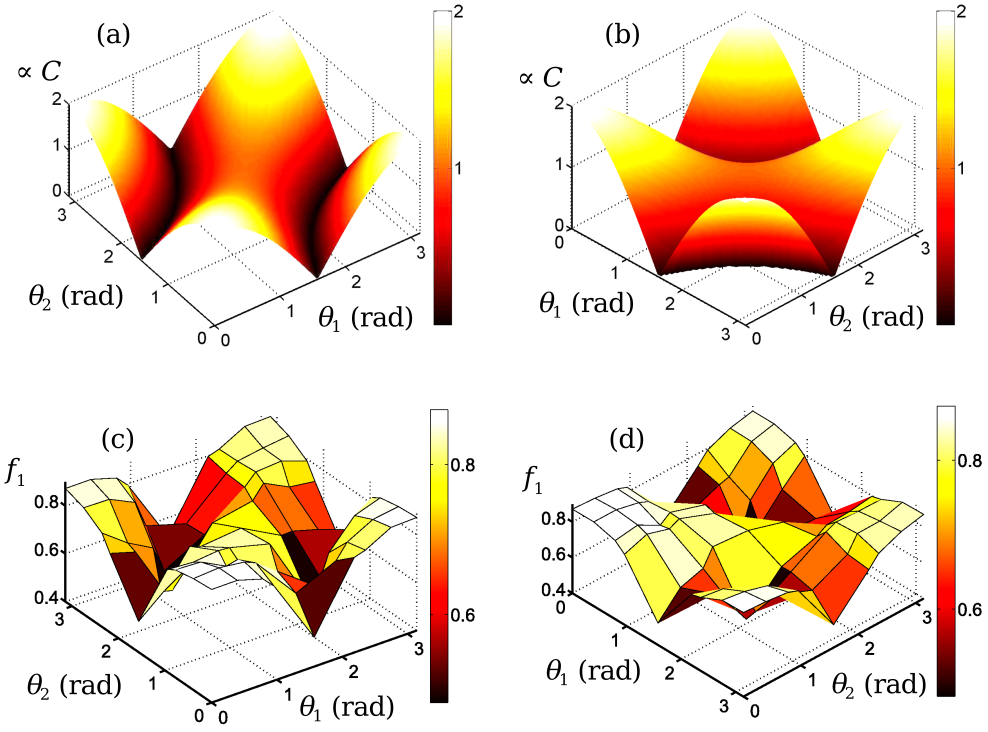

Figure 6.5: There is a strong correlation between the coupling strength and the dominance in the collective dynamics of the longest relaxation mode. (a,b) show two views of the function $|2\cos(\theta_1)\cos(\theta_2) + \sin(\theta_1)\sin(\theta_2)|$, proportional to the coupling parameter $|C|$ between the two beads. Coupling depends on the directions of oscillations θ_1 and θ_2 of the two beads. This function has the same form as the experimentally measured fraction in the longest-lived mode $f_1(\theta_1, \theta_2)$, shown in (c,d). Note that $f_1 \to 1/2$ is a signature of loss of synchronization, since the two modes have equal probability.

equal (52 % and 48 %). This is because in this case the coupling C between the beads is zero: The two modes are degenerate as they have the same relaxation time and there is no preference for the system to oscillate in either mode.

The two particular cases above show two possible regimes: synchronization in AP and no synchronization. We have studied intermediate configurations by varying both θ_1 and θ_2. Eight values of each of the angles were fixed in experiments, mapping out 64 points in the (θ_1, θ_2) space. The magnitude of the theoretical value of coupling, given by $|2\cos\theta_1\cos\theta_2 + \sin\theta_1\sin\theta_2|$, from Eq. (6.14), is shown in Fig. 6.5(a,b), while the experimentally measured fraction f_1 describing the decomposition into the antiphase mode in

Fig. 6.5(c,d). There is a remarkable similarity between these two surfaces. In this simple $N = 2$ case, this fraction is equivalent to the degree of correlation, falling to 1/2 when there is no correlation. In particular the locus of points with zero coupling is known analytically from Eq. (6.14), and describes two arcs in (θ_1, θ_2) space, in agreement with the experimental points where $f_1 \approx 0.5$. Clearly, it is not just the horizontal/vertical perpendicular pair of oscillators that is uncoupled.

Making a quantitative link between $|C|$ and the fraction in antiphase requires not just the construction of deterministic solutions from the normal modes, but also a consideration of the effect of noise. One can use the calculation of the order parameter $\langle Q \rangle$ in Chapter 5, replacing by $|C|$ the $3a/(2d)$ coupling, that was the particular case $(\theta_1, \theta_2) = (0, 0)$.

6.5.2 Three oscillators on a circle

To test the theoretical framework of the effective Oseen tensor for the driven system, and its predictive power for the symmetry and dominant properties of the steady state dynamics, a number of three-bead configurations are explored.

In Fig. 6.6(a), radial oscillations are considered. The normal modes are shown, together with the experimental fractions f_n with $n \in \{1, 2, 3\}$. The same in Fig. 6.6(b) for tangential oscillations. In both cases the normal mode with the highest relaxation time appears dominant in the solution.

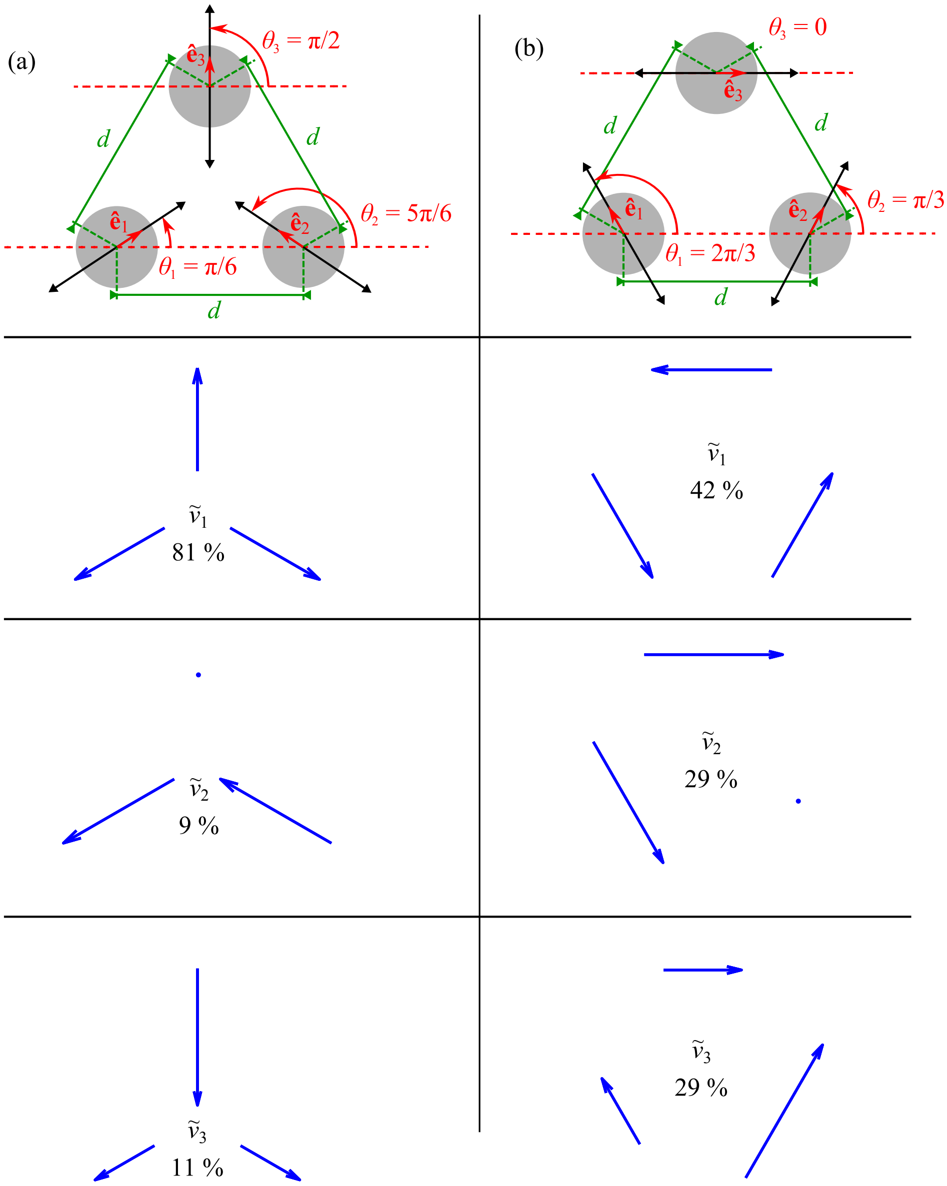

Figure 6.6: Three beads oscillating (a) radially and (b) tangentially to a circle. Panels illustrate the configuration, and the three normal modes for each case. In both systems, the normal mode with the longest relaxation time, $\tilde{v}_1$, is found to be dominant in the experimentally observed steady state solution. The percentages indicate the fraction of amplitude from the decomposition of the steady state solution onto modes, as found in the experiment.

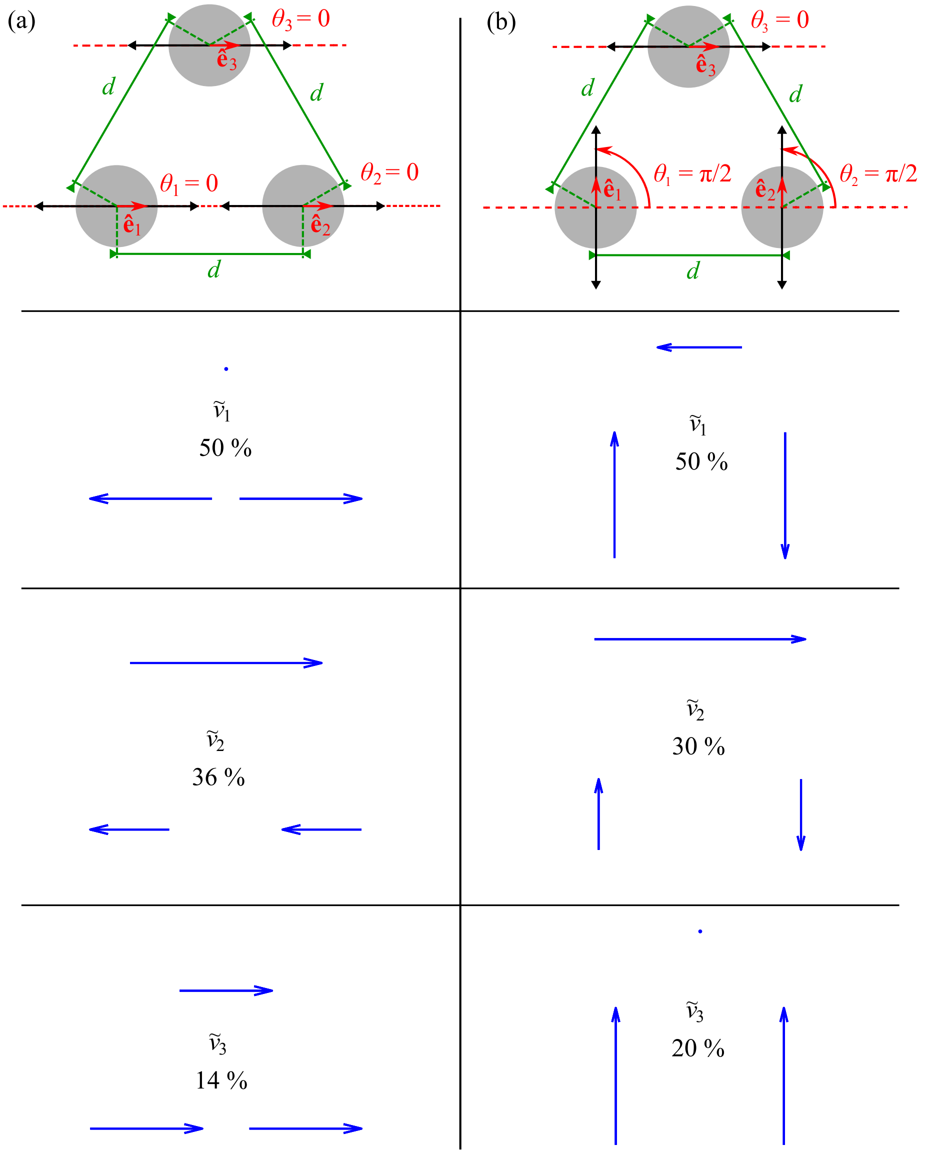

Figure 6.7: Even in configurations that lack the rotational symmetry considered in Fig. 6.6, the dominant mode in the steady state solution is that with longest relaxation time. Three beads are studied, driven to oscillate in (a) a parallel configuration, and (b) in a "bridge" configuration on a the vertices of an equilateral triangle. As before, the normal modes are shown, in order of decreasing relaxation time scale, with the percentages indicating the decomposition of the steady state solution onto modes, as found in the experiment.

In Fig. 6.7, two configurations that lack symmetry are considered. In Fig. 6.7(a) three beads on the vertices of an equilateral triangle are driven in a parallel direction. If one thinks of this arrangement by extension from the two-bead system, the bead at the top vertex could "choose" to synchronize with either of the bottom ones, with no preference; the longest lived mode, shown in the figure, has zero amplitude for the top bead (hence it is clear that it cannot by itself represent the solution to the driven dynamics, which requires that once per period each bead should have a displacement of amplitude A). Aside from these considerations, which can help to build the solution from the normal modes, here too the dominant mode is $\tilde{v}_1$. This is found also for the system in Fig. 6.7(b), where the bottom beads are moved vertically, and the top bead horizontally.

6.5.3 Synchronization through a “master bead”

In [155], the concept of “dynamical motifs” was introduced, as those patterns of dynamics that one might expect to identify locally in a cluster of strongly correlated oscillators, coupled more weakly within a larger system. The most basic of all the motifs is the behaviour of two beads, which we have seen above and can be tuned to be in antiphase all the way to non-coupled, by a choice of orientation. Developing this idea, it is particularly interesting to consider the behaviour of two beads in a condition of no coupling (e.g. perpendicular) when a third bead is introduced into the system (see Fig. 6.8). The third bead is a free-phase oscillator, equivalent to the first two. Its role is only special due to its particular position and orientation. Through this third bead the first two become coupled, and their synchronization state is tuned by the position and the orientation of the third bead, which acts as a control or “master”. Understanding this simple structure might allow some design rules to be found, to make a system of oscillators at prescribed positions and orientations that will self-organize into a dynamical state with some desired properties such as inducing a fluid flow over a length scale larger than the distance between neighbouring oscillators.

In Fig. 6.8(a), the bottom beads 1 and 2 are oscillating along orthogonal axes and are not coupled directly. However each of the two first beads are coupled to the top bead 3 and we can expect synchronization of the bottom beads through the top one.

The equations of motion given by the effective Oseen tensor are

$$\left\{\begin{array}{lcl} v_1 & = & \dfrac{1}{\gamma}\left(F_1 + sF_3\right) \\ v_2 & = & \dfrac{1}{\gamma}\left(F_2 + uF_3\right) \\ v_3 & = & \dfrac{1}{\gamma}\left(sF_1 + uF_2 + F_3\right) \end{array}\right. , \qquad (6.17)$$

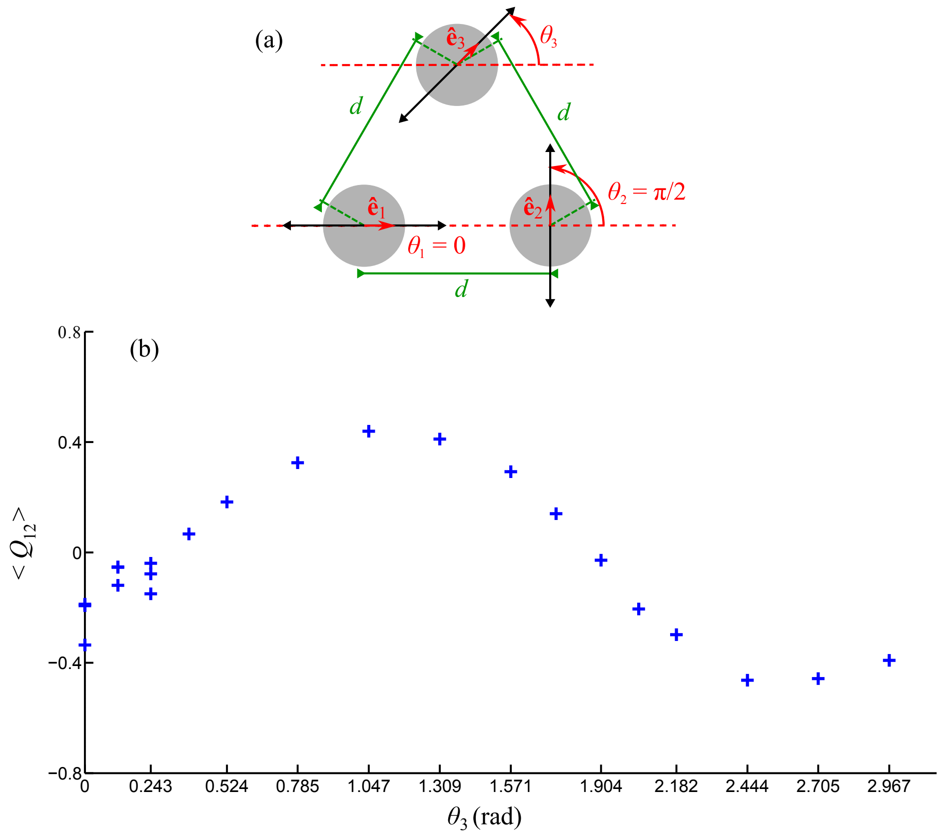

Figure 6.8: Coupling through a "master bead". In the configuration shown in (a), the bottom row beads are not directly coupled. However the presence of the top bead leads to their correlation. By simply tuning the orientation of the top "master" bead, it is possible to switch from in-phase, through no coupling, to antiphase motion of the bottom beads, as shown in (b).

with

$$\left\{\begin{array}{lllll} s &=& \frac{3a}{16d}\left(5\cos\theta_3+\sqrt{3}\sin\theta_3\right) &=& \frac{3\sqrt{7}a}{8d}\sin(\theta_3-\theta_s) \\ u &=& \frac{3a}{16d}\left(-\sqrt{3}\cos\theta_3+7\sin\theta_3\right) &=& \frac{3\sqrt{13}a}{8d}\sin(\theta_3-\theta_u) \end{array}\right. , \tag{6.18}$$

where $\theta_s = -\arcsin\left(\frac{5}{2\sqrt{7}}\right) \approx -1.24$ rad and $\theta_u = \arccos\left(\frac{7}{2\sqrt{13}}\right) \approx 0.24$ rad.

As bead 1 is coupled to bead 3 with a coefficient s and bead 2 is coupled to bead 3 with a coefficient u, the coupling term between 1 and 2 is expected to be of the form su:

$$C_{12}(\theta_3) = su = \frac{9\sqrt{91}}{64}\left(\frac{a}{d}\right)^2 \sin(\theta_3-\theta_s)\sin(\theta_3-\theta_u). \tag{6.19}$$

This second order coupling term between bead 1 and bead 2 is not null in most of the cases. Between 0 and π, $|C_{12}|$ is maximum for $\theta_3 = 1.07$ and 2.64 rad and it is null for $\theta_3 = 0.24$ ($u = 0$) and 1.90 rad ($s = 0$).

An order parameter Q_{12} (similar to Q in Chapter 5) can be defined to describe the state of synchronization between beads 1 and 2, by taking the product of the instantaneous trap states $\sigma_1(t) = \pm 1$ and $\sigma_2(t) = \pm 1$. This is done as an average over the experiment duration t_{tot}:

$$\langle Q_{12}\rangle = \frac{1}{t_{\text{tot}}}\int_0^{t_{\text{tot}}} \mathrm{d}t\, \sigma_1(t)\sigma_2(t)\,. \tag{6.20}$$

In Chapter 5 the directions were parallel, and, by convention, $Q = 1$ represented antiphase motion, and $Q = -1$ in-phase motion. Here, because the oscillators 1 and 2 are orthogonal, the definition of "in-phase" and "antiphase" are not obvious, and we have picked an arbitrary choice of the sign for Q_{12}. The theoretical coupling strength C_{12} reproduces the same θ_3 dependence on the state of correlation as seen experimentally in the correlations between bead 1 and bead 2, shown by Q_{12} in Fig. 6.8(b). In particular the expected maxima and points of zero coupling occur exactly at the master angle θ_3 expected theoretically.

The master bead can induce a (weak) P or AP synchronization, as well as no synchronization, depending on the choice of θ_3. This can be "exploited" to construct more complex collective dynamics, as explored below.

6.5.4 Nine beads

Here a system is made, as shown in Fig. 6.1 and Fig. 6.9(a), in which the nearest neighbour bottom beads are not directly coupled with each other. This is a more complex arrangement than before, but the nine modes are readily calculated from the effective Oseen tensor; the corresponding eigenvalues are $\gamma\lambda = \{0.6320, 0.6541, 0.7969, 0.8347, 0.8566, 0.9314, 1.2393, 1.2820, 1.7731\}$. As expected, the modes with lowest eigenvalue dominate the experimentally observed steady state solution, see Fig. 6.9(b).

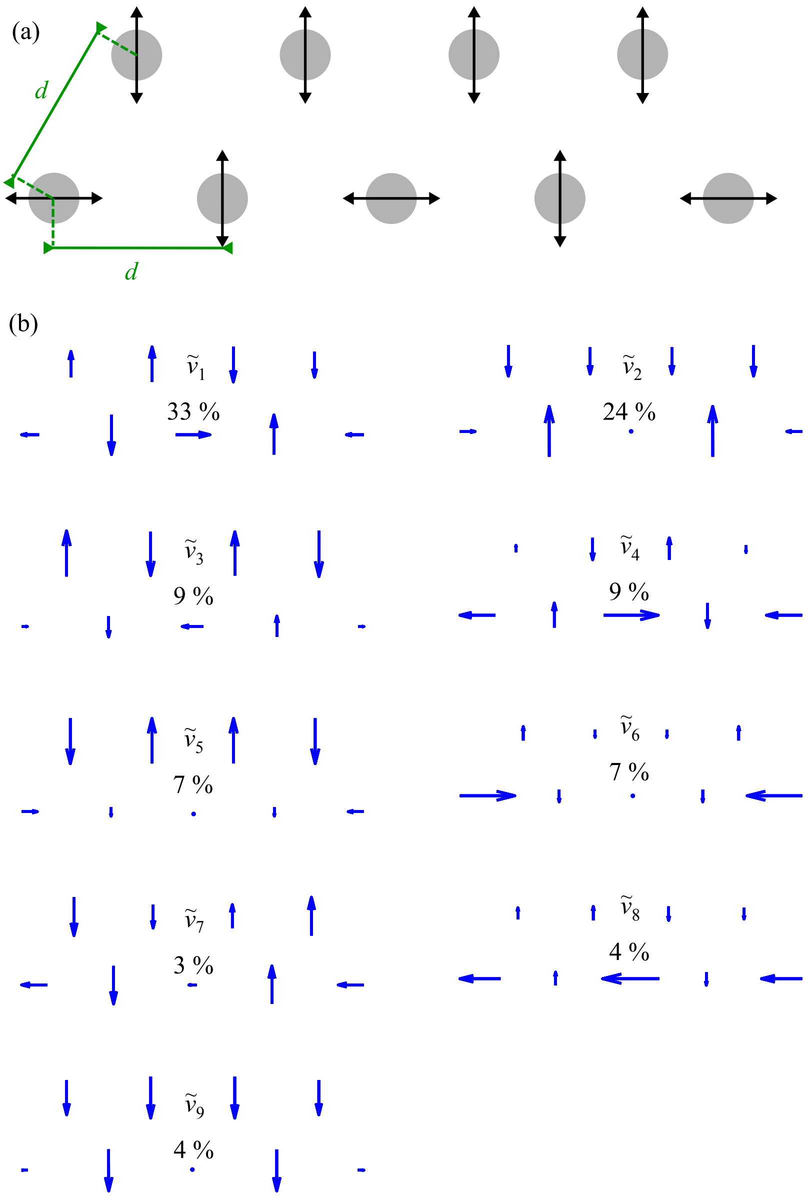

Figure 6.9: (a) A configuration of nine beads (a corresponding image from this experiment is shown in Fig. 6.1), in which the bottom row nearest neighbours are not directly coupled together. The top row beads are coupled to both nearest neighbours on the bottom row, generalizing the 3-bead "master bead" arrangement investigated in Fig. 6.8. (b) Modes for the configuration in panel (a). As seen in the dominant modes 1 and 2, with this spatial configuration the top row induces coupling of the bottom row with short length scale (nearest neighbour) patterns. The eigenvalues of this system are listed in the text, and the longest relaxation time modes are seen experimentally to dominate the steady state dynamics. A spatial arrangement with large scale correlations is shown in Section 6.5.5.

6.5.5 Large collective wavelengths in large arrays

The knowledge built with experimental systems gives confidence that as a general principle the longest lived normal mode will dominate the steady state dynamics for hydrodynamically coupled systems driven by the "geometric switch" rule. The effective Oseen tensor can be readily diagonalized for systems of thousands of oscillators. This should enable configurations to be tested to find patterns that will synchronize into large scale collective dynamics. As a proof of principle, a 2×100 array is considered, testing the effect of choosing angles and distances to show a phase pattern that evolves with a large length scale.

As for the case of nine beads, the lower set of beads is configured with the nearest neighbours vertical/horizontal, so not directly coupled. If beads are put on the top row with a fixed direction, as was the case for nine beads, this leads to collective synchronization, but the emergent states have very short length scale: two consecutive horizontal oscillators move mainly in antiphase. One way to design a system in which the dominant mode has large wavelength (which presumably could be a feature of biological metachronal waves) is to embed a spatial frequency in the structure of the oscillators. In the configuration sketched in Fig. 6.10(a), where only a 9-bead out of 100 section on the bottom row are shown, the top row beads are set to oscillate at angles θ_i that rotate by π radians over p beads. The period p was tested in a wide range; data in Fig. 6.10(b,c) is for $p = 20$. What emerges clearly is that the longest lived modes (the first four are shown in the figure) have a large length scale, which was "coded" in the geometric arrangement (the orientational order in this case). Comparing panels (b) and (c), the observation can be made that subtle adjustments in the positional arrangement influence the details of the dominant eigenmodes, but their large scale structure remains unaffected. Such adjustments are the key to designing arrays to optimally generate particular flow patterns — but as remarked often in this work, this requires either obtaining the deterministic solutions, running a Brownian dynamics simulation, or performing the experiment: the first approach is difficult, and the last two become impractical above a few hundred particles (simulations) or a few tens (driving with optical traps). The set of systems for

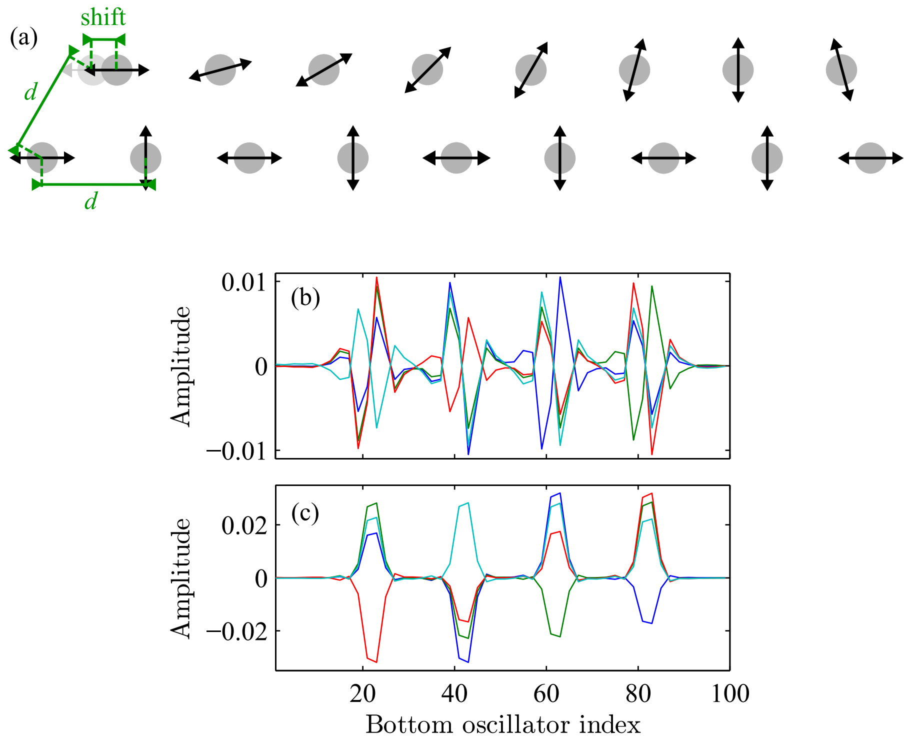

Figure 6.10: (a) Sketch of a configuration in which the lower row nearest neighbours are not coupled directly, and the top row induces coupling. Only a part of the system, which is made up of 2 × 100 beads, is drawn here. The angles in the top row are chosen so that an angle of π is rotated over 20 beads. This spatial structure is observed in the four longest lived modes, represented in (b) by showing the amplitude of the mode on the odd-index bottom row beads (blue, green, red, cyan solid lines, from mode 1 to 4 respectively). In the system studied in (b), the top row beads are staggered exactly at the mid point between beads on the bottom row, whereas in (c) the top row beads are shifted by $0.4d$ from the mid-point. In all cases $d = 8\,\mu$m, and radius $a = 1.74\,\mu$m, as in the rest of this chapter.

which we can get steady state dynamics is therefore limited, but the normal modes remain easily computable for much larger arrays. This is what makes simple models powerful in terms of establishing a "bottom-up" prediction of emerging properties. The complementary challenge, possibly more difficult, remains to determine the microscopic effective properties from the observation of collective dynamics in a large system, for example an array of biological cilia.

6.6 Conclusions on predicting the dynamics of configurations of several rowers

It has been shown that through the analyzis of the mean configurations (position and angles) of driven oscillators we can predict the main properties of the steady state of the collective system undergoing geometric switch oscillations. The method is very general and can describe any planar configuration of oscillators. The mode that contributes the most (and hence sets the symmetry) of the steady state solution is that one with the longest relaxation time. It is remarkable that in this (nonlinear, strongly coupled and actively driven) system, it is possible to make predictions on the out of equilibrium behaviour, based purely on static equilibrium properties.

Periodic solutions of the dynamical system, deterministic i.e. without noise, are a basic ingredient in understanding and predicting the behaviour of the physical system. In general, one such solution, we may call this fundamental, is the attractive trajectory for every initial condition. Other periodic trajectories are unstable. Different orientations of the line of oscillations of the beads and different average distances of the beads affect the hydrodynamic coupling and change the shape of the periodic solutions, still leading the system to synchronization. The effect of the thermal noise is two-fold: (i) it distorts the analytic fundamental solution, leading to a measured fraction f_n larger than expected from the theoretical fraction evaluated from the fundamental solution; (ii) it produces transitions from the fundamental solution to another, unstable, periodic solution. In these unstable solutions, the normal modes associated to the longest relaxation time sometimes have smaller contribution than normal modes with shorter relaxation times. We cannot at the moment separate these two, and we have simply shown that in a variety of systems the measured fraction f_1, associated with the normal mode with longest relaxation time, is always larger than other fractions.

We have shown that in certain geometrical arrangements, the position and orientation of one of the oscillators (having “free” phase, same as the others) is particularly important for the collective symmetry that arises; this oscillator has been called a “master” bead. Of possible interest for future work are the ideas of having one or more oscillators with fixed-phase and the related question of phase front propagation upon an external localized perturbation.

While much work remains to be done to explain in detail the properties of biological cilia, and biologically observed metachronal waves, this shows that in order to understand a phenomenon that emerges at a certain level of complexity (here, the collective dynamics of many cilia), it can be valuable to coarse grain the degrees of freedom of the lower-level elements (here the cilia, which are themselves complex systems, and are reduced to very simple phase oscillators).

Chapter 7

Alignment of rowers with orientational freedom

7.1 Introduction

During their growth stage, biological cilia in large arrays somehow must align their plane of oscillation. This was briefly reviewed in Section 2.2.3.4 in Chapter 2. The conclusion, emerging principally from experimental observations in biological tissues, is that cilia are assembled after the directional symmetry of the tissue is already set, but they initially beat in a random direction. Moreover, these experiments suggest that a positive feedback of the fluid on the orientation of the cilia is initiated by the presence of a directional net fluid flow: the cilia align their beating direction according to the direction of the flow, and then contribute to enhancing that flow.

This chapter presents an alternative process to explain the emergence of polar order by hydrodynamic coupling, supported by simulations and a theoretical argument. The model does not require an average net flow, so that the study differs from [122]. Instead, it involves the time-dependence of the flow generated locally by each cilium, and is therefore related to the relative phase differences between the cilia and hence to the shape of the beating cycle of a single cilium. It is an attempt to explore whether the collective interaction through hydrodynamic interaction can feasibly explain (a) the very robust alignment of basal bodies with each other inside each cell, and (b) the alignment to the axis of the developing tissue. It is found that alignment can emerge spontaneously for certain spatial arrangements of oscillators.

In the spirit of a reductionist model, the highly coarse-grained rower model is used to mimic a cilium, with some modifications in order to allow its beating direction to vary. As in the previous chapters, a great number of factors are neglected: an unbounded fluid (no wall) is assumed, the viscosity is supposed constant (Newtonian fluid), and oscillators are kept far apart.

Despite all these simplifications, the model remains very rich: the basic dynamical rule for each cilium, together with the many-body fluid flow interactions which couple all the active elements with each other, lead to synchronization and polar order in a variety of collective dynamical behaviours. In Chapter 5, it was shown that the curvature of the driving forces controls the state of synchronization of two rowers. In this chapter, it will be seen that this parameter also plays a crucial role in the emergence of polar order in large arrays of rowers. The model is also used to investigate the importance of the geometric placement of the oscillators, in particular the role of local structure (lattice) and boundary conditions.

7.2 Model of active oscillators with orientational freedom

A modified model of rowers is used here to describe motile cilia. Fig. 7.1(a) recalls the geometric switch, already used before and detailed in Section 2.3.2, with the only difference being that the amplitude of the oscillations is called $2R_g$ here instead of A. As in Chapter 5, various external driving potentials are used: $U = k(x - x_0)^{\alpha}$, with x_0 the position of the active trap. In this chapter, only two values of α are used: 0.7 and 2, that are respectively leading to strong in-phase and antiphase synchronization of two oscillators as shown in Chapter 5.

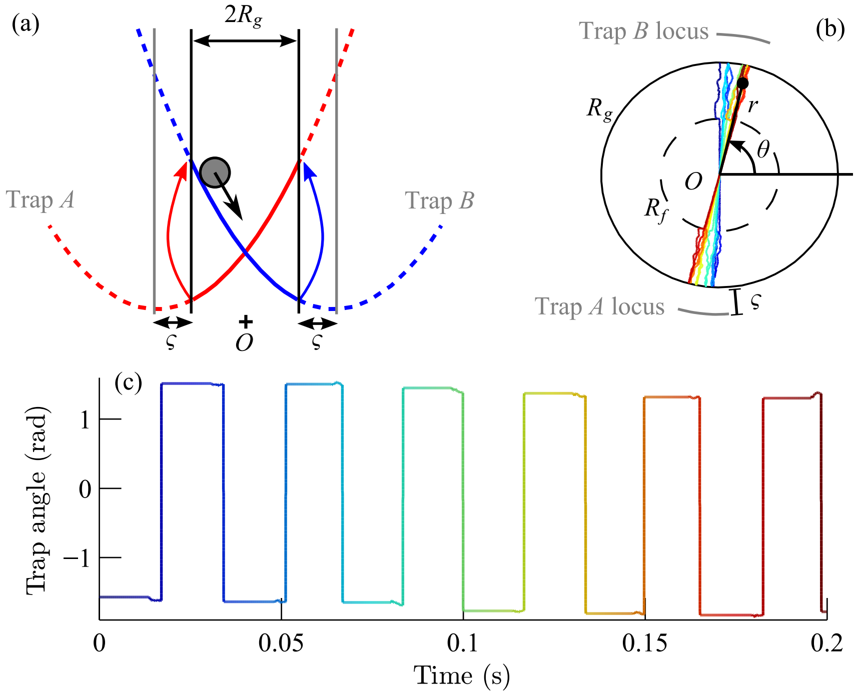

Figure 7.1: (a) One-dimensional model of oscillator. The colloidal particle is driven by two traps A and B switching on and off alternately (with harmonic potentials in this sketch: $\alpha = 2$). The traps switch when the particle reaches a distance ς from the centre of the active trap, leading to oscillations with a constant amplitude $2R_g$. (b) The oscillator in (a) is modified to allow freedom in its direction of oscillation θ. When the particle is at a radial position greater than R_f in the (x, y) plane, the trapping constant in the direction orthogonal to θ is set to 0. Furthermore, when the active trap is also in the same direction as θ, the trap will follow the angular position of the particle. The coloured track of the particle position over a few cycles shows a slow deviation of the angular position. The trap positions are indicated by the grey lines. (c) Evolution of the active trap's angle corresponding to the track in (b). The sharp jumps correspond to trap switches and the slow deviation occurs because of the allowed freedom between R_f and R_g, just before every trap switch.

In order to add freedom in the direction of oscillation of the rower, the particle and the traps are allowed to move in the direction orthogonal to the direction defined by the centre of trap A and trap B [Fig. 7.1(b)]: in the 2-dimensional plane, the bead can move in a disk of radius R_g and the traps can move on a circle of radius $R_g + \varsigma$. The angular freedom is implemented such that the trap moves by following the angular position of the bead only if (i) the bead is outside the disk of radius R_f and (ii) it is on the side of the active trap. When condition (i) is satisfied, the orthogonal trapping force is set to 0; otherwise it is set to a high value such that the bead is strongly confined along the direction defined by the traps. The radius R_f defining the boundary between angular freedom and confinement is a parameter that controls how much angular freedom is allowed. Condition (ii) ensures that an orthogonal displacement of the particle when it is approaching the active trap will not be cancelled by a possible orthogonal displacement in the opposite direction just after the trap switched. Fig. 7.1(b) shows the track of the particle position of a single oscillator over a few cycles of oscillation. The direction of oscillation is slightly changing because of the freedom of rotation when conditions (i) and (ii) are satisfied. Since the particle is not coupled in this figure to any other oscillator, the direction is only changing because of free diffusion of the particle. Fig. 7.1(c) represents the direction of the active trap. The square-like shape is due to the switching between traps A and B, and each jump corresponds to an angular change of π. The angular freedom acts before a trap switch, as a slight change of the trap angle. Since this work focuses on the alignment of oscillators, all angles in later figures will be plotted modulo π in order to remove the square-like shape in the graphs.

7.3 Alignment of two oscillators

7.3.1 Numerical results

In this section, the behaviour of two oscillators, set apart by a distance $d = 10\ \mu$m is studied. The hydrodynamic interaction between the spheres is described by the Oseen tensor, hence assuming a bulk fluid, and the

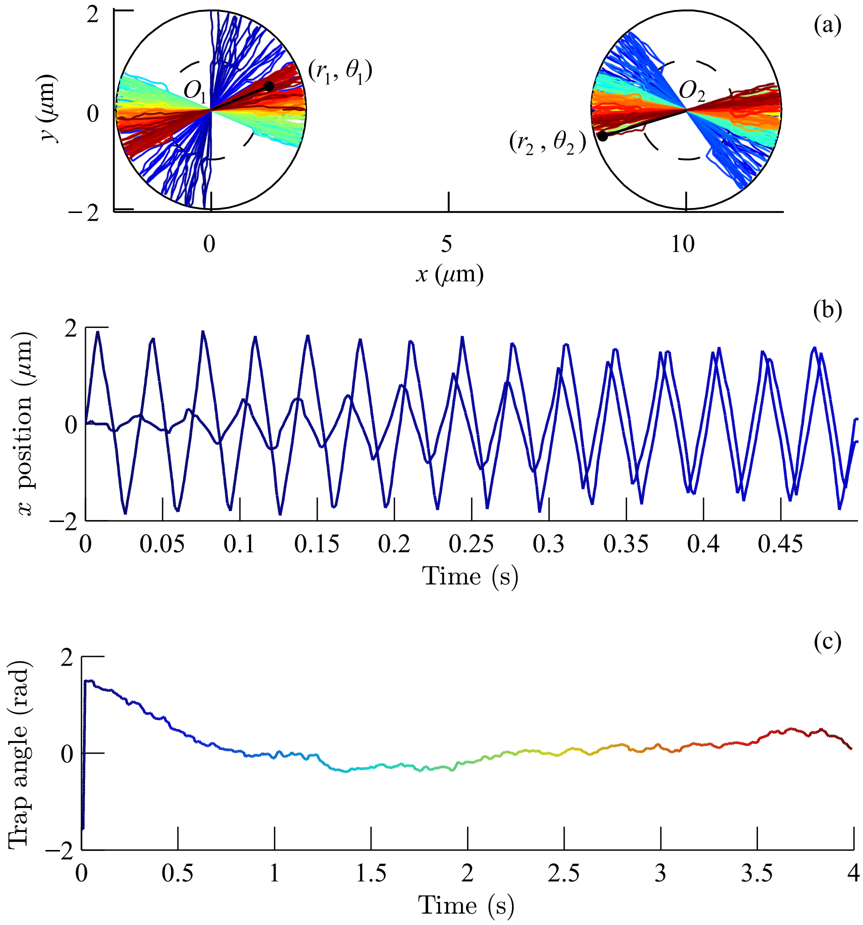

Figure 7.2: (a) Simulated tracks of two beads in oscillators centred on O_1 and O_2 (increasing time from blue to red). The angular positions are coupled by the hydrodynamic interaction between the two beads, leading to alignment along x. (b) x position of the two beads. The positions oscillate and synchronize in a few cycles. The amplitude moves slowly because the positions with varying angles are projected along x. (c) Angle of the trap for each particle. The angle is plotted modulo π, in order to hide the effect of the traps' switches. The angles converge to 0, but with a much longer time scale than the synchronization time scale. In all the figures, unless explicitly specified, most of the parameters for simulations are matching typical cilia: $d = 10$ μm, $a = 0.45$ μm (see Section C.4 for an explanation on this value), $R_g = 2$ μm, $R_f = 1$ μm, $\eta = 1$ mPa·s, $\alpha = 0.7$, $T = 296$ K and k is set such that the frequency of oscillations is 30 Hz (with no thermal fluctuations).

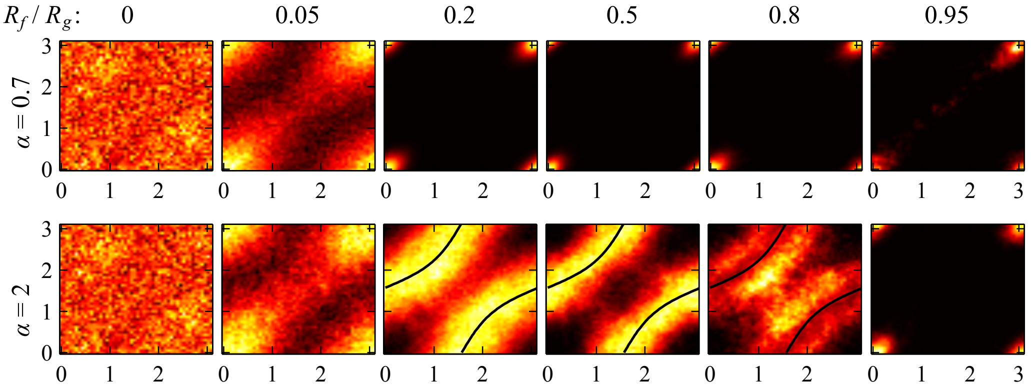

Figure 7.3: Distributions of the traps' angles (modulo π) for two oscillators in the geometric configuration shown in Fig. 7.2. The axes on the graphs are θ_1 and θ_2 in radians and the colour scale is dark (less probable) to bright (most probable). Distributions are plotted for different values of R_f and α for 3000 s long simulations. In the wide range of R_f/R_g from 0.2 to 0.8, the angles align to $(0,0)$ when $\alpha = 0.7$. The alignment occurs in the direction defined by the line joining the two centres of the oscillators (from which the angles are measured). For $\alpha = 2$, the angles do not converge, but tend to explore states close to the locus of points for which the hydrodynamic coupling along the directions of oscillations is 0. Zero-rr-coupling lines, satisfying $h_{rr}(\theta_1, \theta_2) = 0$ are represented in black, see Section 7.3.2.

simulations include thermal noise. Fig. 7.2 shows a simulation for $\alpha = 0.7$ and $R_f/R_g = 0.5$. The other parameters are set to values characteristic of cilia and are given in Fig. 7.2. The relative state of the oscillators has two features. First, the oscillations synchronize in phase within a few cycles [Fig. 7.2(b)] (typically 4 cycles, with the parameters used in this chapter). The synchronized state agrees with the results in Chapter 5 and [146]. Furthermore, the directions of the two oscillators converge to 0 rad, as shown in Fig. 7.2(c). The characteristic time to converge is however much higher than the time to synchronize: about 12 cycles for $R_f/R_g = 0.5$.

When varying α and R_f, different behaviours can be obtained. This is summarized in Fig. 7.3 showing the distribution of the angles (θ_1, θ_2) of the active traps for each oscillator, when running 3000 s long simulations. For $\alpha = 0.7$, leading to in-phase oscillations, the angles converge to $(0,0)$ for all values of R_f/R_g except 0. When $R_f/R_g = 0$, thermal fluctuations tend to randomize the angle of the oscillators each time they cross their centre O_1 and O_2, resulting in a uniform (θ_1, θ_2) distribution. This also broadens the peak at $(0, 0)$ when $R_f/R_g \approx 0$. The case of $\alpha = 2$, which leads to oscillations in antiphase, is more complex. For the same reason as before, the angles distribution is uniform for $R_f/R_g = 0$. When this ratio is increased, the distribution shows peaks at $(0, 0)$ ($R_f/R_g = 0.05$), a locus of angles avoiding the $(0, 0)$ alignment ($0.2 \leq R_f/R_g \leq 0.8$) and again convergence to $(0, 0)$ ($R_f/R_g = 0.95$). In the middle-range of angular freedoms $0.2 \leq R_f/R_g \leq 0.8$, the two oscillators do not align. Instead, the system tends to stay in configurations that minimize the hydrodynamic coupling between the particles [for example the $(0, \pi/2)$ configuration].

7.3.2 An analytical explanation

A model to explain the alignment properties observed in the simulations above is derived here. For simplicity, Brownian fluctuations are neglected, in order to reduce the question to a problem of convergence of the angles of the two oscillators. The distributions in Fig. 7.3 in the middle-range of R_f/R_g can be explained for both $\alpha > 1$ and $\alpha < 1$ by a simple treatment in which the synchronization of the oscillators and their alignment are considered separately.

The state of an oscillator is described by the position r of the particle, the angle of the oscillator (in $[0, \pi[$) and a variable $\sigma = \pm 1$ indicating the direction along θ where the trap is. The first and third parameters can be merged into a single parameter describing the “geometric phase”, ϕ (in $[0, 2\pi[$). Therefore the state of the oscillator is fully described by two parameters: ϕ and θ.

The evolution in time of ϕ_1, θ_1 (left oscillator), ϕ_2 and θ_2 (right oscillator) is a complex problem in which the four variables are coupled. However, in the middle-range of R_f/R_g, the phase difference $\phi_2 - \phi_1$ converges with a much lower relaxation time compared to the characteristic relaxation time of the angles θ_1 and θ_2. When looking at the alignment properties of the oscillators, at time scales at which the directions move, it can be assumed that the synchronization of ϕ_1 and ϕ_2 occurs instantaneously: in-phase if $\alpha < 1$ or in antiphase if $\alpha > 1$, as described by the theory for the one-dimensional version of the oscillator in Chapter 5. The solving of the evolution of the system is reduced to the following question: How do (θ_1, θ_2) evolve in time when the oscillations are assumed in phase (if $\alpha < 1$) or in antiphase (if $\alpha > 1$)?

Starting from an initial condition (θ_1, θ_2) of the traps' positions when the beads pass O_1 and O_2, the angles after the traps switched for both beads become $(\theta_1 + \Delta\theta_1, \theta_2 + \Delta\theta_2)$. It is convenient to introduce here three frames in Fig. 7.2(a): $(\hat{\mathbf{e}}_x, \hat{\mathbf{e}}_y)$, $(\hat{\mathbf{e}}_{r_1}, \hat{\mathbf{e}}_{\theta_1})$ and $(\hat{\mathbf{e}}_{r_2}, \hat{\mathbf{e}}_{\theta_2})$. When the particle i is approaching its active trap, it will undergo the change of angle $\Delta\theta_i$ when it moves from the position R_f to R_g. $\Delta\theta_i$ is related to the velocity of the particle v_{θ_i} along the orthogonal direction and to the time interval during which the particle moves from R_f to R_g in the radial direction:

$$\Delta\theta_i = \sigma_i \int_{t_{f,i}}^{t_{g,i}} \mathrm{d}t \, \frac{v_{\theta_i}}{r} \,, \tag{7.1}$$

where $t_{f,i}$ and $t_{g,i}$ are the instants at which the particle reaches a radial position R_f and R_g respectively. σ_i is the variable describing which of the two traps that is driving the oscillator i is active: $\sigma_i = 1$ if the active trap is in the direction of $\hat{\mathbf{e}}_r$, or $\sigma_i = -1$ if it is in the opposite direction. Between these two positions, the orthogonal trapping force is zero. Neglecting thermal fluctuations, the only contribution to v_{θ_i} is from the hydrodynamic coupling. The coupling is described by the Oseen tensor that relates the velocities $\mathbf{v}_i$ of the particles to the driving forces $\mathbf{F}_j$ acting on them:

$$\begin{cases} \mathbf{v}_1 = \mathbf{H}_{1,1}\mathbf{F}_1 + \mathbf{H}_{1,2}\mathbf{F}_2 \\ \mathbf{v}_2 = \mathbf{H}_{2,2}\mathbf{F}_2 + \mathbf{H}_{2,1}\mathbf{F}_1 \end{cases} , \tag{7.2}$$

with $\mathbf{H}$ the Oseen tensor given in Section 1.6. In its expression, the inter-particle distance is supposed constant to the distance between the centres of the oscillators: $r_{1,2} \approx d$, which is valid when $2R_g \ll d$.

Introducing radial driving forces $\mathbf{F}_j = F_j \hat{\mathbf{e}}_{r_j}$ in Eq. (7.2) and using Eq. (7.1) leads to

$$\begin{cases} \Delta\theta_1 = \sigma_1\sigma_2 h_{r\theta}(\theta_1, \theta_2)\Delta\theta_0 \\ \Delta\theta_2 = \sigma_1\sigma_2 h_{r\theta}(\theta_2, \theta_1)\Delta\theta_0 \end{cases} , \tag{7.3}$$

with

$$h_{r\theta}(\theta_1, \theta_2) = \cos\theta_1 \sin\theta_2 - 2\sin\theta_1 \cos\theta_2 \tag{7.4}$$

and

$$\Delta\theta_0 = \frac{\epsilon}{\gamma} \int_{t_f}^{t_g} \mathrm{d}t \frac{F(r)}{r} \ . \tag{7.5}$$

Here, $\epsilon = 3a/(4d)$, $\gamma = 6\pi\eta a$ and $F(r)$ is the force from the driving potential, which has the same shape from $U(r) \sim r^{\alpha}$ for the two oscillators, so that

$$F(r_i) = \alpha k (R_g + \varsigma - r_i)^{\alpha - 1} \ . \tag{7.6}$$

To write Eqs. (7.3), (7.4) and (7.5), it is assumed that the variations in angle in a half-cycle are small so that the function $h_{r\theta}$ can be put out of the integral in Eq. (7.1). Writing the equations to the highest order, the $t_{f,i}$ and $t_{g,i}$ integration boundaries can also be replaced by generic variables t_f and t_g corresponding to the times at which an uncoupled oscillator would be respectively at positions R_f and R_g, and $r = r(t) \approx r_i(t)$ corresponds to the radial position of that uncoupled oscillator. With these approximations, $\Delta\theta_0$ does not depend on the angles θ_1 and θ_2, nor on the oscillator. This is a constant that depends on how the angular freedom is implemented in the model of oscillator. The $h_{r\theta}(\theta_1, \theta_2)$ term, however, is related to the variation in the hydrodynamic coupling of a bead moving along the radial direction with the velocity of the other bead along the orthogonal direction, depending on the angles of the oscillators.

To go further in the calculation, it is now necessary to include that oscillations are either in phase, if $\alpha < 1$, or in antiphase if $\alpha > 1$. This is introduced through a variable δ, equal to 1 for oscillations in phase and to -1 for oscillations in antiphase. The state of synchronization δ determines the sign of the product $\sigma_1\sigma_2$ [related to the sign of the coupling function $C(\theta_1, \theta_2)$ in Eq. (6.14)]. More precisely,

$$\sigma_1\sigma_2 = \delta \, \mathrm{sign}[h_{rr}(\theta_1, \theta_2)] \tag{7.7}$$

with

$$h_{rr}(\theta_1, \theta_2) = 2\cos\theta_1 \cos\theta_2 - \sin\theta_1 \sin\theta_2 \ . \tag{7.8}$$

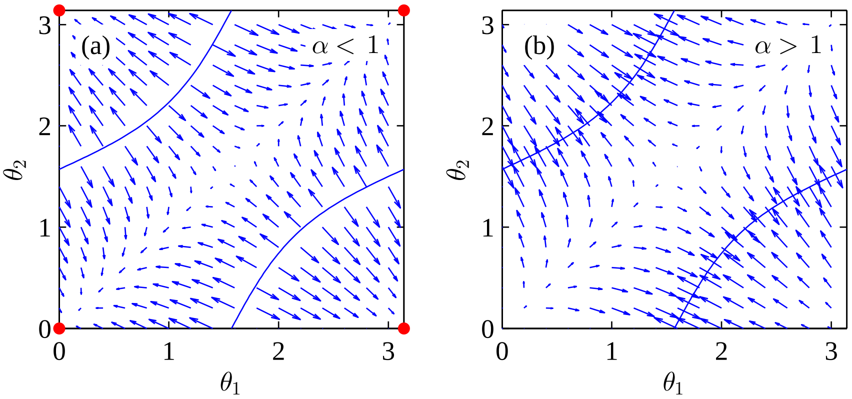

Figure 7.4: Theoretical convergence maps for two oscillators in the configuration shown in Fig. 7.3 for (a) $\alpha < 1$ and (b) $\alpha > 1$. The set of angles (θ_1, θ_2) evolves in time by following the arrows. When $\alpha < 1$, the angles converge to $(0, 0)$ (large dots). When $\alpha > 1$, the direction of the arrows are all swapped, and the angles converge towards a point on the blue zero-rr-coupling lines, leading to a temporary loss of synchronization. These graphs agree with the distributions in Fig. 7.3 in the middle-range of R_f/R_g.

The quantity $\gamma\epsilon h_{rr}$ represents the coupling force on bead 1 and projected along $\hat{\mathbf{e}}_{r_1}$, coming from a radial force acting on bead 2 along $\hat{\mathbf{e}}_{r_2}$. Eqs. (7.3) and (7.7) lead to the iterative map

$$\begin{cases} \Delta\theta_1 = \delta \,\mathrm{sign}(h_{rr}) h_{r\theta}(\theta_1, \theta_2)\Delta\theta_0 \\ \Delta\theta_2 = \delta \,\mathrm{sign}(h_{rr}) h_{r\theta}(\theta_2, \theta_1)\Delta\theta_0 \end{cases} . \tag{7.9}$$

This system of equations can be studied by linear stability analyzis for $\delta = -1$ and $\delta = 1$ ($\Delta\theta_0$ being positive), by separating the regions of different signs. Instead, in Fig. 7.4, Eq. (7.9) is simply plotted in the (θ_1, θ_2) plane by representing the evolution of an initial condition (θ_1, θ_2) as an arrow centred on (θ_1, θ_2) and of direction $(\Delta\theta_1, \Delta\theta_2)$. For $\alpha < 1$ [$\delta = 1$, Fig. 7.4(a)], the system converges from any initial condition to $(\theta_1, \theta_2) = (0, 0)$, in agreement with the simulations in Fig. 7.3. For $\alpha > 1$, in Fig. 7.4(b), the system moves towards a position on the locus of points defined by $h_{rr}(\theta_1, \theta_2) = 0$ (solid lines). However, because the angular speed does not converge to zero around this line, the system will jump from one side to the other side of the line. This results in a change of sign of h_{rr}. Therefore, the oscillations that were in the synchronized state in antiphase before the jump, become in phase. The system will tend to return to the stable state of oscillations in phase, but since the rr-coupling is close to 0 nearby the line, this takes several cycles of oscillations. Therefore, when crossing the zero-rr-coupling line, the angles will move away from the line for several cycles, following, for a while, arrows in the opposite direction as the ones indicated in Fig. 7.4(b). Once the system has returned in the synchronized state in antiphase, the angles will follow the convergence map for $\alpha > 1$ again. Therefore the system constantly oscillates between the two sides of the zero-rr-coupling line, with a large amplitude, related to how fast the oscillations converge to the synchronized state. This agrees again with the simulations in Fig. 7.3 in the middle-range for R_f/R_g. When $R_f \sim R_g$, the assumption that oscillations are exactly in phase or in antiphase becomes wrong, as thermal fluctuations and coupling introduce little delays between the switches of the traps of the two oscillators. When the delays become of the order of the time an oscillator spends in the $0.2 \leq R_f/R_g \leq 0.8$ region, Eq. (7.7) does not apply.

To summarize, when $\alpha < 1$, the oscillators align to the direction of highest synchronization strength (or highest rr-coupling), while for $\alpha > 1$, they take orientations that minimize the synchronization and the system is barely synchronized.

7.4 Linear array of oscillators

When increasing the number of oscillators, various geometric configurations can be studied numerically; the resultant dynamics of the system can be represented by plotting the angle of each oscillator as a function of time.

Fig. 7.5 shows simulations of 60 oscillators equally spaced by a distance $d = 10\ \mu$m along a line [“chain” configuration, (a) to (d)] and a circle “ring” configuration [(e) to (h)]. In the chain configuration, the angles are measured from the direction of the line of oscillators, while in the ring configurations the angle of an oscillator is measured from the tangent to the circle at the position of the oscillator. As for two oscillators, the cases $\alpha = 0.7$ (typical for $\alpha < 1$) and $\alpha = 2$ (typical for $\alpha > 1$) lead to different behaviours. For $\alpha < 1$,

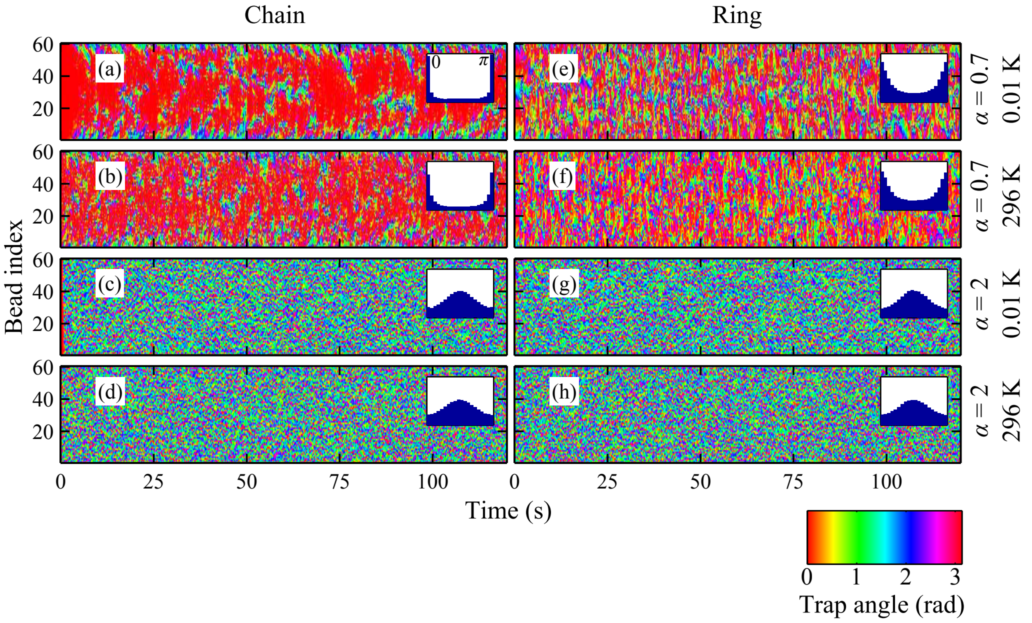

Figure 7.5: Traps angles depending on time in chains [(a) to (d)] and rings [(e) to (h)] of 60 oscillators for $\alpha = 0.7$ and 2, at low (0.01 K) and room (296 K) temperature ($R_f = 0.7$ μm). Angles are measured from the axis of the line in the chain configuration and from the tangent to the circle at the position of the oscillator for the ring configuration. For $\alpha = 0.7$, most of the oscillators align to $\theta = 0$ (overall angle distribution as inset), while neighbouring oscillators tend to have different angles when $\alpha = 2$. Brownian motion, controlled by the temperature, has very little effect on the patterns of angles.

two neighbouring oscillators tend to be parallel. In the chain configuration, the system shows a strong alignment of the oscillators along the direction of the line ($\theta_i = 0$). In the more symmetric ring configuration, the oscillators tend to align tangentially to the circle ($\theta_i = 0$ again). The alignment is weaker in the ring configuration, as shown by the width of the peak in the distribution of the angle displayed as insets in Fig. 7.5 (distributions over time and oscillator index). In both chains and rings, the oscillators align in the configuration that maximizes the hydrodynamic rr-coupling. For $\alpha > 1$, the graphs are more "granulated": neighbouring oscillators tend to minimize their coupling, leading to different angles between consecutive oscillators. However, the average distribution shows a single, very wide peak at $\pi/2$, orthogonal to the direction of the line in the chain and orthogonal to the tangent to the circle in the ring. In all cases, the thermal noise has little effect on the width of the peaks in the angle distribution for the parameters used here.

7.5 2d arrays of oscillators

Cilia in biological systems are usually arranged on two-dimensional carpets rather than chains or rings. To capture this, rectangular $N_x \times N_y$ arrays of about 64 oscillators with square and hexagonal lattices are simulated. Fig. 7.6 shows phase angles for two lattices, with $T = 296$ K. The distance between neighbouring oscillators is kept the same between the two lattices, and only simulations for $\alpha < 1$ are shown, since $\alpha > 1$ does not display strong alignment properties. The angles are measured from the x axis, and the oscillators are indexed as indicated in Fig. 7.6(a) and (d). The first result is that the oscillators show a cooperative behaviour, and tend to align with the same angle at a given time in the four configurations studied. This is even visible in the highly symmetric 8×8 square lattice simulation that shows no preferred average direction of oscillation. The second result, shown by the angle distributions in the insets, is that except for the 8×8 square lattice simulation [Fig. 7.6(b)] the system has a preferred direction of either 0 or $\pi/2$ rad. The preference for one direction could have two origins: the boundary conditions (shape of the surface covered by the array), or the type (square or hexagonal) and orientation of the lattice. The surface of the array is an $N_x d \times N_y d$ rectangle for the square lattice and an $N_x d \times (\sqrt{3}/2) N_y d$ rectangle for the hexagonal lattice. Therefore, the rectangular surface is stretched along y in (c) and (f), stretched along x in (e) and a square in (b). It follows from the angles distributions that the oscillators align along the direction of stretching of the array, which is a configuration of higher rr-coupling than the other axis of the rectangle. This behaviour is inherent to the higher hydrodynamic coupling in the Oseen tensor in the x direction $[3a/(2d)]$ than y direction $[3a/(4d)]$, for two particles at positions on the $\hat{\mathbf{e}}_x$ axis. The type of the lattice has a negligible effect on the alignment compared to the aspect ratio of the array.

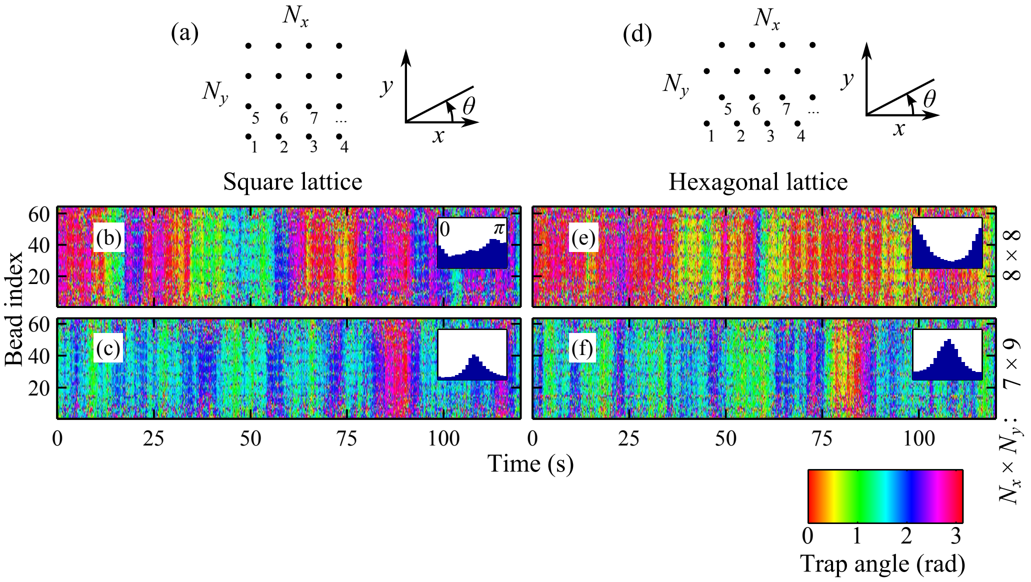

Figure 7.6: Evolution of the angles, and distributions in 2d arrays oscillators on a square (b, c) and hexagonal (e, f) lattices in 8×8 (b, e) and 7×9 (c, f) arrays for $\alpha = 0.7$ ($T = 296$ K and $R_f = 0.7$ μm). The oscillators are indexed as indicated in the geometric configurations of the array represented in (a) and (b). The oscillators show a cooperative behaviour by tending to have the same angle at a given time. The average orientation is along the axis of the long edge of the rectangular array: the angles distribution is centred on $\theta = 0$ in (e), $\theta = \pi/2$ in (c) and (f), and uniform in the square configuration in (b).

7.6 Discussion

The rower model oscillator was modified to add the ability to change its direction of oscillation (the beating plane), in order to describe the collective alignment of multiple cilia subject to hydrodynamic interaction. The oscillation direction is free in the way that, on each cycle, it adjusts by an angle proportional to the velocity of the fluid flow projected orthogonally to the oscillator. While how this freedom is allowed in real cilia is not discussed, many models can lead to a such response of the angle to an external flow. A specific model was chosen in order to calculate its emergent properties, but the details of how angular freedom is implemented are not crucial to the results: the quantity $\Delta\theta_0$ in Eq. (7.5) depends on the details, but this enters as a constant in Eq. (7.3), setting the amplitude of the response to the flow. It is the structure of this equation, that underlies the results, so other ways to implement flexibility would lead to similar conclusions as the ones drawn in this chapter.

The alignment properties of a system of oscillators depend on the details of the driving force, which are matched very simply to the synchronized state of a system of two oscillators. Here, the synchronized state is tuned by the parameter α, which characterizes the driving force, and is either in-phase or in antiphase. An empirical rule, that emerges from all the simulations in this chapter, is that a given configuration of oscillators tends to put itself in angular configurations of highest (for in-phase synchronization) or lowest (antiphase synchronization) coupling (in absolute value) between the oscillators, projected along their directions of oscillation (rr-coupling). This rule is confirmed by a theoretical model in the case of two oscillators, for which, the locus of maxima of $|h_{rr}|$ is reduced to a single point (θ_1, θ_2) when $\alpha < 1$ and the locus of minima is a curve when $\alpha > 1$. For that reason, and because synchronization tends to be lost near the zero-rr-coupling line, only oscillators with an in-phase stable state display strong alignment. This study provides a link between the beating pattern of the cilia (widely believed to determine the synchronized state) and the orientation in arrays of cilia. It is interesting to note here that “real” cilia actually beat in phase with their neighbours. This makes the case $\alpha < 1$ more relevant for cilia, and the study shows that it is the case that leads to alignment. This work also suggests that the loss of polar order in motile mutant cilia could be due to a modified driving potential acting on them.

While the meaning of “highest” and “lowest” coupling in a system of more than two oscillators is not precisely defined, simulations with large number of oscillators seem to confirm a similar rule that could be used to predict the state of alignment of a system. The rule could be related to how the relaxation times of the normal modes of oscillation depend on the angles, as the normal modes already play a key role in determining the state of synchronization, when no angular freedom is added (see Chapter 6). Also, in an array of cilia, the synchronized state as a metachronal wave can be seen as a state minimizing the energy required for the beating [123]. Similarly, the rule aligning the oscillators could therefore be related to a problem of energy minimization or maximization.

Alignment properties in large arrays is described both in terms of cooperative behaviour between oscillators and in estimations of the preferred direction of oscillation (if any). The rule sets conditions on both properties. States with all oscillators aligned in the same direction at a given time have high rr-coupling and are therefore seen in all the simulations for $\alpha < 1$, leading to high cooperativity between the oscillators. Non-symmetric configurations such as chains of oscillators or rectangular arrays also tend to confine the angles in a particular direction, which is the direction in which the system is elongated. In 2d arrays, the type of lattice could also affect the alignment of oscillators. However, it appears that in arrays of below ~ 100 oscillators, the effect of the shape of the array is more important than the lattice to determine the preferred direction of oscillation. It can be noted here that different lattices exist in biological tissues: cells in some systems as e.g. *Paramecium* show very regularly spaced cilia [108, 185], possibly defining axes of alignment, whereas in the airways the cilia distribution is more random within cells, and the distribution of the multiciliated cells themselves is also not completely regular.

This chapter used parameters close to motile cilia conditions (except for d). The size of the array varies a lot with the biological system: thousands of cilia can be arranged in a dense array like in the alga *Volvox carteri* [109], or in *Paramecium* [186]; or a few hundred cilia can be packed on the surface of a multi-ciliated airway cell, this cluster interacting with the clusters on other cells in the tissue [116]. In all these cases, the boundary conditions could have a determinant role in the choice of the direction of alignment.

A *quantitative* connection to the biological question of how airway epithelium gains its full organization in development (once cells are elongated) will clearly need further development of this or related models. In this biological system, the cells are elongated along the proximal/distal axis, conferring polarity to the airway tissue as a whole, and the cilia within each cell become aligned to each other. Furthermore they become aligned with the tissue axis.

As a consequence of the small size of cilia, the Brownian motion leads to non-negligible fluctuations of the phase of the oscillators. However, the simulations with large number of oscillators suggest that the thermal noise is irrelevent when looking at the alignment properties of the oscillators.

The current model and the behaviour highlighted in this chapter show that hydrodynamic coupling is able, at least in principle and qualitatively, to lead to orientation of active oscillators, and that the resulting collective dynamical state responds to the symmetry of the shape of the array (symmetry of the boundary condition). The case of 2d arrays with cilia described by a driving force with $\alpha < 1$ could explain how cilia distributed on the surface of an elongated cell align with each other, and pick the axis of stroke from the cell's elongation. In this speculative scenario, the microtubule networks which link the basal bodies within the cells, and are seen to correlate with polarity [114], might act to freeze in place the orientation of the basal bodies.

Spontaneous alignment is observed here, in the absence of an external flow. Various ciliated tissues (described in Section 2.2.3.4) initially develop in the absence of flow. The presence of a directed external flow (which is possible in some systems, such as the developing airways) would be an even stronger aligning factor. In general, the importance at various stages of development of flow and mechanical force transduction, which are undeniably present between cilia, remain an open question clearly requiring multidisciplinary approaches.

Part IV

Synchronization of rotors

Chapter 8

Optimal synchronization of two rotors

8.1 Introduction

Part III focused on the first class of oscillators studied in this thesis, rowers. From this point onwards, the synchronization of a second model, rotors, is investigated. The rotor model is described in Section 2.3.1. Briefly, a rotor corresponds to a colloidal particle driven by optical tweezers along a predefined orbit $\mathbf{r}(\phi)$ and with a driving force $F(\phi)$ that is tangent to the orbit. Since the orbit is closed, $\mathbf{r}$ and F can be written as a function of a phase parameter ϕ in $[0, 2\pi]$.

A general principle is that synchronization at low *Re* is possible only by breaking time reversal symmetry (see Chapter 5 and [143, 187]). Section 2.3.1 summarized two mechanisms promoting symmetry breaking, and hence synchronization: the choice of the functions $\mathbf{r}(\phi)$ and $F(\phi)$ (leading to phase-locking called here "Golestanian synchronization" [142, 143]), and possible flexibility of the particle position along the trajectory ("Lenz synchronization" [88]). Two rotors, driven along circular trajectories $\mathbf{r}(\phi) = r_0\hat{\mathbf{e}}_r(\phi)$, are considered in this chapter. The flexibility in the orbit is characterized by a harmonic restoring force of stiffness k_r. This system,

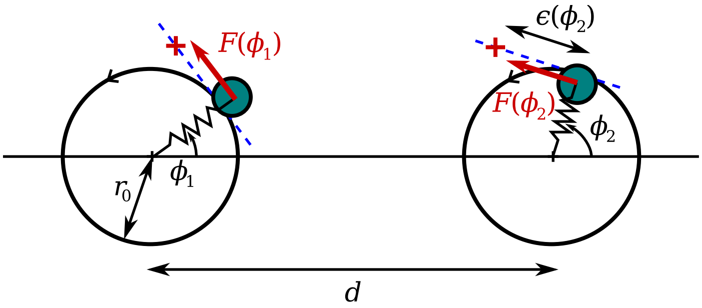

Figure 8.1: Two colloidal rotors are obtained by driving particles along predefined closed circular trajectories. The driving forces have a component $F(\phi_i)$ parallel to the tangent to the circle and a component in the radial direction, represented as springs. The traps' minima are marked by red crosses. The F driving component may be maintained constant, or may be modulated as a predefined function of the phase angle ϕ (see Fig. 8.2). ϕ is free to vary (i.e. its time dependence is not predefined) under the net action of the driving force and any other forces acting on the particle.

represented in Fig. 8.1, combines the Lenz and Golestanian models together. In other words, Fig. 8.1 is a combination of the oscillators sketched in Figures 2.9 and 2.10, as different functions $F(\phi)$ can be tested and flexibility is present.

The two models have been developed separately, studied in numerical simulations and/or by stability analyzis (without thermal noise), and two limit cases can be considered. A force profile $F(\phi) = \text{cnst}$ corresponds to the Lenz model only, that predicts synchronization in phase. There, synchronization becomes stronger when flexibility is increased [88]. On the opposite, an infinite stiffness k_r is the limit of the Golestanian model of the rotor, in which the bead is confined on the orbit. In this case, Uchida and Golestanian showed in [142] that synchronization is optimal for a force profile of the form

$$F(\phi) = F_0[1 - A_2 \sin(2\phi)] \tag{8.1}$$

with F_0 and $A_2 \in [0, 1[$ two constants. Synchronization is expected to be stronger when A_2 is increased. In the particular case where $A_2 = 0$ and $k_r = \infty$, the system should not synchronize.

In my work, initially two circular rotors are implemented experimentally. The aim is, first to recover the decay times into the in-phase state in both the

Lenz and Golestanian limits, and second to observe how strongly the system synchronizes when both mechanisms could be relevant at the same time, when $k_r < \infty$ and $A_2 \neq 0$, addressing the open question of the relative importance of the two factors.

This work was done in collaboration with the group of Simon Hanna (University of Bristol), involving Luke Debono, Stuart Box, Dave Phillips and Stephen Simpson. Experiments and simulations (that include thermal fluctuations) were conducted in both the Cambridge and Bristol groups. However, this chapter and Appendix D only show experimental data from my setup, and numerical data from Bristol, except where indicated otherwise. The experiments in Bristol use holographic optical tweezers, rather than acousto-optic deflectors to produce the potential landscapes.

8.2 Implementation of the experimental rotors

The rotors with circular trajectories of radius r_0 are implemented with the optical tweezers by using the feedback-controlled force driving described in Section 3.2.6, in which the position of the traps are updated based on the position of the particles. Here, the traps are maintained a distance $\epsilon(\phi)$ ahead of the projection of the position of the particle on the predefined trajectory (see Fig. 8.1). The optical force acting on the particle $i \in \{1, 2\}$ is written

$$\mathbf{F}_i = k\epsilon(\phi_i)\hat{\mathbf{e}}_{\phi_i} - k(r_i - r_0)\hat{\mathbf{e}}_{r_i} \ . \tag{8.2}$$

The $\hat{\mathbf{e}}_{\phi_i}$ component maintains the driving of the particles, while the radial $\hat{\mathbf{e}}_{r_i}$ component is a restoring force that tends to keep the particle on the circle of radius r_0. Hence, the product $k\epsilon(\phi_i)$ determines the driving force and k the flexibility. Since the parameters k (related to the intensity of the laser beam) and $\epsilon(\phi)$ (related to the way the traps are positioned in the real-time feedback) are controlled independently in the experiments, it is possible to vary the driving forces and the flexibility independently.

Eq. (8.3) assumes that the traps, represented by red crosses in Fig. 8.1, are harmonic ("simple traps" in Chapter 3). In practice, the use of simple harmonic traps does not allow to vary the flexibility and the driving forces in sufficiently wide ranges to highlight clearly the effect of both parameters on synchronization. To increase the size of the range of flexibilities available experimentally, complex potential landscapes are used (see Section 3.2.4). 21 simple traps with the same intensity are placed along a line in the $\hat{\mathbf{e}}_r$ direction centred at the position of the red crosses in Fig. 8.1. While this does not change a lot the force along the $\hat{\mathbf{e}}_\phi$ direction, the flexibility along $\hat{\mathbf{e}}_r$ can be tuned by controlling both the intensity of the traps and the length of the segment of 21 simple traps. Increasing this length reduces the stiffness in the radial direction, hence lowering the minimal stiffness experimentally accessible. With the trapping lasers modulated to create a potential landscape like the line segment above, the force acting on particle i can be rewritten

$$\mathbf{F}_i = k_\phi \epsilon(\phi_i)\hat{\mathbf{e}}_{\phi_i} - k_r(r_i - r_0)\hat{\mathbf{e}}_{r_i} \ , \tag{8.3}$$

with k_ϕ depending mainly on the traps' intensities and k_r depending on both the intensities and the size of the segment of simple traps. In the experiments shown here the segment size has been varied from 0 to 4.4 μm.

Significant efforts are made to achieve the driving force profile $F(\phi)$. The desired shape of the driving force is obtained by setting the function $\epsilon(\phi)$ (particle-to-trap distance in the $\hat{\mathbf{e}}_\phi$ direction). Before a coupling experiment is carried out, the driving force is calibrated on a single rotor, see Fig. 8.2. Force profiles of the form given by Eq. (8.1) with $F_0 \approx 5.9$ pN were chosen since they correspond to the most efficient profiles to generate synchronization in circular trajectories [143]. For each set of parameters, a first profile is measured on a single bead for which ϵ is set proportional to $1 - A_2 \sin(2\phi)$. Because of nonlinearities in the trapping force at displacements $\gtrsim 1$ μm from the trap centre, this profile does not match the expected function precisely, so the relative difference between the expected and measured profiles is then used as a factor $c(\phi)$ correcting the original profile into $\epsilon \propto c(\phi)[1 - A_2 \sin(2\phi)]$.

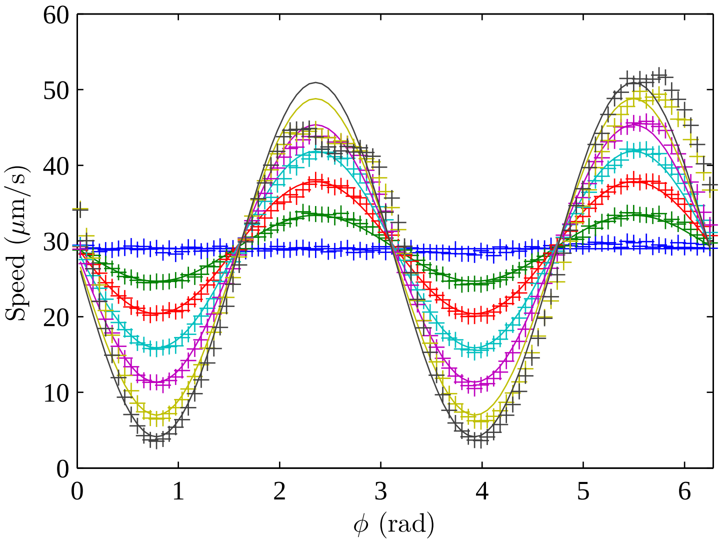

Figure 8.2: The orbital velocity (proportional to the force at low *Re*) can either be held constant, or modulated so that it is anisotropic: the functional form of the force $F(\phi) = F_0[1 - A_2 \sin(2\phi)]$ has been chosen in this work, studying the effect of the modulation parameter A_2 following [142]. The velocity of a single orbiting particle is shown here for $A_2 = 0$, 0.15, 0.3, 0.45, 0.6, 0.75 and 0.85 (increasing modulation). Markers are measured velocities and lines are the expected shape, proportional to $[1 - A_2 \sin(2\phi)]$. For high A_2 it can be seen that the force saturates a little for some angles, i.e. it is not possible to move any faster. Parameters are $a = 1.74$ μm (silica beads), $r_0 = 3.2$ μm and $\eta = 6$ mPa·s.

8.3 Results

The relative phase of two rotors separated by a distance d can be measured. This remains constant over successive cycles of oscillation if there is phase locking and if there are no thermal fluctuations. In the systems studied here, synchronization is always in phase (with small fluctuations due to Brownian motion). Two measurements of the strength of synchronization are possible: the time required to reach synchronization from an arbitrary initial condition, or, exploiting the presence of Brownian noise, the relaxation time scale in the autocorrelation of the phase difference at steady state. In both cases, the "natural" unit of time is the period of one rotation.

Fig. 8.3 shows the effect of both parameters k_r and A_2 on synchronization. The experiments confirm the two theoretical predictions from [88] and [142] claiming that increasing the flexibility (by decreasing k_r) or increasing the asymmetry A_2 of the driving potential should lead to stronger synchronization (lower relaxation time).

Although the trends in Fig. 8.3 are very clear, the experimental relaxation times appear systematically higher than in the simulations (Brownian dynamics, with the Oseen tensor to describe the interaction between the particles), i.e. the rotors synchronize less than expected. This problem is investigated carefully in Appendix D and it appears that several factors are increasing the relaxation time. The main contribution comes from the delay in moving the traps ahead of the particles: simulations in Appendix D show that realistic values of the experimental delay (5 to 20 ms) can lead to an increase of the relaxation times by up to nearly a factor of 2. Smaller contributions to the increase in relaxation time are attributed to wall effects and to a detuning between the intrinsic periods of the two oscillators. The appendix provides a detailed analyzis of the possible origins of the discrepancy between experiments and simulations.

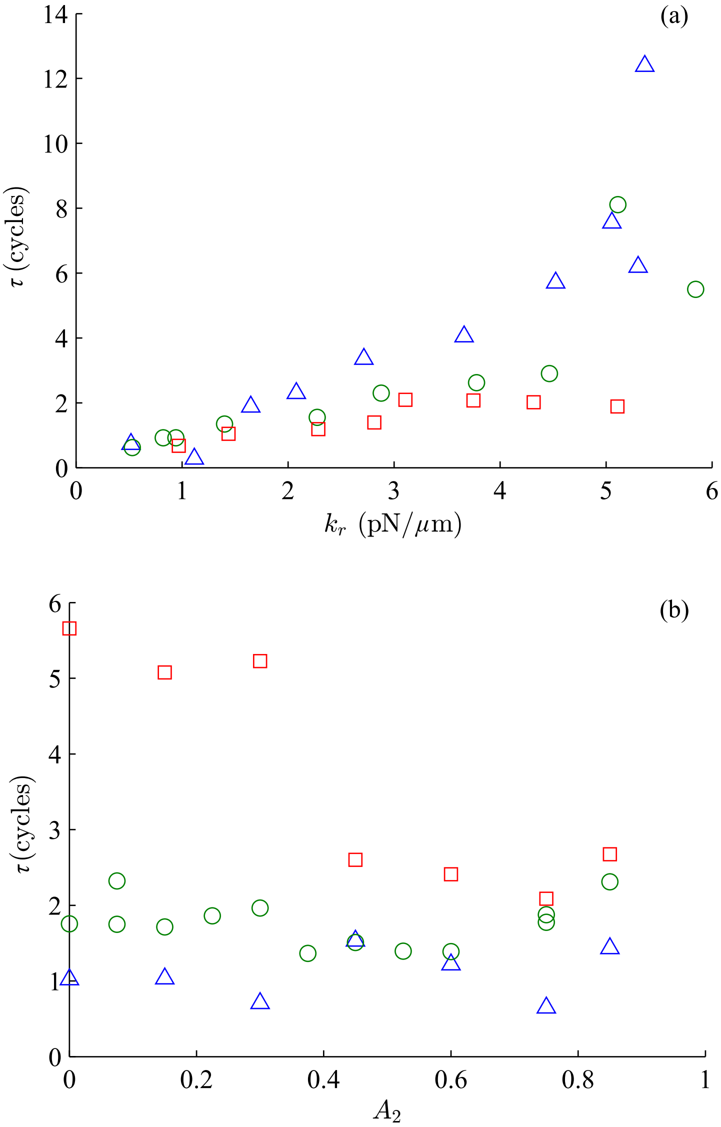

Figure 8.3: Relaxation time depending on k_r and A_2 for the parameters in Fig. 8.2 and $d = 25.4$ μm. In (a), k_r is varied for $A_2 = 0$ (△), 0.4 (○) and 0.7 (□). In (b), A_2 is varied for $k_r = 0.76$ (△), 1.8 (○) and 4.5 (□) pN/μm. Decreasing k_r and increasing A_2 produces stronger synchronization. A comparison with simulations is shown in Appendix D.

8.4 Joining up the Lenz and Golestanian synchronization models

The experiments above show clearly that both the radial flexibility and the modulation of $F(\phi)$ contribute to the strength of synchronization. A rigorous calculation of the strength of synchronization including both parameters can be carried out, as done in [188], based on a calculation in [143] for a slightly different system.

For small A_2, the same result can be obtained by accounting by linear superposition for both the Lenz (Γ_L) and Golestanian (Γ_G) decay rate parameters (known respectively from [88] and [142]). The evolution of the phase difference can be represented by a discrete equation of the form

$$\Delta\phi(i+1) - \Delta\phi(i) = -\Gamma\Delta\phi(i) \ , \tag{8.4}$$

where $\Delta\phi = \phi_2 - \phi_1$, i indexes the cycle (counted on either rotor), and Γ is the decay rate to the synchronized state. Then, Γ is the sum of the components Γ_L and Γ_G:

$$\begin{aligned} \Gamma &= \Gamma_L + \Gamma_G \\ &= 2\pi\frac{3a}{4d}\left(\frac{3F_0}{k_r r_0}\sqrt{1-A_2^2} + A_2\right) \ . \end{aligned} \tag{8.5}$$

In Eq. (8.5), the term $3a/(4d)$ corresponds to the hydrodynamic coupling, with a the beads' radii and d the mean separation between the particles. The two terms in brackets correspond respectively to the contribution of the "Lenz model" (L), and the "Golestanian model" (G) to synchronization. Note that the Lenz contribution depends itself also on A_2, since the period of the oscillators depends on the force profile. From Eq. (8.4), the relaxation time is then related to Γ_L and Γ_G by

$$\frac{1}{\tau} = -\ln\left[1 - (\Gamma_L + \Gamma_G)\right] \ . \tag{8.6}$$

This theoretical model combining both the L and G models is plotted

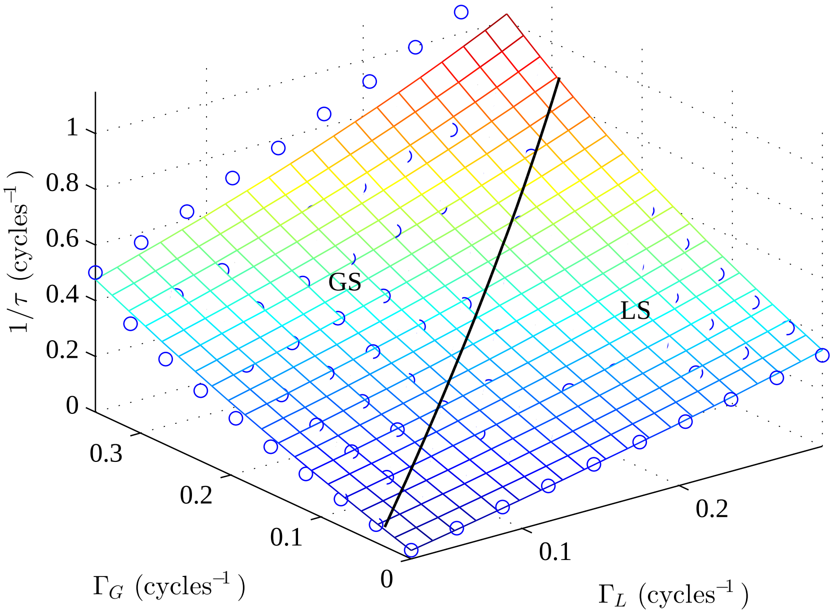

Figure 8.4: Relaxation time depending on the Lenz (Γ_L) and Golestanian (Γ_G) dimensionless control parameters. Simulations (circles) are in excellent agreement with the theoretical model in Eqs. (8.5) and (8.6) (coloured surface). The thick line separates the regions in which synchronization is dominated by the flexibility of the rotor (Lenz synchronization, LS), or by the angular modulation of the driving force (Golestanian synchronization, GS). For $\Gamma_L + \Gamma_G$ close to 0, synchronization can be lost because of thermal fluctuations, but simulations were performed in a range in which rotors are synchronized, for which the relaxation time can be easily extracted.

in Fig. 8.4, and agrees very well with simulations (with no adjustable parameters). Depending on the choice of parameters F_0, k_r, r_0 and A_2, the synchronization can be dominated by either the Lenz or Golestanian contribution. A threshold between these two regions can be defined when the two terms in brackets in Eq. (8.5) are the same; this boundary line is plotted in Fig. 8.4.

8.5 Effect of thermal fluctuations

Brownian motion leads to fluctuations of $\Delta\phi$ over time. Fluctuations can be estimated by analogy with a particle in a confining harmonic potential. The fluctuations in displacement x of such a particle satisfy, by the equipartition theorem, $\langle x^2 \rangle = k_B T/\kappa$ with κ the harmonic trapping constant. The relaxation time of the position decaying to 0 in the confined particle problem can then be matched with the relaxation time of the phase difference: $\gamma/\kappa \sim t_0/\Gamma$, where t_0 is the intrinsic period of the rotors and $\gamma = 6\pi\eta a$ the drag coefficient. Since $\langle x^2 \rangle \sim \langle (r\Delta\phi)^2 \rangle$, the relation leads to

$$\left\langle \Delta\phi^2 \right\rangle \sim \frac{t_0 k_B T}{\Gamma \gamma r_0^2} \ . \tag{8.7}$$

Simulations in Fig. 8.5(a) show $\langle \Delta\phi^2 \rangle$ plotted against the quantity above, for a large variety of parameters; the data collapse onto lines, with a slope depending only on A_2. Since synchronization will be lost above a certain threshold of $\langle \Delta\phi^2 \rangle$, the scaling above gives insight into the range of parameters that will allow synchronization in the presence of noise.

The slopes from panel (a) are plotted in Fig. 8.5(b), and show a non-trivial dependence on A_2, initially constant and then growing at larger A_2. The reason of this dependence on A_2 is still unclear, but it can be noted that with non-zero A_2, the synchronization strength varies as the beads go around their orbits. It would then be expected that the variance of fluctuations could be affected in a way that is not simply described by the cycle-average of the potential, as discussed in [189].

The dependence of $\langle \Delta\phi^2 \rangle$ on temperature is shown in Fig. 8.5(c): at very low temperatures it is linear, meaning that the phase difference can be described by a variable confined around 0 with a harmonic effective restoring potential, as explained previously. When the temperature increases, the variance becomes super-linear, implying that the restoring strength is less than linear for large phase shifts. At very high temperatures, synchronization is lost and the distribution of $\Delta\phi$ becomes uniform in the finite-range $[0, 2\pi]$, so that the variance converges to a constant value.

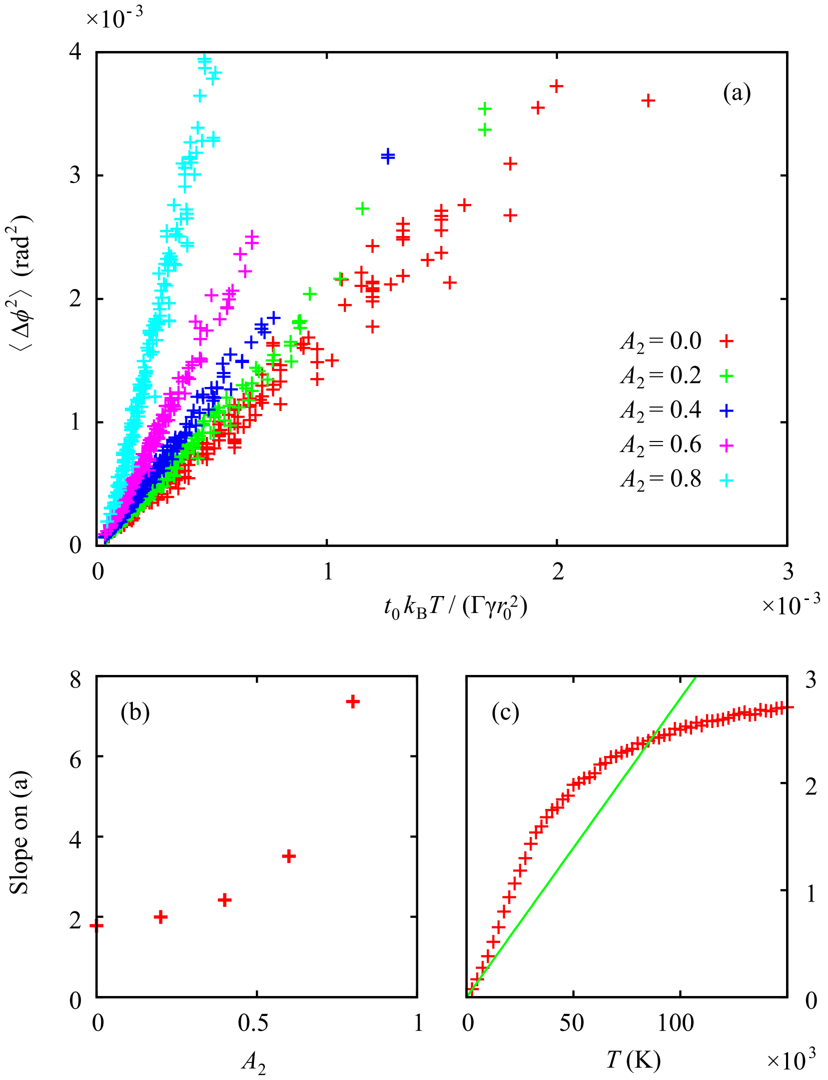

Figure 8.5: Thermal noise leads to fluctuations of $\Delta\phi$ around 0 (the in-phase state). (a) Simulations at $T = 10$ K for variable values of A_2, k_r, a, r_0, F_0, d, and η in a regime of small fluctuations of the phase difference. The variance of $\Delta\phi$ exhibits a linear dependence on the group $t_0 k_B T/(\Gamma\gamma r_0^2)$, with a coefficient that depends only on A_2. (b) The slopes of the data in (a) have a non-trivial dependence on the modulation factor A_2. (c) For $a = 1$ μm, $d = 20$ μm, $r_0 = 2$ μm, $F_0 = 16$ pN, $k_r = 32$ pN/μm and $A_2 = 0.4$, the temperature is varied. The line shows the variance from Eq. (8.7).

8.6 Outlook

The rotor model is promising as it can describe more oscillating objects than the rower model, which is one-dimensional. The rower model might indeed be a particular case of a Golestanian squeezed orbit. In the future, it should be possible to parameterize and coarse-grain complex biological cilia, or flexible artificial systems driven by complex mechanisms, into a corresponding system of “rotors”. That would require to match the period, radius, deformability, and angular anisotropy. The results obtained in this chapter will then allow a direct understanding of the synchronization strength, particularly (a) its magnitude relative to thermal noise (thus the likelihood of phase slips, and loss of synchronization by thermal fluctuations), and (b) the main mechanism determining it. Conversely, the results here also indicate that hydrodynamic synchronization can be easily tuned through various parameters, and can be made strongest by allowing simultaneously great deformability and significant modulation of the orbital drive. It will be fascinating to explore where biological systems have evolved on this parameter space, and to understand the role of additional constraints such as optimal flow generation.

Chapter 9

Synchronization of assemblies of rotors

9.1 Introduction

Assemblies of more than two oscillators can exhibit various types of collective behaviour. The elements can all oscillate in phase, or synchronize in other phase-locked states characterized by phase differences between the oscillators independent on time: $\phi_{i+1}(t) - \phi_i(t) = C_i$. Configurations of rowers can also display more complex dynamics such as solutions periodic in time. This is the case for rowers equally spaced on a circle and oscillating tangentially [154]. For more general configurations, it is not obvious that periodic solutions exist, but Chapter 6 described a method allowing to gain information on time-average quantities (dominance of a mode of oscillation).

Cilia often synchronize in a metachronal wave, a phase-locked state for which the constant C_i does not depend on the oscillator index i. It is therefore important to search for such states in the simple models of cilia. For example, metachronal waves were observed in simulations of chains of rowers interacting through the Oseen tensor, without thermal noise [146]. The simulations were also supported by an analytical model taking into account only nearest-neighbours interactions. However, metachronal waves have never been seen before in experiments with rowers or rotors.

This chapter presents experiments on assemblies of rotors, driven along circular trajectories by a constant force $F(\phi) = F_0$. It was shown in Chapter 8 that two such oscillators, synchronize in phase thanks to the radial flexibility in their trajectories (Lenz model). Simulations by Niedermayer and Lenz [88] suggest that, for large arrays of rotors, the radial stiffness is still a parameter that controls the collective state of the array and that various phase-locked states can be obtained. In particular, a linear chain of rotors with periodic boundary conditions can synchronize in a metachronal wave state if the rotors are flexible enough, and a linear chain with free boundary conditions can show a phase-locked "chevron" state, for which the phase of the i^{th} oscillator ($i \in \{1, \dots, N\}$) is approximately [88]:

$$\phi_{i+1}(t) - \phi_i(t) \approx \begin{cases} \chi & \text{if } i < N/2 \\ -\chi & \text{else} \end{cases} \tag{9.1}$$

with χ a positive constant. Other states, such as "tilted chevrons"

$$\phi_{i+1}(t) - \phi_i(t) \approx \begin{cases} \chi_0 + \chi & \text{if } i < N/2 \\ \chi_0 - \chi & \text{else} \end{cases} \tag{9.2}$$

are also possible.

Here, several complex configurations of rotors are explored experimentally, some aimed at finding metachronal waves. This is still ongoing work, and most of the results are qualitative. In particular, some parameters were not calibrated or measured. However, simple rules that could help in determining the synchronized state of a given configuration are deduced empirically. In particular, these rules can explain qualitatively the "chevron" state cited above.

9.2 Effect of the symmetry of the configuration on the state of synchronization

9.2.1 In-phase synchronization in a symmetric configuration

N rotors are arranged at the edges of a regular polygon with vertices size d (see Fig. 9.1). The choice of the number of oscillators is limited experimentally to $N \lesssim 10$, because of two reasons. First, the laser beam is shared between all the oscillators. The trap stiffness is therefore smaller when the number of beads is increased, and a too small optical trapping along z cannot overcome the gravitational force. Second, increasing the number of oscillators increases the time needed to analyze the bead positions, hence reducing the frame rate that can be used in the feedback loop (see Section 3.2.6). To avoid any undesirable effect of the feedback time, the time between two frames should however remains negligible compared to the characteristic time scales in the system, in particular, the rotors period and the relaxation time of the radial position. Typically, frame rates of 200 fps or more should be used.

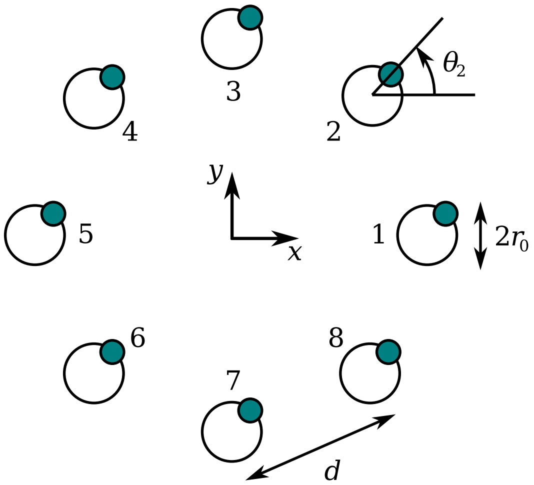

Figure 9.1: Ring configuration for $N = 8$ rotors.

Fig. 9.2 shows the phases of the oscillators ϕ_i depending on time for $N = 8$. The parameters are $\eta = 3$ mPa·s, $a = 1.74$ μm, $d = 7.0$ μm, $r_0 = 1.6$ μm, $F_0 \approx 3.9$ pN and $k_r \approx 2.5$ pN/μm. The rotors are lying in a 2d plane at a

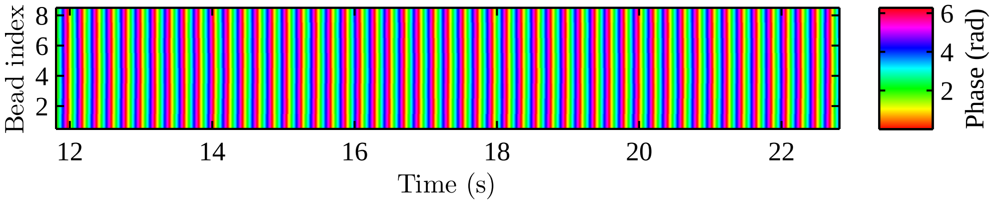

Figure 9.2: Synchronization of eight rotors arranged on a ring with regular spacing. The system synchronizes in phase.

distance $h = 50$ μm away from the coverslip.

The phase of the oscillator i is measured as the angle the bead makes on its circular trajectory with an arbitrary horizontal axis $\hat{\mathbf{e}}_x$. Fig. 9.2 displays vertical wave fronts that are characteristic of a synchronized state in phase. In this figure, the initial condition was with all the oscillators in phase. Other initial conditions of the form $\phi_{i+1}(0) - \phi_i(0) = \chi$ have been tested for different values of χ. In all cases the system was converging in the in-phase phase-locked state

$$\phi_{i+1}(t) - \phi_i(t) \approx 0 \ . \tag{9.3}$$

Thermal fluctuations have little effect on the synchronization state.

Other rings with $N = 3$ and $N = 6$ have been tested, and all led to synchronization in phase. From Chapter 8, it is also known that two rotors synchronize in phase. An empirical rule to determine the state of synchronization can be deduced: symmetric configurations of rotors have a preference to synchronize in phase. By “symmetric” it is meant that the oscillators are all equivalent by symmetries of rotation and translation of the geometric configuration.

The rule above assumes phases measured from a common axis for all the oscillators. There is however another way to interpret the synchronization of rotors on a ring. Such a configuration can be seen as a finite chain, but with periodic boundary conditions. In the spirit of a one dimensional chain, the phase of an oscillator should be measured from the direction of the chain, in this case, the tangent to the circle at the position of the oscillator. The “in-phase” state in Eq. (9.3), becomes, in the new phase coordinates $(\tilde{\phi}_i)_i$, a metachronal wave with a wavelength of the size of the chain:

$$\tilde{\phi}_{i+1}(t) - \tilde{\phi}_i(t) \approx \frac{2\pi}{N} \ . \tag{9.4}$$

However, since for $N = 8$, the distance between oscillators on opposite sides of the ring is not negligible compared to d, it might be possible that the ring cannot be approximated by a one dimensional chain with periodic boundary conditions.

9.2.2 Phase-locked states in an asymmetric configuration

Most configurations that can be imagined are asymmetric. This section highlights the consequence of the asymmetry of the geometry on the synchronized state.

Five identical rotors are placed in the configuration shown in Fig. 9.3. Note that the orbits overlap. In Fig. 9.3(a), the rotors have an initial condition in phase. When they start to be driven at a constant force, they do not move all at the same speed, although the magnitude of the driving force is the same for all the oscillators. The upper middle rotor (black track) goes faster than the two lower rotors (yellow and green) that go themselves faster than the left and right upper rotors (blue and red), see the snapshot for $t = 1.81$ s. It can be concluded that the in-phase state is not a stable state of the system. Since after a few cycles, the particles collide, it is not clear if the system could still synchronize in another state or not.

It is however possible to modify the five rings configuration above, such that it synchronizes (almost) in phase. This is shown in Fig. 9.3(b). Since the left and right upper oscillators were progressing too slowly in (a), their driving forces F_1 have been increased in (b). The three other rotors are still driven by a force F_0. In Fig. 9.3(b), $F_1/F_0 = 1.10$. This results in a synchronized system with all the oscillators phase-locked, and the three upper oscillators in phase.

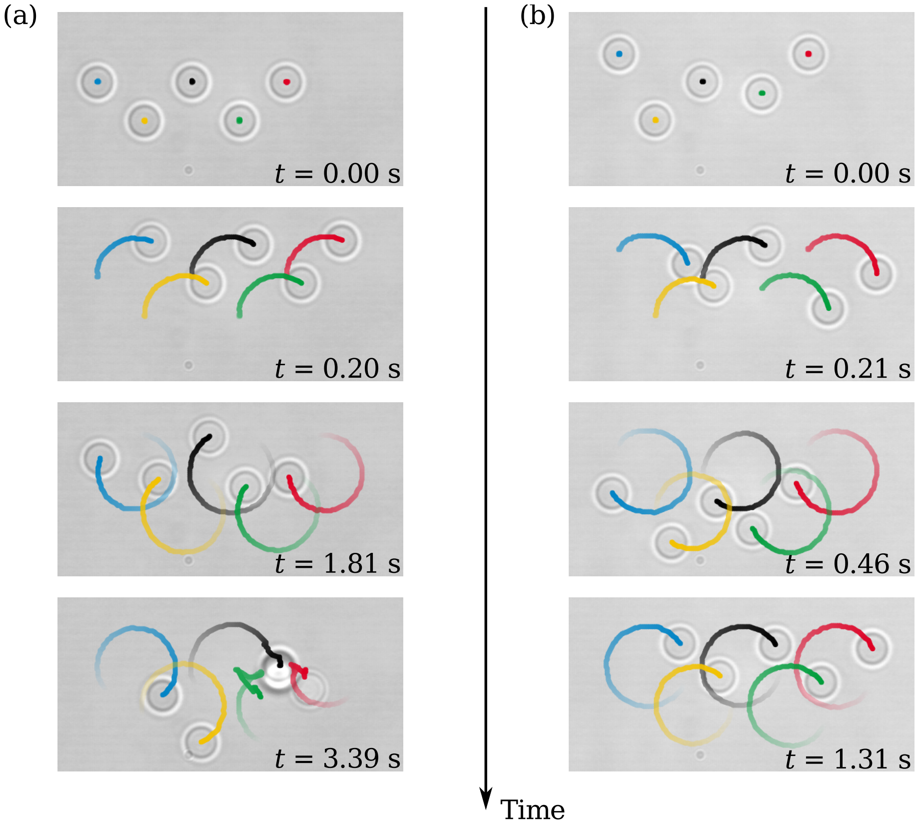

Figure 9.3: Configuration of five overlapping rotors ($a = 1.74\ \mu$m). Snapshots of the beads are shown for different instants. The coloured "comet tails" show a short history of the position of the beads before the time of the snapshot. (a) The beads are driven by a constant force with the same amplitude F_0. Because of the asymmetry of the configuration, the system does not synchronize in phase, leading to collisions between the particles. The rotors start to move with an initial condition in phase. (b) Increasing the driving forces of the left and right upper oscillators to $F_1 = 1.10F_0$ leads to a synchronized system. Starting from an arbitrary initial condition, the system converges to a locked state with all the upper oscillators in phase and the lower oscillators having a slightly delayed phase compared to the upper row.

Interestingly, the two lower oscillators manage to synchronize with the upper middle bead, although they were not moving at the same speed in (a). This can be linked to the single *rower* perturbed by a clock signal ticking at a frequency different from the intrinsic period of the oscillator (Chapter 4). In this chapter it was shown that, when the clock was detuned by a small value, the colloidal rower could adjust its phase in order to adapt its period so that it can stay synchronized with the clock. If the clock is detuned too much, synchronization is lost. Here, although the oscillators are rotors, a similar behaviour arises. When the same driving force is used for all the rotors, the system is in fact already detuned, because of the asymmetry of the configuration. For example, the upper middle oscillator is more coupled to the four other beads, than the left and right upper oscillators are. In the case of rotors, and for an initial condition close to in-phase, a rotor with higher coupling will see its phase grow faster than the phase of the other oscillators. Therefore, the detuning embedded in the configuration can be corrected by adjusting the driving forces. The forces can be tuned to put the system in a synchronized state, and even — with finely tuned forces — in phase. In Fig. 9.3(b), the ratio F_1/F_0 was chosen such that the upper oscillators would synchronize in phase. The lower oscillators are still detuned (lower coupling) compared to the upper middle bead. This detuning is small enough so that the five rotors are synchronized, but the lower beads are slightly delayed compared to all the upper rotors [see the steady state in Fig. 9.3(b) for $t = 1.31$].

From the observations above, a second rule to determine the state of a given configuration emerges. In asymmetric configurations, the stable state — if any — corresponds to a state in which oscillators that are more coupled (closer) to all the others will have a phase ahead of the phases of less coupled oscillators.

The rule can be used to explain qualitatively the "chevron" state in Eq. (9.1) observed numerically by Niedermayer and Lenz in the linear chain of rotors with free ends. An oscillator $i < N/2$, is less coupled to the others than its neighbour $i+1$, which is closer to the middle of the chain. Therefore, using the rule above, $\phi_{i+1}(t) - \phi_i(t) > 0$. Similarly, it is found that $\phi_{i+1}(t) - \phi_i(t) < 0$ for $i > N/2$. This is consistent with Eq. (9.1).

9.3 Waves in chains of rotors

The synchronization of a chain, sketched in Fig. 9.4, of N rotors equally spaced along a line is studied in this section. According to the rule in Section 9.2.2 and the simulations in [88], it should be possible to observe a "chevron" state if the rotors are driven with the same driving force. Furthermore, detuning the rotors should change the synchronized state. With the rotors indexed from 1 (left) to N (right), the driving force for the oscillator i is set to the following value:

$$F_i = F_0 \rho^{i-(N+1)/2} \,. \tag{9.5}$$

With this expression, the driving forces of two neighbours are detuned by a factor ρ, and for small detunings ($\rho \approx 1$), the average force obtained by Taylor expansion is $\langle F_i \rangle_i \approx F_0$.

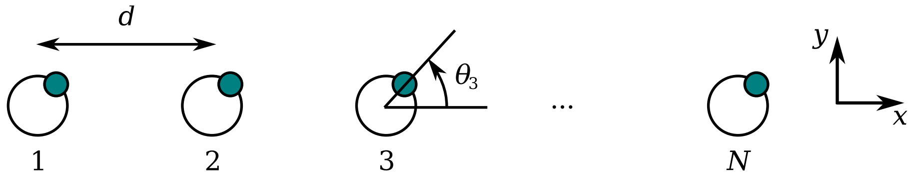

Figure 9.4: Chain configuration of N rotors.

Fig. 9.5 represents the evolution of the phases ϕ_i with time for different values of the detuning ρ in a chain of $N = 8$ rotors. Various states can be obtained. For high or low detuning ($\rho = 0.96$ and 1.04), the chain is not entirely synchronized, as the intrinsic periods of beads 1 and 8 are too much different. For a value of the detuning closer to unity, decreasing the detuning leads to a transition from a wave propagating in the $+\hat{\mathbf{e}}_x$ (increasing bead indexes) direction ($\rho = 1.005$, characterized by diagonal wave fronts in Fig. 9.5) to a wave in the $-\hat{\mathbf{e}}_x$ direction. A very narrow region of ρ leads to an intermediate state: for $\rho = 1.0075$, the chain spends some time in a wave state along $+\hat{\mathbf{e}}_x$ (up to $t = 42$ s), moving then to a "chevron" state, in which the central oscillators are ahead of the rotors on the sides. The "chevron" is not precisely described by a formula of the form of Eq. (9.1), because of the small number of oscillators.

$\rho = 1.0075$ represents the middle of the transition. It is not 1 in the

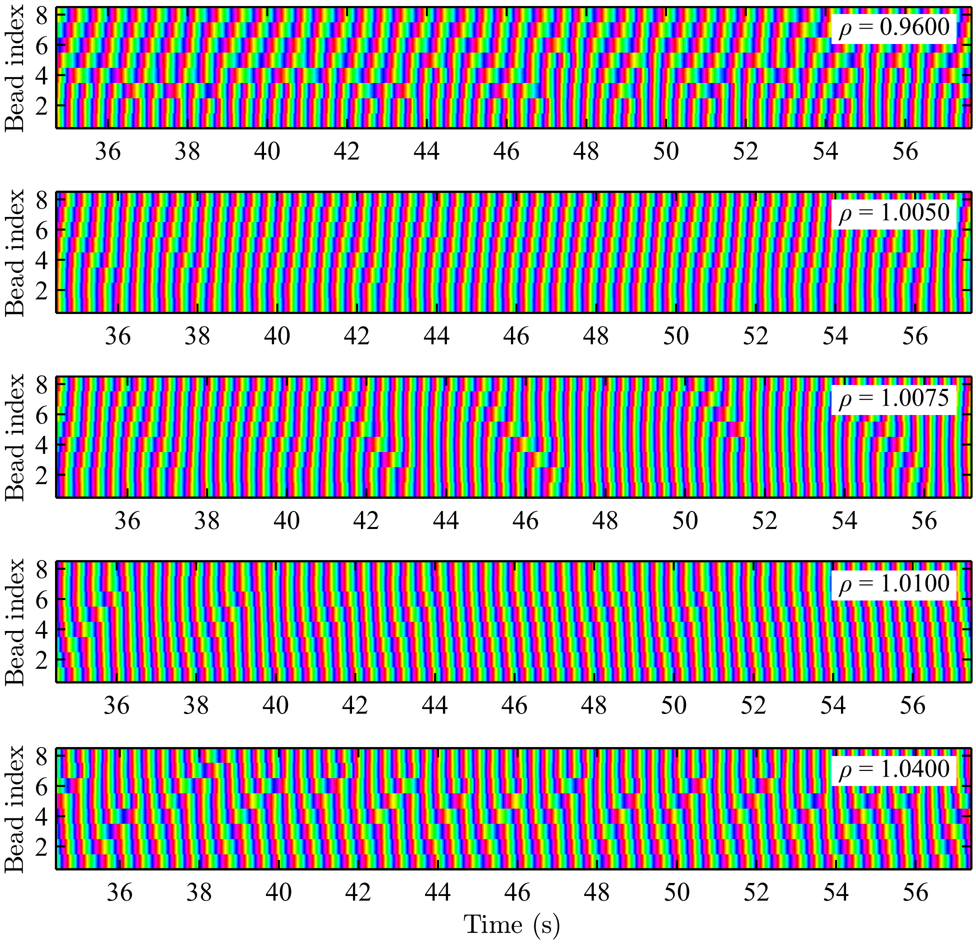

Figure 9.5: Synchronization of a linear chain of eight rotors for different values of the detuning ρ in the driving forces between neighbours. The system is not entirely phase-locked for large detuning ($\rho = 0.96$ and 1.04). Inbetween, the system shows a transition from a wave propagating along $+\hat{\mathbf{e}}_x$ to a wave propagating along $-\hat{\mathbf{e}}_x$ ($\rho = 1.005$ and 1.01 repectively). Parameters are $\eta = 2$ mPa·s, $a = 1.74$ μm, $d = 7.0$ μm, $r_0 = 1.6$ μm, $F_0 = 1.5$ pN, $k_r \approx 2.1$ pN/μm and $h = 75$ μm.

experiments because of a residual detuning existing for $\rho = 1$, although extra care was taken to avoid this by calibrating the periods of the oscillators individually just before realizing the chain.

When the system is mainly synchronized, a few defects occur in the locked states. These are clearly visible for $\rho = 1.0075$, but also exist (and are more probable) for $\rho = 1.005$ and 1.01. Interestingly, the defects seem to be created at one of the sides of the chain and to always propagate in the direction opposite to the wave (see Fig. 9.5 for $\rho = 1.005$ and 1.01).

The phases are recorded for 3 min, repeating the experiment for several values of the detuning. The state of the system can be characterized in many ways by averaged quantities. In Fig. 9.6, two variables are plotted against ρ. First, the quantity

$$\langle\langle\phi_{i+1}(t) - \phi_i(t)\rangle_t\rangle_i \tag{9.6}$$

gives the average relative phase difference between neighbours. Since it is averaged in time, but also in bead indexes, its value is expected to be a non-zero value for a wave with a clear direction of propagation and zero for a “chevron” state. This quantity shows a sharp transition from a wave in the $-\hat{\mathbf{e}}_x$ to the $+\hat{\mathbf{e}}_x$ direction. The saturation values at -0.7 and 0.6 rad can be compared to the wavelength of a metachronal wave with a period of one chain length: $2\pi/N = 0.79$ rad per bead index. A careful look at the waves in Fig. 9.5 shows that the wavefronts are not perfectly straight lines, indicating that the wavelength depends slightly on the bead index. Such states were observed in [88], but this might be due to an experimental issue as well.

The second variable used to characterize the state of the system in Fig. 9.6 is

$$\langle \mathrm{std}_t\left[\phi_{i+1}(t) - \phi_i(t)\right]\rangle_i \tag{9.7}$$

with std_t the standard deviation over time. This is a measure of the number of defects propagating in the locked state, as a defect leads to temporary changes of the phase difference between neighbours. Fig. 9.6 shows that defects are more frequent far from the transition. Therefore, the loss of synchronization at high detuning can be seen as defects perturbing the locked state so much that it prevents seing synchronization of the whole chain.

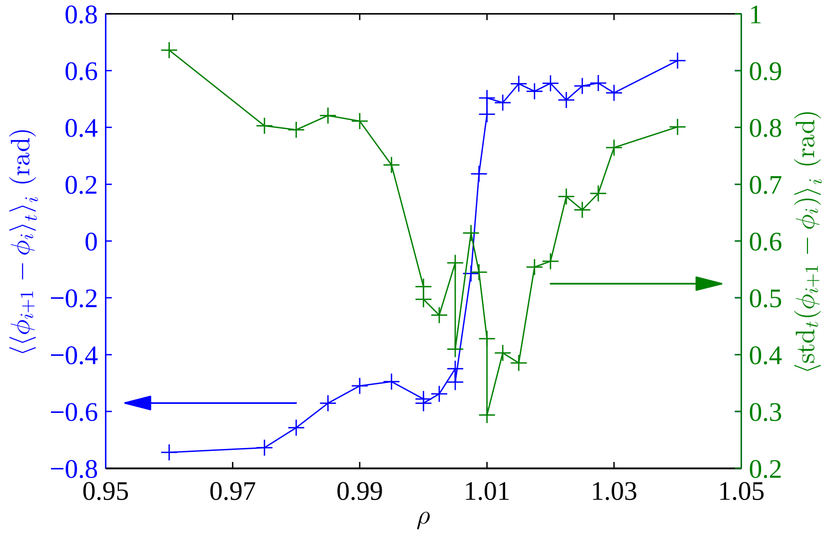

Figure 9.6: Mean phase difference between neighbours (blue) and measure of their fluctuations in time (green), depending on the pair-detuning ρ. The first quantity shows a sharp transition from a wave propagating along the $-\hat{\mathbf{e}}_x$ to the $+\hat{\mathbf{e}}_x$ direction, with a wavelength close to the size of the chain. The number of defects, measured by the second quantity (green) increases when moving away from the middle of the transition.

9.4 Conclusion on the phase-locking of N rotors

Although increasing the number of rotors in a system can increase the complexity of the collective behaviour of the oscillators, results on the synchronization of two rotors (Chapter 8), and even ideas developed in the study of the phase-locking of a rower to a clock (Chapter 4) could be reused. In the few configurations investigated in this chapter, both phase-locked and non-synchronized states were obtained. All the states could be explained in a qualitative manner.

The general idea that emerges from the states obtained here is that, as for two rotors, a system of N rotors seems to have a preference to synchronize in phase. However, when all the oscillators in the geometry of the configuration are not equivalent in terms of coupling relative to the others, this in-phase state is perturbed: the oscillators that are highly coupled to the others tend to go faster than the less coupled oscillators. Similarly to the rower coupled to a clock signal, this can lead to two behaviours. If the coupling effect does not detune too much the oscillators relatively to each other, the system can sychronize by adapting the phases of the oscillators, with the phase of the highly coupled oscillators being ahead of the others. Too big coupling-induced detunings, however, cannot be corrected by phase shifts and, in that case, the whole system would not synchronize. Subparts of the system can still be phase locked.

To exhibit the effect of the detuning induced by coupling, the driving forces of some of the oscillators were changed. In a five-rotors configuration, it was possible to synchronize in phase the highly asymmetric configuration by adjusting the magnitude of the driving forces acting on the beads.

In a chain of oscillators, the state of the system could be controlled by the force-detuning parameter ρ. Interestingly, the mean phase difference between the oscillators does not evolve linearly with ρ, and displays instead a sharp transition between two waves propagating in opposite directions, with an average wavelength close to the size of the chain. Waves are seen in a wide range of values of ρ and seem pretty stable. In the middle of the transition, a “chevron” phase-locked state was observed, recovering findings in [88]. This state could be explained qualitatively by using the ideas summarized above. For small detunings ($\rho \approx 1$), the chain is mainly phase-locked. However, some defects seem to propagate in the direction opposite to the wave. In simulations with no Brownian noise, defects still exist and seem to appear at regular time intervals [190]. Hence the pattern of phase differences between the oscillators might be periodic in time and not (but almost) phase-locked.

Only a few systems of several rotors have been studied in this chapter. To confirm the rules determining the state of synchronization, they should be tested on more configurations. The rules might not apply in the general case. It is indeed likely that some configurations could lead to several stable states. When more than two oscillators are present, wall interactions also change the coupling to a local interaction (decaying with the distance in $1/r^3$ instead of $1/r$), possibly affecting the way a big system synchronizes.

Part V

Conclusions

Chapter 10

Conclusions and outlook

The interaction between cilia (or flagella) and the fluid that surrounds them is complex to describe in detail. To focus on how several of these oscillators couple and synchronize through the fluid, I have used coarse-grained models of a cilium, by representing it as a hard sphere. This simplification brings a lot of advantages, that are exploited in this thesis. Firstly, experiments could be performed with optical tweezers driving colloidal particles. Secondly, simulations were realized, without having to solve the Stokes equation numerically: the hydrodynamic interaction is simply described by a tensor relating the velocities of the particles to the driving forces, resulting in a simple Langevin equation that includes thermal noise and can be integrated step by step. Thirdly, the simplicity of the equations allowed to derive in some cases theoretical models to explain the cooperative behaviour seen in the experiments and simulations. These theoretical analyzes are important to understand what are the parameters that control the synchronization.

Two main models have been considered: a one-dimensional free-phase oscillator, called “rower”, in which a particle moves between two traps that are switched on and off in turn, following a configuration-dependent rule, and a “rotor” model, where the particle moves along a circular two-dimensional trajectory.

With the first rower model, a single oscillator coupled to a periodic signal has been used to study how thermal fluctuations can lead to a loss of synchronization, and the results were summarized on a phase diagram, involving the ratio of a dimensionless parameter characteristic of the noise amplitude and a parameter describing the amplitude of the coupling force. For two coupled rowers, the state of synchronization depends on the curvature of the driving forces from the optical tweezers. An in-phase to antiphase transition in the synchronization was observed when varying the curvature. Here, the effect of the thermal noise is to smooth the transition. The results were used to explain the state of synchronization of the two flagella in the alga *C. reinhardtii*. On configurations of more than two rowers, it has been shown that the oscillations of the beads can be decomposed in a space of equilibrium "normal modes". By testing several arrangements of oscillators, it appeared that, for harmonic driving, the system puts itself in a state in which the mode that decays with the highest relaxation time dominates. This could help designing configurations that require a given state of oscillations, or seek for configurations leading to metachronal waves. Finally, the rower model has also been modified to allow it to change its beating direction freely. In numerical simulations, arrays of these modified rowers synchronize and also align their oscillations, because of the hydrodynamic interaction. The alignment of a rower occurs relatively to the direction of the others, but also, when the array is not symmetric, in the direction of elongation of the array. This could be applicable to *Paramecium*, since it is an elongated cell that moves in the direction of its elongation.

The second model, rotors, has been implemented experimentally for the first time. Two separate mechanisms for rotor synchronization had been proposed by theoretical groups, and the experiments in this thesis recover qualitatively their findings. A simple analytical argument has also been used to join the two models together and a phase diagram showing which mechanism is dominant has been obtained. The collective behaviour of more than two rotors arranged along chains, rings and other configurations has also been explored experimentally. Qualitative rules for determining the possible phase-locked state were deduced. In linear chains of rotors, patterns of propagating waves were observed when the rotors were driven by forces with different magnitudes, i.e. rotors of varying frequency. This is one of the first experimental observation of waves in coarse-grained models of cilia.

Another experiment reporting propagating waves of phase patterns in active colloidal systems uses ellipsoidal particles trapped with static optical tweezers on a surface. Such particles, elongated like cilia, undergo oscillations [191] and rings of these oscillators can synchronize in propagating waves [192].

The main conclusion drawn by this principally experimental work is that the hydrodynamic interaction can lead to strong synchronization through various mechanisms (choice of the driving force, shape of the orbit and flexibility in the trajectories), even in the presence of thermal noise. Other coupling channels have been proposed to explain the cooperative behaviour of cilia and flagella: mechanical through the cell body and contact forces between cilia. They might be relevant in particular cases. However, which of the mechanisms are dominant is still an open question and the answer might depend on the biological system. Also, a possible coupling between these different mechanisms cannot be excluded. For example, this thesis does not consider oscillators in a net flow. Adding the fact that cilia and flagella swim or generate a net flow could change the way synchronization emerges.

The experimental work in this thesis, in which the oscillators were located far from any surface, shows a very good agreement with previously published theoretical models for the synchronization of rotors and rowers. This means that the hydrodynamic interaction is well described by the Oseen tensor, and that the equations of motion describing these coupled systems are accurate. However, cilia are anchored on a surface. The presence of a static wall should therefore be taken into account. Some theoretical and numerical work on rowers and rotors has already considered the presence of a wall [88, 146], but experiments are lacking. While a wall with no-slip boundary conditions is not expected to change the mechanisms at play for the synchronization of two oscillators far away (it only changes the value of the coupling constant in the equations of motion), it might affect considerably the way chains and arrays of oscillators synchronize. The presence of a wall changes indeed the power of the decay of the interaction with distance, making the hydrodynamic interaction more local.

Relating the findings in the synchronization of rowers and rotors to real biological systems is crucial. This was done where possible throughout this work, for example on *Chlamydomonas*. The main issue is that, currently, only few physical parameters have been extracted from living cilia and flagella. To pursue a comparison with the coarse-grained models of oscillators, it will be necessary to gain more quantitative knowledge on the shape of ciliary oscillations in various systems and the stiffness of the filaments.

The colloidal oscillators developed here can be used to explore more realistic models of cilia. For example, a possible viscoelasticity of the fluid could be added, since it might enhance flow generation [193], and since mucus in the airways is a non-Newtonian fluid. Viscoelasticity of the fluid could enhance swimming. Also, the coarse-grained oscillators in this thesis are only a good approximation to cilia or flagella spaced by a much higher distance than the size of the filaments they represent. Real cilia on tissues can be densely packed, and bacteria like *E. coli* have filaments that are much longer than their separation. Understanding in more details the synchronization properties in this case requires to model elongated filaments. For *E. coli*, such models already exist and synchronize because of the flexibility at the base of the relatively stiff helical filaments [17], hence obtaining a qualitatively similar result as in the flexible rotors.

The rowers and rotors models that I have studied here in experiments, simulations and by theoretical models have brought new knowledge in the field of synchronization of micrometric oscillators that interact through a fluid in a low Reynolds number environment. But the physics of hydrodynamically coupled actively driven systems is very rich and many aspects — some being mentioned in this conclusion — remain to be investigated.

Appendices

Appendix A

Fluctuations around the fixed point in the perturbed single rower

This appendix presents in more detail the calculation that leads to an estimate of the fluctuations around the synchronized state in the system of a single rower coupled to a “clock” signal (Chapter 4).

A.1 Cycle of oscillation

The oscillation represented in Fig. 4.1 is considered. The initial condition is the position $A/2$, following a geometric switch. The time $t_1(i)$ between the geometric switch and the previous clock switch, at cycle i, can be used to measure synchronization. The aim is to estimate the distribution of $t_1(i+1)$ after one cycle, and use it in a fixed-point argument for the noise.

A cycle corresponds to a sequence of four stages. During the first, the bead has velocity $-v(1-\epsilon)$ during a time $t_2(i) = T_c/2 - t_1(i)$. Subsequently, between the clock switch and the next geometric switch, the velocity is $-v(1+\epsilon)$ during a time $t_3(i)$. The third and fourth stages describe the other half of the oscillation, with (positive) velocity $v(1-\epsilon)$ for a time $T_c/2 - t_3(i)$ and $v(1+\epsilon)$

for a time $t_1(i+1)$.

This calculation requires to evaluate how thermal noise affects the cycle in two ways. First, in the time between a geometric switch and a clock switch, the bead is subject to a driving force and diffusion, which makes the arrival position $r_j(i)$ (where $j \in \{1,2\}$ indexes the half-cycle bead positions) at the clock switch stochastic. Second, the evaluation of the time between the position $r_j(i)$ and the position of the next geometric switch is a first-passage time problem that contributes to the stochasticity of the times $t_3(i)$ and $t_1(i+1)$.

A.2 Equation of evolution of time t_1

To find the equation of evolution of t_1, the different stages of the cycle need to be detailed. As the delay $t_1(i)$ between the starting geometric switch and the previous clock switch is known, the duration of the random walk between the geometric switch and the next clock switch is prescribed, $t_2(i) = T_c/2 - t_1(i)$. The position of the particle at the clock switch is given by $r_1(i) = v(1-\epsilon)t_2(i) + x_1(i)$. $v(1-\epsilon)t_2(i)$ is the deterministic arrival time and $x_1(i)$ corresponds to the fluctuations due to the diffusion of the particle: $\langle x_1(i)\rangle = 0$ and $\langle x_1^2(i)\rangle = 2Dt_2(i) = 2D[T_c/2 - t_1(i)]$ with D the diffusion coefficient. In order to carry out the argument, it is assumed that any transient behaviour is past, and that $t_1(i)$ can be approximated by its average t_1^{fp} in the expression of the variance.

After the clock switch, the bead moves over a distance $A' = A - r_1(i)$ at an average velocity $v' = -v(1+\epsilon)$. The arrival time $t_3(i)$ of this process is described by the first-passage time probability density $\mathcal{P}[t_3(i)]$, where $\mathcal{P}$ is the inverse Gaussian [181]:

$$\mathcal{P}(t) = \frac{1}{\sqrt{4\pi D t^3}} \mathrm{e}^{-\frac{(A'-v't)^2}{4Dt}} \ . \tag{A.1}$$

This probability density is well approximated by a Gaussian in the small diffusion limit, i.e. when $A'/v' \ll A'^2/(2D)$ (in this case the skewness of this distribution is small). Equivalently, this approximation holds for times t such as $v't/A' \in \left[1-\sqrt{\xi'}, 1+\sqrt{\xi'}\,\right]$ with $\xi' = 2D/(A'v')$.

This condition is satisfied for $\xi' \ll 1$, so that the first-passage time distribution $\mathcal{P}$ is well-approximated by a Gaussian centred on $[A - r_1(i)]/[v(1+\epsilon)]$ and of variance $2DA'/[v^3(1+\epsilon)^3]$. Since A' is itself a random variable, as above, A' is replaced by its average value in the variance: $\langle A' \rangle = v(1+\epsilon)t_1^{\mathrm{fp}}$. These two assumptions lead to the following formula for the time $t_3(i)$:

$$\begin{aligned} t_3(i) &= \frac{A - r_1(i)}{v(1+\epsilon)} + \zeta_1(i) && \text{(A.2)} \\ &= \frac{A/v - (1-\epsilon)T_c/2}{1+\epsilon} + \kappa t_1 - \frac{x_1(i)}{v(1+\epsilon)} + \zeta_1(i) && \text{(A.3)} \\ &= h[t_1(i)] \ , && \text{(A.4)} \end{aligned}$$

with $\langle \zeta_1 \rangle = 0$, $\langle \zeta_1^2 \rangle = 2D \langle t_1 \rangle / [v^2(1+\epsilon)^2]$ and $\kappa = (1-\epsilon)/(1+\epsilon)$.

Eq. (A.4) describes only the first half of the cycle. The second half is symmetric, with the only difference that the velocities become positive. The time $t_1(i+1)$ is therefore obtained by iterating Eq. (A.4):

$$\begin{aligned} t_1(i+1) &= h\{h[t_1(i)]\} && \text{(A.5)} \\ &= (1+\kappa)\frac{A/v - (1-\epsilon)T_c/2}{1+\epsilon} + \kappa^2 t_1(i) + \chi(i) \ , && \text{(A.6)} \end{aligned}$$

with

$$\chi(i) = \kappa\left[\frac{x_1(i)}{-v(1+\epsilon)} + \zeta_1(i)\right] + \frac{x_2(i)}{-v(1+\epsilon)} + \zeta_2(i) \ . \tag{A.7}$$

Here, $x_2(i)$ and $\zeta_2(i)$ represent the fluctuations in the second half of the cycle and are defined similarly as in the first half-cycle. In this approximation, since all the random variables are assumed Gaussian, $\chi(i)$ also follows a Gaussian distribution centred on 0 and with variance

$$\begin{aligned} \mathrm{var}\,(\chi) &= (1+\kappa^2)\left[\frac{\mathrm{var}\,(x_1)}{v^2(1+\epsilon)^2} + \mathrm{var}\,(\zeta_1)\right] && \text{(A.8)} \\ &= (1+\kappa^2)(V_1 + V_2) \ , && \text{(A.9)} \end{aligned}$$

with

$$\begin{cases} V_1 = 2D\dfrac{T_c/2 - \langle t_1 \rangle}{v^2(1+\epsilon)^2} \\ V_2 = 2D\dfrac{\langle t_1 \rangle}{v^2(1+\epsilon)^2} \end{cases} . \tag{A.10}$$

Assuming now that the clock period is set to the natural particle period $2A/v$, the evolution equation over one full cycle becomes

$$t_1(i+1) = (1+\kappa)\frac{A\epsilon}{v(1+\epsilon)} + \kappa^2 t_1(i) + \chi(i) \tag{A.11}$$

with

$$\operatorname{var}\chi = (1+\kappa^2)\frac{DT_c}{v^2(1+\epsilon)^2} . \tag{A.12}$$

Removing the noise term $\chi(i)$ in Eq. (A.11) gives the deterministic fixed point $t_1^{\mathrm{fp}} = A/(2v) = T_c/4$. Since the noise only adds fluctuations around this fixed point, only the deterministic the deviation $q(i) = t_1(i) - t_1^{\mathrm{fp}}$ is considered. Expressed with q, Eq. (A.11) becomes

$$q(i+1) = \kappa^2 q(i) + \chi(i) , \tag{A.13}$$

or

$$\delta q = q(i+1) - q(i) = -\frac{4q\epsilon}{(1+\epsilon)^2} + \chi(i) . \tag{A.14}$$

Eq. (A.13) shows the contribution of the deterministic part, due to the system geometry which makes q decay to 0 with the typical decay time of $(1+\epsilon)^2/(4\epsilon)$ cycles, and the noise, which adds fluctuations.

The two following sections present two methods to carry out the argument leading to the quantification of the fluctuations for q.

A.3 Solving using the continuous Langevin equation

Chapter 4 contains an approximated solution [Eq. (4.13)] in which the main equation is treated as a continuous Langevin equation, although it is discrete.

This procedure requires to convert Eq. (A.14) into a continuous equation. One way to perform this task rigorously is to reduce the size of the steps at each iteration, hence looking for an equation of the form

$$q\left(i+\frac{1}{n}\right)=\alpha q(i)+\delta(i) \tag{A.15}$$

that would describe the system. n is an integer that allows to take the continuum limit. α is a coefficient and $\delta(i)$ a Gaussian random variable. These coefficients can be found by iterating Eq. (A.15) n times and identifying the coefficients with Eq. (A.13). The procedure leads to the following evolution equation

$$q\left(i+\frac{1}{n}\right)-q(i)=-\left(1-\kappa^{\frac{2}{n}}\right)q(i)+\delta(i) \tag{A.16}$$

with

$$\operatorname{var}(\delta)=\frac{1-\kappa^{\frac{4}{n}}}{1-\kappa^{4}}\operatorname{var}(\chi)\ . \tag{A.17}$$

Eq. (A.16) is a continuous Langevin equation when n tends to infinity. Therefore, the variance of q at long times is estimated by

$$\begin{aligned}\operatorname{var}[q(\infty)] &= \lim_{n\to\infty}\frac{\operatorname{var}(\delta)}{2(1-\kappa^{\frac{2}{n}})} && \text{(A.18)}\\ &= \lim_{n\to\infty}\frac{1+\kappa^{\frac{2}{n}}}{2(1-\kappa^{4})}\operatorname{var}(\chi) && \text{(A.19)}\\ &= \frac{\operatorname{var}(\chi)}{1-\kappa^{4}} && \text{(A.20)}\\ &= \frac{DT_c}{4\epsilon v^2}\ . && \text{(A.21)}\end{aligned}$$

This can be expressed in dimensionless parameters as the fluctuations of the phase ϕ_1,

$$\operatorname{var}(\phi_1)=\operatorname{var}\left[\frac{q(\infty)}{T_c}\right]=\frac{\xi}{16\epsilon}\ . \tag{A.22}$$

When the clock period does not match the natural oscillation time of the oscillator, but is longer or shorter, $T_c=2A/v+\delta$, the calculation follows the same steps, starting from Eq. (A.11) and replacing the clock period with $T_c=2A/v+\delta$, instead of $2A/v$.

A.4 Solving by iterating the equation for the variance

In order to estimate the fluctuations of q, Eq. (A.13) can also be directly iterated, starting from an initial condition $q(0)$. After $n+1$ iterations

$$q(n+1) = \kappa^{2(n+1)} q(0) + \sum_{i=0}^{n} \kappa^{2i} \chi(n-i) \ . \tag{A.23}$$

Evaluating the fluctuations of $q(\infty) = \lim_{n\to\infty} q(n+1)$, one gets

$$q(\infty) = \sum_{i=0}^{\infty} \kappa^{2i} \chi(n-i) \ . \tag{A.24}$$

This is a Gaussian random variable with variance

$$\begin{aligned} \mathrm{var}\left[q(\infty)\right] &= \sum_{i=0}^{\infty} \kappa^{4i}\, \mathrm{var}\left(\chi\right) && \text{(A.25)} \\ &= \frac{1}{1-\kappa^4}\, \mathrm{var}\left(\chi\right) && \text{(A.26)} \\ &= \frac{DT_c}{4\epsilon v^2} \ . && \text{(A.27)} \end{aligned}$$

This is the same result as Eq. (A.21).

Appendix B

Calculation of the phase-antiphase transition for two rowers

B.1 Introduction

This appendix provides details of the calculation estimating the fluctuations of the delay time t_1 and the average value of the synchronization order parameter Q, together with additional simulations performed with various functional forms of the potential.

It is organized as follows. First, a derivation of the evolution equation for the delay time t_1 in absence of noise is given. Then the effect of noise on t_1 is considered, allowing to derive estimates for (a) the distribution of Q and (b) the average $\langle Q \rangle$. In Section B.3 simulations are presented that justify the choice of the "curvature" parameter c as a control parameter for the transition of synchronization states.

B.2 Derivation of $\langle Q \rangle$

B.2.1 Evolution of t_1 without noise, and synchronized states

The calculation is based on the simplifying assumption that the potentials are composed of two linear sections (two slopes). For one single bead, and considering the origin of the positions $x = 0$ in the middle of the two geometric switching conditions, this "two-slopes" potential [the purple lines in Fig. 5.3(b)] can be characterized by the driving force

$$F(x) = \begin{cases} \sigma F_b & \text{if } \sigma x > \dfrac{A}{2} - x_0 \\ \sigma F_e & \text{otherwise} \end{cases} . \tag{B.1}$$

Here $\sigma = \pm 1$ is the state of the geometric switch, A the amplitude (see Fig. 5.1), and x_0 is a parameter that describes at what position the force will switch between $\pm F_b$ and $\pm F_e$. In other words, the bead is driven by a force $\pm F_b$ just after a geometric switch, until it moves a distance x_0 far from the switch position. Then the force becomes $\pm F_e$, until the next geometric switch.

For two beads, the equation of motion (5.2), can be written (without noise) as

$$\begin{cases} \dot{x}_1 = \dfrac{1}{\gamma} F_1(x_1, t) + \epsilon \dot{x}_2 \\ \\ \dot{x}_2 = \dfrac{1}{\gamma} F_2(x_2, t) + \epsilon \dot{x}_1 \end{cases} , \tag{B.2}$$

where $\epsilon = 3a/(2d)$ quantifies the strength of the hydrodynamic coupling coefficient between bead 1 and 2. Between geometric switches, or "slope break" events[1], the forces are constant and the system is solved immediately ($F_1 = \pm F_u$ and $F_2 = \pm F_v$ with $u, v \in \{`b', `e'\}$). The velocities of the beads

---

[1] A "geometric switch" refers to a change of σ and a "slope break" refers to a change of the absolute force from F_b to F_e (but not F_e to F_b, which occurs at a geometric switch).

are

$$\begin{cases} \dot{x}_1 = \dfrac{1}{\gamma(1-\epsilon^2)}\left(F_u + \epsilon F_v\right) \\ \dot{x}_2 = \dfrac{1}{\gamma(1-\epsilon^2)}\left(F_v + \epsilon F_u\right) \end{cases} . \tag{B.3}$$

In order to advance, one needs to assume an order in which geometric switches and slope breaks occur. Two general cases need to be considered. These are sketched in Fig. B.1 and correspond to oscillations that are almost in phase or almost in antiphase. In both cases, each half-cycle is split into four pieces, for which the forces are constant and lead to velocities given by Eq. (B.3). The half-cycle can be expressed as a linear system of eight equations describing the position of each of the two beads in the four parts, depending on the times t_1 to t_4, t'_1 and the distances δ_1 to δ_4 (see notations in Fig. B.1). For the case of configurations close to in-phase motion [Fig. B.1(a)], the linear system is

$$\begin{cases} \delta_1 &= \dfrac{1}{\gamma(1-\epsilon^2)}(F_b - \epsilon F_e)t_1 \\ \delta_2 &= \dfrac{1}{\gamma(1-\epsilon^2)}(F_b + \epsilon F_b)t_2 \\ x_0 - \delta_1 &= \dfrac{1}{\gamma(1-\epsilon^2)}(F_b + \epsilon F_b)t_2 \\ x_0 - \delta_2 &= \dfrac{1}{\gamma(1-\epsilon^2)}(F_b + \epsilon F_e)t_3 \\ A - x_0 - \delta_3 &= \dfrac{1}{\gamma(1-\epsilon^2)}(F_e + \epsilon F_b)t_3 \\ A - x_0 - \delta_4 &= \dfrac{1}{\gamma(1-\epsilon^2)}(F_e + \epsilon F_e)t_4 \\ \delta_3 &= \dfrac{1}{\gamma(1-\epsilon^2)}(F_e + \epsilon F_e)t_4 \\ \delta_4 &= \dfrac{1}{\gamma(1-\epsilon^2)}(F_e - \epsilon F_b)t'_1 \end{cases} . \tag{B.4}$$

This set of equations can be solved to find a discrete evolution map for the time delay t'_1 after a half cycle, depending on t_1:

$$t'_1 = \kappa_P t_1 \tag{B.5}$$

with

$$\kappa_P = \frac{F_e + \epsilon F_b}{F_e - \epsilon F_b}\,\frac{F_b - \epsilon F_e}{F_b + \epsilon F_e} . \tag{B.6}$$

t_1 is a proxy for the phase difference between the two oscillators, and is zero when they are synchronized. If the considered half-cycle is the k^{th}, $t_1 = t_1^{(k)}$ and $t_1' = t_1^{(k+1)}$, giving the equation of evolution found in Chapter 5, which predicts in-phase synchronization for $\kappa_P < 1$ with a characteristic relaxation time $1/\kappa_P$ (in half-cycles). It is interesting to note that this equation does not depend on the geometric parameter x_0 that appears in the definition of the potential. Only the driving forces near the geometric switches need to be considered. However, the solution assumes that the oscillations are described by a cycle as sketched in Fig. B.1(a), which makes the equations invalid for large t_1, or x_0 close to 0 or to A. This approximation can explain the discrepancy between theoretical estimate and simulations in Fig. 5.6. The effect of the parameter x_0 on the transition is discussed in Section B.3.1.

The corresponding map for t_1 for the case of oscillations that are almost in antiphase can be obtained from the previous result by noting that the interaction of the second particle on the the first one is the same but with an opposite sign. Therefore, κ_{AP} is the same as κ_P but with ϵ replaced by $-\epsilon$:

$$\kappa_{AP} = \frac{F_e - \epsilon F_b}{F_e + \epsilon F_b} \frac{F_b + \epsilon F_e}{F_b - \epsilon F_e} \ . \tag{B.7}$$

While not formally necessary here, both the perturbations with respect to a synchronized state and ϵ can be considered to be small parameters as already done in [147] and Chapter 4. The above expressions for κ_P and κ_{AP} can then be easily recast in the expressions given in Chapter 5 by expanding in ϵ to first order.

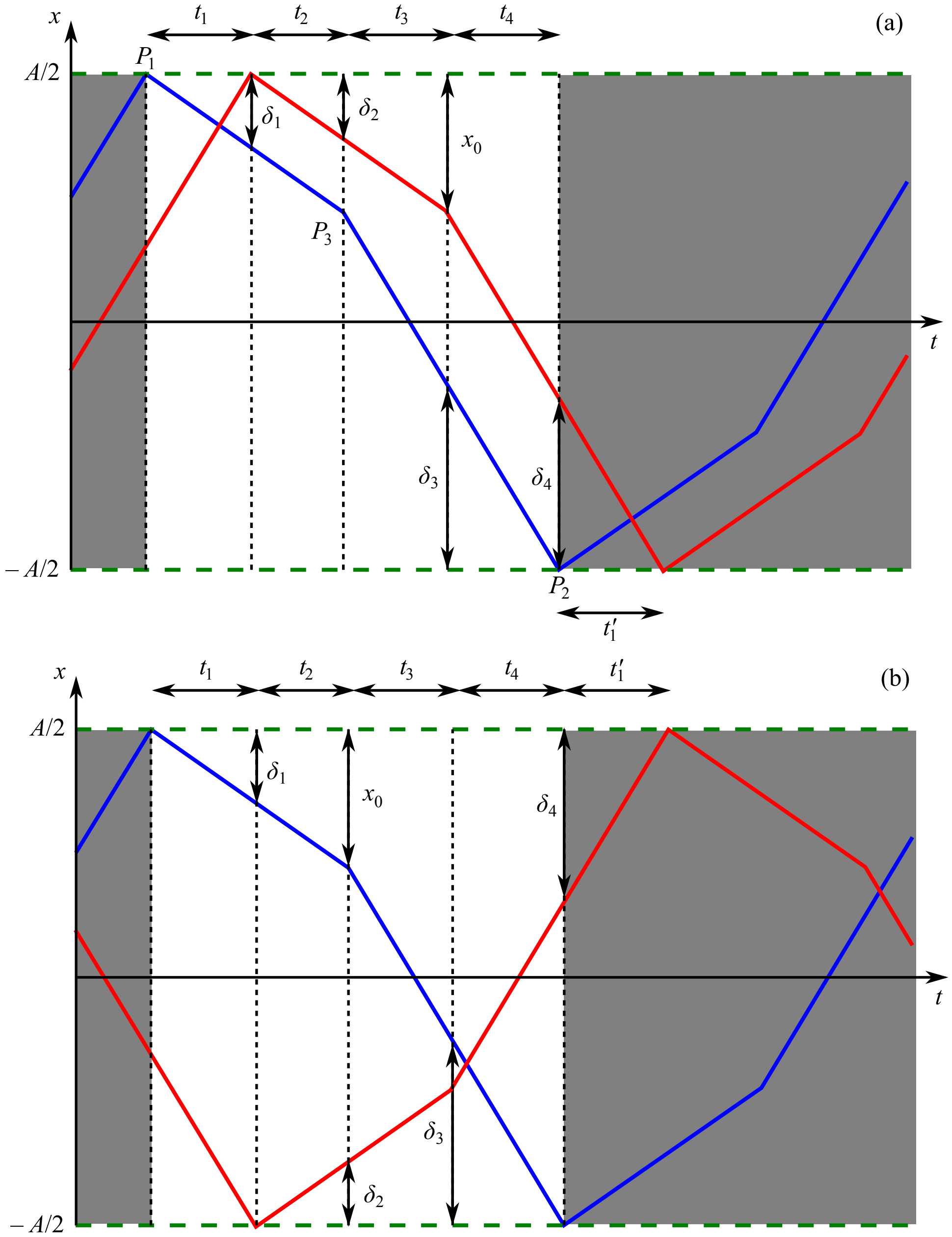

Figure B.1: Schematics and parameters of a half-cycle dynamics in the two-slope approximation. A generic potential is approximated by a two-slopes linear potential, leading to piece-wise constant bead velocities. The time t_1 is estimated by considering two possible half-cycles: (a) for oscillations close to in-phase motion and (b) for oscillations close to antiphase. For simplicity, the slope breaks in the position of one bead due to geometric switches or $F_b \to F_e$ switches of the other bead are not displayed here, but are taken into account in the calculation. The simplicity of the model allows to obtain the time t_1' depending on t_1, even when noise is added to the system.

B.2.2 Effect of the noise on t_1

Starting from an initial condition t_1, the noise will affect t'_1 by modifying the arrival times of the beads at each geometric switch or slope break. As each half-cycle is composed of four parts, this is in principle a complex, coupled first-passage time (FPT) problem. In the analytical estimates of the effect of noise, in order to make the problem tractable, the coupling between the two beads is neglected, so that the two beads can be treated separately (the full model is however solved numerically). Without coupling, the half-cycle of the blue bead in Fig. B.1(a) is made of two parts. Starting from a position $A/2$ (point P_1), the position decreases at a velocity $-v_b = -F_b/\gamma$ during a time $t_1 + t_2$, until the bead reaches the point P_3 (defined by its position $A/2 - x_0$), where the velocity will become $-v_e = -F_e/\gamma$. The position continues to decrease for a time $t_3 + t_4$ until the end of the half-cycle (point P_2, position $-A/2$). The first part is a simple FPT problem and the distribution of the arrival time $t_1 + t_2 = t$ is given by the probability density [181]:

$$\mathcal{P}_{\mathrm{FPT}_1}(t) = \frac{1}{\sqrt{4\pi D t^3}} \mathrm{e}^{-\frac{(x_0 - v_b t)^2}{4Dt}} \ . \tag{B.8}$$

The second part is also described by a similar FPT distribution, except that when starting after point P_3, the bead can go backwards and spend some time in a potential corresponding to the previous velocity $-v_b$. This effect is likely happening just after P_3, during a time t_c defined as $v_e t_c = \sqrt{2Dt_c}$ which represents the possibility that the noise pushes the bead back towards the position $A/2 - x_0$ despite the average tendency to move at velocity $-v_e$. The effect is negligible when $t_c \ll \langle t_3 + t_4 \rangle$, or equivalently $2D/v_e \ll A - x_0$. For a choice of x_0 and c such that the quantity $A - x_0$ is of the same order of magnitude as A, and v_e is of the same order of magnitude as $v_0 = F_0/\gamma$, this condition is equivalent to $\xi \ll 1$ where $\xi = 2D/(Av_0)$ is a dimensionless expression of the noise strength. In this case, the distribution of $t_3 + t_4 = t$ is well approximated by

$$\mathcal{P}_{\mathrm{FPT}_2}(t) = \frac{1}{\sqrt{4\pi D t^3}} \mathrm{e}^{-\frac{(A - x_0 - v_e t)^2}{4Dt}} \ . \tag{B.9}$$

When $\xi \ll 1$, the distributions $\mathcal{P}_{\mathrm{FPT}_1}$ and $\mathcal{P}_{\mathrm{FPT}_2}$ can also be approximated by Gaussians. In this case, the random variable $t_1 + t_2 + t_3 + t_4$ is described by a Gaussian distribution, of mean value $x_0/v_b + (A - x_0)/v_e$ and variance

$$2D\left(\frac{x_0}{v_b^3} + \frac{A - x_0}{v_e^3}\right) \; . \tag{B.10}$$

Fig. B.2 shows simulations comparing this approximated probability distribution with models using power-law potentials as well as with direct simulation of the two-slopes model. The effect of varying the value of x_0 is also discussed.

The difference of the arrival times of the two beads t_1 can be written as

$$t_1' = \kappa t_1 + \zeta \; , \tag{B.11}$$

and at the general k^{th} step:

$$t_1^{(k+1)} = \kappa t_1^{(k)} + \zeta(k) \; , \tag{B.12}$$

with $\kappa = \kappa_P$ or κ_{AP} depending on the sign of c and $\zeta(k)$ a Gaussian random variable characterized by

$$\langle \zeta \rangle = 0 \tag{B.13}$$

and

$$\left\langle \zeta^2 \right\rangle = 4D\left(\frac{x_0}{v_b^3} + \frac{A - x_0}{v_e^3}\right) \; . \tag{B.14}$$

The extra factor 2 compared to Eq. (B.10) accounts for the summation of the variances of each of the two beads.

ζ characterizes the fluctuations of t_1 that need to be added at each half-cycle of oscillation. The fluctuations of the steady state $t_1^{(\infty)}$ are given by iterating Eq. (B.12) as in Appendix A, leading to the following estimates for the first two moments of the $t_1^{(\infty)}$ random variable (assumed Gaussian):

$$\left\langle t_1^{(\infty)} \right\rangle = 0 \tag{B.15}$$

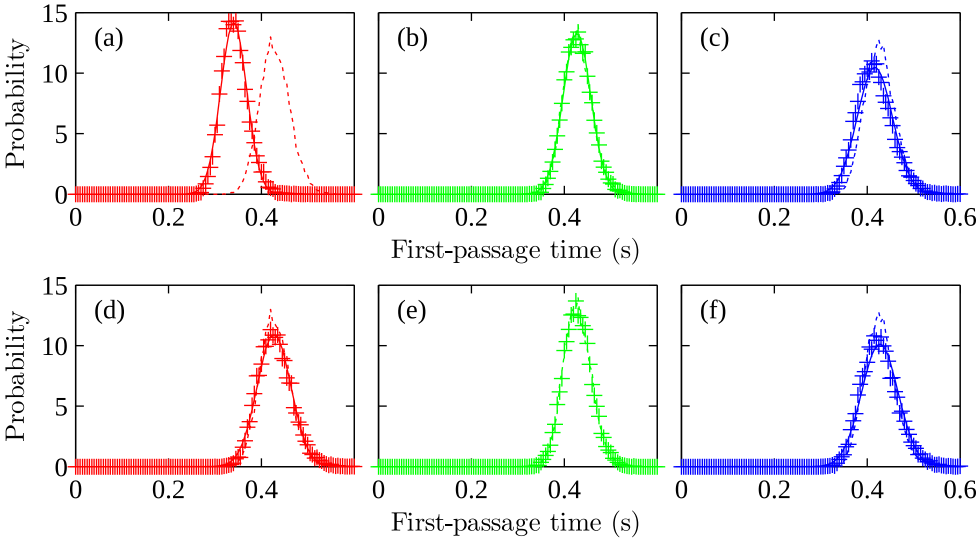

Figure B.2: First-passage time distributions for different values of the parameter c: -0.42 (red), 0 (green) and 0.42 (blue). (a,b,c) For each c, three distributions are compared, coming from a simulation with a power-law potential (dashed line), a simulation of the corresponding two-slopes model (+ markers) and the approximating Gaussian distribution Eq. (B.10) (solid line). In the two-slopes model, F_b and F_e are chosen such as they match the values of the force of the power law potential at the geometric switches and x_0 satisfies $x_0/v_b = (A - x_0)/v_e$. (d,e,f) shows a comparison of the FPT from power law potentials (+) with two-slopes potentials (dashed lines) and its theoretical distribution (plain lines) for which x_0 is chosen such as the deterministic period is the same in all the potentials. The distributions in (d,e,f) fit very well. However, in order to keep the calculation of $\langle Q \rangle$ simple and reduce the number of parameters, we used the two-slopes model displayed in (a,b,c). In this case, for highly negative values of c [worst case in (a)], the average value of the FPT of the power law potentials differ from the two-slopes model by 30 %. However, in the definition of $\langle Q \rangle$ in Eq. (5.5), the relevant quantity to estimate is the ratio $\langle |t_1| \rangle / \langle \tau \rangle \propto \mathrm{std}(t_1)/\langle t_1 \rangle$. Between simulations with power law potentials and with the two-slopes model, this quantity differs only by 6 % in (a), 3 % in (b) and 15 % in (c). Parameters: $a = 1.735$ μm, $\eta = 2.21$ mPa·s, $T = 296$ K, $A = 3.12$ μm, $L = 1$ μm, $\alpha = 0.37$ (red), 1 (green) and 1.63 (blue).

and

$$\left\langle \left(t_1^{(\infty)} \right)^2 \right\rangle = \frac{1}{1-\kappa^2} \left\langle \zeta^2 \right\rangle \ . \tag{B.16}$$

From here on, as an assumption, x_0 is imposed so that the two-slope potential satisfies the condition $x_0/v_b = (A - x_0)/v_e$. This means that, in the absence of coupling, a bead would spend on average an equal time in the high-gradient and low-gradient potential steps. A consequence is that the average period of oscillation becomes $2A/v_0$ and does not depend on c. Note that the choice of x_0 is arbitrary, provided that it is chosen within a "reasonable" range. Namely, that the "v_b to v_e" switch at x_0 happens far away from the geometric switches in order to satisfy first that the oscillations stay in a cycle described either as (a) or (b) in Fig. B.1, and second that the approximation of t_1 as a Gaussian random variable is valid. This choice of x_0 does not give the best two-slope estimate (see Fig. B.2), but is convenient to keep the algebra simple and obtain closed expressions.

It is also supposed that the coupling term ϵ is small, so that κ can be expanded to the first order in ϵ. Including both assumptions in the noise on $t_1^{(\infty)}$ leads to the simplified expression:

$$\rho^2 = \left\langle \left(t_1^{(\infty)} \right)^2 \right\rangle = \left(\frac{A}{v_0} \right)^2 \frac{1+c^2}{1-c^2} \frac{\xi}{8\,|c|\,\epsilon} \ . \tag{B.17}$$

The absolute value ensures that this formula is valid for both $c > 0$ and $c < 0$. Fig. B.3 shows distributions of t_1, corresponding to the simulations presented in Chapter 5. The simulations agree very well with the approximated Gaussian distribution obtained above.

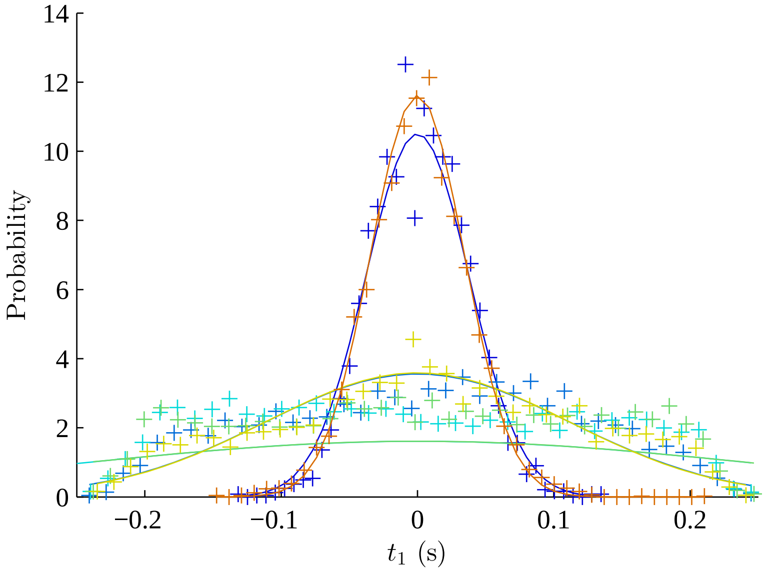

Figure B.3: Numerical distributions of the times t_1 for different values of c (0.42, 0.035, 0.0071, -0.0071, -0.035 and -0.42 from blue to orange). Even for high values of $|c|$, the distributions are in very good agreement with the analytical estimate (solid lines).

B.2.3 Probability distribution of Q

The probability distribution of the synchronization order parameter Q, given in Fig. 5.5, is estimated, within the assumption that $x_0/v_b = (A - x_0)/v_e$. From its definition in Chapter 5, the parameter Q can be expressed piece-wise for negative and positive values of c as a function of $|t_1|$:

$$Q(k) = \begin{cases} 1 - 2\dfrac{|t_1(k)|}{\tau_P(k)} & \text{if} \quad c < 0 \\ -1 + 2\dfrac{|t_1(k)|}{\tau_{AP}(k)} & \text{if} \quad c > 0 \end{cases} . \tag{B.18}$$

Here, $\tau_P(k)$ (or τ_{AP} if $c > 0$) is the duration of the half-cycle k. Its expression at the first order in ϵ is

$$\tau_P(k) = t_{1,P}(k) + t_{2,P}(k) + t_{3,P}(k) + t_{4,P}(k) \tag{B.19}$$

$$= (1 - \epsilon)\frac{A}{v_0} + 2\epsilon\left(1 + \frac{2c}{1 - c^2}\right)\left|t_1^{(k)}\right| . \tag{B.20}$$

For positive "curvatures" c, $\tau_P(k)$ has to be replaced by τ_{AP}, for which ϵ is changed to $-\epsilon$. The in-phase and antiphase periods differ slightly, so the cycle average $\langle Q\rangle$ is not identical to a time average, accounting for the offset of $\langle Q\rangle_k$ at $c = 0$ in Fig. 5.5.

In order to obtain the distribution of Q, we need the probability distribution of $t' = \left|t_1^{(\infty)}\right|$. As $t_1^{(\infty)}$ is supposed to follow a Gaussian random variable, t' has the half-normal distribution

$$\mathcal{P}_a(t) = \sqrt{\frac{2}{\pi\rho^2}} \exp\left(-\frac{t^2}{2\rho^2}\right) . \tag{B.21}$$

The probability distribution of Q_P, $\mathcal{P}_{Q_P}(q)$, is then deduced from Eqs. (B.21) and (B.18):

$$\mathcal{P}_{Q_P}(q) = \left|\frac{\mathrm{d}}{\mathrm{d}q} Q_P^{-1}(q)\right| \mathcal{P}_a\left[Q_P^{-1}(q)\right] , \tag{B.22}$$

leading to

$$\mathcal{P}_{Q_P}(q) = \mathcal{P}_a\left(\frac{A}{v_0}\,\frac{1-q}{B+K(1-q)}\right)\frac{B}{\left[B+K(1-q)\right]^2} , \tag{B.23}$$

where

$$\left\{\begin{array}{lcl} B & = & \dfrac{2}{1-\epsilon} \\ K & = & \dfrac{-2\epsilon}{1-\epsilon}\left(1+\dfrac{2c}{1-c^2}\right) \end{array}\right. . \tag{B.24}$$

$\mathcal{P}_{Q_{AP}}$ is obtained similarly and results in the same formula, but with ϵ replaced by $-\epsilon$ in the expressions of the parameters B and K. $\mathcal{P}_{Q_P}$ and $\mathcal{P}_{Q_{AP}}$ are represented in Fig. 5.5(d).

B.2.4 Order parameter $\langle Q\rangle$

As $|t_1|$ appears both in the numerator and denominator in Eq. (B.18), the exact probability distribution of Q is hard to derive. To keep the calculation simple, $\tau_P(k)$ is replaced by $\langle\tau_P\rangle + u(k)$ in Eq. (B.18) and the denominator is

Taylor-expanded, leading, for $c < 0$, to:

$$Q(k) = 1 - 2\frac{|t_1(k)|}{\langle\tau_P\rangle}\left(1 - \frac{u(k)}{\langle\tau_P\rangle} + \left[\frac{u(k)}{\langle\tau_P\rangle}\right]^2 + \ldots\right) . \tag{B.25}$$

When taking the average $\langle Q\rangle$, the first correction term is $\mathrm{var}\,[u(k)]/\langle\tau_P\rangle^2 \sim \mathrm{var}(t_1)/\langle\tau_P\rangle^2$. It is negligible when both $\epsilon \ll 1$ and $\xi\epsilon/|c| \ll 1$. At room temperature and with our experimental parameters, $\xi = 4.96 \times 10^{-3}$ and $\epsilon = 0.26$, and the correcting term can be dropped for all curvatures except in the tiny range $|c| < 10^{-3}$. This simplification leads to the expression of $\langle Q\rangle$ plotted in Fig. 5.5(a):

$$\langle Q\rangle = \begin{cases} 1 - 2\dfrac{\langle|t_1|\rangle}{\langle\tau_P\rangle} & \text{if} \quad c < 0 \\ -1 + 2\dfrac{\langle|t_1|\rangle}{\langle\tau_{AP}\rangle} & \text{if} \quad c > 0 \end{cases} \tag{B.26}$$

$$= \begin{cases} 1 - \dfrac{\alpha}{\sqrt{\epsilon}}\left[1 - \beta\sqrt{\epsilon} + (\beta^2 + 1)\,\epsilon\right] & \text{if} \quad c < 0 \\ -1 + \dfrac{\alpha}{\sqrt{\epsilon}}\left[1 + \beta\sqrt{\epsilon} + (\beta^2 - 1)\,\epsilon\right] & \text{if} \quad c > 0 \end{cases} \tag{B.27}$$

where

$$\alpha = \sqrt{\frac{\xi}{\pi|c|}\frac{1 + c^2}{1 - c^2}} \tag{B.28}$$

and

$$\beta = \left(1 + \frac{2c}{1 - c^2}\right)\alpha \ . \tag{B.29}$$

Note that $\langle Q\rangle$ diverges when c tends to 0, since α tends towards ∞. In fact, κ tends to 1 in that case, and the phase difference between the two particles becomes free. The initial assumption that the cycle could be described by Fig. B.1(a) for $c < 0$ and Fig. B.1(b) for $c > 0$ fails in that particular case. This is however happening in a small range of c for moderate noise levels.

B.3 Additional control simulations

B.3.1 Simulated two-slopes model

In the estimation of the effect of the noise on the P/AP transition, the two-slopes model required the use of the parameter x_0 which defines at what position the potential switches from F_b to F_e. It is already shown that this parameter does not affect the relaxation time $1/\kappa$, at least at small levels of noise. However, it does appear in the calculation of the half-period τ of oscillations, and therefore $\langle Q \rangle$. Fig. B.4 displays simulations of the transition by using two-slopes potentials for different values of x_0. It appears that, except for values of x_0/A close to 0 or 1, the shape of the transition is always the same. When x_0/A approaches 0 or 1, the changes in the transition can be explained as a failure to apply the approximation on the shape of the cycle: the slope breaks occur so close to the geometric switches that the cycle cannot be described as in Fig. B.1(a or b).

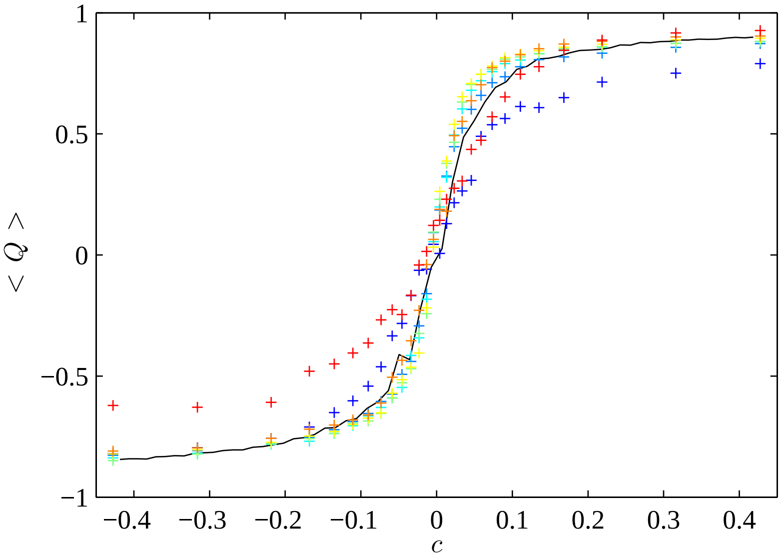

Figure B.4: $\langle Q \rangle$ transition for several values of x_0. x_0/A is 0.1, 0.25, 0.4, 0.5, 0.5, 0.6, 0.75 and 0.9 from blue to red. As a comparison, the black line is the transition from simulations obtained in Chapter 5 by using power laws. All the curves fit to the same transition except for values of x_0/A close to 0 or 1.

B.3.2 Power law potentials with different values of ς

The simulated two-slopes model shows that the information on the whole shape of the potentials is not needed to describe the synchronized state. Only the forces F_b and F_e, from which the parameters F_0 and c are deduced, are relevant to the problem. As a complementary empirical proof of this assumption, we also performed simulations with power law potentials by varying both the parameter α, controlling c, and ς, which provides a way to change the whole shape of the potential [see Eq. (5.3)]. Fig. B.5 summarizes the different transitions obtained. For each curve, ς is constant and α is varied to change the "curvature" c. Again, all the curves fit remarkably well.

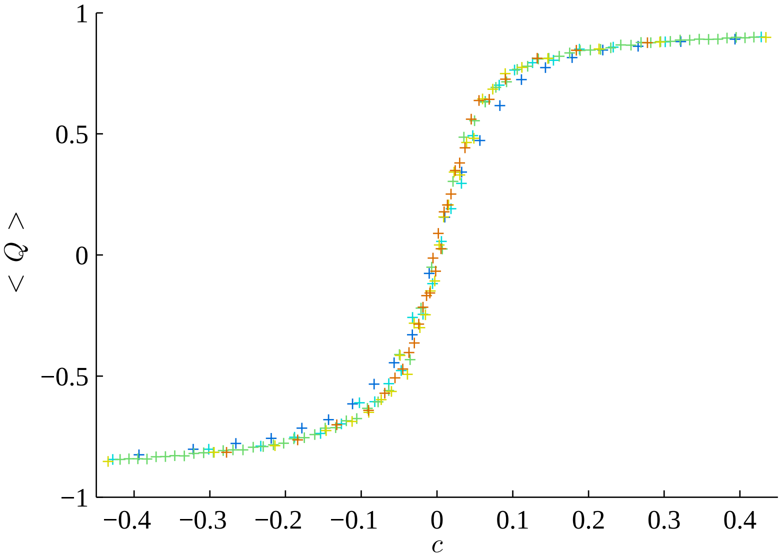

Figure B.5: $\langle Q \rangle$ transition for power-law potentials with several values of ς: A/ς is 0.94, 0.76, 0.61, 0.44 and 0.28 from blue to red. When ς is changed, λ is also modified in order to keep the amplitude constant between the different simulations. For each curve, c is changed through the parameter α and k_α is changed so that the average period of oscillations remains the same. All curves lead to the same transition.

Appendix C

Synchronization of the two flagella in *C. reinhardtii*

C.1 Introduction

This appendix describes how data of the force generated by a single flagellum of *Chlamydomonas* were used to match the model with experimental data concerning the synchronization of two flagella, and represented by the dashed line in Fig. 5.5(a) (inset). Data on the position of a flagellum and the force exerted on it by the fluid during a cycle was kindly provided by Bayly and coworkers, and is the result of experimental image analyzis from movies of an uniflagellated *Chlamydomonas* cell [64].

The aim is to describe effectively the two flagella of a *Chlamydomonas* alga as two rowers, for which the state of synchronization should be determined by the curvature of the potentials, according to Chapter 5 and Appendix B. An effective position of the flagellum and an effective driving potential need to be determined from the experimental data. In general, any attempt to reduce such a complex dynamics to a simple system is forcedly, at least to some extent, arbitrary. In this case, one main choice is how to decompose the beating motion into two one-dimensional oscillations.

When the flagella are synchronized, it is known that they beat most of the time in phase along the direction of propulsion and in antiphase along the transverse direction [57]. Two configurations of rowers are therefore considered, which define two axes used for the projection of the position and force as shown in Fig. 5.7. From the effective potentials, the expected synchronized state of the flagella (AP synchronization along the direction transverse to the swimming direction, y) is recovered. As explained in this appendix, it is believed that this axis leads to the main contribution to the synchronization. Section C.4 also presents direct simulations of the two rowers oscillating in the extracted effective potentials that confirm this argument.

C.2 Computation of an effective potential

Fig. C.1 shows processed data of the position of the flagellum and its force on the fluid. Reconstructing an effective potential acting on the flagellum requires the knowledge of the driving force field; this can be obtained from the data of position and driving force as a function of time. The position is simply given by the centre of mass of the flagellum, which is represented by the red line in Fig. C.1. For the driving force, the total force from the fluid acting on the flagellum is calculated, taking its opposite as $\mathbf{F}_{\text{tot}}$:

$$\mathbf{F}_{\text{tot}} = -\int_0^{s_0} f(s)\,\mathrm{d}\mathbf{s}\ , \tag{C.1}$$

where $f(s)\mathrm{d}\mathbf{s}$ is the force from the fluid acting on the small element of flagellum of length $\mathrm{d}\mathbf{s}$, and s_0 the total length of the flagellum. This definition of the total force excludes the force from the body of the alga acting at the base of the flagellum, and explains why $\mathbf{F}_{\text{tot}}$ is not exactly tangential to the orbit of the centre on mass in Fig. C.1.

The second step necessary to obtain data that can be used for rowers is to project the force along an axis. Synchronized states are described by a different locked phase depending on the axis of projection. As discussed above, the x (propulsion) and y (transverse) axes were chosen, as these are the well-defined directions along which synchronized flagella can be said to be experimentally in phase or in antiphase. By considering for example the x projection, two

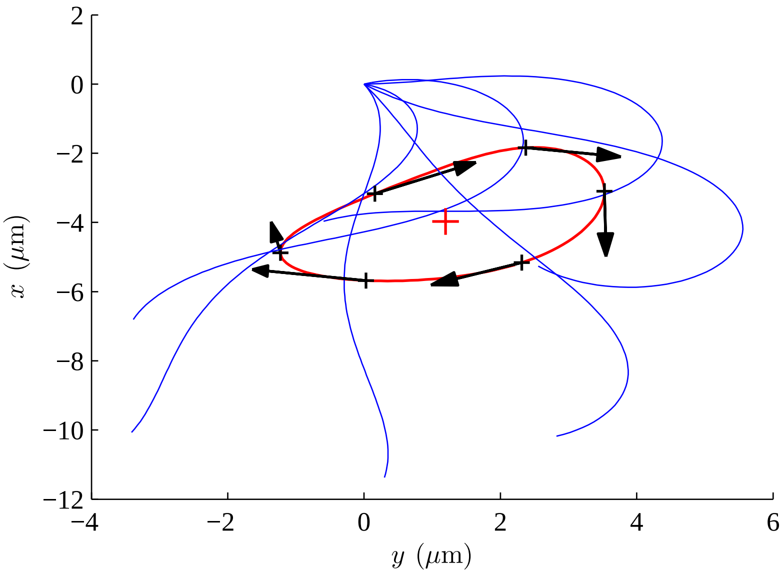

Figure C.1: Cycle of oscillation of a flagellum. In blue: flagellum at six different instants on the cycle. The motion of the centre of mass of the flagellum is represented by the red line. The opposite of the total force $\mathbf{F}_{\text{tot}}$ from the fluid on the flagellum (black arrows) is closely tangent to the motion of the centre of mass and is used to obtain the effective driving potential acting on the flagellum. The red marker is the average position of the centre of mass and is used to estimate the distance between the rowers.

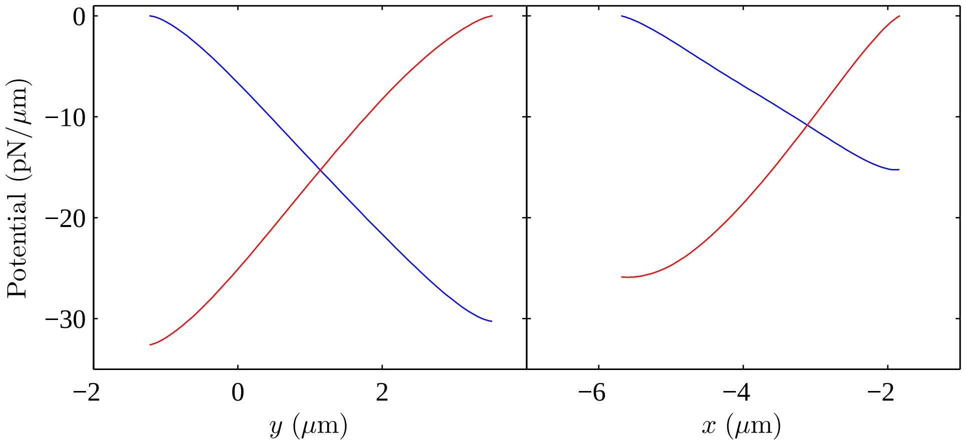

Figure C.2: Experimental effective potentials U_x^i, U_y^i (blue) and U_x^d and U_y^d (red). The highest curvature is for U_y^d and is the main contribution to the synchronization of the two flagella.

values of the force are obtained for a given x: one for increasing x positions and one for decreasing positions:

$$\begin{cases} F_x^i(x) = \mathbf{F}_{\mathrm{tot}}(x) \cdot \hat{\mathbf{e}}_x & \text{for increasing } x \\ F_x^d(x) = \mathbf{F}_{\mathrm{tot}}(x) \cdot \hat{\mathbf{e}}_x & \text{for decreasing } x \end{cases} . \tag{C.2}$$

Therefore, two different potentials $U_x^i(x)$ and $U_x^d(x)$ for the motion along the x axis are obtained. The same analyzis can be carried along the y direction. The effective potentials are represented in Fig. C.2.

C.3 Synchronized state

The highest curvature appears in U_y^d. Furthermore, the coupling coefficient ϵ is $3a/(2d)$ in the configuration of rowers oscillating along y while it is only $3a/(4d)$ along x. Therefore, the model predicts that the main contribution to the synchronization of the two flagella comes from the oscillations along the y axis. Along this direction, U_y^d has a positive curvature while U_y^i has a small, negligible curvature. The model predicts synchronization in antiphase in this direction, in agreement with experimental observations.

C.4 Simulations of two rowers under effective potentials

As a control, the effective potentials of the previous section were used as an input to the Brownian dynamics simulations of two rowers. The distance between the two rowers can be estimated by knowing (a) the average position of one of the flagellum in the data of Fig. C.1 and (b) the distance between the bases of the two flagella of a *Chlamydomonas* alga. This distance has been estimated to 3 μm from the first snapshot of Fig. 2 in [82]. The (a) and (b) contributions lead to an average distance of 11 μm between the two rowers that model the flagella. The parameters in the simulations are $d = 10$ μm and $\eta = 1$ mPa·s. The switching positions are set to the extremes of the range of definition of the potentials in Fig. C.2. Beyond this range of positions (i.e. overshooting the switch as can happen in the presence of noise), the driving forces are set to the value of the nearest position where the potential is defined in Fig. C.2. The radius of the spherical rowers has been chosen so that the frequency of the simulated oscillations matches the experimental beat frequency of the flagellum. The radius is found to be the same for oscillations along x or y ($a = 0.45$ μm). This radius is in agreement with the resistive coefficient C_N in [64], the viscous friction coefficient $6\pi\eta a$ is equal (within 15 %) to the friction coefficient $4\pi\eta L/[\ln(2q/r) + 0.5]$ with the notations and numerical values from [64]. Fig. C.3 summarizes the results of the simulations, and confirms the results given in Section C.4.

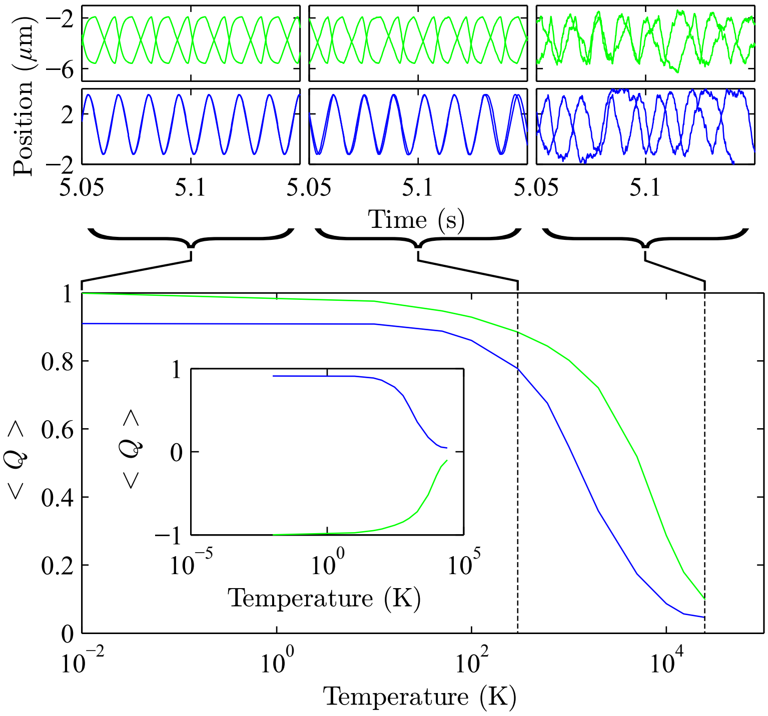

Figure C.3: Synchronization of two rowers under the effective potentials along the x (blue) and y (green). Oscillations are represented for three different temperatures. The inset shows that at low temperature, the system is synchronized in phase along x and in antiphase along y, in agreement with experimental observations on *Chlamydomonas*. However, the main graph shows that for middle range temperatures (including room temperature), synchronization is stronger along the y direction.

C.5 Where is *C. reinhardtii* on the noise/curvature phase diagram?

The position of *Chlamydomonas* in the phase diagram in Fig. 5.5(a) can now be estimated. The phase diagram is drawn for oscillations that are symmetric for decreasing and increasing positions. In the case of *Chlamydomonas*, for the data projected along y, only one of the two potentials is curved. During a cycle of oscillation, only one half of it will contribute to synchronization. However, thermal fluctuations are still present in both halves of the cycle. Therefore, in the non-symmetric system, the noise parameter ξ is estimated by

$$\xi = 2k_BT/(AF') \ , \tag{C.3}$$

where $F' = \gamma A/T_0$, with T_0 the period of oscillation, which leads approximately to a factor two compared to the definition in Chapter 5. This definition avoids using F_b and F_e (through F_0) that are not the same for increasing and decreasing positions in the non-symmetric system. By this mean, ξ is estimated to 1×10^{-3} for the *Chlamydomonas* data.

The curvature c is harder to estimate, since the projection of the force along the orbit naturally gives forces that approach 0 rather smoothly at the assumed geometric switches[1]. In an attempt to obtain a value, the oscillation of a single rower was fitted at 0 K in the U_i^d potential with two slopes, with the slope break at a position such as $x_0/v_b = (A - x_0)/v_e$ with the notations of Section B.2.2. This leads to the estimate $c \approx 0.75$.

---

[1] Exactly null forces would be found at the switches if the force field was exactly tangential to the orbit.

Appendix D

Investigation of the discrepancy in strength of synchronization between the two-rotors experiments and simulations

This appendix describes in detail the different checks done on the data in the synchronization experiment of two rotors (Chapter 8), and provides possible explanations of the lower strength of synchronization observed in the experiments.

D.1 Calibration of the force profile

The first rotors experiments were using force profiles created by setting the separation between the bead and the trap ϵ proportional to the desired force profile $F(\phi)$. The trapping force along the direction of driving is however slightly anharmonic. Hence, calibrated force profiles were used as described in Section 8.2, resulting in refined profiles shown in Fig. 8.2 that are very close to the expected sinusoidal profiles.

D.2 Measure of the radial stiffness

D.2.1 Trapping in the radial direction

In the radial direction, the driving trap of a rotor is made of a line of 21 harmonic traps (with same intensity) that are scanned at 20 kHz. In the case of two rotors, the 21 traps of the first rotor are scanned, then the 21 traps of the other, etc. The separation between two traps is set between 0 and 0.2 μm in order to tune the radial trapping constant k_r. The size of the line segment is therefore varied between 0 and 4.4 μm. The trapping in the radial direction is not strictly harmonic over a wide range, but can be approximated by a harmonic trap for small fluctuations of the radius (see Section D.2.2).

D.2.2 Measure of the radial stiffness

The radial stiffness is measured for 50 different angles ϕ on a single-rotor movie. For each angle, it is defined as

$$k_r(\phi) = \frac{k_B T}{\mathrm{var}\left[r(\phi)\right]} \ , \tag{D.1}$$

with $\mathrm{var}\left[r(\phi)\right]$ the variance of the radius for the given angle ϕ. The radial stiffness inputted in the theoretical formula is the average of $k_r(\phi)$ over all angles. The radial stiffness cannot be measured by taking the standard deviation of the radial fluctuations at all angles, because the radius of the trajectory is not perfectly constant (about 0.2 μm standard deviation, which is bigger than the standard deviation due to thermal fluctuations).

Fig. D.1 shows distributions of r for four different angles. First, all these distributions look like Gaussians, so that the trap can be described by a harmonic potential in the range of thermal fluctuations. Second, although the average value varies with the angle, the standard deviation remains fairly constant, at least for small A_2. This is also shown for more angles in the plot of $k_r(\phi)$ (Fig. D.2).

k_r is measured by looking at the thermal fluctuations along the radial direction. The displacements are of the order of

$$\delta r^{\text{therm}} \sim \sqrt{\frac{k_B T}{k_r}} \; . \tag{D.2}$$

However, in the 2-rotors experiment, the fluctuations of the radial position of a particle due to the interaction with the other particle has a magnitude

$$\delta r^{\text{coupl}} \sim \frac{a}{d} \times \frac{6\pi\eta a v}{k_r} \; , \tag{D.3}$$

where v is the typical tangential velocity of the oscillators. With usual values of the parameters, $\delta r^{\text{therm}} \sim 0.04\ \mu$m and $\delta r^{\text{coupl}} \sim 0.1\ \mu$m. Therefore, thermal fluctuations do not probe a range of positions wide enough to claim that the potential is harmonic. However, measures of the anharmonicity of the potential of a single trap far from the centre showed that at a distance of 1 μm from the centre, the measured trapping force only differs by 30 % compared to the value calculated by using the trap constant k_r measured from thermal fluctuations. Therefore, it is likely to be correct to approximate the radial potential as harmonic in the relevant range δr^{coupl} of fluctuations of the radial position.

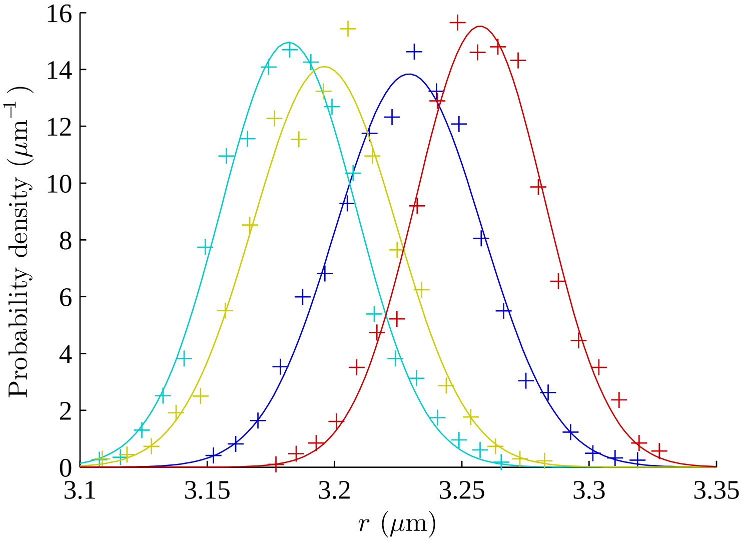

Figure D.1: Distribution of the radial position of a single rotor for four different angles ϕ: 0 (blue), $\pi/2$ (cyan), π (yellow) and $3\pi/2$ (red). The Gaussian fits (lines) match the experimental data (+) very well. The fitting parameters give values of k_r in agreement with the method used in Chapter 8, in which the standard deviation of the radius was simply measured.

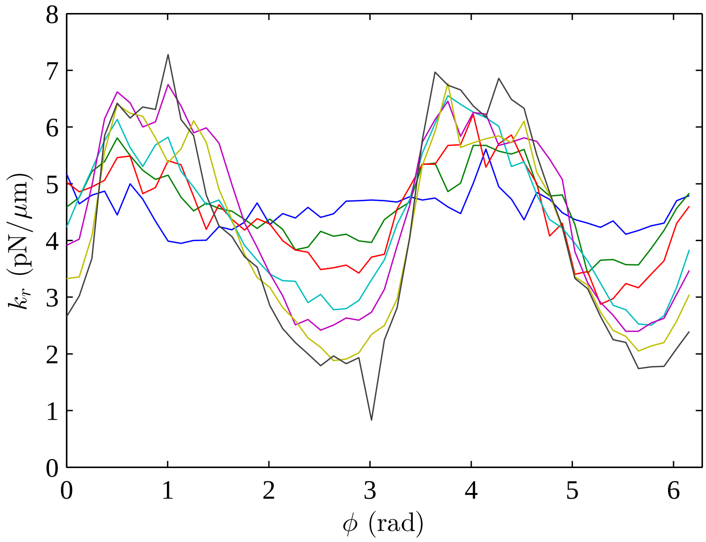

Figure D.2: Radial stiffness, measured as a function of the angle for a single rotor for different values of A_2. A_2 is changed as indicated in Fig. 8.2. For small A_2, the radial stiffness is fairly flat.

D.3 Detuning between the two oscillators

Since the coupling between the two rotors is quite small [$3a/(4d) < 0.1$, see Section D.8], the system is not strongly synchronized and the relaxation time is highly sensitive to a detuning in the intrinsic periods of each oscillator. The system is corrected for possible detunings by slightly increasing or decreasing the average (over all angles) of the bead-to-trap distance ϵ of one of the oscillators. Since the synchronized state is expected to be in-phase, the detuning is adjusted such that the mean phase difference $\langle \Delta\phi \rangle$ between the two rotors is close to 0. Experimentally, the system was considered as not detuned when $\langle \Delta\phi \rangle$ was in the $[-0.1, 0.1]$ rad range.

Figures D.3 and D.4 show an experiment and the corresponding simulation, realized in Cambridge, in which detuning was deliberately introduced.

To remain synchronized in presence of detuning, the system adjusts its phase difference (Fig. D.3), similarly to the experiment of a rower in an oscillating coupling signal (Chapter 4). A mean phase difference of 0 should correspond to no detuning. The mean phase difference appears to move in a wider range in the experiments than in the simulations, for a given range of detuning.

Fig. D.4 shows that the detuning has a strong effect on the relaxation time. The experimental and simulated (Cambridge) curves have a similar shape, but experiments are shifted towards a higher relaxation time. But there is also the possibility that the detuning is fluctuating over the duration (10 min) of an experiment. While the mean phase difference can still be set to zero, it only makes the average detuning equal to zero. Fluctuations of the detuning lead to less synchronization, and simulations in Fig. D.4 suggest that it can account for a big part of the discrepancy.

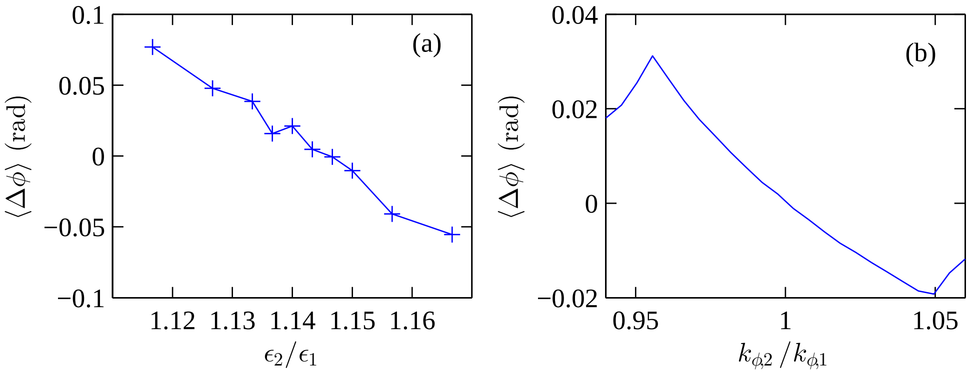

Figure D.3: Experiment (a) and simulation (b): Mean phase difference between the two oscillators depending on the detuning. In the experiments, detuning is controlled by changing the bead-to-trap distance ϵ_2 of the second oscillator, while in the simulation, the tangential trap stiffness $k_{\phi,2}$ is changed. In the experiments, the system is not detuned (in average) when ϵ_2/ϵ_1 is about 1.14.

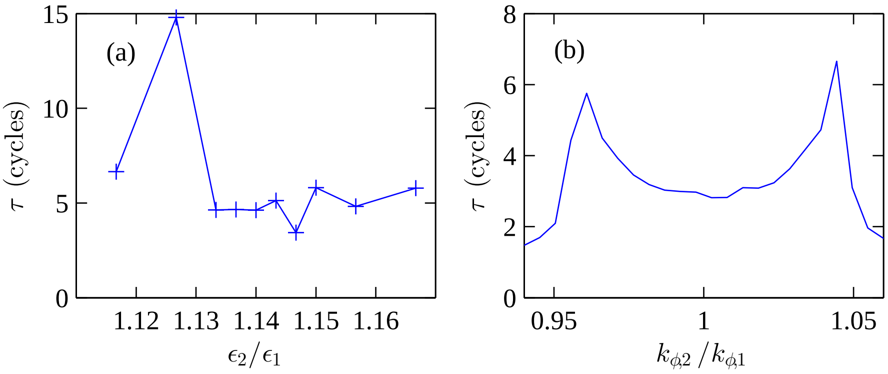

Figure D.4: Experiment (a) and simulation (b): Relaxation time depending on the detuning as explained in Fig. D.3. One experimental point seems to be anomalous. Note that the range of detuning explored in the experiments is smaller than the one in the simulations. In the simulations, the sharp decrease in τ at extreme detuning corresponds to a loss of synchronization. The expected relaxation time in the absence of detuning is about 3 cycles.

D.4 Feedback time: sampling and delay

In the setup, the computer analyzes frames at a rate of 229 frames per second (fps), and updates the position of the traps lines at the same frequency. The feedback loop involves the time corresponding to this sampling frequency, but also any delay in the transmission of the images to the computer, and from the computer to the laser beam steering electronics (see Section 3.2.6). The total delay between the time at which a picture of the beads is taken and the time at which the traps are moved is 6.5 ± 0.1 ms (measurement on a single 1 min long movie).

This overall feedback time has an effect on the synchronization strength. The main time interval (i.e. the largest delay) occurs when the computer decides to move a trap: a command is sent to the AODs, but this is carried through the USB port which can have a latency time of up to 10 ms (see Fig. 3.4). It is under control of the operating system, and is difficult to reduce even in the Linux system patched for real-time operation. Once the command has been transmitted, the traps are moved essentially instantaneously by the electronics controlling the AODs.

The effect of the sampling time (corresponding to the feedback frequency) is explored first. The experiment in Fig. D.5 shows that increasing the sampling frequency from 200 fps to higher values does not change significantly the strength of synchronization. Simulations also supports this conclusion.

In a second set of simulations, the sampling is chosen extremely fast, but included a delay in the motion of the traps. This delay appears to have a large effect on the strength of synchronization (Figures D.6 and D.7). Even small delays of about 1/100 of a cycle increase dramatically the relaxation time, and moves it towards the experimental points. However, a delay of the order of the one measured in the experiments (~ 6.5 ms) is not sufficient to explain by itself the shift between experimental and simulated curves.

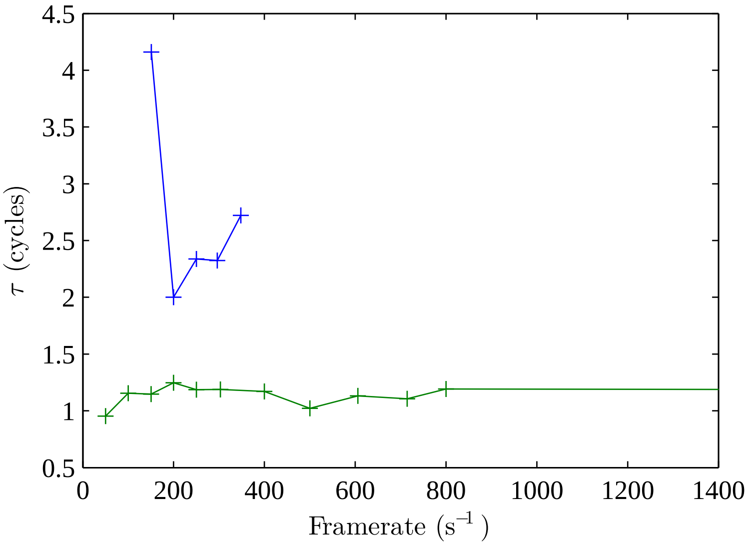

Figure D.5: Strength of synchronization depending on the sampling (feedback) frequency. Experiments in blue and simulations (Cambridge) in green. From this analyzis, looking at both experiments and simulations, it was concluded that a sampling frequency greater than 200 fps was adequate.

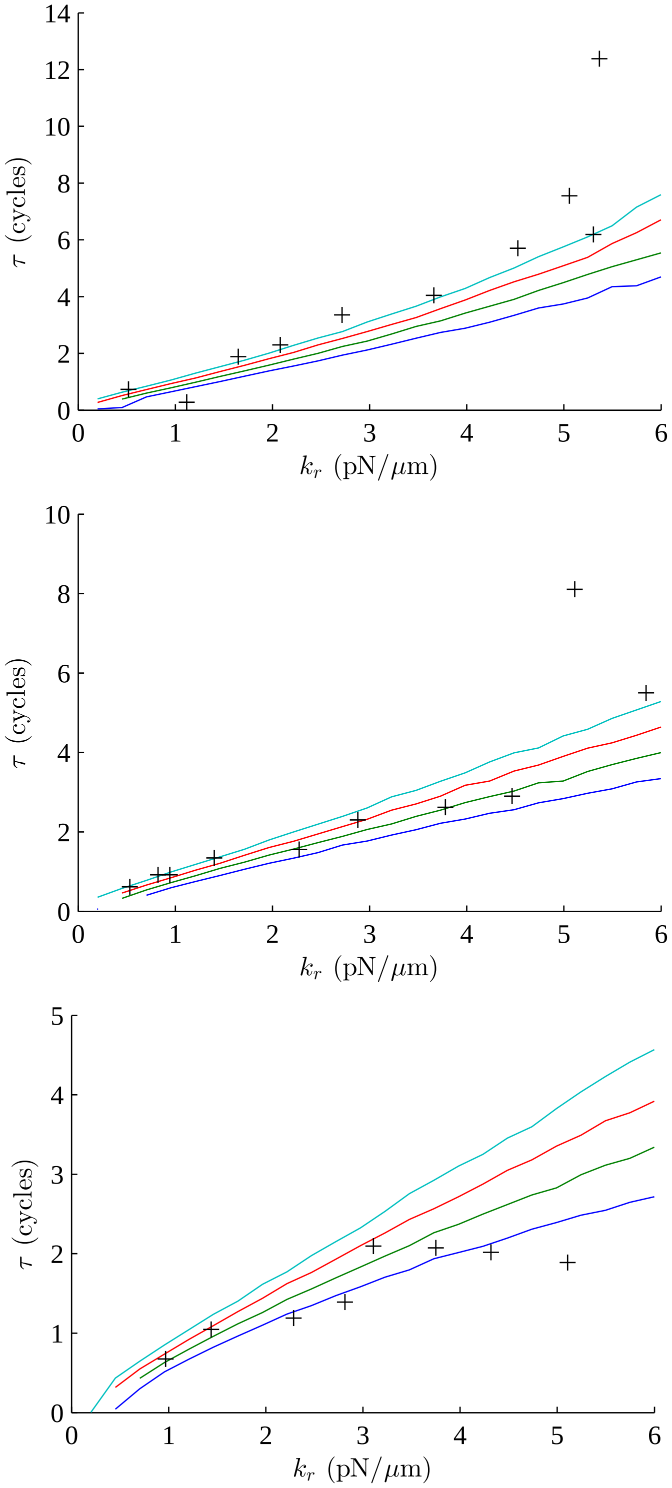

Figure D.6: Strength of synchronization in experiments and simulations. The parameter k_r is varied for several values of A_2: 0, 0.4 and 0.7 (from top to bottom). Markers are experimental points and the solid lines are simulations with a delay of 5, 10, 15 and 20 ms (from blue to cyan).

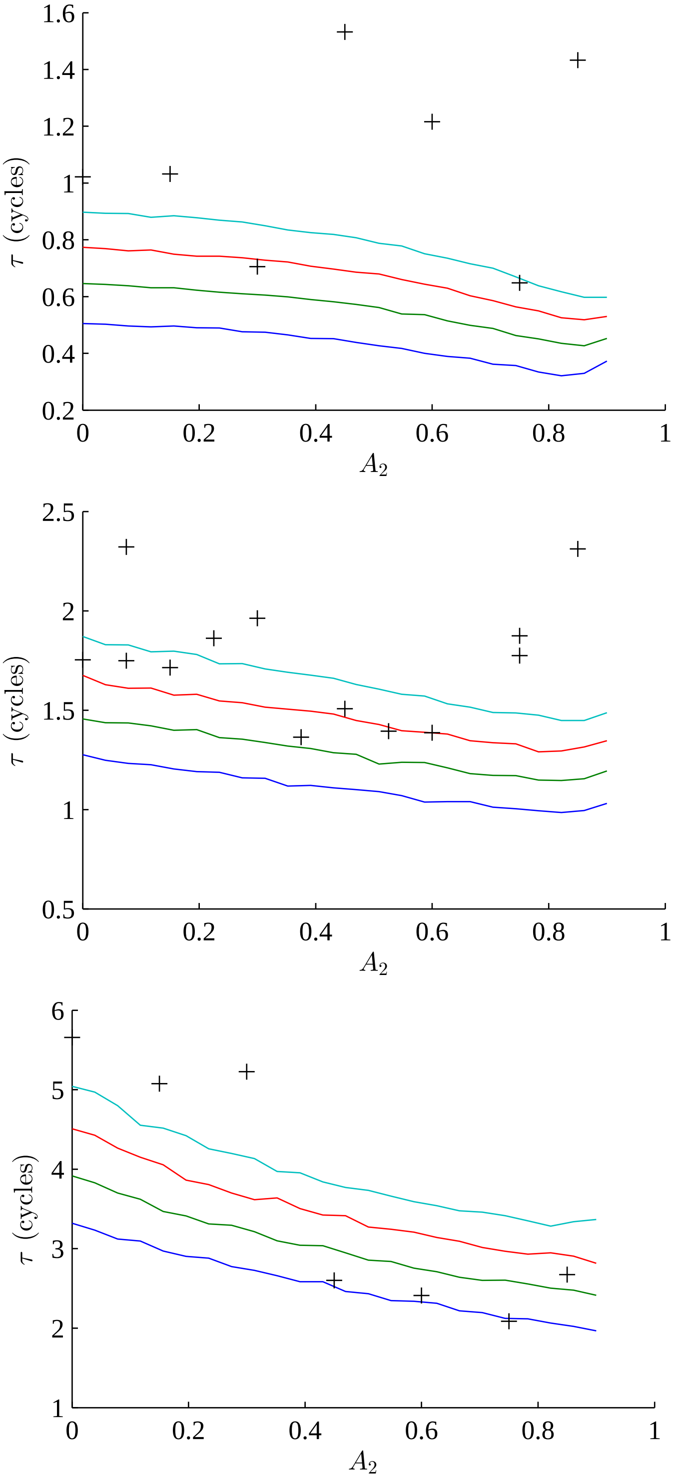

Figure D.7: Strength of synchronization in experiments and simulations. The parameter A_2 is varied for several values of k_r: 0.762, 1.814 and 4.480 pN/μm (from top to bottom). Markers are experimental points and the solid lines are simulations with a delay of 5, 10, 15 and 20 ms (from blue to cyan).

D.5 Freedom along rotational axes

In the simulations and theory, the model for hydrodynamic interactions assumes point-like particles and a coupling described by a 2d Oseen tensor in the (x, y) plane. In the experiments, it might be possible that the particles rotate. However, if it is assumed that the tweezers are only applying translational forces, this does not induce any rotation of the particles up to $\mathcal{O}\left[(a/d)^6\right]$ [19].

D.6 Relaxation time of the trap along the radial direction

There is a relaxation time $6\pi\eta a/k_r$ linked to the radial stiffness. If this relaxation time is longer or of the same magnitude as the period of oscillation of a rotor, it could play a role in the state of synchronization. By using usual values for all the parameters, a “radial” relaxation time of 0.04 cycles is found, well below the period of the oscillators.

D.7 Viscosity and local heating

The laser beam of the tweezers delivers a few hundreds of milliwatts after the objective. When entering the sample, the beam heats the fluid. This can create convection and affect the local viscosity.

Viscosity is chosen by preparing water/glycerol solutions. Solutions of 49.6 % in mass glycerol are made, which corresponds to an expected viscosity of 6 mPa·s at 25 °C. The viscosity is measured by looking at the autocorrelation of the position of a particle in a static harmonic trap and $\eta = 5.5$ mPa·s was found (average over x and y and over several trapping constants; points are spread with a ~ 0.3 mPa·s standard deviation).

The measured value is slightly lower than the expected value. This could be due to heating of the fluid from the laser beam (about 5 °C, measured using the ratio of two fluorescent dyes), or to the uncertainty in the beads' radii (10 % according to manufacturer).

D.8 Wall interaction

The sample is made of a (very) dilute colloids solution sealed between a microscope slide and a cover slip (see Section 3.2.1). The film of fluid between the slides is about 150 μm thick. The two rotors are created at a height of 50 μm from the coverslip. Wall effects are not included in the simulations and the theory used in this thesis, and they could explain the difference observed in the experiments.

The hydrodynamic coupling term is estimated by calculating the x, x and y, y components of the mobility matrix by using different tensors. Coupling is defined by

$$c^{\alpha,\beta} = \frac{\boldsymbol{\mu}_{1,1}^{\alpha,\beta}}{\boldsymbol{\mu}_{1,2}^{\alpha,\beta}} \tag{D.4}$$

with $\alpha, \beta \in \{`x', `y'\}$.

To estimate the coupling in the presence of the wall, the Blake tensor corrected for finite-sized particles is used (see Section 1.8, and more particularly 1.8.2). In the geometry here, the coupling depends on the distance between the beads d, the distance h between the oscillators and the wall, and the size of the particles a. This geometry reduces the components of the Blake mobility matrix to:

$$\begin{aligned}\boldsymbol{\mu}_{1,2}^{x,x} = \frac{1}{12\pi\eta d^3\bar{r}^9}\Big[&- 4a^4d^3\left(d^4 - 27d^2h^2 + 16h^4\right) \\ &- 3d^3\bar{r}^4\left(d^4 + 4h^2d^2 + 12h^4\right) \\ &+ 3d^2\bar{r}^5\left(d^4 + 8h^2d^2 + 16h^4\right) \\ &- 2a^2d^3\bar{r}^2\left(-d^4 + 22d^2h^2 - 16h^2\right) \\ &- 8a^2\bar{r}^3h^2\left(3d^4 + 12d^2h^2 + 16h^4\right)\Big] ,\end{aligned} \tag{D.5}$$

$$\boldsymbol{\mu}_{1,2}^{y,y} = \frac{1}{24\pi\eta d^3 \bar{r}^7} \Big[3\bar{r}^4 d^2 \left(-d^3 - 6dh^2 + \bar{r}^3\right) + 2a^2\bar{r}^2 \left(-d^5 + 8d^3h^2 + d^4\bar{r} + 8d^2h^2\bar{r} + 16h^4\bar{r}\right) + 2a^4d^3\left(d^2 - 16h^2\right) \Big] \tag{D.6}$$

and

$$\boldsymbol{\mu}_{1,1}^{x,x} = \boldsymbol{\mu}_{1,1}^{y,y} = \frac{1}{6\pi\eta a} \left[1 - \frac{9}{16}\frac{a}{h} + \frac{1}{8}\left(\frac{a}{h}\right)^3 - \frac{1}{16}\left(\frac{a}{h}\right)^5 \right] , \tag{D.7}$$

where

$$\bar{r} = \sqrt{d^2 + (2h)^2} \; . \tag{D.8}$$

The couplings from the Oseen and Blake tensors were plotted with the parameters of the rotors experiment in Fig. 1.3 in Chapter 1 for various heights. At $h = 50$ μm, the wall reduces the coupling by 15 % in the x, x direction and 30 % in the y, y direction, hence increasing the relaxation time.

D.9 Asymmetries in the setup

The experimental setup might introduce some asymmetries not included in the simulations. Especially, aberrations of the laser beam and calibration of the centre of a trap relative to the video image distort the expected force profile. Therefore, the force profile (see Section D.1) is calibrated from experimental data. However, other variables could suffer from asymmetries and change the strength of synchronization.

Fig. D.8 shows experiments with the same parameters, except that the orientation of the rotors relative to the rest of the setup is varied. The angle of the line between the centres of the two oscillators is changed between 0 and 90°. The force profiles and the radial stiffness (not shown here) remain constants and the relaxation time fluctuates slightly, but is still much higher than expected for all angles.

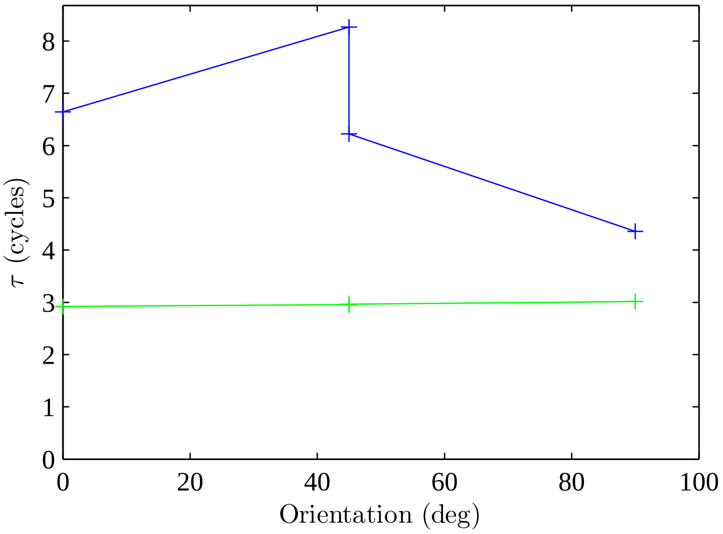

Figure D.8: Relaxation time of the phase difference in a two rotors experiments. Experiments in blue, theory in green. The orientation of the system is varied by changing the angle between 0 and 90°. It can be interesting to appreciate how optical trap potentials are not "perfectly" rotationally symmetric, but nothing here indicates that this imperfection has any relation to the weaker than expected synchronization.

D.10 Conclusion on the discrepancy in strengths of synchronization

From all these checks, it emerges that several points can lead to significantly longer relaxation times in the experiments. The three most significant are:

- The experimental delay between the decision to move a trap and the actual change of the trap position,
- The wall interactions that tend to reduce the hydrodynamic coupling,
- The experimental detuning between the intrinsic periods of the two oscillators.

Each of these three are possible reasons behind the increase of the relaxation time in experiments compared to theory; each one is estimated to account for a factor smaller, but of the order of, the discrepancy that is observed. It is therefore very likely that a combination of these factors is present, leading to the overall weaker synchronization in the experiments compared to the simulations and theory. Fitting the experiments with numerical simulations would require to include several new parameters in the system, with some of them not being known with good accuracy in the experiments. Therefore, I did not attempt to fit data with simulations including corrections.

Bibliography

[1] D. P. Mckenzie, J. M. Roberts, and N. O. Weiss, "Convection in the earth's mantle: towards a numerical simulation", *J. Fluid Mech.*, vol. 62, pp. 465–538, 1974.

[2] D. A. Yuen and G. Schubert, "Mantle Plumes: A Boundary Layer Approach for Newtonian and Non-Newtonian Temperature-Dependent Rheologies", *J. Geophys. Res.*, vol. 81, pp. 2499–2510, 1976.

[3] E. M. Purcell, "Life at low Reynolds number", *Am. J. Phys.*, vol. 45, pp. 3–11, 1977.

[4] M. J. McHenry, E. Azizi, and J. A. Strother, "The hydrodynamics of locomotion at intermediate Reynolds numbers: undulatory swimming in ascidian larvae (*Botrylloides sp.*)", *J. Exp. Biol.*, vol. 206, pp. 327–343, 2003.

[5] J. K. G. Dhont, "An Introduction to Dynamics of Colloids", Elsevier Science, 1996.

[6] E. Lauga, M. Brenner, and H. Stone, "Handbook of Experimental Fluid Dynamics", chap. 19, pp. 1219–1240, Springer, New York, 2007.

[7] Y. Zhu and S. Granick, "Limits of the Hydrodynamic No-Slip Boundary Condition", *Phys. Rev. Lett.*, vol. 88, p. 106102, 2002.

[8] J. Happel and H. Brenner, "Low Reynolds Number Hydrodynamics: with special applications to particulate media", Kluwer, 1983.

[9] G. Taylor, "Analysis of the Swimming of Microscopic Organisms", *Proc. R. Soc. A*, vol. 209, pp. 447–461, 1951.

[10] E. Lauga, “Life around the scallop theorem”, *Soft Matter*, vol. 7, pp. 3060–3065, 2011.

[11] G. Subramanian and P. R. Nott, “The Fluid Dynamics of Swimming Microorganisms and Cells”, *J. Ind. Inst. Sci.*, vol. 91, pp. 283–313, 2011.

[12] T. Faber, “Fluid dynamics for physicists”, Cambridge University Press, 1995.

[13] A. T. Chwang and T. Y.-T. Wu, “Hydromechanics of low-Reynolds-number flow. Part 2. Singularity method for Stokes flows”, *J. Fluid Mech.*, vol. 67, pp. 787–815, 1975.

[14] M. Doi and S. F. Edwards, “The Theory of Polymer Dynamics”, Oxford University Press, USA, 1986.

[15] G. J. Hancock, “The Self-Propulsion of Microscopic Organisms through Liquids”, *Proc. R. Soc. A*, vol. 217, pp. 96–121, 1953.

[16] M. Kim and T. R. Powers, “Hydrodynamic interactions between rotating helices”, *Phys. Rev. E*, vol. 69, p. 061910, 2004.

[17] M. Reichert and H. Stark, “Synchronization of rotating helices by hydrodynamic interactions”, *Eur. Phys. J. E*, vol. 17, pp. 493–500, 2005.

[18] R. Golestanian, J. M. Yeomans, and N. Uchida, “Hydrodynamic synchronization at low Reynolds number”, *Soft Matter*, vol. 7, pp. 3074–3082, 2011.

[19] M. Reichert, “Hydrodynamic Interactions in Colloidal and Biological Systems”, Ph.D. thesis, Universität Konstanz, 2006.

[20] G. Perkins and R. Jones, “Hydrodynamic interaction of a spherical particle with a planar boundary: II. Hard wall”, *Physica A*, vol. 189, pp. 447–477, 1992.

[21] M. Vilfan, A. Potonik, B. Kavi, N. Osterman, I. Poberaj, A. Vilfan, and D. Babi, “Self-assembled artificial cilia”, *Proc. Natl. Acad. Sci. USA*, vol. 107, pp. 1844–1847, 2010.

[22] J. R. Blake, "A note on the image system for a stokeslet in a no-slip boundary", *Math. Proc. Camb. Phil. Soc.*, vol. 70, pp. 303–310, 1971.

[23] C. Pozrikidis, "Introduction to Theoretical and Computational Fluid Dynamics", Oxford University Press, USA, 1996.

[24] G. Bossis, A. Meunier, and J. D. Sherwood, "Stokesian dynamics simulations of particle trajectories near a plane", *Phys. Fluids A*, vol. 3, pp. 1853–1858, 1991.

[25] E. Gauger, M. Downton, and H. Stark, "Fluid transport at low Reynolds number with magnetically actuated artificial cilia", *Eur. Phys. J. E*, vol. 28, pp. 231–242, 2009.

[26] P. Cicuta, "Experimental and Theoretical Physics part II, Soft Condensed Matter", 2011.

[27] T. Franosch, M. Grimm, M. Belushkin, F. M. Mor, G. Foffi, L. Forro, and S. Jeney, "Resonances arising from hydrodynamic memory in Brownian motion", *Nature*, vol. 478, pp. 85–88, 2011.

[28] U. F. Keyser, "Statistical physics: Self-aware particles", *Nature*, vol. 478, pp. 45–46, 2011.

[29] J.-C. Meiners and S. R. Quake, "Direct Measurement of Hydrodynamic Cross Correlations between Two Particles in an External Potential", *Phys. Rev. Lett.*, vol. 82, pp. 2211+, 1999.

[30] G. M. Cicuta, J. Kotar, A. T. Brown, J.-H. Noh, and P. Cicuta, "Hydrodynamic coupling in polygonal arrays of colloids: Experimental and analytical results", *Phys. Rev. E*, vol. 81, p. 051403, 2010.

[31] M. Reichert and H. Stark, "Hydrodynamic coupling of two rotating spheres trapped in harmonic potentials", *Phys. Rev. E*, vol. 69, p. 031407, 2004.

[32] B. W. Bisgrove and H. J. Yost, "The roles of cilia in developmental disorders and disease", *Development*, vol. 133, pp. 4131–4143, 2006.

[33] N. Sharma, N. F. Berbari, and B. K. Yoder, “Chapter 13 Ciliary Dysfunction in Developmental Abnormalities and Diseases”, in “Ciliary Function in Mammalian Development,” Academic Press, 2008.

[34] N. Sharma, N. Berbari, and B. Yoder, “Ciliary dysfunction in developmental abnormalities and diseases”, *Curr. Top. Dev. Biol.*, vol. 85, pp. 371–427, 2008.

[35] F. Qiu, L. Zhang, S. Tottori, K. Marquardt, K. Krawczyk, A. Franco-Obregón, and B. J. Nelson, “Bio-inspired microrobots”, *Materials Today*, vol. 15, pp. 463+, 2012.

[36] D. Bray, “Cell Movements: From Molecules to Motility”, Garland Science, 2000.

[37] D. Tam and A. E. Hosoi, “Optimal feeding and swimming gaits of biflagellated organisms”, *Proc. Natl. Acad. Sci. USA*, 2011.

[38] E. Govorunova and O. Sineshchekov, “Chemotaxis in the Green Flagellate Alga Chlamydomonas”, *Biochem. (Moscow)*, vol. 70, pp. 717–725, 2005.

[39] H. C. Berg and D. A. Brown, “Chemotaxis in Escherichia coli analysed by three-dimensional tracking”, *Nature*, vol. 239, pp. 500–504, 1972.

[40] H. Berg, “Chemotaxis in Bacteria”, *Annu. Rev. Biophys. Bioeng.*, vol. 4, pp. 119–136, 1975.

[41] S. H. Larsen, R. W. Reader, E. N. Kort, W.-W. Tso, and J. Adler, “Change in direction of flagellar rotation is the basis of the chemotactic response in *Escherichia coli*”, *Nature*, vol. 249, pp. 74–77, 1974.

[42] N. Liron and F. Meyer, “Fluid transport in a thick layer above an active ciliated surface”, *Biophys. J.*, vol. 30, pp. 463–472, 1980.

[43] L. Gheber and Z. Priel, “Metachronal activity of cultured mucociliary epithelium under normal and stimulated conditions”, *Cell Motil. Cytoskeleton*, vol. 28, pp. 333–345, 1994.

[44] J. J. Breunig, J. I. Arellano, and P. Rakic, “Cilia in the brain: going with the flow”, *Nat. Neurosci.*, vol. 13, pp. 654–655, 2010.

[45] R. Lyons, E. Saridogan, and O. Djahanbakhch, “The reproductive significance of human Fallopian tube cilia”, *Hum. Reprod. Update*, vol. 12, pp. 363–372, 2006.

[46] J. J. Essner, K. J. Vogan, M. K. Wagner, C. J. Tabin, H. J. Yost, and M. Brueckner, “Left-right development: Conserved function for embryonic nodal cilia”, *Nature*, vol. 418, pp. 37–38, 2002.

[47] J. McGrath and M. Brueckner, “Cilia are at the heart of vertebrate left-right asymmetry”, *Curr. Opin. Genet. Dev.*, vol. 13, pp. 385–392, 2003.

[48] J. H. E. Cartwright, O. Piro, and I. Tuval, “Fluid-dynamical basis of the embryonic development of left-right asymmetry in vertebrates”, *Proc. Natl. Acad. Sci. USA*, vol. 101, pp. 7234–7239, 2004.

[49] I. R. Gibbons, “Cilia and flagella of eukaryotes”, *J. Cell Biol.*, vol. 91, pp. 107s–124s, 1981.

[50] A. Ashkin, J. M. Dziedzic, J. E. Bjorkholm, and S. Chu, “Observation of a single-beam gradient force optical trap for dielectric particles”, *Opt. Lett.*, vol. 11, pp. 288–290, 1986.

[51] D. G. Grier, “Optical tweezers in colloid and interface science”, *Curr. Opin. Colloid Interface Sci.*, vol. 2, pp. 264–270, 1997.

[52] K. Dholakia and P. Reece, “Optical micromanipulation takes hold”, *Nano Today*, vol. 1, pp. 18–27, 2006.

[53] P. Satir and S. T. Christensen, “Overview of Structure and Function of Mammalian Cilia”, *Annu. Rev. Physiol.*, vol. 69, pp. 377–400, 2007.

[54] L. Vincensini, T. Blisnick, and P. Bastin, “1001 model organisms to study cilia and flagella”, *Biol. Cell*, vol. 103, pp. 109–130, 2011.

[55] N. Osterman and A. Vilfan, “Finding the ciliary beating pattern with optimal efficiency”, *Proc. Natl. Acad. Sci. USA*, vol. 108, pp. 15727–15732, 2011.

[56] C. Eloy and E. Lauga, “Kinematics of the Most Efficient Cilium”, *Phys. Rev. Lett.*, vol. 109, p. 038101, 2012.

[57] R. E. Goldstein, M. Polin, and I. Tuval, "Noise and Synchronization in Pairs of Beating Eukaryotic Flagella", *Phys. Rev. Lett.*, vol. 103, p. 168103, 2009.

[58] A. J. Cann, `http://www.flickr.com/photos/ajc1/8498002874/`, Retrieved on 26/07/2013. Licence: Creative Commons BY-SA 2.0.

[59] L. Howard, `http://commons.wikimedia.org/wiki/File:Bronchiolar_epithelium_4_-_SEM.jpg`, Retrieved on 26/07/2013. Licence: Public domain.

[60] B. Kachar, `https://en.wikipedia.org/wiki/File:Stereocilia_of_frog_inner_ear.01.jpg`, Retrieved on 26/07/2013. Licence: Public domain.

[61] G. J. Pazour and G. B. Witman, "The vertebrate primary cilium is a sensory organelle", *Curr. Opin. Cell Biol.*, vol. 15, pp. 105–110, 2003.

[62] C. Anderson, A. Castillo, S. Brugmann, J. Helms, C. Jacobs, and T. Stearns, "Primary cilia: cellular sensors for the skeleton", *Anat. Rec.*, vol. 291, pp. 1074+, 2008.

[63] S. C. Goetz and K. V. Anderson, "The primary cilium: a signalling centre during vertebrate development", *Nat. Rev. Genet.*, vol. 11, pp. 331–344, 2010.

[64] P. V. Bayly, B. L. Lewis, E. C. Ranz, R. J. Okamoto, R. B. Pless, and S. K. Dutcher, "Propulsive Forces on the Flagellum during Locomotion of *Chlamydomonas reinhardtii*", *Biophys. J.*, vol. 100, pp. 2716–2725, 2011.

[65] R. R. Mercer, M. L. Russell, V. L. Roggli, and J. D. Crapo, "Cell number and distribution in human and rat airways", *Am. J. Respir. Cell. Mol. Biol.*, vol. 10, pp. 613–624, 1994.

[66] P. L. Leopold, M. J. O'Mahony, X. J. Lian, A. E. Tilley, B.-G. Harvey, and R. G. Crystal, "Smoking Is Associated with Shortened Airway Cilia", *PLoS ONE*, vol. 4, p. e8157, 2009.

[67] Dartmouth Electron Microscope Facility, Dartmouth College, `http://commons.wikimedia.org/wiki/File:Chlamydomonas_TEM_17.jpg`, Retrieved on 27/07/2013. Licence: Public domain.

[68] C. B. Lindemann and K. A. Lesich, "Flagellar and ciliary beating: the proven and the possible", *J. Cell Sci.*, vol. 123, pp. 519–528, 2010.

[69] I. H. Riedel-Kruse, A. Hilfinger, J. Howard, and F. Jülicher, "How molecular motors shape the flagellar beat", *HFSP Journal*, vol. 1, pp. 192–208, 2007.

[70] J. Blake and A. Chwang, "Fundamental singularities of viscous flow", *J. Eng. Math.*, vol. 8, pp. 23–29, 1974.

[71] D. Woolley and G. Vernon, "A study of helical and planar waves on sea urchin sperm flagella, with a theory of how they are generated", *J. Exp. Biol.*, vol. 204, pp. 1333–1345, 2001.

[72] A. Hilfinger and F. Jülicher, "The chirality of ciliary beats", *Phys. Biol.*, vol. 5, p. 016003, 2008.

[73] A. Hilfinger, A. K. Chattopadhyay, and F. Jülicher, "Nonlinear dynamics of cilia and flagella", *Phys. Rev. E*, vol. 79, p. 051918, 2009.

[74] C. J. Brokaw, "Thinking about flagellar oscillation", *Cell Motil. Cytoskeleton*, vol. 66, pp. 425–436, 2009.

[75] C. J. Brokaw, "Simulation of Cyclic Dynein-Driven Sliding, Splitting, and Reassociation in an Outer Doublet Pair", *Biophys. J.*, vol. 97, pp. 2939–2947, 2009.

[76] P. Martin and A. J. Hudspeth, "Active hair-bundle movements can amplify a hair cell's response to oscillatory mechanical stimuli", *Proc. Natl. Acad. Sci. USA*, vol. 96, pp. 14306–14311, 1999.

[77] A. Hudspeth, "How the ear's works work: mechanoelectrical transduction and amplification by hair cells", *Comptes Rendus Biologies*, vol. 328, pp. 155–162, 2005.

[78] C. Brennen and H. Winet, "Fluid Mechanics of Propulsion by Cilia and Flagella", *Annu. Rev. Fluid Mech.*, vol. 9, pp. 339–398, 1977.

[79] C. Bechinger, F. Sciortino, and P. Ziherl, editors, “Physics of Complex Colloids”, 2012.

[80] H. C. Berg and R. A. Anderson, “Bacteria Swim by Rotating their Flagellar Filaments”, *Nature*, vol. 245, pp. 380–382, 1973.

[81] G. Lowe, M. Meister, and H. C. Berg, “Rapid rotation of flagellar bundles in swimming bacteria”, *Nature*, vol. 325, pp. 637–640, 1987.

[82] R. E. Goldstein, M. Polin, and I. Tuval, “Emergence of Synchronized Beating during the Regrowth of Eukaryotic Flagella”, *Phys. Rev. Lett.*, vol. 107, p. 148103, 2011.

[83] E. Gaffney, H. Gadelha, D. Smith, J. Blake, and J. Kirkman-Brown, “Mammalian Sperm Motility: Observation and Theory”, *Annu. Rev. Fluid Mech.*, vol. 43, p. 501, 2011.

[84] C. S. Peskin, “Mathematical aspects of heart physiology”, Courant Institute of Mathematical Sciences, New York University, 1975.

[85] D. Difrancesco and P. Tortora, “Direct Activation Of Cardiac-Pacemaker Channels By Intracellular Cyclic-Amp”, *Nature*, vol. 351, pp. 145–147, 1991.

[86] J. T. Ariaratnam and S. H. Strogatz, “Phase Diagram for the Winfree Model of Coupled Nonlinear Oscillators”, *Phys. Rev. Lett.*, vol. 86, pp. 4278–4281, 2001.

[87] A. Pikovsky, M. Rosenblum, and J. Kurths, “Synchronization: A Universal Concept in Nonlinear Science”, Cambridge University Press, 2002.

[88] T. Niedermayer, B. Eckhardt, and P. Lenz, “Synchronization, phase locking, and metachronal wave formation in ciliary chains”, *Chaos*, vol. 18, p. 037128, 2008.

[89] Y. Yang, J. Elgeti, and G. Gompper, “Cooperation of sperm in two dimensions: Synchronization, attraction, and aggregation through hydrodynamic interactions”, *Phys. Rev. E*, vol. 78, p. 061903, 2008.

[90] I. H. Riedel, K. Kruse, and J. Howard, "A Self-Organized Vortex Array of Hydrodynamically Entrained Sperm Cells", *Science*, vol. 309, pp. 300–303, 2005.

[91] J. Elgeti, "Sperm and Cilia Dynamics", Ph.D. thesis, Universität Köln, 2006.

[92] D. M. Woolley, "Motility of spermatozoa at surfaces", *Reproduction*, vol. 126, pp. 259–270, 2003.

[93] M. Polin, I. Tuval, K. Drescher, J. P. Gollub, and R. E. Goldstein, "*Chlamydomonas* Swims with Two Gears in a Eukaryotic Version of Run-and-Tumble Locomotion", *Science*, vol. 325, pp. 487–490, 2009.

[94] K. Josef, J. Saranak, and K. W. Foster, "An electro-optic monitor of the behavior of *Chlamydomonas reinhardtii* cilia", *Cell Motil. Cytoskeleton*, vol. 61, pp. 83–96, 2005.

[95] B. M. Friedrich and F. Jülicher, "Flagellar Synchronization Independent of Hydrodynamic Interactions", *Phys. Rev. Lett.*, vol. 109, p. 138102, 2012.

[96] A. Vilfan, "Out of Touch, But Not Out of Sync", *Physics*, vol. 5, p. 107, 2012.

[97] V. Geyer, F. Jülicher, J. Howard, and B. M. Friedrich, "Cell body rocking is a dominant mechanism for flagellar synchronization in a swimming algae", *Arxiv*, 2013.

[98] D. L. Kirk, "Volvox: Molecular-genetic Origins of Multicellularity and Cellular Differentiation", Cambridge University Press, 1998.

[99] J. R. Blake and M. A. Sleigh, "Mechanics of Ciliary Locomotion", *Biol. Rev.*, vol. 49, pp. 85–125, 1974.

[100] S. L. Tamm, T. M. Sonneborn, and R. V. Dippell, "The role of cortical orientation in the control of the direction of ciliary beat in *Paramecium*", *J. Cell Biol.*, vol. 64, pp. 98–112, 1975.

[101] K. Okamoto and Y. Nakaoka, "Reconstitution of Metachronal Waves in Ciliated Cortical Sheets of *Paramecium* — Asymmetry of the Ciliary Movements", *J. Exp. Biol.*, vol. 192, pp. 73–81, 1994.

[102] S. Gueron, "Cilia internal mechanism and metachronal coordination as the result of hydrodynamical coupling", *Proc. Natl. Acad. Sci. USA*, vol. 94, pp. 6001–6006, 1997.

[103] E. Aiello and M. A. Sleigh, "The metachronal wave of lateral cilia of *Mytilus edulis*", *J. Cell Biol.*, vol. 54, pp. 493–506, 1972.

[104] M. J. Sanderson and M. A. Sleigh, "Ciliary activity of cultured rabbit tracheal epithelium: beat pattern and metachrony", *J. Cell Sci.*, vol. 47, pp. 331–347, 1981.

[105] C. Mettot and E. Lauga, "Energetics of synchronized states in three-dimensional beating flagella", *Phys. Rev. E*, vol. 84, p. 061905, 2011.

[106] Naparazzi, `http://www.flickr.com/photos/28990363@N05/2984375333`, Retrieved on 26/07/2013. Licence: Creative Commons BY-SA 2.0.

[107] N. Mizuno, M. Taschner, B. D. Engel, and E. Lorentzen, "Structural Studies of Ciliary Components", *J. Mol. Biol.*, vol. 422, pp. 163–180, 2012.

[108] J. Beisson and M. Jerka-Dziadosz, "Polarities of the centriolar structure: Morphogenetic consequences", *Biol. Cell*, vol. 91, pp. 367–378, 1999.

[109] D. R. Brumley, M. Polin, T. J. Pedley, and R. E. Goldstein, "Hydrodynamic Synchronization and Metachronal Waves on the Surface of the Colonial Alga *Volvox carteri*", *Phys. Rev. Lett.*, vol. 109, p. 268102, 2012.

[110] R. J. B. Francis, B. Chatterjee, N. T. Loges, H. Zentgraf, H. Omran, and C. W. Lo, "Initiation and maturation of cilia-generated flow in newborn and postnatal mouse airway", *Am. J. Physiol.*, vol. 296, pp. L1067–L1075, 2009.

[111] J. L. Stubbs, E. K. Vladar, J. D. Axelrod, and C. Kintner, "Multicilin promotes centriole assembly and ciliogenesis during multiciliate cell differentiation", *Nat. Cell. Biol.*, vol. 14, pp. 140–147, 2012.

[112] E. Dubaissi and N. Papalopulu, "Embryonic frog epidermis: a model for the study of cell-cell interactions in the development of mucociliary disease", *Dis. Model. Mech.*, vol. 4, pp. 179–192, 2011.

[113] B. Button, L.-H. Cai, C. Ehre, M. Kesimer, D. B. Hill, J. K. Sheehan, R. C. Boucher, and M. Rubinstein, "A Periciliary Brush Promotes the Lung Health by Separating the Mucus Layer from Airway Epithelia", *Science*, vol. 337, pp. 937–941, 2012.

[114] B. Mitchell, J. L. Stubbs, F. Huisman, P. Taborek, C. Yu, and C. Kintner, "The PCP Pathway Instructs the Planar Orientation of Ciliated Cells in the *Xenopus* Larval Skin", *Curr. Biol.*, vol. 19, pp. 924–929, 2009.

[115] B. Mitchell, R. Jacobs, J. Li, S. Chien, and C. Kintner, "A positive feedback mechanism governs the polarity and motion of motile cilia", *Nature*, vol. 447, pp. 97–101, 2007.

[116] W. F. Marshall and C. Kintner, "Cilia orientation and the fluid mechanics of development", *Curr. Opin. Cell Biol.*, vol. 20, pp. 48–52, 2008.

[117] J. B. Wallingford, "Planar cell polarity signaling, cilia and polarized ciliary beating", *Curr. Opin. Cell Biol.*, vol. 22, pp. 597–604, 2010.

[118] J. B. Freund, J. G. Goetz, K. L. Hill, and J. Vermot, "Fluid flows and forces in development: functions, features and biophysical principles", *Development*, vol. 139, pp. 1229–1245, 2012.

[119] E. Vladar, R. Bayly, A. Sangoram, M. Scott, and J. Axelrod, "Microtubules Enable the Planar Cell Polarity of Airway Cilia", *Curr. Biol.*, vol. 22, pp. 2203–2212, 2012.

[120] B. Guirao, A. Meunier, S. Mortaud, A. Aguilar, J.-M. Corsi, L. Strehl, Y. Hirota, A. Desoeuvre, C. Boutin, Y.-G. Han, Z. Mirzadeh, H. Cremer,

M. Montcouquiol, K. Sawamoto, and N. Spassky, "Coupling between hydrodynamic forces and planar cell polarity orients mammalian motile cilia", *Nat. Cell Biol.*, vol. 12, pp. 341–350, 2010.

[121] M. Werner and B. Mitchell, "Understanding ciliated epithelia: The power of *Xenopus*", *Genesis*, vol. 50, pp. 176–185, 2012.

[122] B. Guirao and J.-F. Joanny, "Spontaneous Creation of Macroscopic Flow and Metachronal Waves in an Array of Cilia", *Biophys. J.*, vol. 92, pp. 1900–1917, 2007.

[123] S. Gueron and K. Levit-Gurevich, "Energetic considerations of ciliary beating and the advantage of metachronal coordination", *Proc. Natl. Acad. Sci. USA*, vol. 96, pp. 12240–12245, 1999.

[124] S. Furlan, D. Comparini, M. Ciszak, L. Beccai, S. Mancuso, and B. Mazzolai, "Origin of Polar Order in Dense Suspensions of Phototactic Micro-Swimmers", *PLoS ONE*, vol. 7, p. e38895, 2012.

[125] G. J. Elfring and E. Lauga, "Hydrodynamic Phase Locking of Swimming Microorganisms", *Phys. Rev. Lett.*, vol. 103, p. 088101, 2009.

[126] J. Gray and G. J. Hancock, "The Propulsion of Sea-Urchin Spermatozoa", *J. Exp. Biol.*, vol. 32, pp. 802–814, 1955.

[127] J. Lighthill, "Flagellar Hydrodynamics: The John von Neumann Lecture, 1975", *SIAM Review*, vol. 18, pp. 161–230, 1976.

[128] S. Gueron and N. Liron, "Ciliary motion modeling, and dynamic multicilia interactions", *Biophys. J.*, vol. 63, pp. 1045–1058, 1992.

[129] N. Coq, A. Bricard, F.-D. Delapierre, L. Malaquin, O. du Roure, M. Fermigier, and D. Bartolo, "Collective Beating of Artificial Microcilia", *Phys. Rev. Lett.*, vol. 107, p. 014501, 2011.

[130] A. Keißner and C. Brücker, "Directional fluid transport along artificial ciliary surfaces with base-layer actuation of counter-rotating orbital beating patterns", *Soft Matter*, vol. 8, pp. 5342–5349, 2012.

[131] S. Sareh, J. Rossiter, A. Conn, K. Drescher, and R. E. Goldstein, “Swimming like algae: biomimetic soft artificial cilia”, *J. R. Soc. Interface*, 2012.

[132] J. Elgeti and G. Gompper, “Emergence of metachronal waves in cilia arrays”, *Proc. Natl. Acad. Sci. USA*, 2013.

[133] S. Khaderi, J. M. J. den Toonder, and P. R. Onck, “Fluid flow due to collective non-reciprocal motion of symmetrically-beating artificial cilia”, *Biomicrofluidics*, vol. 6, p. 014106, 2012.

[134] M. Vilfan, G. Kokot, A. Vilfan, N. Osterman, B. Kavčič, I. Poberaj, and D. Babič, “Analysis of fluid flow around a beating artificial cilium”, *Beilstein J. Nanotechnol.*, vol. 3, pp. 163–171, 2012.

[135] R. Dreyfus, J. Baudry, M. L. Roper, M. Fermigier, H. A. Stone, and J. Bibette, “Microscopic artificial swimmers”, *Nature*, vol. 437, pp. 862–865, 2005.

[136] C. E. Sing, L. Schmid, M. F. Schneider, T. Franke, and A. Alexander-Katz, “Controlled surface-induced flows from the motion of self-assembled colloidal walkers”, *Proc. Natl. Acad. Sci. USA*, vol. 107, pp. 535–540, 2010.

[137] A. Vilfan and F. Jülicher, “Hydrodynamic Flow Patterns and Synchronization of Beating Cilia”, *Phys. Rev. Lett.*, vol. 96, p. 058102, 2006.

[138] P. Lenz and A. Ryskin, “Collective effects in ciliar arrays”, *Phys. Biol.*, vol. 3, pp. 285–294, 2006.

[139] A. Najafi and R. Golestanian, “Simple swimmer at low Reynolds number: Three linked spheres”, *Phys. Rev. E*, vol. 69, p. 062901, 2004.

[140] A. Najafi and R. Golestanian, “Coherent hydrodynamic coupling for stochastic swimmers”, *Europhys. Lett.*, vol. 90, p. 68003, 2010.

[141] N. Uchida and R. Golestanian, “Synchronization and Collective Dynamics in a Carpet of Microfluidic Rotors”, *Phys. Rev. Lett.*, vol. 104, p. 178103, 2010.

[142] N. Uchida and R. Golestanian, “Generic Conditions for Hydrodynamic Synchronization”, *Phys. Rev. Lett.*, vol. 106, p. 058104, 2011.

[143] N. Uchida and R. Golestanian, “Hydrodynamic synchronization between objects with cyclic rigid trajectories”, *Eur. Phys. J. E*, vol. 35, p. 135, 2012.

[144] R. R. Bennett and R. Golestanian, “Emergent Run-and-Tumble Behavior in a Simple Model of *Chlamydomonas* with Intrinsic Noise”, *Phys. Rev. Lett.*, vol. 110, p. 148102, 2013.

[145] R. R. Bennett and R. Golestanian, “Phase Dependent Forcing and Synchronization in the three-sphere model of Chlamydomonas”, *Arxiv*, 2013.

[146] C. Wollin and H. Stark, “Metachronal waves in a chain of rowers with hydrodynamic interactions”, *Eur. Phys. J. E*, vol. 34, p. 42, 2011.

[147] J. Kotar, M. Leoni, B. Bassetti, M. Cosentino Lagomarsino, and P. Cicuta, “Hydrodynamic synchronization of colloidal oscillators”, *Proc. Natl. Acad. Sci. USA*, vol. 107, pp. 7669–7673, 2010.

[148] M. Leoni, J. Kotar, B. Bassetti, P. Cicuta, and M. C. Lagomarsino, “A basic swimmer at low Reynolds number”, *Soft Matter*, vol. 5, pp. 472–476, 2009.

[149] M. Leoni, B. Bassetti, J. Kotar, P. Cicuta, and M. Cosentino Lagomarsino, “Minimal two-sphere model of the generation of fluid flow at low Reynolds numbers”, *Phys. Rev. E*, vol. 81, p. 036304, 2010.

[150] M. Leoni and T. B. Liverpool, “Hydrodynamic synchronization of nonlinear oscillators at low Reynolds number”, *Phys. Rev. E*, vol. 85, p. 040901, 2012.

[151] M. Leoni, “A geometric approach to the synchronization of a pair of two-state switching rowers interacting hydrodynamically”, *Nonlinearity*, vol. 25, p. 2953, 2012.

[152] M. Cosentino Lagomarsino, B. Bassetti, and P. Jona, “Rowers coupled hydrodynamically. Modeling possible mechanisms for the cooperation of cilia”, *Eur. Phys. J. B*, vol. 26, pp. 81–88, 2002.

[153] M. Cosentino Lagomarsino, P. Jona, and B. Bassetti, “Metachronal waves for deterministic switching two-state oscillators with hydrodynamic interaction”, *Phys. Rev. E*, vol. 68, p. 021908, 2003.

[154] G. M. Cicuta, E. Onofri, M. C. Lagomarsino, and P. Cicuta, “Patterns of synchronization in the hydrodynamic coupling of active colloids”, *Phys. Rev. E*, vol. 85, p. 016203, 2012.

[155] L. Damet, G. M. Cicuta, J. Kotar, M. C. Lagomarsino, and P. Cicuta, “Hydrodynamically synchronized states in active colloidal arrays”, *Soft Matter*, vol. 8, pp. 8672–8678, 2012.

[156] R. Lhermerout, N. Bruot, G. M. Cicuta, J. Kotar, and P. Cicuta, “Collective synchronization states in arrays of driven colloidal oscillators”, *New J. Phys.*, vol. 14, p. 105023, 2012.

[157] N. Bruot, L. Damet, J. Kotar, P. Cicuta, and M. Cosentino Lagomarsino, “Noise and Synchronization of a Single Active Colloid”, *Phys. Rev. Lett.*, vol. 107, p. 094101, 2011.

[158] N. Bruot, J. Kotar, F. de Lillo, M. Cosentino Lagomarsino, and P. Cicuta, “Driving Potential and Noise Level Determine the Synchronization State of Hydrodynamically Coupled Oscillators”, *Phys. Rev. Lett.*, vol. 109, p. 164103, 2012.

[159] N. Bruot and P. Cicuta, “Emergence of polar order and cooperativity in hydrodynamically coupled model cilia”, *J. R. Soc. Interface*, vol. 10, 2013.

[160] M. P. Curtis and E. A. Gaffney, “Three-sphere swimmer in a nonlinear viscoelastic medium”, *Phys. Rev. E*, vol. 87, p. 043006, 2013.

[161] N. Koumakis and R. Di Leonardo, “Stochastic Hydrodynamic Synchronization in Rotating Energy Landscapes”, *Phys. Rev. Lett.*, vol. 110, p. 174103, 2013.

[162] V. Lobaskin, D. Lobaskin, and I. M. Kulić, "Brownian dynamics of a microswimmer", *Eur. Phys. J. Special Topics*, vol. 157, pp. 149–156, 2008.

[163] V. A. Vladimirov, "On self-propulsion of N-sphere micro-robot", *Arxiv*, 2012.

[164] V. A. Vladimirov, "Self-propulsion of V-shape micro-robot", *Arxiv*, 2012.

[165] J. R. Blake, N. Liron, and G. K. Aldis, "Flow patterns around ciliated microorganisms and in ciliated ducts", *J. Theor. Biol.*, vol. 98, pp. 127–141, 1982.

[166] S. Y. Reigh, R. G. Winkler, and G. Gompper, "Synchronization and bundling of anchored bacterial flagella", *Soft Matter*, pp. 4363–4372, 2012.

[167] B. Qian, H. Jiang, D. A. Gagnon, K. S. Breuer, and T. R. Powers, "Minimal model for synchronization induced by hydrodynamic interactions", *Phys. Rev. E*, vol. 80, p. 061919, 2009.

[168] E. Lauga and R. E. Goldstein, "Dance of the microswimmers", *Physics Today*, vol. 65, pp. 30–35, 2012.

[169] R. Golestanian and A. Ajdari, "Analytic results for the three-sphere swimmer at low Reynolds number", *Phys. Rev. E*, vol. 77, p. 036308, 2008.

[170] R. Golestanian and A. Ajdari, "Mechanical Response of a Small Swimmer Driven by Conformational Transitions", *Phys. Rev. Lett.*, vol. 100, p. 038101, 2008.

[171] D. J. Earl, C. M. Pooley, J. F. Ryder, I. Bredberg, and J. M. Yeomans, "Modeling microscopic swimmers at low Reynolds number", *J. Chem. Phys.*, vol. 126, p. 064703, 2007.

[172] Bangs Laboratories, "Product data sheet 702, silica microspheres", `http://www.bangslabs.com/sites/default/files/bangs/docs/pdf/PDS%20702%20Web.pdf`, Retrieved on 01/08/2013.

[173] M. J. O'Neil, "The Merck Index, 13th Ed.", Merck & Co., 2001.

[174] J. E. Curtis, B. A. Koss, and D. G. Grier, "Dynamic holographic optical tweezers", *Opt. Commun.*, vol. 207, pp. 169–175, 2002.

[175] M. Woerdemann, "Holographic Optical Tweezers", in "Structured Light Fields," Springer Berlin Heidelberg, 2012.

[176] M. Polin, K. Ladavac, S.-H. Lee, Y. Roichman, and D. Grier, "Optimized holographic optical traps", *Opt. Express*, vol. 13, pp. 5831–5845, 2005.

[177] Y. Sokolov, D. Frydel, D. G. Grier, H. Diamant, and Y. Roichman, "Hydrodynamic Pair Attractions between Driven Colloidal Particles", *Phys. Rev. Lett.*, vol. 107, p. 158302, 2011.

[178] D. L. Ermak and J. A. McCammon, "Brownian dynamics with hydrodynamic interactions", *J. Chem. Phys.*, vol. 69, pp. 1352–1360, 1978.

[179] L. Damet, "Hydrodynamic synchronisation at low Reynolds number", Master's thesis, Université Paris Sud XI, 2010.

[180] V. Putz and J. Yeomans, "Hydrodynamic Synchronisation of Model Microswimmers", *J. Stat. Phys.*, vol. 137, pp. 1001–1013, 2009.

[181] S. Redner, "A Guide to First-passage Processes", Cambridge University Press, 2007.

[182] J. Baumgart, M. Fleischer, Y. M. Yarin, and R. Grundmann, "Fluid Flow around the Stereocilia", in "8th International Symposium on Experimental and Computational Aerothermodynamics of Internal Flows," 2007.

[183] M. Polin, D. G. Grier, and S. R. Quake, "Anomalous Vibrational Dispersion in Holographically Trapped Colloidal Arrays", *Phys. Rev. Lett.*, vol. 96, p. 088101, 2006.

[184] R. Di Leonardo, S. Keen, J. Leach, C. D. Saunter, G. D. Love, G. Ruocco, and M. J. Padgett, "Eigenmodes of a hydrodynamically

coupled micron-size multiple-particle ring", *Phys. Rev. E*, vol. 76, p. 061402, 2007.

[185] N. Garreau De Loubresse, G. Keryer, B. Vigus, and J. Beisson, "A contractile cytoskeletal network of Paramecium: the infraciliary lattice", *J. Cell Sci.*, vol. 90, pp. 351–364, 1988.

[186] F. Iftode, J. Cohen, F. Ruiz, A. Rueda, L. Chen-Shan, A. Adoutte, and J. Beisson, "Development of surface pattern during division in *Paramecium* — I. Mapping of duplication and reorganization of cortical cytoskeletal structures in the wild type", *Development*, vol. 105, pp. 191–211, 1989.

[187] K. Polotzek and B. M. Friedrich, "A three-sphere swimmer for flagellar synchronization", *New J. Phys.*, vol. 15, p. 045005, 2013.

[188] J. Kotar, L. Debono, N. Bruot, S. Box, D. Phillips, S. Simpson, S. Hanna, and P. Cicuta, "Optimal hydrodynamic synchronization of colloidal rotors", *Submitted*, 2013.

[189] Y. Deng, J. Bechhoefer, and N. R. Forde, "Brownian motion in a modulated optical trap", *J. Opt. A: Pure Appl. Opt.*, vol. 9, p. S256, 2007.

[190] D. Brumley and M. Polin, Private communication, 2013.

[191] B. Mihiretie, J.-C. Loudet, and B. Pouligny, "Optical levitation and long-working-distance trapping: From spherical up to high aspect ratio ellipsoidal particles", *J. Quant. Spectrosc. Radiat. Transfer*, vol. 126, pp. 61–68, 2013.

[192] I. Kavre, Private communication, 2013.

[193] J. Espinosa-Garcia, E. Lauga, and R. Zenit, "Fluid elasticity increases the locomotion of flexible swimmers", *Phys. Fluids*, vol. 25, p. 031701, 2013.

Copyright © 2013 Nicolas Bruot.

You are free to print and keep copies in electronic format of this document for personal use. For other uses and reproductions, please visit `http://www.bruot.org/contact` to contact me.